


Spring 2012

Single and Double Spin Asymmetries for Pion Electro-Production From the Deuteron in the Resonance Region

Sharon L. Careccia
Old Dominion University

Follow this and additional works at: https://digitalcommons.odu.edu/physics_etds

 Part of the [Elementary Particles and Fields and String Theory Commons](#), and the [Nuclear Commons](#)

Recommended Citation

Careccia, Sharon L.. "Single and Double Spin Asymmetries for Pion Electro-Production From the Deuteron in the Resonance Region" (2012). Doctor of Philosophy (PhD), dissertation, Physics, Old Dominion University, DOI: 10.25777/ezgf-7q33
https://digitalcommons.odu.edu/physics_etds/35

This Dissertation is brought to you for free and open access by the Physics at ODU Digital Commons. It has been accepted for inclusion in Physics Theses & Dissertations by an authorized administrator of ODU Digital Commons. For more information, please contact digitalcommons@odu.edu.

**SINGLE AND DOUBLE SPIN ASYMMETRIES FOR
 π^- ELECTRO-PRODUCTION FROM THE DEUTERON IN THE
RESONANCE REGION**

by

Sharon L. Careccia
M.S. Old Dominion University (2003)
B.S. Old Dominion University (2001)

A Dissertation Submitted to the Faculty of
Old Dominion University in Partial Fulfillment of the
Requirements for the Degree of

DOCTOR OF PHILOSOPHY

PHYSICS

OLD DOMINION UNIVERSITY

May 2012

Approved by:

Gail E. Dodge (Director)

Sebastian E. Kuhn (Member)

Deposava Vuskoviq (Member)

Anatoly Radyushkin (Member)

Margaret Muholland (Member)

ABSTRACT

SINGLE AND DOUBLE SPIN ASYMMETRIES FOR π^- ELECTRO- PRODUCTION FROM THE DEUTERON IN THE RESONANCE REGION

Sharon L. Careccia
Old Dominion University, 2012
Director: Dr. Gail E. Dodge

The single and double spin asymmetries A_t and A_{et} have been measured in π^- electro-production off the deuteron using a longitudinally polarized electron beam and a polarized ND_3 target. The electron beam was polarized using a strained GaAs cathode and the target was polarized using Dynamic Nuclear Polarization. The data were collected at beam energies of 1.6, 1.7, 2.5 and 4.2 GeV in Hall B at Jefferson Lab in the spring of 2001. The final state particles were detected in the CEBAF Large Acceptance Spectrometer (CLAS). The $d(e, e' \pi^- p)p$ exclusive channel was identified using the missing mass technique and the asymmetries were extracted as a function of the momentum transfer Q^2 , invariant mass W , and center of mass pion angles $\cos(\theta^*)$ and ϕ^* . The results are generally in agreement with the phenomenological model MAID at low energies, but there are discrepancies in the 2nd and 3rd resonance regions, as well as at forward angles.

© Copyright, 2012, by Sharon L. Careccia, All Rights Reserved.

This thesis is dedicated to my parents, Thomas and Mary Thompson

ACKNOWLEDGMENTS

I thank my advisor Gail Dodge for her help and guidance. I thank my committee members, Sebastian Kuhn, Lepsha Vuskovic, Anatoly Radyushkin and Margaret Mulholland for their support. I thank the EG1 working group including Angela Biselli, Yelena Prok, Vipuli Dharmawardane, Peter Bosted and Ralph Minehart for their input, help and support. I thank my fellow graduate students in the EG1 group, including Josh Pierce for all the work he did with the polarized target group and his input on the DST reader, Nevzat Guler, Rob Fersch and Mike Mayer for their advice on analysis as well as their help on programming issues. I thank Jixie Zhang for all his help on computer and programming problems. I thank my fellow ODU graduate students including Donika Plyku, Krishna Adhikari and Suman Koirala for our hallway asymmetry discussions, and a special thank you to Mike Shafer, Jan Drake and Jason Martinez for being great and true friends. Finally I would like to thank the faculty and staff of the ODU Physics Department.

TABLE OF CONTENTS

	Page
LIST OF TABLES	ix
LIST OF FIGURES	x
1. INTRODUCTION	1
1.1 STRONG FORCE.....	1
1.2 HADRONS	1
1.2.1 MESONS	3
1.2.2 BARYONS	3
1.3 ELECTRON SCATTERING.....	4
1.4 PION ELECTRO-PRODUCTION	7
2. MOTIVATION	10
2.1 FORMALISM AND KINEMATICS	10
2.2 DIFFERENTIALCROSS SECTIONS.....	13
2.3 HELICITY AMPLITUDES	15
2.4 RESPONSE FUNCTIONS	18
2.5 CGLN AMPLITUDES	22
2.6 ASYMMETRIES.....	24
2.6.1 INCLUSIVE ASYMMETRIES	25
2.7. BARYON RESONANCES	28
2.7.1 THE DELTA REGION	29
2.7.2 THE SECOND RESONANCE REGION	30
2.7.2.1 THE ROPER RESONANCE	31
2.7.2.2 THE $D_{13}(1520)$ AND $S_{11}(1535)$ RESONANCES.....	31
2.7.3 HIGHER RESONANCES	32
2.8 THEORETICAL MODELS.....	32
2.8.1 THE HAMILTONIAN FORMULATION.....	35
2.8.2 MAID	38
2.8.3 SAID.....	40
2.9 NUCLEON RESONANCES	41
3. EXPERIMENTAL SET-UP.	43
3.1 INTRODUCTION	43
3.2 THE POLARIZED BEAM.....	43
3.2.1 POLARIZATION MECHANISM	44
3.2.2 SPIN PROCESSION.....	46
3.2.3 HELICITY SWITCHING	46
3.2.4 POLARIZATION MEASUREMENT	47
3.2.5 BEAM POSITION AND RASTER	48
3.2.6 ADDITIONAL SCALARS	49

3.3 POLARIZED TARGET.....	50
3.3.1 POLARIZATION MECHANISM	50
3.3.2 DYNAMIC NUCLEAR POLARIZATION (DNP)	52
3.3.3 THE CLAS POLARIZED TARGET	53
3.3.4 THE TARGET STICK.....	55
3.3.5 NMR MEASUREMENT.....	56
3.4 THE CLAS DETECTOR.....	58
3.4.1 THE TORUS MAGNET	58
3.4.2 DRIFT CHAMBERS.....	60
3.4.3 ČERENKOV DETECTORS	62
3.4.4 TIME OF FLIGHT	64
3.4.5 ELECTROMAGNETIC CALOREMETER	65
3.5 DATA ACQUISITION AND TRIGGER.....	67
3.6 TRACKING AND START TIME RECONSTRUCTION.....	69
4. DATA ANALYSIS.....	71
4.1 INTRODUCTION	71
4.2 DETECTOR CALIBRATION.....	71
4.2.1 TIME OF FLIGHT CALIBRATION	72
4.2.2 ČERENKOV DETECTOR CALIBRATION	74
4.2.3 DRIFT CHAMBER CALIBRATION.....	74
4.2.4 ELECTROMAGNETIC CALORIMETER CALIBRATION	76
4.3 RUN SELECTION	80
4.3.1 TARGET MATERIAL.....	81
4.3.2 EVENT RATES	81
4.4 CORRECTIONS	82
4.4.1 RASTER CORRECTIONS	83
4.4.2 Z VERTEX CORRECTIONS	85
4.4.3 BEAM HELICITY SWITCHING.....	85
4.4.4 TARGET AND BEAM HELICITY SIGN	86
4.4.5 MOMENTUM CORRECTIONS	86
4.4.6 MULTIPLE SCATTERING CORRECTIONS.....	87
4.4.7 ENERGY LOSS	87
4.4.8 TARGET MAGNETIC FIELD.....	88
4.5 FIDUCIAL CUTS.....	88
4.5.1 DETERMINING INEFFICIENT CC REGIONS	88
4.5.2 DETERMINING FIDUCIAL CUT BOUNDARIES.....	89
4.6 PARTICLE IDENTIFICATION	90
4.6.1 ELECTRON IDENTIFICATION	91
4.6.2 π^- IDENTIFICATION	94
4.6.3 PROTON IDENTIFICATION	96
4.7 EXCLUSIVE CHANNEL SELECTION	96
4.7.1 EXCLUSIVE $n(e,e'\pi^-)p$ CHANNEL	96
4.7.2 EXCLUSIVE $d(e,e'\pi^-)p$ CHANNEL	97
4.8 BACKGROUND	97

4.9 PION CONTAMINATION	100
4.10 BEAM AND TARGET POLARIZATION ($P_B P_T$).....	104
4.10.1 EXCLUSIVE $P_B P_T$	106
5. RESULTS	113
5.1 INTRODUCTION	113
5.2 ASYMMETRIES.....	113
5.2.1 BINNING	120
5.2.2 COMBINING ASYMMETRIES	121
5.2.3 DETERMINING THE RATIO OF TARGET THICKNESS R_T	136
5.3 THE BEAM SPIN ASYMMETRY	136
5.4 THE TARGET SPIN ASYMMETRY.....	138
5.5 THE DOUBLE SPIN ASYMMETRY	143
5.6 CORRECTIONS TO ASYMMETRIES.....	157
5.6.1 ACCEPTANCE.....	157
5.6.2 RADIATIVE CORRECTIONS.....	157
5.7 SYSTEMATIC ERRORS.....	158
5.7.1 BACKGROUND.....	158
5.7.2 ACCEPTANCE.....	158
5.7.3 EVENT SELECTION	159
5.7.4 $P_B P_T$	160
5.7.5 SUMMARY OF OVERALL SYSTEMATIC ERRORS.....	160
6. OUTLOOK AND CONCLUSION.....	165
REFERENCES	168
APPENDIX A	173
APPENDIX B	175
APPENDIX C	177
APPENDIX D.....	178
APPENDIX E	179
APPENDIX F.....	180
VITA.....	186

LIST OF TABLES

Table	Page
1. Properties of quarks	2
2. Pion properties	3
3. Decomposition of Pion Photoproduction Amplitudes into Multipole Components	22
4. Target chamber parameters.....	53
5. Torus currents for EG1b	58
6. The data run set for EG1b.....	80
7. Standard electron cuts	94
8. G_E and G_M Form Factors.....	105
9. Proton Identification.....	110
10. Elastic event cuts.....	111
11. Values of $P_B P_T$ for EG1b data.....	112
12. Kinematic binning for the invariant mass W	124
13. Kinematic binning for the square of the momentum transfer Q	124
14. Kinematic binning for ϕ^*	125
15. Kinematic binning for $\cos(\theta^*)$	125
16. Mean of the T-test Distribution and Expected Statistical Uncertainty for 1.6 GeV Data.....	162
17. Mean of the T-test Distribution and Expected Statistical Uncertainty for 2.5 GeV Data	163
18. Mean of the T-test Distribution and Expected Statistical Uncertainty for 4.2 GeV Data	164

19. Properties of Resonances in the First Three Regions.....179

LIST OF FIGURES

Figure	Page
1. Inclusive electron scattering cross-sections	6
2. Diagram for the one photon exchange for pion electro-production.....	10
3. Diagram showing the two step electro-production resonance reaction	11
4. The $(e,e'\pi)$ scattering process showing kinematic variables of interest.....	12
5. Helicity amplitude representation	17
6. Previous double spin asymmetries.....	28
7. Feynmann diagrams for pion photo or electro-production	34
8. Tree diagrams for meson-baryon interactions	36
9. Schematic of the Jefferson Lab accelerator components.....	44
10. A comparison of the energy gap between pure and strained GaAs	46
11. Harp scan showing the x and y position of the beam	49
12. Energy level diagram for an electron proton pair	53
13. Cross-section of the target chamber in CLAS	54
14. Front and side views of the target stick	56
15. The CLAS torus coils.....	59
16. One drift chamber wedge.....	60
17. Schematic showing two super-layers of the drift chamber wires	61
18. The Čerenkov detector for one sector.....	63
19. Scintillators for the time of flight detector.....	65
20. Cross-section of the forward calorimeter showing the lead scintillator Sandwich and exploded view.....	68

21.	Particle tracks showing the matching of tracks from the drift chamber to the other detector elements	70
22.	Time difference between particles at the time of flight and the electromagnetic calorimeter before and after EC timing calibrations	78
23.	Scatter plots of events vs. time before and after EC timing calibrations.....	79
24.	Inclusive count rates due to target thickness for 2.5 GeV outbending data.....	82
25.	Helicity sync bit and helicity bit	86
26.	The W spectrum before and after momentum corrections	87
27.	Drift chamber angles θ vs ϕ for the number of photoelectrons for each sector....	90
28.	The number of photoelectrons in the Čerenkov detector.....	92
29.	Energy deposited in the electromagnetic calorimeter	93
30.	Energy deposited in the electromagnetic calorimeter as a function of momentum	94
31.	Time difference for negatively charged particles	95
32.	The missing mass spectrum for ND ₃ , carbon and the deuteron	99
33.	Missing mass spectrum using standard electron cuts and using “pion” cuts.....	101
34.	The missing mass spectrum for ND ₃ , carbon and the deuteron for each W bin for $n(e,e'\pi^-)X$	102
35.	The missing mass spectrum for ND ₃ , carbon and the deuteron for each W bin for $d(e,e'\pi^-)p$	103
36.	$\Delta\phi$ for ND ₃ , carbon and the deuteron.....	109
37.	Missing energy plots.....	109
38.	Missing transverse momentum plots.....	110
39.	Exclusive $P_B P_T$	111
40.	Regions of Acceptance for Q^2 and W	122

41.	Regions of Acceptance for $\cos\theta^*$ and ϕ^*	123
42.	T-test for channel comparison between $n(e,e'\pi^-)p$ and $d(e,e'\pi^-)p$ for A_{et} and A_t for 1.6 GeV positive toruse current.....	127
43.	T-test for channel comparison between $n(e,e'\pi^-)p$ and $d(e,e'\pi^-)p$ for A_{et} and A_t for 1.7 GeV negative toruse current.....	128
44.	T-test for channel comparison between $n(e,e'\pi^-)p$ and $d(e,e'\pi^-)p$ for A_{et} and A_t for 2.5 GeV positive toruse current.....	129
45.	T-test for channel comparison between $n(e,e'\pi^-)p$ and $d(e,e'\pi^-)p$ for A_{et} and A_t for 2.5 GeV negative toruse current.....	130
46.	T-test for channel comparison between $n(e,e'\pi^-)p$ and $d(e,e'\pi^-)p$ for A_{et} and A_t for 4.2 GeV positive toruse current.....	131
47.	T-test for channel comparison between $n(e,e'\pi^-)p$ and $d(e,e'\pi^-)p$ for A_{et} and A_t for 4.2 GeV negative toruse current.....	132
48.	T-test on the comparison between inbending data with outbending data for 1.6 GeV and 1.7 GeV.....	133
49.	T-test on the comparison between inbending data with outbending data for 2.5 GeV.....	134
50.	T-test on the comparison between inbending data with outbending data for 4.2 GeV.....	135
51.	A_e as a function of ϕ^* for 1.6 GeV positive torus current.....	137
52.	A_e as a function of W for 1.6 GeV positive torus current.....	137
53.	A_t as a function of ϕ^* for three W regions for 1.6 GeV positive torus current.....	139
54.	A_t as a function of ϕ^* in five $\cos(\theta^*)$ bins and two Q^2 bins in the delta region for 1.6 GeV data.....	140
55.	A_t as a function of ϕ^* in five $\cos(\theta^*)$ bins and two Q^2 bins in the S_{11} region for 1.6 GeV data.....	141
56.	A_t as a function of ϕ^* in five $\cos(\theta^*)$ bins and two Q^2 bins in the third resonance region for 1.6 GeV data.....	142
57.	A_{et} as a function of W for 1.6 GeV, 2.5 GeV and 4.2 GeV data.....	144

58.	A_{et} as a function of W for three Q^2 bins for 1.6 GeV data.....	145
59.	A_{et} as a function of W for three Q^2 bins for 2.5 GeV data.....	146
60.	A_{et} as a function of W for three Q^2 bins for 4.2 GeV data.....	147
61.	A_{et} as a function of ϕ^* in five $\cos(\theta^*)$ bins and two Q^2 bins in the delta region for 1.6 GeV data.....	148
62.	A_{et} as a function of ϕ^* in five $\cos(\theta^*)$ bins and two Q^2 bins in the S_{11} region for 1.6 GeV data.....	149
63.	A_{et} as a function of ϕ^* in five $\cos(\theta^*)$ bins and two Q^2 bins in the third resonance region for 1.6 GeV data.....	150
64.	A_{et} as a function of ϕ^* in five $\cos(\theta^*)$ bins and two Q^2 bins in the delta region for 2.5 GeV data.....	151
65.	A_{et} as a function of ϕ^* in five $\cos(\theta^*)$ bins and two Q^2 bins in the S_{11} region for 2.5 GeV data.....	152
66.	A_{et} as a function of ϕ^* in five $\cos(\theta^*)$ bins and two Q^2 bins in the third resonance region for 2.5 GeV data.....	153
67.	A_{et} as a function of ϕ^* in five $\cos(\theta^*)$ bins and two Q^2 bins in the delta region for 4.2 GeV data.....	154
68.	A_{et} as a function of ϕ^* in five $\cos(\theta^*)$ bins and two Q^2 bins in the S_{11} region for 4.2 GeV data.....	155
69.	A_{et} as a function of ϕ^* in five $\cos(\theta^*)$ bins and two Q^2 bins in the third resonance region for 4.2 GeV data.....	156
70.	Systematic change on event secection by comparing low missing mass cut to high missing mass cut.....	161
71.	Systematic change on event selection by comparing narrow missing mass cut to the missing mass region wings	161
72.	The missing mass spectrum for ND ₃ , carbon and the deuteron for each W bin for $n(e,e'\pi^-)X$ for 1.7GeV.....	180
73.	The missing mass spectrum for ND ₃ , carbon and the deuteron for each W bin for $n(e,e'\pi^-)X$ for 2.5 GeV.....	181

74. The missing mass spectrum for ND₃, carbon and the deuteron for each
W bin for n(e,e'π⁻)X for 4.2 GeV.....182
75. The missing mass spectrum for ND₃, carbon and the deuteron for each
W bin for d(e,e'π⁻p)X for 1.7GeV.....183
76. The missing mass spectrum for ND₃, carbon and the deuteron for each
W bin for d(e,e'π⁻p)X for 2.5 GeV.....184
77. The missing mass spectrum for ND₃, carbon and the deuteron for each
W bin for d(e,e'π⁻p)X for 4.2 GeV.....185

CHAPTER 1

INTRODUCTION

1.1 STRONG FORCE

By the latter half of the 20th century, physicists had learned that there are four fundamental forces, the gravitational force, the electromagnetic force, the weak force and the strong force. The primary goal of modern nuclear physics is to study the nucleus of the atom including the strong and weak force contributions to its properties. An atom is composed of a dense nucleus in the center of an electron cloud. It was once believed that the nucleus was made entirely from protons. Chadwick made the discovery of a neutral object, the neutron. This discovery showed that the nucleus is a composite object, composed of neutrons and protons (ie, nucleons). Since the protons in the nucleus are positively charged objects, they should repel one another strongly instead of staying closely packed together at the center of the atom. The fact that they do stay together shows that there is a force holding the nucleons together that is much stronger than the repulsive electromagnetic force. This is the nuclear strong force, which has a finite range of the order of 1.4 fermi, unlike its electromagnetic counterpart, which varies proportional to $1/r^2$ and whose range extends throughout all space.

1.2 HADRONS

One of the goals of strong interaction physics is to obtain information on the structure of the nucleon and other strongly interacting particles. In 1964, Gell-Mann and Zweig independently proposed that all strongly interacting particles (hadrons) are in fact composite particles themselves, composed of smaller particles which Gell-Mann called quarks [1]. Today we know that hadronic matter, including protons and neutrons, are

This dissertation follows the style of *Physical Review D*.

composed of six “flavors” of quarks: up (u), down(d), strange (s), charm (c), bottom (b) and top (t).

Table 1 Properties of quarks [2,3,4].

Name	Quark	Spin	Charge (e)	Mass (GeV/c ²)	Isospin
Up	u	1/2	2/3	0.0015 – 0.005	1/2
Down	d	1/2	-1/3	0.003 – 0.009	1/2
Strange	s	1/2	-1/3	0.06 – 0.17	0
Charm	c	1/2	2/3	1.1 – 1.4	0
Bottom	b	1/2	-1/3	4.1 – 4.4	0
Top	t	1/2	2/3	168.6 – 179.0	0

To explain the electric charge and other quantum numbers of hadronic particles, the six flavors of quarks were assigned fractional electric charges as shown in Table 1. For example, the proton is the bound state of the three quarks (uud), and neutron is the bound state of the three quarks (ddu). These quarks are spin 1/2 particles or fermions.

In the beginning of the 1900s it was known that the electromagnetic force between two charged objects is produced by the exchange of virtual photons. Because this is a long range force, the exchange field particles (photons) have zero mass. Likewise, to describe the nature of the short range strong force in terms of the exchange of virtual particles, H. Yukawa postulated the existence of a particle that would have a mass 300 times more than an electron or 1/6 the mass of a proton [5]. This particle is called the pion.

1.2.1 Mesons

Mesons are composed of quark-antiquark pairs giving the meson either spin-1 or spin-0. Pions are the lightest mass particles in the meson group. Pions are found in three different states: two charged states, the π^+ and π^- , and a neutral or uncharged state, the π^0 .

Table 2 Pion properties [6].

Particle	Charge	Isospin	I_z	J^P	Mass (GeV/c ²)
π^+	+1	1	+1	0^-	0.140
π^-	-1	1	-1	0^-	0.140
π^0	0	1	0	0^-	0.135

Pions shown in Table 2 are, in fact, mesons. Pions are formed from up – anti-down ($u \bar{d}$), down – anti-up ($d \bar{u}$) or a linear combination of $u \bar{u}$ and $d \bar{d}$ quarks.

1.2.2 Baryons

Baryons, such as protons, neutrons, Δ , Σ , and Ω are formed from three quarks. Anti-baryons are formed from three anti-quarks. Since baryons are half integer spin, then some baryons such as the Δ^{++} and the Ω^- which are made up from (uuu) and (sss), respectively, would seem to violate the Pauli exclusion principle which states that no two particles can occupy the same state. This was originally stated for electrons but does apply to all half integer spin particles. O. W. Greenberg suggested that quarks not only have flavor (udscbt), but also have a “color” charge namely, red, green and blue [7]. Baryons have three quarks, one of each “color”, whereas mesons have quarks with color

and anti-color. Quarks are bound inside hadrons and interact by the exchange of gluons that couple to color charge. The quark gluon structure of all strongly interacting particles is described by a fundamental theory known as quantum chromodynamics (QCD).

1.3 ELECTRON SCATTERING

Scattering experiments are a means of gaining an understanding of all observable objects in our daily lives. For example, in order to take a picture one must perform a scattering experiment. A stream of visible light in the form of particles (photons) from the sun or a lamp scatters off of the object of interest and into our “detector” the camera, which records the intensity (brightness) and energy (color) onto film (or memory chip) in the camera. According to quantum mechanics, the resolution of the object of interest is proportional to the wavelength of the photons, which is inversely proportional to the photon energy. We can observe objects with a size on the order of a few hundred nanometers with photons in the visible light range. To probe objects smaller than a few hundred nanometers, we need higher energy photons. In nuclear physics we are interested in atomic nuclei and their constituents, protons and neutrons, which are of the order of 10^{-15} m or smaller. To achieve this resolution, we need wavelengths of that order or smaller. One method to achieve very small wavelengths is by electron scattering.

Electron scattering from a nuclear target is a useful tool for the exploration of QCD for two reasons. First, the electron is not a strongly interacting particle and its interaction is governed by Quantum Electrodynamics (QED), which is well understood and carefully tested, and will not interfere with the QCD system. The accuracy of the known parameters of QED allows the contribution of the electron to be taken into account in the scattering process. The second reason is that electrons can be accelerated

to high energies and therefore small wavelengths quite easily.

The rate of scattered particles in a scattering experiment depends on the luminosity and the cross section. The luminosity is the total number of electrons per second times the number of target particles per unit area. The cross section is the probability that scattering will occur. The statistical error is proportional to the square root of the number of detected scattered particles. The more scattered particles there are, the lower the percent error becomes. It is clear that having as high a luminosity as possible is important for an accurate measurement.

The development of high intensity, high duty cycle electron accelerators such as BATES (MIT), MAMI (Mainz) and Jefferson Lab (Newport News, Virginia) has made possible many experiments that were previously not feasible. These accelerators allow coincidence experiments, and beam quality sufficient for use with high-resolution spectrometers. If the collision is elastic, then the target remains in its ground state. Only its momentum changes. If the collision is inelastic, then some of the energy is deposited in the nucleon, exciting it to higher energy states. If the deposited energy is high enough, then the electron can scatter elastically off a single quark in the nucleon, which is known as deep inelastic scattering (DIS). At lower energies, the nucleon as a whole absorbs the deposited energy, leading to excited states of the nucleon. These states are also known as resonances. Fig. 1 shows the cross sections from inclusive electron scattering, where only the scattered electron is detected. The top plot is electron scattering off the proton, where three resonance regions are clearly visible. The most prominent resonant state is the $\Delta(1232)$ [8, 9]. The second and third resonance regions are made up from overlapping resonances. The bottom plot in Fig. 1 shows inclusive scattering off of the

deuteron. The resonances are clearly smeared out because of effects such as binding effects (ie, what holds the nucleon together) and (Fermi) motion of nucleons in the nucleus due to the fact that the deuteron is a bound state of a proton and a neutron.

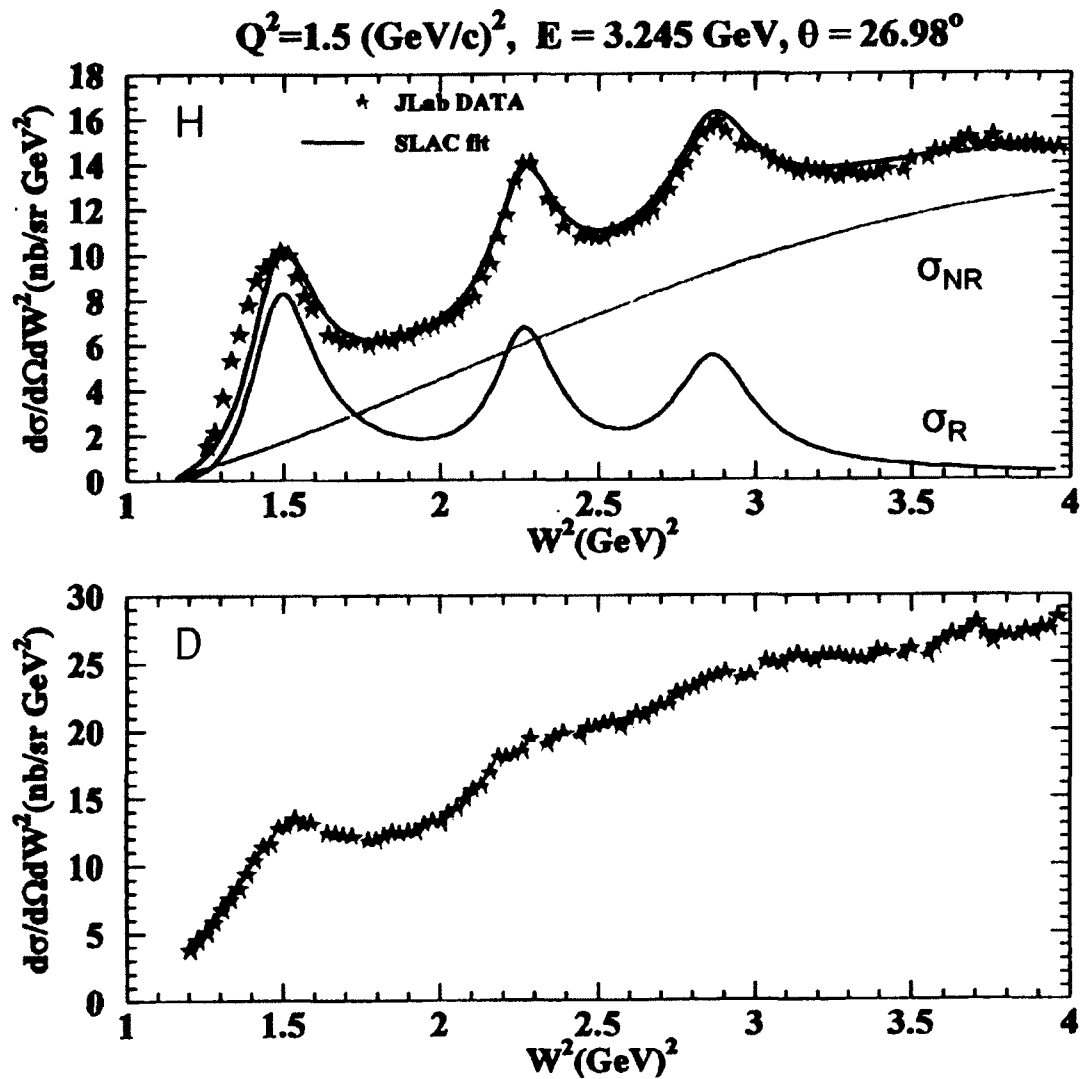


FIG. 1 Inclusive electron scattering cross-sections for the proton (top) and the deuteron (bottom) measured at Jefferson Lab. The elastic peak (at $W = 0.938 \text{ GeV}$) is not shown. The curve overlay on the data points on the top plot is a fit to Stanford Linear Accelerator Center data and the σ_R and σ_{NR} are resonance fit and the non-resonance background fit [10].

These effects further smear out the cross-section. Exclusive channel measurements where we measure multiple particle final states will provide further information on the resonance region especially for deuteron targets. While there is a wealth of information on the proton, there is little information on the neutron. Since there are no free neutron targets, the deuteron target is chosen to access the neutron. Information about the resonance region is critical for the understanding of nucleon structure.

1.4 PION ELECTRO-PRODUCTION

Pion electro-production is an inelastic electron scattering process in which a nucleon produces one or more pions. Single pion electro-production and photo-production are promising sources of information on the structure of the nucleon and its resonances. There are four single pion electro-production channels:

$$e + p \rightarrow e' + n + \pi^+ \quad (1)$$

$$e + p \rightarrow e' + p + \pi^0 \quad (2)$$

$$e + n \rightarrow e' + n + \pi^0 \quad (3)$$

$$e + n \rightarrow e' + p + \pi^- \quad (4)$$

There have been extensive study of the first two channels (see e.g., Refs 11, 12). The third channel is difficult to measure due to the fact that there are two neutral particles in the final state. The last channel is the reaction of interest for this thesis, and enables one to study the structure of the neutron.

Some properties of the resonance regions of interest, including the mass, have been explored by inclusive cross sections. Still, more information, such as the quantum numbers and branching ratios of these states is needed. An exclusive reaction is one way of isolating information about the resonance region from the final state particles in the

reaction. A deuteron target is used to access information on the neutron. This will ultimately gain information about the neutron structure.

Additional information on the nucleon can be obtained using a variety of polarization observables. For this analysis, the way to access information on the structure of the nucleon is to align the spin of the electron and target either parallel or anti-parallel to the beam direction. From this, the dependence of the scattering probability on the relative spins of the particles can be measured. One of the main programs in Hall B, which houses the CEBAF Large Acceptance Spectrometer (CLAS) at the Thomas Jefferson National Laboratory in Newport News, Virginia, is the study of spin observables. The EG1 experiment which is a part of the program in Hall B used a longitudinally polarized electron beam incident on longitudinally polarized ammonia (NH_3) and deuterated ammonia (ND_3) targets. CLAS was used for particle detection. CLAS has nearly a 4π acceptance which allows the detection of multiple-particle final states in exclusive reactions. The first part of the EG1 data were taken in the fall of 1998. A second, longer run took place from September 8, 2000 through April 20, 2001. About 23 billion electron scattering events were recorded. Beam energies ranging from 1.6 – 5.8 GeV were used. The EG1 run consisted of several experiments where inclusive and exclusive electron scattering data were taken on ND_3 and NH_3 targets [13, 14, 15].

The main goal of this analysis is to extract the double polarization asymmetry in exclusive $en \rightarrow e\pi^-p$ scattering as a function of the electron and pion kinematics. A secondary goal is to extract single target spin asymmetries. These data will provide a large amount of new information that can be used to improve models of the nucleon resonance states. In Chapter 2, the physics motivation for this experiment, including the

formalism and theoretical overview is presented. The experimental set-up including the beam, CLAS and target design and operation is discussed in Chapter 3. In Chapter 4, event selection and data analysis are described. Physics results and asymmetries are discussed in Chapters 5. A summary and conclusions are presented in Chapter 6.

CHAPTER 2

MOTIVATION

2.1 FORMALISM AND KINEMATICS

In this chapter we define the kinematics of single pion electro-production and introduce the polarized and un-polarized cross sections, helicity amplitudes, asymmetries and resonances. The well-known nature of the electromagnetic interactions defined by quantum electro-dynamics (QED) make electron scattering ideal for studying the nucleon. The coupling strength is given by the fine structure constant $\alpha = e^2/\hbar c = 1/137$, which is introduced at each vertex defined in the Feynmann diagram of the electromagnetic interaction [6]. Because α is much smaller than one, Feynmann diagrams with more vertices contribute much less to the cross section (because they depend on α^2 or higher orders of α), so only the lowest order process in which a single virtual photon is exchanged will be considered. This is known as the one photon exchange (OPE) approximation and is illustrated in Fig. 2.

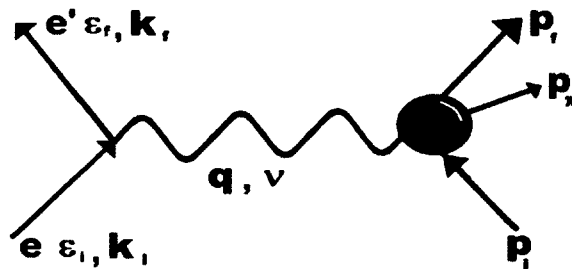


FIG. 2 Diagram for the one photon exchange approximation for pion-electroproduction.

In single pion electro-production, the reaction can be described in two steps. As seen in Fig. 3, the electron emits a virtual photon, which is absorbed by the target nucleon. The second step is the decay of the excited state through the emission of the pion.

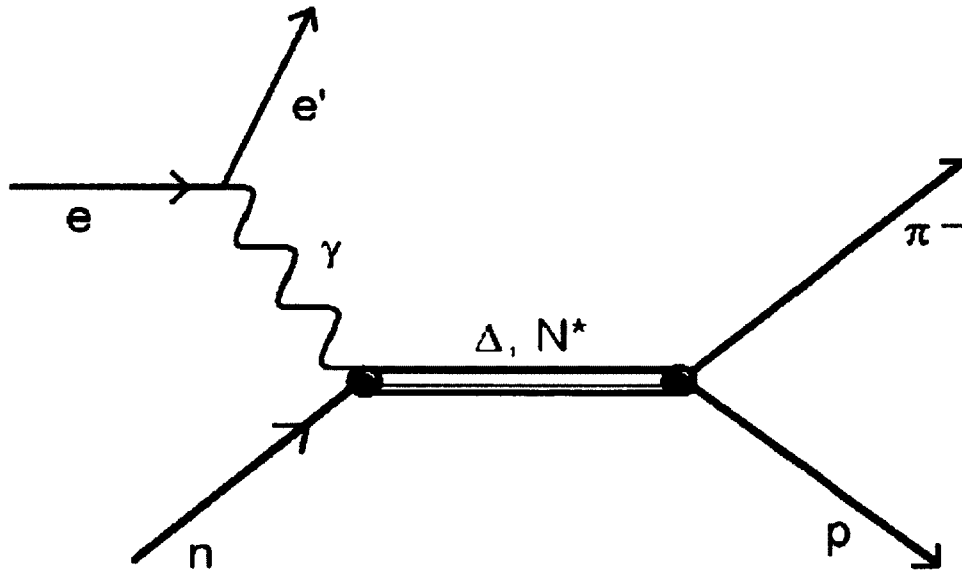


FIG. 3 Diagram showing the two step electro-production resonance reaction.

Virtual photons have three possible angular momentum orientations, $m = -1, 0$ or 1 and have non-zero mass. On the other hand, real photons have angular momentum orientations $m = -1$ or 1 and have zero mass. If the angular momentum orientation of a photon is 1 or -1 , its electric and magnetic fields are perpendicular to the direction of propagation, and it is a transverse photon. If the angular momentum orientation is zero ($m = 0$), then the photon can couple to the electric charge of the target nucleon and it is labeled as longitudinal.

Pion electroproduction is described in terms of four kinematic quantities, the invariant mass of photon and nucleon W , the four momentum transfer q , the pion scattering angle θ^* , and the angle ϕ^* between the leptonic plane, defined by the incident electron, scattered electron and virtual photon, and the hadronic plane, defined by the virtual photon and scattered pion.

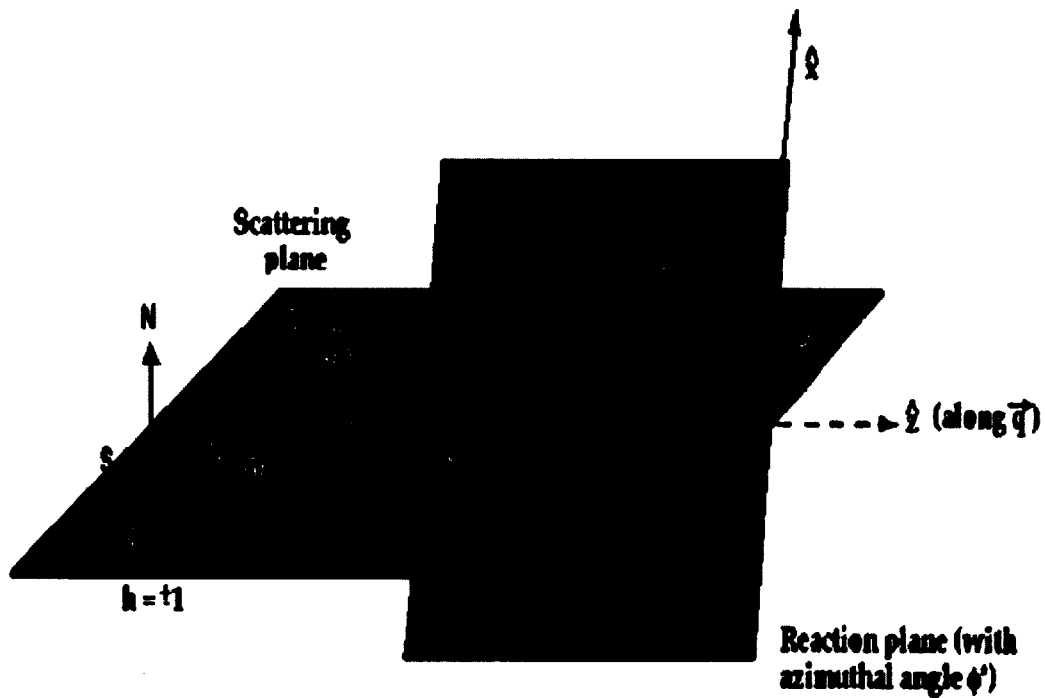


FIG. 4 The $(e,e'\pi)$ scattering reaction. The initial and final electron momenta k_i and k_f , define the leptonic plane; the virtual photon direction and the emitted pion define the hadronic plane. The center of mass angle θ^* of the emitted pion, the center of mass angle ϕ^* between the leptonic plane and hadronic plane, and the helicity $h = \pm 1$ representing the polarization state of the electron beam direction are also indicated.

In Fig. 4, the incident and scattered electron are denoted by the four-momentum

$k_i = (\varepsilon_i, \vec{k}_i)$ and $k_f = (\varepsilon_f, \vec{k}_f)$ respectively. The interaction of the electron with the

nucleon can be described by the exchange of a virtual photon with an energy $\nu = \varepsilon_i - \varepsilon_f$ and a three-momentum $\vec{q} = \vec{k}_i - \vec{k}_f$. The four-momentum transfer is given by $q = (\nu, \vec{q})$.

Varying E' and θ_e can access ν and q . To access θ^* and ϕ^* one needs to detect the pion with large acceptance. The four-momentum transfer squared is given by

$$Q^2 = -q^2 = 4\varepsilon_i\varepsilon_f \sin^2\left(\frac{\theta}{2}\right), \quad (5)$$

where θ is the angle between the incident (beam) direction and the scattered electron. Q^2 is an invariant quantity, as is the invariant mass of the struck or excited hadronic system, which is given by

$$W = (M_N^2 + 2M_N\nu - Q^2)^{\frac{1}{2}}. \quad (6)$$

M_n is the target nucleon mass. In the case of real photons, Q^2 is zero. The hadronic system is described by the four-momentum of the initial nucleon, the final nucleon, and the emitted pion, $p_i = (E_i, \vec{p}_i)$, $p_f = (E_f, \vec{p}_f)$ and $p_\pi = (E_\pi, \vec{p}_\pi)$, respectively. The kinematic quantities of interest for single pion electro-production are the center of mass (cm) angles θ^* and ϕ^* for the emitted pion, as well as Q^2 and W , which completely describe the electron scattering vertex.

2.2 DIFFERENTIAL CROSS SECTIONS

The differential cross section for the production of a pion from electron scattering off a nucleon is given by [16]

$$d\sigma = \frac{\varepsilon_i}{k_i} \frac{M_e}{\varepsilon_i} \frac{M_p}{E_i} \frac{M_e}{\varepsilon_f} \frac{d^3\vec{k}_f}{(2\pi)^3} \frac{1}{2E_\pi} \frac{d^3\vec{p}_\pi}{(2\pi)^3} \frac{M_N}{E_f} \frac{d^3\vec{p}_f}{(2\pi)^3} (2\pi)^4$$

$$* \delta(p_i + q - p_\pi - p_f) * \left| \langle p_f, p_\pi | J^\mu | p_i \rangle q^{-2} \langle k_f | j_\mu | k_i \rangle \right|^2. \quad (7)$$

This cross section depends on the earlier described kinematic factors along with the energy and momentum conserving delta function, the electromagnetic current j_μ and the hadronic current J^μ . The matrix elements in Equation 7 can be re-written in the OPE approximation as a product of two second-rank tensors, the leptonic tensor $\eta_{\mu\nu}$ and the hadronic tensor $W^{\mu\nu}$ [17]. Using the notation of Drechsel and Tiator [18], the lepton tensor can be written

$$\eta_{\mu\nu} = \sum_{sf} (\bar{u}(k_f, s_f) \not{\epsilon} \gamma_\mu u(k_i, s_i)) (\bar{u}(k_f, s_f) \not{\epsilon} \gamma_\nu u(k_i, s_i))^*, \quad (8)$$

where u and \bar{u} are the Dirac spinors for the incoming and outgoing electron with four-momentum k_i and k_f and spins s_i and s_f , respectively. The sum is over all spin observables in the final state and is written

$$\eta_{\mu\nu} = \frac{e^2}{4m_e^2} \left((k_{f\mu} + k_{i\mu})(k_{f\nu} + k_{i\nu}) + q^2 i h \epsilon_{\mu\nu\alpha\beta} q^\alpha (k_f^\beta + k_i^\beta) \right), \quad (9)$$

where m_e is the electron mass and h is the electron longitudinal polarization helicity, with $h = \vec{\sigma} \cdot \hat{k}_i = \pm 1$, ($\vec{\sigma}$ are the Pauli spin matrices), $g_{\mu\nu}$ is the symmetrical metric tensor and $\epsilon_{\mu\nu\alpha\beta}$ is the anti-symmetrical tensor with $\epsilon_{0123} = 1$, and with gauge invariance $q^\mu \eta_\nu = \eta_\mu q^\nu = 0$. The hadronic tensor is written as

$$W_{\mu\nu} = \langle p_f, p_\pi | J^\mu | p_i \rangle \langle p_f, p_\pi | J^\nu | p_i \rangle^*. \quad (10)$$

$W_{\mu\nu}$ depends on the structure of the particles involved in the process as well as the excitation mechanism and can only be parameterized. A typical choice is given by the helicity basis in which the transition amplitudes between states have well defined helicity.

Starting out with the unpolarized case in which the electron and nucleon in the initial state are unpolarized and the recoil polarization of the final state nucleon is undetected the cross section for single pion production using the one photon exchange approximation can be expressed by

$$\frac{d\sigma}{d\varepsilon_f d\Omega_i d\Omega_\pi} = \Gamma \frac{d\sigma}{d\Omega_\pi}. \quad (11)$$

The expression Γ describes the flux of virtual photons produced from the electron beam [19, 20], and can be written as

$$\Gamma = \frac{\alpha}{2\pi^2} \frac{W^2 - m_N^2}{2m_N Q^2} \frac{\varepsilon_f}{\varepsilon_i} \frac{1}{1 - \varepsilon}, \quad (12)$$

where the term $\frac{W^2 - m_N^2}{2m_N}$ is the equivalent photon energy or the energy the photon needs

to excite the hadronic system with center of mass energy W . The ε term is the degree of transverse polarization of the photon and is written using quantities in the lab frame

$$\varepsilon = \left(1 + \frac{2\bar{q}^2}{Q^2} \tan^2 \frac{\theta}{2} \right)^{-1}. \quad (13)$$

2.3 HELICITY AMPLITUDES

The hadronic matrix element of the electromagnetic current, $\langle p_f, p_\pi | J^\mu | p_i \rangle$ is expressed in the form of helicity amplitudes in the center of mass frame for the virtual process $\gamma + N \rightarrow \pi + N$ where the photon, a spin 1 object, is absorbed by the spin $\frac{1}{2}$ nucleon to produce a spin $\frac{1}{2}$ and a spin 0 object in the final state [21]. This is expressed by

$$H = \varepsilon_\mu(\lambda) \langle p_f, p_\pi | J^\mu | p_i \rangle = \langle \lambda_\pi, \lambda_f | T | \lambda_i, \lambda_\gamma \rangle, \quad (14)$$

Where $\varepsilon_\mu(\lambda)$ is the polarization vector of the virtual photon, λ_i , λ_f , λ_π and λ_γ are the helicities of the initial state nucleon, final state nucleon, final state pion and the virtual photon respectively. This process gives rise to twelve complex helicity amplitudes, but only six of these amplitudes are independent due to parity symmetry. There are four transverse helicity amplitudes, $H_i (i = 1 \text{ to } 4)$ which correspond to $\lambda_\gamma = 1$ and $(\lambda_f, \lambda_i) = (\frac{1}{2}, \frac{1}{2}), (\frac{1}{2}, -\frac{1}{2}), (-\frac{1}{2}, \frac{1}{2})$ and $(-\frac{1}{2}, -\frac{1}{2})$. There are also two longitudinal amplitudes that can only be accessed from the absorption of a longitudinal photon via electron scattering. This gives a total of six independent helicity amplitudes;

$$H = \langle \lambda_\pi, \lambda_f | T | \lambda_\gamma, \lambda_i \rangle \quad (15)$$

$$H_1 = \left\langle 0, \frac{1}{2} | T | 1, \frac{1}{2} \right\rangle$$

$$H_2 = \left\langle 0, \frac{1}{2} | T | 1, -\frac{1}{2} \right\rangle$$

$$H_3 = \left\langle 0, -\frac{1}{2} | T | 1, \frac{1}{2} \right\rangle$$

$$H_4 = \left\langle 0, -\frac{1}{2} | T | 1, -\frac{1}{2} \right\rangle$$

$$H_5 = \left\langle 0, \frac{1}{2} | T | 0, \frac{1}{2} \right\rangle$$

$$H_6 = \left\langle 0, \frac{1}{2} | T | 0, -\frac{1}{2} \right\rangle.$$

It is also useful to construct linear combinations of the first four complex helicity amplitudes;

$$h_{\pm}^N = \frac{1}{\sqrt{2}}(H_4 \pm H_1) \quad (16)$$

$$h_{\pm}^F = \frac{1}{\sqrt{2}}(H_3 \mp H_2), \quad (17)$$

where $h_{+}^{N,F}$ refers to the case in which the incident photon is polarized perpendicular to the scattering plane and $h_{-}^{N,F}$ represents photons that are polarized parallel to the scattering plane. The subscripts N and F refer to the baryon non-flip and baryon spin flip. The helicity amplitudes $H_1 - H_4$ are summarized in Fig. 5.

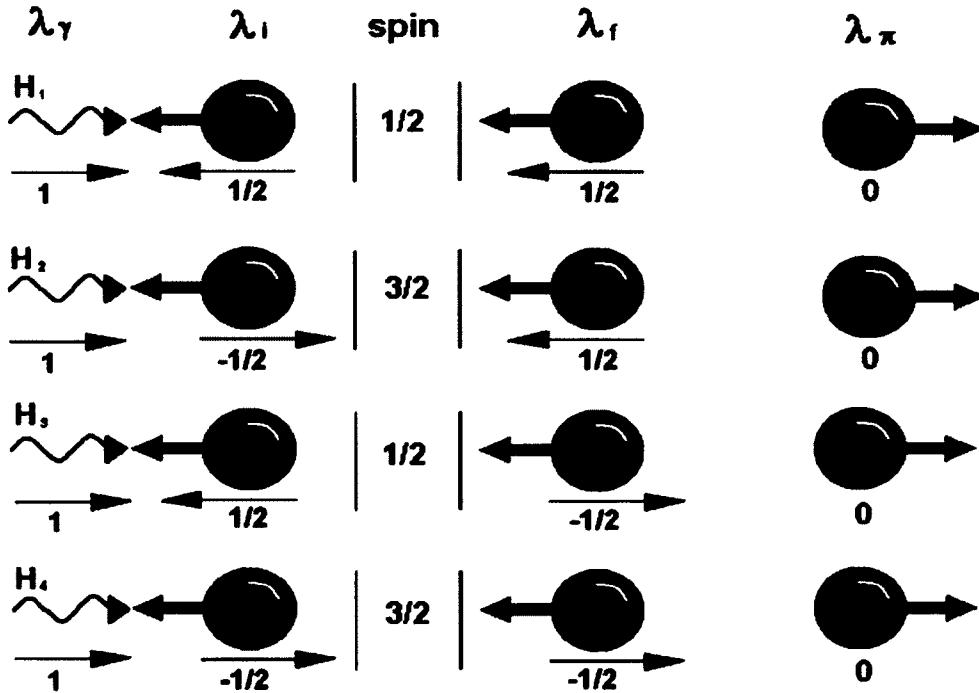


FIG. 5 Helicity amplitude representation. On the left is shown the interaction of the photon with the nucleon in the center of mass frame where they are traveling towards each other. The spin direction is shown by the arrows underneath each particle. The pion and nucleon may also have non-zero relative angular momentum in the final state.

Using this basis, it is possible to express the hadronic current J in terms of its spherical

components, $J_{\pm,0}$ with $J_{\pm} = \pm(J_x \pm J_y)/\sqrt{2}$ where $J_0 = J_z$. Since the components of the current operator are defined in two dimensional Pauli spin space, they can be expressed in two by two matrices in terms of helicity amplitudes,

$$J_+ = \begin{pmatrix} H_1 & H_2 \\ H_3 & H_4 \end{pmatrix}, \quad J_- = \begin{pmatrix} H_4 & -H_3 \\ -H_2 & H_1 \end{pmatrix}, \quad \text{and} \quad J_0 = \begin{pmatrix} H_5 & H_6 \\ H_6 & -H_5 \end{pmatrix}. \quad (18)$$

Based on this parameterization, the transition matrix elements of the currents in Equation 7 can be expressed in terms of the helicity amplitudes in Equation 15 [17].

2.4 RESPONSE FUNCTIONS

The cross section in Equation 16 can be written in terms of response functions $R_i = R_i(Q^2, W, \phi^*)$. These response functions are bilinear combinations of the helicity amplitudes. In general, for unpolarized beam and target, the virtual photon cross section can be written as a function of the response functions; R_T , R_L , R_{LT} and R_{TT} , as shown in the following expression [22]:

$$\frac{d\sigma}{d\Omega_\pi} = \frac{|\vec{q}|}{q_\gamma^{cm}} \left[R_T + \varepsilon_L R_L + \sqrt{2\varepsilon_L(1+\varepsilon)} R_{LT} \cos \phi^* + \varepsilon R_{TT} \cos 2\phi^* \right] \quad (19)$$

The L term corresponds to the longitudinal component of the virtual photon polarization, whereas the T term corresponds to the transverse component. The TT and LT terms refer to the interference terms. The term q_γ^{cm} is the energy that would be required for a real photon to excite a mass state W . The term ε is the degree of transverse polarization of the photon while ε_L is the longitudinal polarization of the photon,

$$\varepsilon_L = \frac{Q^2}{\nu} \varepsilon. \quad (20)$$

For this analysis the projections of the response functions onto the polarization of the

target, as well as the helicity of the electron, are considered. If the polarization of the target is

$$\vec{P} = P_x \hat{x} + P_y \hat{y} + P_z \hat{z}, \quad (21)$$

as described by the reference frame in Fig. 4, the virtual photon cross section can now be expressed as

$$\begin{aligned} \frac{d\sigma}{d\Omega_\pi} = & \frac{|\vec{q}|}{q_\gamma^{cm}} [R_T + P_y R_T^y + \varepsilon_L (R_L + P_y R_L^y) \\ & + \sqrt{2\varepsilon_L(1+\varepsilon)} ((R_{LT} + P_y R_{LT}^y) \cos \phi^* + (P_x R_{LT}^x + P_z R_{LT}^z) \sin \phi^*) \\ & + \varepsilon ((R_{TT} + P_y R_{TT}^y) \cos 2\phi^* + (P_x R_{TT}^x + P_z R_{TT}^z) \sin 2\phi^*) \\ & + h\sqrt{2\varepsilon_L(1-\varepsilon)} ((R_{LT'} + P_y R_{LT'}^y) \sin \phi^* + (P_x R_{LT'}^x + P_z R_{LT'}^z) \cos \phi^*) \\ & + h\sqrt{1-\varepsilon^2} (P_x R_{TT'}^x + P_z R_{TT'}^z)]. \end{aligned} \quad (22)$$

The interference terms are from the symmetric combinations of the longitudinal and transverse terms and the primed terms come from the anti-symmetric combinations. In the case of EG1b, the target was polarized parallel or anti-parallel to the beam direction, with h being the beam helicity. The \hat{x} , \hat{y} and \hat{z} components of the target polarization can be written in terms of the target polarization in the laboratory frame as a function of ϕ^* (see Fig. 3) and θ_γ , which is the angle between the beam line and the virtual photon.

$$\begin{aligned} P_x &= P_T \sin \theta_\gamma \cos \phi^* \\ P_y &= -P_T \sin \theta_\gamma \sin \phi^* \\ P_z &= P_T \cos \theta_\gamma. \end{aligned} \quad (23)$$

The cross section can now be written

$$\begin{aligned}
\frac{d\sigma}{d\Omega_\pi} = & \frac{|\vec{q}|}{q_\gamma^{cm}} [R_T - P_T \sin \theta_\gamma \sin \phi^* R_T^y + \varepsilon_L (R_L - P_T \sin \theta_\gamma \sin \phi^* R_L^y) \\
& + \sqrt{2\varepsilon_L(1+\varepsilon)} ((R_{LT} - P_T \sin \theta_\gamma \sin \phi^* R_{LT}^y) \cos \phi^* \\
& + (P_T \sin \theta_\gamma \cos \phi^* R_{LT}^x + P_T \cos \theta_\gamma R_{LT}^z) \sin \phi^*) \\
& + \varepsilon ((R_{TT} - P_T \sin \theta_\gamma \sin \phi^* R_{TT}^y) \cos 2\phi^* \\
& + (P_T \sin \theta_\gamma \cos \phi^* R_{TT}^x + P_T \cos \theta_\gamma R_{TT}^z) \sin 2\phi^*) \\
& + h\sqrt{2\varepsilon_L(1-\varepsilon)} ((R_{LT'} - P_T \sin \theta_\gamma \sin \phi^* R_{LT'}^y) \sin \phi^* \\
& + (P_T \sin \theta_\gamma \cos \phi^* R_{LT'}^x + P_T \cos \theta_\gamma R_{LT'}^z) \cos \phi^*) \\
& + h\sqrt{1-\varepsilon^2} (P_T \sin \theta_\gamma \cos \phi^* R_{TT'}^x + P_T \cos \theta_\gamma R_{TT'}^z)].
\end{aligned} \tag{24}$$

This cross section has four terms, an unpolarized term that is not dependent on beam or target polarization (σ_0), a target polarization dependent term (σ_t), a beam helicity dependent term (σ_e), and a term that is dependent on both the beam helicity and target polarization (σ_{et}). The cross section can be re-written in these terms, with P_B corresponding to the beam helicity and P_T the target polarization.

$$\sigma = \sigma_0 + P_B \sigma_e + P_T \sigma_t - P_B P_T \sigma_{et} \tag{25}$$

$$\sigma_0 = \frac{|\vec{q}|}{q_\gamma^{cm}} [R_T + \varepsilon_L R_L + \sqrt{2\varepsilon_L(1+\varepsilon)} R_{LT} \cos \phi^* + \varepsilon R_{TT} \cos 2\phi^*] \tag{26}$$

$$\sigma_e = \frac{|\vec{q}|}{q_\gamma^{cm}} \sqrt{2\varepsilon_L(1-\varepsilon)} R_{LT'} \sin \phi^* \tag{27}$$

$$\begin{aligned}
\sigma_t = & \frac{|\vec{q}|}{q_\gamma^{cm}} [\varepsilon (R_{TT}^x \sin \theta_\gamma \cos \phi^* + R_{TT}^z \cos \theta_\gamma) \sin 2\phi^* \\
& - \varepsilon R_{TT}^y \sin \theta_\gamma \sin \phi^* \cos 2\phi^* \\
& + \sqrt{2\varepsilon_L(1+\varepsilon)} (R_{LT}^x \sin \theta_\gamma \cos \phi^* + R_{LT}^z \cos \theta_\gamma) \sin \phi^* \\
& - \sqrt{2\varepsilon_L(1+\varepsilon)} R_{LT}^y \sin \theta_\gamma \sin \phi^* \cos \phi^* \\
& - (R_T^y + \varepsilon_L R_L^y) \sin \theta_\gamma \sin \phi^*]
\end{aligned} \tag{28}$$

and

$$\begin{aligned} \sigma_{ei} = & \frac{|\vec{q}|}{q_\gamma^{cm}} [\sqrt{2\varepsilon_L(1-\varepsilon)}(R_{LT}^x \sin \theta_\gamma \cos \phi^* + R_{LT}^z \cos \theta_\gamma) \cos \phi^* \\ & - \sqrt{2\varepsilon_L(1-\varepsilon)}(R_{LT}^y \sin \theta_\gamma \sin \phi^* \sin \phi^*) \\ & + \sqrt{1-\varepsilon^2}(R_{TT}^x \sin \theta_\gamma \cos \phi^* + R_{TT}^z \cos \theta_\gamma)]. \end{aligned} \quad (29)$$

These four cross section terms have a different angular dependence. For example, the σ_e term clearly has a $\sin \phi^*$ dependence. The cross section must be measured for different combinations of beam and target polarizations, in order to extract the largest number of observables. During the EG1b experiment we had both beam and target polarization for that reason.

The unpolarized, polarized beam, polarized target and polarized beam and target cross sections in Equation 24 can be expressed in terms of the helicity amplitudes discussed in section 2.3. The six helicity amplitudes involve at most eleven independent quantities that are measured for a complete description of the process [21]. The relationships between the cross sections and helicity amplitudes are expressed in Appendix A.

2.5 CGLN AMPLITUDES

The response functions described in section 2.4 can also be expressed in terms of the Chew, Goldberger, Low, Nambu (CGLN) [23] amplitudes $F_1 - F_6$. These amplitudes are expressed in terms of electric and magnetic multipoles, which arise from expanding the photon wave function into vector spherical harmonics Y_{JL} . For each eigenvalue J of the photon total angular momentum there are the electric ($L = J \pm 1$) and magnetic ($L = J$) multipoles, where L is the orbital angular momentum. An electric 2^J -pole has parity $(-1)^J$,

and a magnetic 2^J -pole has parity $-(-)^J$. If the photon multipoles are combined with the spin of the nucleon, one has total angular momentum $j = J \pm 1/2$ and parity P for the γN state. The possible configurations are listed in Table 3.

Table 3 Decomposition of pion photoproduction amplitudes into multipole components [9].

Photon J	Photon Multipole	Total j	Total P	Pion l	Multipole Amplitude
1	$E1$	$1/2$	-	0	E_{0+}
1	$E1$	$3/2$	-	2	E_{2-}
1	$M1$	$1/2$	+	1	M_{1-}
1	$M1$	$3/2$	+	1	M_{1+}
2	$E2$	$3/2$	+	1	E_{1+}
2	$E2$	$5/2$	+	3	E_{3+}
2	$M2$	$3/2$	-	2	M_{2-}
2	$M2$	$5/2$	-	2	M_{2+}
3	$E3$	$5/2$	-	2	E_{2+}
3	$E3$	$7/2$	-	4	E_{4-}
3	$M3$	$5/2$	+	3	M_{3-}
3	$M3$	$7/2$	+	3	M_{3+}
4	$E4$	$7/2$	+	3	E_{3+}
4	$E4$	$9/2$	+	5	E_{5-}
4	$M4$	$7/2$	-	4	M_{4-}
4	$M4$	$9/2$	-	4	M_{4+}

Assuming the γN state decays to $\pi^+ N$, the resulting multipole amplitudes are listed in the last column of Table 3. The value l indicates the angular momentum values allowed for the pion. Because of the pion negative intrinsic parity, only the values of l such that $-(-1)^l = P$ are allowed. For each pair of values of j and P there are two possible channels through which the reaction can proceed: an electric and a magnetic multipole transition. The amplitudes for these channels are assigned the symbols given in the last column. The E or M comes from the photon multipole character. The first subscript

indicates the angular momentum l of the pion and the second one is the total angular momentum of the intermediate state. The \pm stands for $j = l = \pm 1/2$. For most angular momentum values of the pion, there are four different amplitudes: $E_{l\pm}$ and $M_{l\pm}$ [9].

Similarly, there are $S_{l\pm}$ multipoles for longitudinal photon excitations.

Like the helicity amplitudes, the first four CGLN amplitudes represent the transverse current with the last two representing the longitudinal current. These amplitudes are expressed as the multi-pole de-composition of the derivative of Legendre Polynomials

$$F_1 = \sum_{l \geq 1} \left[(lM_{l+} + E_{l+})P'_{l+1} + ((l+1)M_{l-} + E_{l-})P'_{l-1} \right] \quad (30)$$

$$F_2 = \sum_{l \geq 1} [(l+1)M_{l+} + lM_{l-}]P'_l$$

$$F_3 = \sum_{l \geq 1} [(E_{l+} - M_{l+})P''_{l+1} + (E_{l-} + M_{l-})P''_{l-1}]$$

$$F_4 = \sum_{l \geq 2} [M_{l+} - M_{l-} - E_{l+} - E_{l-}]P''_l$$

$$F_5 = \sum_{l \geq 0} [(l+1)S_{l+}P'_{l+1} - M_{l-} - lS_{l-}P'_{l-1}]$$

$$F_6 = \sum_{l \geq 1} [S_{l-} - (l+1)S_{l+}]P'_l$$

where $E_{l\pm}$ are the electric terms, $M_{l\pm}$ are the magnetic terms and $S_{l\pm}$ are the longitudinal terms [24]. The advantage of the CGLN amplitude is that it allows for comparisons to be made between the results of different experiments and phenomenological models. As long as data on the same multi-pole terms exist, the comparison can be made. Appendix B through D show the relationship between helicity amplitudes, response functions and CGLN amplitudes.

2.6 ASYMMETRIES

Asymmetries are a method of comparing the total count rates in different helicity configurations, thus enabling us to isolate polarization dependent terms in the cross section. There are two main reasons for measuring asymmetries in addition to unpolarized cross sections. The first reason is that asymmetries depend on different combinations of helicity amplitudes. The advantage of spin observables is that many of the component terms result from interference between different amplitudes. Therefore measuring asymmetries can be a good technique for extracting small helicity amplitudes. The second reason is experimental. Variations in detector efficiency or acceptance must be taken into account when calculating cross sections. Since asymmetries are ratios of cross sections, the acceptance and efficiency cancel (to first order) in that ratio. This means that asymmetry measurements are generally independent of acceptance, detector efficiency or luminosity as long as these factors do not change rapidly over the measurement bin in a way that results in different values for different spin configurations. Since these factors can all have large systematic uncertainties associated with their determination, the ability to make a measurement independent of these factors can greatly lower the total systematic uncertainty.

The simplest asymmetry measurement would involve an unpolarized target with a 100% polarized electron beam with identical luminosities for each beam polarization,

$$A_{\parallel} = \frac{N_+ - N_-}{N_+ + N_-}, \quad (31)$$

where N_+ is the count rate for positive beam helicity and N_- is the count rate for negative beam helicity.

For EG1b, both beam and target were polarized. This allows both the beam and target polarizations to be reversed, allowing for the construction of three independent asymmetries. These asymmetries can be related to the ratio of different spin dependent parts of the cross section.

$$A_e = \frac{\sigma_e}{\sigma_0} = \frac{(\sigma_{++} - \sigma_{-+}) + (\sigma_{+-} - \sigma_{--})}{(\sigma_{++} + \sigma_{-+}) + (\sigma_{+-} + \sigma_{--})} \quad (32)$$

$$A_t = \frac{\sigma_t}{\sigma_0} = \frac{(\sigma_{++} + \sigma_{-+}) - (\sigma_{+-} + \sigma_{--})}{(\sigma_{++} + \sigma_{-+}) + (\sigma_{+-} + \sigma_{--})} \quad (33)$$

$$A_{et} = \frac{\sigma_{et}}{\sigma_0} = \frac{(\sigma_{-+} - \sigma_{++}) + (\sigma_{+-} - \sigma_{--})}{(\sigma_{++} + \sigma_{-+}) + (\sigma_{+-} + \sigma_{--})}, \quad (34)$$

where the + and – subscripts refer to the polarization of beam and target. The first term refers to the beam helicity with + indicating helicity in the direction of the beam, and the second term refers to the target polarization. Equations 28-30 show the asymmetries with an assumption of 100% polarization. Previous asymmetries are shown in Fig. 6. In reality corrections due to beam and target polarizations must be applied, as discussed in chapter 4.

2.6.1 Inclusive Asymmetries

We can also define an “inclusive” asymmetry $A_{//}$ which does not require both target polarization orientations to be measured. Spin structure functions can be measured in inclusive electron scattering (see Fig. 2). It is the virtual photon that probes the nucleon but it is the electron that is detected. The virtual photon cross sections are given in terms of helicity amplitudes $A_{1/2}$, $A_{3/2}$ and $S_{1/2}$, where the subscripts 1/2 or 3/2 refer to the final spin states. Since the target spin is not aligned with the virtual photon direction, there are longitudinal and transverse cross section terms. In addition, the transverse and

the longitudinal part of the cross section can interfere which introduces an interference cross section term σ_{LT} [25].

$$\sigma_{1/2}^T = \frac{4\pi^2\alpha}{k} |A_{1/2}|^2 \quad (35)$$

$$\sigma_{3/2}^T = \frac{4\pi^2\alpha}{k} |A_{3/2}|^2 \quad (36)$$

$$\sigma_{1/2}^L = \frac{4\pi^2\alpha}{k} |S_{1/2}|^2 \quad (37)$$

$$\sigma_{1/2}^{LT} = \frac{4\pi^2\alpha}{k} \left[|A_{1/2}|^2 + |S_{1/2}|^2 \right]^{1/2} \frac{Q}{M\nu} (g_1 + g_2), \quad (38)$$

where $k = \nu - Q^2/2M$ is the equivalent photon energy, and g_1 and g_2 are polarized structure functions, giving rise to scattering asymmetries. We define the virtual photon asymmetries:

$$A_1 = \frac{\sigma_{1/2}^T - \sigma_{3/2}^T}{\sigma_{1/2}^T + \sigma_{3/2}^T} \quad (39)$$

and

$$A_2 = \frac{2\sigma_{1/2}^{LT}}{\sigma_{1/2}^T + \sigma_{3/2}^T}. \quad (40)$$

The measured electron asymmetries are defined as

$$A_{\perp} = \frac{\sigma_{+T} - \sigma_{-T}}{\sigma_{+T} + \sigma_{-T}} \quad (41)$$

and

$$A_{\parallel} = \frac{\sigma_{+} - \sigma_{-}}{\sigma_{+} + \sigma_{-}} \quad (42)$$

where the spin configurations + and – refer to nucleon and electron spins aligned (anti-

aligned). The measured electron asymmetries can be related to the desired virtual photon asymmetries by;

$$A_{\parallel} = D(A_1 + \eta A_2) \quad (43)$$

$$A_{\perp} = d(A_2 - \zeta A_1) \quad (44)$$

where

$$D = \frac{1 - \varepsilon E' / E}{1 + \varepsilon R} \quad (45)$$

$$R = \frac{\sigma_L}{\sigma_T} \quad (46)$$

$$d = D \sqrt{\frac{2\varepsilon}{1 + \varepsilon}} \quad (47)$$

$$\eta = \frac{\varepsilon \sqrt{Q^2} / E}{1 - \varepsilon E' / E} \quad (48)$$

and

$$\zeta = \eta \frac{1 + \varepsilon}{2\varepsilon}. \quad (49)$$

If integration occurs over the pion azimuthal center of mass angle ϕ^* , σ_e and σ_i integrate to zero. In this case, A_{\parallel} reduces to A_{et} which can be expressed as

$$A_{et} = \sqrt{1 - \varepsilon^2} \cos \theta_{\gamma} \frac{A_1 + \eta A_2}{1 + \varepsilon R}, \quad (50)$$

which follows the formalism of inclusive asymmetries [25, 26].

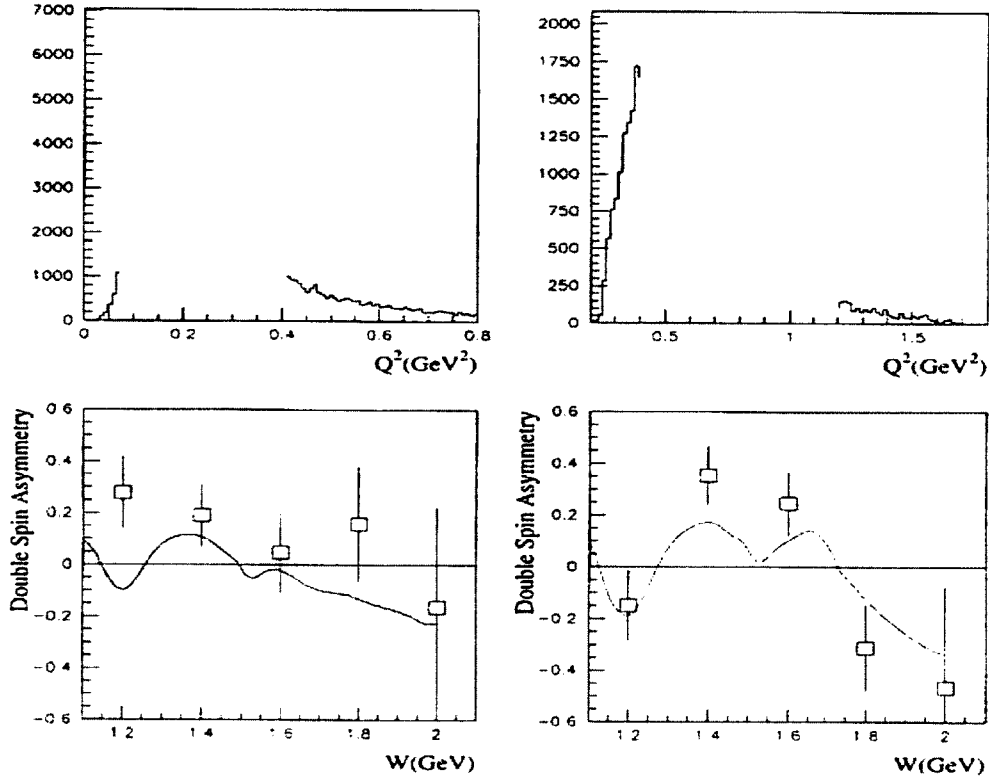


FIG. 6 Previous double spin asymmetries for the $n(e,e'\pi^-)$ electro-production reaction using 2.565 and 2.494 GeV beam energies. The Q^2 distributions are given on the top: the bottom plots show the double spin asymmetries. The left and right plots are from data sets with different kinematic acceptance (electron bent away from and toward the beamline respectively). The shaded regions indicate the range of Q^2 that was accepted to extract the double spin asymmetries in the bottom plot. The curves on the bottom plots are the MAID predictions. Plot courtesy of Mehmet Bektasoglu [27].

2.7 BARYON RESONANCES

One goal of this analysis is to study regions of low to moderate Q^2 , ($Q^2 \leq 1 \text{ GeV}^2$), where scattering experiments probe the transition from hadronic to partonic degrees of freedom. Nucleon resonance and multi-pion states are important in this region, which is known as the resonance region. Experiments in photo and electroproduction along with πN scattering experiments are the main source of data on baryonic resonances currently

available. However, there are still questions to be answered, including;

- What is the Q^2 dependence of the E_{1+}/M_{1+} and the S_{1+}/M_{1+} ratio of the P_{33} (1232) or Δ resonance?
- What is the structure of the Roper resonance?
- Can we find the missing resonances predicted by the constituent quark model?

With current experimental programs using high duty cycle accelerators and large acceptance detectors that improve the quality of the information as well as increased kinematic coverage of these measurements new experiments to probe the resonance region are underway or have been completed. Study of these nucleon resonance excitation will yield information on the photo coupling amplitudes at the γNN^* vertex as a function of four momentum transfer Q^2 . A recent review of the electron excitation of nucleon resonances is given in Reference 30.

2.7.1 The Delta Region

The $P_{33}(1232)$ known as the delta resonance is the most dominant of all the resonance states at low momentum transfer. It is also the lowest mass state. The Δ has been studied extensively in early experiments at DESY [29] and NINA [30] as well as current experiments at Jefferson Lab. The reason it is well known is that it is the only resonance that does not strongly overlap with other resonances and it decays primarily by single pion production.

As mentioned in section 2.5, the transition amplitudes can be written as a function of electromagnetic multipoles, in this case an electric quadrupole E_{1+} , a magnetic dipole M_{1+} and a scalar quadrupole S_{1+} . These multipoles may contribute to the $N \rightarrow \Delta$ transition.

In this notation the subscript l_{\pm} denotes the orbital angular momentum l of the final state and the total spin $j = l \pm 1/2$. In the quark model based on SU(6) symmetry, the Δ has all three quarks in an s-state and the $N \rightarrow \Delta$ transition is induced by a single quark spin-flip [31]. In this model, only the M_l is non zero which corresponds to a pure magnetic dipole transition [32]. Therefore the ratio $E_{l+}/M_{l+} = 0$. Non zero E_{l+} and S_{l+} multipoles are possible if there is a d-state ($l = 2$) component in the ground state and/or excited states. Recent results by [28] show that E_{l+}/M_{l+} remains small and negative up to $Q^2 = 6$ or 7 GeV^2 and S_{l+}/M_{l+} is negative with increasing magnitude. The size of the E_{l+}/M_{l+} ratio is predicted to be small from low to intermediately high Q^2 by current quark models that include one gluon exchange. However at high Q^2 , helicity conservation predicts that this ratio approaches unity while the ratio S_{l+}/M_{l+} should be constant [28]. The assumption made in order to extract quadrupole amplitudes from measured angular distributions is that only the s-state and p-state wave functions are important in the πN system, and only the dominant M_{l+} multipole along with its interferences are included in the response functions.

2.7.2 The Second Resonance Region

For inclusive cross sections, there is an enhancement at $W \sim 1.5 \text{ GeV}$ see Fig. 1. Three resonance states, the $P_{11}(1440)$, the $D_{13}(1520)$, and the $S_{11}(1535)$ contribute to that observed enhancement, but strongly overlap in that region. For this reason inclusive cross sections do not draw the whole picture, and experiments in which specific decay channels are detected (exclusive processes) can help in studying these overlapping resonances.

2.7.2.1 The Roper Resonance

The P_{11} (1440) or Roper resonance is a well established 4-star nucleon resonance found in πN scattering. In pion photoproduction, the P_{11} (1440) contribution appears as a shoulder on the D_{13} (1520) and S_{11} (1535) resonances. In the non relativistic constituent quark model (NRCQM) the P_{11} (1440) is interpreted as a radial excitation of the nucleon with $SU(6) \times O(3)$ multipole $[56, 0^+]$ ($l = 2, N = 2$), where 56 is the dimensionality of the $SU(6)$ representation, 0 is the total quark angular momentum, and + is the total parity. However the structure of the Roper resonance was a puzzle for many years. Recent CLAS measurements [33] of the $A_{1/2}$ and $S_{1/2}$ amplitudes for the Roper resonance have enabled comparison with increasingly precise theoretical prediction. Light front relativistic quark models that combine a 3q radial excitation with a meson cloud are able to describe the data well over the entire Q^2 range [28].

2.7.2.2 The D_{13} (1520) and S_{11} (1535) Resonances

Unlike the Roper resonance, the D_{13} (1520) and S_{11} (1535) are in a $[70, 0^-]$ supermultiplet [34]. The S_{11} (1535) state has a large decay branch to ηN and has been studied at Jefferson Lab [35]. The behavior of the virtual photon asymmetry A_l as a function of Q^2 is predicted by the CQM to change from -1 at $Q^2 = 0$ to +1 at large Q^2 [36]. Recent CLAS data follow that prediction [28]. Neutrons and protons have different sensitivity to different model assumptions [37], and unlike protons, the zero point crossing is at a higher Q^2 for the neutron [34]. This is one reason why it is important to information on both proton and neutron resonances.

2.7.3 Higher Resonances

The F_{15} (1680), S_{11} (1650), D_{15} (1675), and the S_{31} (1620) are among the resonance states which appear in the third enhancement of the inclusive cross section. In $SU(6)$

symmetry, the $F_{15}(1680)$ is a member of the $[56, 2_2^+]$ supermultiplet, whereas the other resonances are in the $[70, 1_1^-]$ supermultiplet. For the $F_{15}(1680)$ resonance, at $Q^2 = 0$, the transition is dominated by helicity 3/2 and $A_{1/2} \sim 0$, with a helicity asymmetry $A_1 \sim -1$ [38], while for $Q^2 > 0$, theory predicts a rapid switching from helicity 3/2 to helicity 1/2 dominance. Current data support this prediction [39]. Appendix C shows the properties of the various resonances.

2.8 THEORETICAL MODELS

Obtaining a basic understanding of the structure and interaction of hadrons has been the motivation for model descriptions of strong interaction physics for decades. The constituent quark model (CQM) is the first successful model [40, 41].

Quantum Chromodynamics (QCD) is the fundamental theory of the strong interaction in terms of the nucleon constituents called quarks. The interaction between quarks or between quark-antiquark pairs is mediated by gluons. This is analogous to the photon in Quantum Electrodynamics (QED). One major difference is that quarks, anti-quarks and gluons carry a strong charge called color, whereas the photon carries no charge. This makes QCD a non-Abelian field theory which is a theory in which the field quanta, the gluons, are also a field source. Gluons self interaction gives rise to additional vertex couplings. However, the theory is difficult to solve, because QCD is non-perturbative at low energies [26].

Perturbative QCD (pQCD) applies corrections to the cross section for point like quarks. These corrections are needed due to the fact that quarks can radiate extra gluons in the reaction process. This is analogous to the radiative corrections in QED. Perturbative QCD gives an effective explanation of these interactions at very high energies and short

distances where the strong coupling constant is small [42]. However, the coupling constant is also Q^2 dependent and becomes too large at low Q^2 and perturbative QCD can no longer be applied. An alternative approach for low energy approximations to QCD, is Chiral Perturbation Theory (ChPT) [43, 44, 45]. This is an effective field theory of QCD including all interactions among pions, nucleons and delta isobars that are permitted by QCD symmetries, and in particular, broken chiral symmetry.

Chiral symmetry states that the number of left-handed quarks is not related to the number of right-handed quarks. In perfect chiral symmetry, the light u and d flavor quarks are massless which would imply that pions are massless. Chiral symmetry is explicitly broken due to the fact that u and d quarks have finite mass, therefore it is spontaneously broken in nature leading to Goldstone bosons which have zero mass and spin. The pion in this case appears as a Goldstone particle in the models with vanishing current quark masses.

ChPT gives a successful description for near threshold pion-pion scattering, pion-nucleon scattering and pion photoproduction cross sections, where the non-resonant part of the cross section is dominant. This non-resonant or background term is due to the Born part of the pion production amplitude. In the case of pseudoscalar coupling between pions and nucleons, the Born terms consist of s- and u- channel nucleon pole diagrams and t- channel meson exchange processes, and the amplitude is gauge invariant, (Fig. 7 top). However, an additional diagram, the seagull or contact term is needed, in order to maintain gauge invariance for pseudovector coupling (Fig. 7 bottom right). ChPT is formulated in terms of hadron degrees of freedom and constrained by the symmetry properties of QCD. ChPT is not always successful at low Q^2 near the photon point, nor is

it successful in the resonance region (Fig. 7 bottom). The resonance region is due to internal excitations of the nucleon and can best be described with phenomenological models. These models of hadron structure use parameterizations of existing experimental data in their calculations. Lattice QCD or LQCD may one day be able to describe these resonances well. Due to the complexity of the theory, we are a long way from a complete description of hadronic structure in the resonance region.

One approach to resolve this difficulty is the use of lattice QCD simulations [46].

Lattice QCD is an accurate numerical simulation of QCD on the lattice.

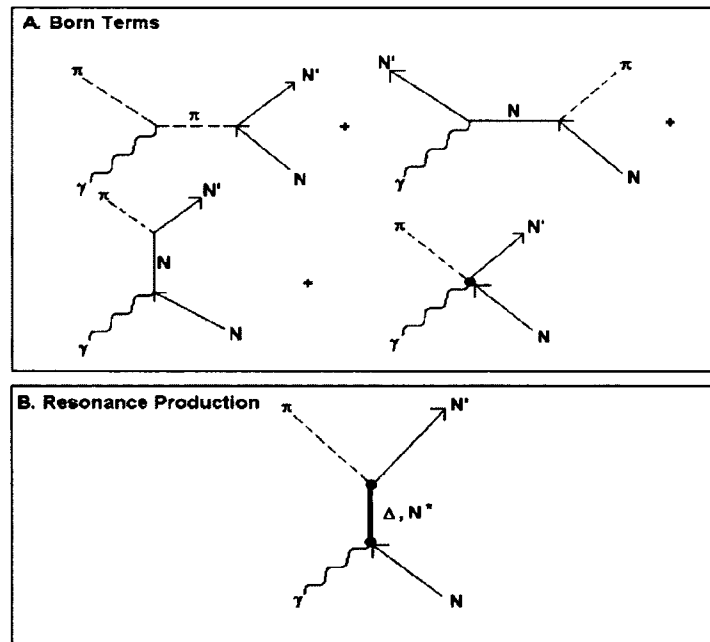


FIG. 7 Feynmann Diagrams for pion photo-production. A) Born terms. B) Resonance contributions.

This works well for heavy quark systems in predicting accurate quantities for interpreting

the data. For light quark systems, the small quark masses are difficult to implement and approximations have been necessary in LQCD calculations.

The dispersion relation approach became the basis of interpretation of pion-production data especially in the Δ resonance region [47]. For investigation of higher energy data with two pion production or other meson-production such as η , k , ω and ϕ , the isobar models [48] were developed. These models could be used to extract higher mass nucleon resonances. In the 1980s the k-matrix method and isobar parameterization were used to develop models to perform amplitude analysis of the data to determine the resonance parameters. Two useful examples of these models are SAID [49] and MAID [50]. These codes allow the user to specify kinematic region of interest and to select specific resonant terms to calculate response functions, multipoles or cross sections.

2.8.1 Hamiltonian Formulation

Most of the existing models that use t- and k-matrices to analyze electromagnetic meson production can be schematically derived from a Hamiltonian formulation [51]. The assumption is that the meson-baryon reaction can be described by a Hamiltonian of the form

$$H = H_0 + V, \quad (51)$$

with H_0 being the free Hamiltonian, and

$$V = v^{bg} + v^R. \quad (52)$$

The term v^{bg} is the background or non-resonant term and v^R describes nucleon or N^* excitation which can be written

$$v^R(E) = \sum_{N_i^*} \frac{\Gamma_i' \Gamma_i}{E - M_i^0}, \quad (53)$$

where Γ_i defines the decay of the i^{th} N^* state into its meson and baryon final states, and M_i^0 is the mass parameter of the resonance position. The background terms arise from the tree diagram mechanisms illustrated in Fig. 8.

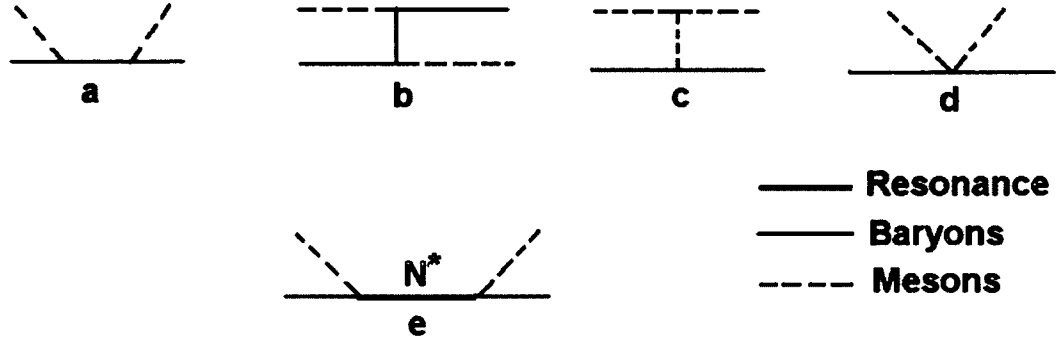


FIG. 8 Tree diagrams for meson-baryon interactions. N^* is a nucleon resonance.

Next, the channel space defined by the meson-baryon channel of interest is defined. Such channels include γN , πN , ηN , $\pi\Delta$, and ρN . The S-matrix for this reaction is expressed

$$S(E)_{ab} = \delta_{a,b} - 2\pi i \delta(E - H_0) \mathcal{T}_{a,b}(E), \quad (54)$$

where a and b are the meson and baryon decay products. The scattering T-matrix $T_{ab}(E)$ can be defined by the coupled-channel equation

$$T_{a,b}(E) = V_{a,b} + \sum_c V_{a,c} g_c(E) \mathcal{T}_{c,b}(E). \quad (55)$$

The meson-baryon propagator of channel c is

$$g_c(E) = \langle c | g(E) | c \rangle, \quad (56)$$

with

$$\begin{aligned}
g(E) &= \frac{1}{E - H_0 + i\epsilon} \\
&= g^P(E) - i\pi\delta(E - H_0),
\end{aligned} \tag{57}$$

and the term $g^P(E)$ is expressed

$$g^P(E) = \frac{P}{E - H_0}, \tag{58}$$

where P is the principle value part of any integration over the propagator. Likewise, the K-matrix can be expressed

$$K_{a,b}(E) = V_{a,b} + \sum_c V_{a,c} g_c^P(E) K_{c,b}(E). \tag{59}$$

The following relation between K-matrix and T-matrix can be defined

$$T_{a,b}(E) = K_{a,b}(E) - \sum_c T_{a,c}(E) [i\pi\delta(E - H_0)]_c K_{c,b}(E). \tag{60}$$

From the two potential formalis [51], the T-matrix Equation (55) can be expressed in the following form

$$T_{a,b}(E) = t_{a,b}^{bg}(E) + t_{a,b}^R(E), \tag{61}$$

with the first term determined only by the non-resonance interaction

$$t_{a,b}^{bg}(E) = v_{a,b}^{bg} + \sum_c v_{a,c}^{bg} g_c(E) t_{c,b}^{bg}(E). \tag{62}$$

The second term is the resonance term and can be expressed as

$$t_{a,b}^R(E) = \sum_{N_i^* N_j^*} \bar{\Gamma}_{N_i^*,a}^i(E) [G(E)]_{i,j} \bar{\Gamma}_{N_j^*,b}(E). \tag{63}$$

The resonant amplitude in Equation (63) is determined by the dressed vertex

$$\bar{\Gamma}_{N^*,a}(E) = \Gamma_{N^*,a} + \sum_b \Gamma_{N^*,b} g_b(E) t_{b,a}^{bg}(E), \tag{64}$$

with the dressed propagator

$$\left[G(E)^{-1} \right]_{i,j}(E) = (E - M_{N_i}^0) \delta_{i,j} - \sum_{i,j}(E), \quad (65)$$

where $M_{N_i}^0$ is the N^* resonance state bare mass and the self-energy is

$$\sum_{i,j}(E) = \sum_a \bar{\Gamma}_{N_i,a}^t g_a(E) \bar{\Gamma}_{N_j,a}(E). \quad (66)$$

It must be noted that for channels including an unstable particle, such as $\pi\Delta$, ρN , or σN , the meson-baryon propagator $g_a(E)$ should be modified to include a width due to their decay into $\pi\pi N$ channels. This will modify the Hamiltonian

$$g_a(E) \rightarrow \left\langle a \left| \frac{1}{E - H_0 - \sum_v(E)} \right| a \right\rangle, \quad (67)$$

with an energy shift,

$$\sum_v(E) = \sum_i \Gamma_v^t(i) \frac{P_{\pi\pi N}}{E - H_0 - i\epsilon} \Gamma_v(i), \quad (68)$$

where Γ_v describes the decay of ρ , σ , or Δ in the quasi-particle channels.

It should be noted that these models will consider the formulation in the partial-wave representation [52]. The channel labels (a,b,c) will also include the usual angular momentum and isospin quantum numbers.

2.8.2 MAID

MAID is a unitary isobar model (UIM) developed by the Mainz group [50] and is based on the on-shell relation (Equation 57). By including only one hadron channel, πN for example, Equation 58 leads to

$$\begin{aligned} T_{\pi N, \gamma N} &= \frac{1}{1 + iK_{\pi N, \pi N}} K_{\pi N, \gamma N} \\ &= e^{i\delta_{\pi N}} \cos(\delta_{\pi N}) K_{\pi N, \gamma N}. \end{aligned} \quad (69)$$

With the relationship $K_{\pi N, \pi N} = -\tan(\delta\pi N)$ with $\delta\pi N$ being the pion-nucleon phase shift. By making another assumption $K = V = v^{bg} + v^R$, the above equation can be cast into the following form

$$T_{\pi N, \gamma N}(UIM) = e^{\delta\pi N} \cos(\delta\pi N) [v_{\pi N, \gamma N}^{bg}] + \sum_{N_i^*} T_{\pi N, \gamma N}^{N_i^*}(E). \quad (70)$$

As can be seen, the non-resonant multi-channel effects such as $\gamma N \rightarrow (\rho N, \pi \Delta) \rightarrow \pi N$, which are important in the second and third resonance region, are neglected in MAID. In addition, MAID calculates the non-resonant amplitude $v_{\pi N, \gamma N}^{bg}$ using an energy-dependent mixture of pseudo-vector and pseudo-scalar πNN coupling

$$L_{\pi NN} = \frac{\Lambda_m^2}{\Lambda_m^2 + q_0^2} L_{\pi NN}^{PV} + \frac{q_0^2}{\Lambda_m^2 + q_0^2} L_{\pi NN}^{PS}, \quad (71)$$

where q_0 is the on-shell photon momentum.

With a cutoff at 450 MeV for Λ_m , one gets pseudo-vector coupling at low energies and pseudo-scalar coupling at high energies. For the resonance term, MAID uses the Walker's parameterization [48]

$$T_{\pi N, \gamma N}^{N_i^*}(E) = f_{\pi N}^i(E) \frac{\Gamma_{tot} M_i e^{i\phi}}{M_i^2 - E^2 - iM_i \Gamma_{tot}} f_{\gamma N}^i(E) \bar{A}^i, \quad (72)$$

where $f_{\pi N}^i(E)$ and $f_{\gamma N}^i(E)$ are the form factors which describe the decays of the N^* , Γ_{tot} is the total decay width, \bar{A}^i is the $\gamma N \rightarrow N^*$ excitation strength and ϕ is the phase shift determined by the unitary condition and an assumption that the phase ψ of the total amplitude is related to πN phase shift and the inelasticity $\eta_{\pi N}$ is given by

$$\Psi(E) = \tan^{-1} \left[\frac{1 - \eta_{\pi N}(E) \cos 2\delta_{\pi N}(E)}{\eta_{\pi N}(E) \sin 2\delta_{\pi N}(E)} \right]. \quad (73)$$

The MAID model uses a phenomenological fit to previous photo and electroproduction data covering mass energy W up to 2 GeV and Q^2 up to 4 GeV. There is also a Jlab/Yereran UIM [53] which is similar to MAID, but implements the Regge parameterization in calculating the amplitudes at high energies. MAID2000 incorporates the improved Unitary Isobar Model developed in Mainz on pion photo and electroproduction. MAID2000 covers a range in W from the pion threshold up to approximately 2 GeV and includes all the main resonances: P_{33} (1232), P_{11} (1440), D_{13} (1520), S_{11} (1535), F_{15} (1680) and D_{33} (1700) [26]. The non resonance terms are described using the standard Born terms with a mixed pseudovector - pseudoscalar πNN coupling and vector meson (ρ and ω) exchange. The mixed πNN coupling is chosen since it guarantees a good reproduction of the data both at the low and consistent with low energy theorems and chiral perturbation theory, and at high energies where the renormalizing pseudoscalar coupling leads to better description of existing data. The Q^2 dependence for the Born terms is introduced explicitly with nucleon and pion form factors and expressed in standard dipole form. Both Born and vector meson exchange terms are fitted to existing data [50, 54, 55].

2.8.3 SAID

SAID is a multi-channel K-matrix model [56] which is based on the on-shell relation in (Equation 58) with three channels: γN , πN and πA , which represent all other open channels. This solution results in a 3 x 3 matrix equation which can be expressed

$$T_{\pi N, \gamma N}(SAID) = A_I (1 + iT_{\pi N, \pi N}) + A_R T_{\pi N, \pi N}, \quad (74)$$

in which A_I and A_R are expressed

$$A_I = K_{\gamma N, \pi N} - \frac{K_{\gamma N, \pi \Delta} K_{\pi N, \pi N}}{K_{\pi N, \pi \Delta}}, \quad (75)$$

$$A_R = \frac{K_{\gamma N, \pi \Delta}}{K_{\pi N, \pi \Delta}}. \quad (76)$$

For simplicity, the parameterizations of A_I and A_R become

$$A_I = [v_{\gamma N, \pi N}^{bg}] + \sum_{n=0}^M \bar{P}_n z Q_{l\alpha} + n(z), \quad (77)$$

$$A_R = \frac{m_\pi}{k_0} \left(\frac{q_0}{k_0} \right)^{l\alpha} \sum_{n=0}^N P_n \left(\frac{E_\pi}{m_\pi} \right)^n, \quad (78)$$

where k_0 and q_0 are the on-shell momentum for the pion and photon respectively,

$$z = \sqrt{k_0^2 + 4m_\pi^2} / k_0, \quad Q_L(z) \text{ is the Legendre polynomial of second kind,}$$

$E_\pi = E_\gamma - m_\pi (1 + m_\pi / 2m_M)$, and p_n and \bar{p}_n are free parameters. SAID calculates $v_{\gamma N, \pi N}^{bg}$

of Equation 75 from the standard pseudo-scalar Born terms in ρ and ω exchanges. The

empirical πN amplitude $T_{\pi N, \pi N}$ needed to evaluate Equation 72 is also available in SAID.

Once the free parameters p_n and \bar{p}_n are determined, the N^* parameters are then extracted

by fitting the resulting amplitude $T_{\gamma N, \pi N}$ at energies near the resonance position to a Breit-

Wigner parameterization similar to Equation 69.

2.9 NEUTRON RESONANCES

The goal of this analysis is to provide new information on neutron resonances.

Because of the fact that there are no free neutron targets, a deuteron target is used. The

deuteron contains both a proton and a neutron, so the exclusive channel, in which the

scattered electron, π^- and one proton are detected in the final state, was chosen for

analysis. With polarized deuterons and a polarized electron beam, we can determine double polarization and target single spin asymmetries for the $D(e,e'\pi^-)p$ reaction. These data will be used as part of the fits to world data, with the goal of extracting the helicity amplitudes for neutron resonances.

CHAPTER 3

EXPERIMENTAL SET-UP

3.1 INTRODUCTION

The EG1b experiment used the longitudinally polarized electron beam and the CEBAF Large Acceptance Spectrometer (CLAS) housed in Hall B at the Thomas Jefferson National Accelerator Facility in Newport News, Virginia. The experimental apparatus will be described in this chapter, including the electron beam delivered to the experimental set-up, the polarized target and the CLAS detector package.

3.2 THE POLARIZED ELECTRON BEAM

The longitudinally polarized electron beam is produced by the Continuous Electron Beam Accelerator Facility (CEBAF). Fig. 9 shows the accelerator which is 7/8 of a mile total circumference in an oval race track configuration with linear accelerators on the north and south straight-a-ways, connected by two recirculating arcs at the east and west ends [57]. The electron can make as many as five passes around the track resulting in electron beam energies as high as 6 GeV, with an energy spread of $\Delta E/E \leq 2.5 \times 10^{-5}$ at currents up to 300 μA delivered in 1497 MHz RF modulated pulses split between the three halls [58]. An upgrade of the linacs to achieve beam energies up to 12 GeV is now in progress.

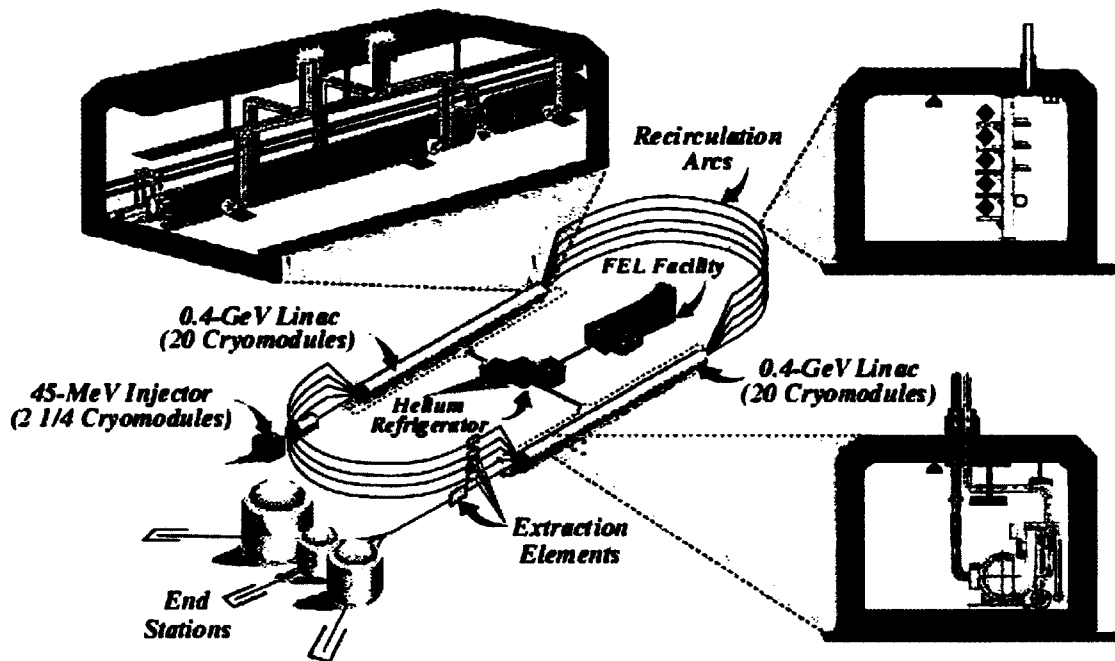


FIG. 9 Schematic of the Jefferson Lab accelerator components.

The electrons are accelerated to 45 MeV from the beam injector and then are accelerated up to 600 MeV in each linac. This is a continuous wave accelerator, which means that it operates at a much higher duty cycle than traditional accelerators. This is achieved by employing specially designed five-celled super-conducting RF cryomodules that are cooled by a central LHe refrigeration system.

3.2.1 Polarization Mechanism

Polarized electrons are produced by hitting a GaAs cathode with a circularly polarized laser, which results in an electron with linear polarization. With pure GaAs, the heavy hole (HH) valence band electrons are excited from the $m = 3/2$ to the $m = 1/2$ state by the $m = -1$ circularly polarized photon. The heavy hole valence band is the band

with higher effective mass. However, the light hole (LH) valence band electrons are excited from the $m = 1/2$ to the $m = -1/2$ state by the $m = -1$ photon. Likewise, the light hole valence band is a band with lower effective mass. The LH band has the same small energy gap as the HH band in the region from the valence band up to the conduction band, which produces an energy degeneracy in the electron excited states resulting in 50% polarization because the HH band is three times more likely than the LH band.

To avoid this degeneracy, the pure GaAs cathode was replaced with a strained GaAs cathode. The GaAs is strained by growing the GaAs lattice on a substrate of $\text{GaAs}_{0.72}\text{P}_{0.28}$ [59]. At the interface between the two lattices, a strain, which eliminates the degeneracy, is created on the GaAs due to the slightly smaller lattice spacing of the substrate. With the created degeneracy gap (see Fig. 10), the laser wavelength can now be selected to provide enough energy to excite the transition from the valence $m = 3/2$ to the conduction $m = 1/2$ state but exclude the valence $m = 1/2$ to the conduction $m = -1/2$ state. All these transitions are valid for $m = -1$ photons as well as the $m = 1$ photons, so that the electron polarization can be flipped from positive helicity to negative helicity. With the strained GaAs cathode, we can achieve polarizations 80% or greater. This configuration has been available since 1998, and is the configuration for the EG1 experiment.

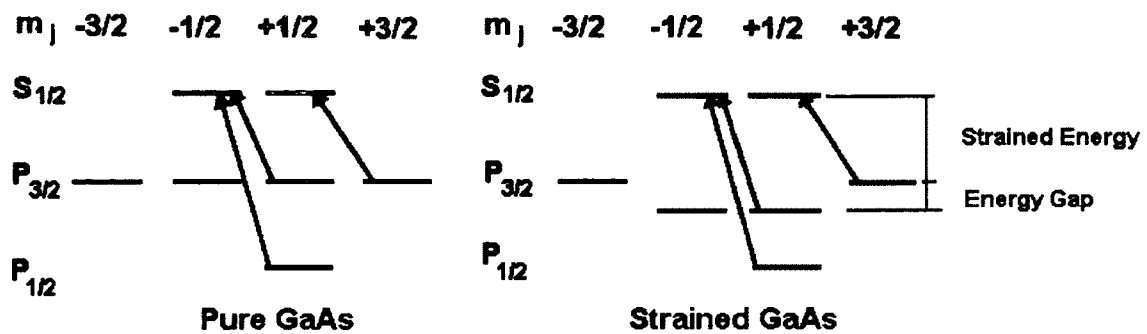


FIG. 10 Comparison of the energy gap between pure and strained GaAs. The conduction band is shown on top, and the valence band is shown on the bottom. The diagram on the left shows the degeneracy from the P_{3/2} to S_{1/2} state (blue arrows) for pure GaAs. The diagram on the right shows the splitting of this degeneracy (green and blue arrows) for strained GaAs.

3.2.2 Spin Precession

After the electrons travel through the linacs for energy gain, they are steered through the recirculating arcs which are a series of bending magnets. The electron spin can be affected by the various components of the beam optics especially the bending magnets. Since the electron spin precesses in the presence of magnetic fields, the orientation of the electron spin must be adjusted to align with the beam direction before entering the hall. This is done with a Wien filter which produces electric and magnetic fields that are perpendicular to the beam direction [26]. The magnetic field will cause the electron spin to precess back to the desired orientation while the electric field will preserve the electron momentum by compensating for the deflection caused by the magnetic field.

3.2.3 Helicity Switching

As mentioned in section 2.6, asymmetry measurements are dependent on a reversal of beam and/or target helicity, which means that the electron helicity has to be reversed often. This is done quickly by using a Pockel cell that reverses the helicity of the laser light which in turn reverses the electron helicity. The helicity is reversed in a pseudo-random order in which the first helicity state is chosen at random and is followed by the opposite helicity state. The helicity of the circularly polarized laser beam that is incident on the GaAs target can also be reversed by the insertion of a half-wave plate. This is done at a much slower rate over the course of many runs. Both methods are used, and it is this combination of both fast and slow methods that reduces systematic errors that might have been caused by any differences in the beam conditions over time in either helicity state.

3.2.4 Polarization Measurement

Elastic scattering of incident beam electrons from free target electrons is called Møller scattering, and is used to measure the beam polarization. The Møller polarimeter has a 20 μm iron foil that is placed in a magnetic field and located in the beam upstream from the target. Beam electrons scatter off of the free foil electrons, which are polarized in the magnetic field. The scattered and recoiled electrons are deflected away from the beamline by a quadrupole magnet and detected in coincidence by two down-stream scintillation counters. The detection of both electrons in coincidence makes a clear distinction between electrons from Rosenbluth scattering and electrons from Møller scattering. By collecting counts for each beam helicity and calculating an asymmetry, a comparison to the known Møller asymmetry A enables us to determine the polarization of

the electron beam. The Møller asymmetry is a function of electron polarization and scattering angle [60], and can be expressed

$$A = \frac{\sin^2 \theta}{(4 - \sin^2 \theta)^2} (\sin^2 \theta P_y^B P_y^T - (8 - \sin^2 \theta) P_z^B P_z^T), \quad (79)$$

where P^B is the beam polarization, P^T is the Møller target polarization, and θ is the scattering angle. The \hat{z} direction is along the beam and the \hat{y} direction is chosen so that the target polarization lies in the $\hat{y} - \hat{z}$ plane. From this comparison, the polarization of the electron beam can be extracted.

3.2.5 Beam Position and Raster

There are several devices that measure the beam position and beam profile. The harp which is upstream from CLAS is used to monitor the beam profile. The harp is made up of a system of thin wires that pass through the beam to measure the x and y position of the beam. The acceptable beam width is less than 200 μm . A harp scan is performed frequently during the experiment Fig. 11 shows an example of a typical harp scan. There are also three beam position monitors that are used to ensure that the beam passes through the target.

There are beam raster magnets as well. The raster magnets are two pairs of dipole magnets that affect the beam position; the beam position can be determined for each event because the currents in the magnet are measured for each event. Rastering is important when solid polarized target materials are used in the experiment. This reduces radiation damage in a concentrated area of the target, which would tend to de-polarize the target material. Rastering the beam allows the beam to move over the entire face of the target.

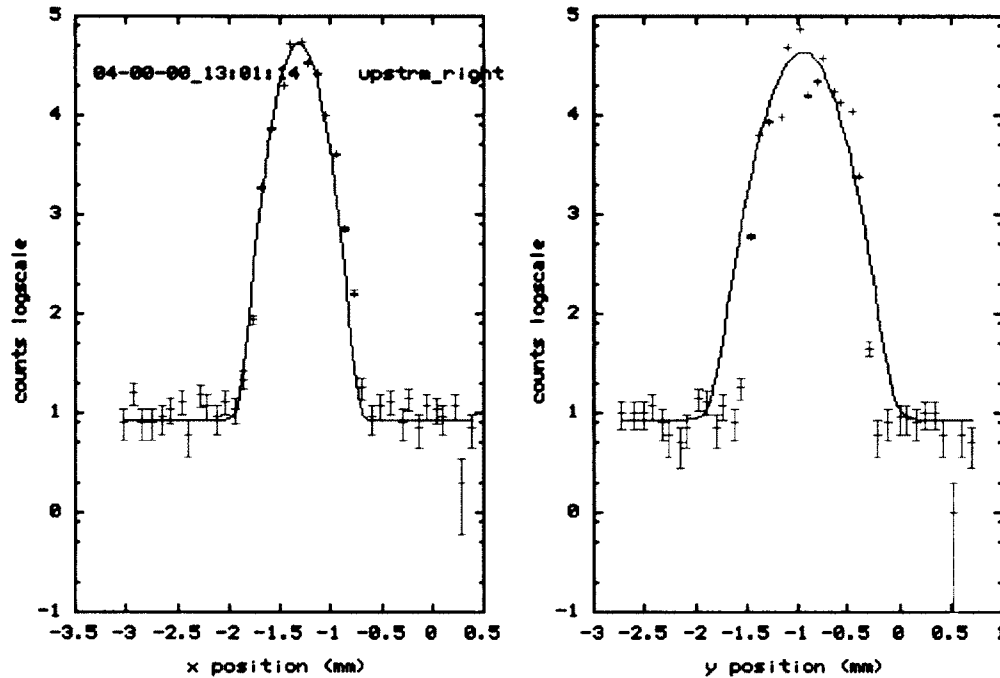


FIG. 11 Harp scan showing the x and y position of the beam.

3.2.6 Additional Scalars

Additional information is required for data analysis. This information includes the electron helicity state, RF signal and Faraday cup. The helicity synchronization signal is actually two signals, one that measures when the helicity is being changed, and the other that measures what the helicity state is. Both pulses determine the state of the beam, since the beam helicity is changed in a pseudo-random order on a pair by pair basis. This guarantees an equal number of pulses for each state. The RF signal sends a signal to the hall when an electron bunch is being sent from the machine. Bunch lengths are usually 1.7 ps. This information is used to determine event start time. Finally, the Faraday cup is used to determine the total number of electrons delivered over a given period of time.

3.3 POLARIZED TARGET

In the EG1 experiment, the polarized target is made up of frozen ammonia (NH₃) and deuterated ammonia (ND₃) beads.

3.3.1 Polarization Mechanism

A particles spin can be aligned with an external magnetic field due to the interaction of the particles magnetic moment μ with that external magnetic field B. This interaction, which is called the Zeeman effect, produces a set of $2I+1$ sublevels, where, I is the angular momentum of the particle. $I=1/2$ for protons and $I=1$ for deuterons. At thermal equilibrium (TE) the population of the magnetic sublevels is described by the Boltzmann law,

$$N_1 = N_2 \exp\left(\frac{-\Delta E}{k_B T}\right), \quad (80)$$

where

$$\Delta E = -\left(\frac{\mu}{I}\right)B(m_1 - m_2), \quad (81)$$

T is the temperature of the system, k_B is the Boltzmann constant, $N_{1,2}$ are the number of particles in the magnetic sublevels and $m_{1,2}$ are the particle's magnetic quantum numbers.

The polarization is defined according to the distribution of particles in the magnetic sublevels. For example,

$$P\left(\frac{1}{2}\right) = \frac{N_{\frac{1}{2}} - N_{-\frac{1}{2}}}{N_{\frac{1}{2}} + N_{-\frac{1}{2}}}, \quad (82)$$

is the polarization for a spin $\frac{1}{2}$ particle such as a proton, and

$$P(1) = \frac{N_1 - N_{-1}}{N_1 + N_0 + N_{-1}} \quad (83)$$

is the polarization of a spin 1 particle such as the deuteron. These polarizations can be expressed at thermal equilibrium by

$$P\left(\frac{1}{2}\right) = \tanh\left(\frac{\mu B}{k_B T}\right) \quad (84)$$

and

$$P(1) = \frac{4 \tanh\left(\frac{\mu B}{2k_B T}\right)}{3 + \tanh^2\left(\frac{\mu B}{2k_B T}\right)}. \quad (85)$$

A particle with a large magnetic moment can reach a high degree of polarization in a high magnetic field at low temperatures. For example, electrons ($\mu = 660\mu_p$) can reach a polarization of 92% in a 2.5 Tesla magnetic field at a temperature of 1K [61]. However the target materials of interest are protons and deuterons, which unfortunately have low polarizations (0.25% for protons and 0.05% for deuterons) due to their small magnetic moments. One way of overcoming this is to increase the magnetic field and lower the temperature such that the ratio of B/T is at a maximum [62]. Such high magnetic fields are unrealistic and cannot be produced.

3.3.2 Dynamic Nuclear Polarization (DNP)

It is possible to transfer high electron polarizations to nuclei using a microwave field. This process is called dynamic nuclear polarization (DNP), and for target polarization, high electron polarization at magnetic fields as high as 5 Tesla at temperatures as low as 1 K can be transferred to target nuclei using the microwave field. In theory, we are not limited to 5 T or 1 K - these values are due to experimental

limitations. Using DNP requires a high concentration of polarizable nucleons lightly doped with paramagnetic centers like free electrons for the purpose of transferring the high electron polarization to the proton. These centers are introduced by either chemical means or radiation to provide a large number of unpaired electron spins. The Hamiltonian that describes this system has a perturbation term coming from the spin-spin interaction between the unpaired electron spin and the nucleon spin. This allows for new eigenstates of this system which are given by a linear combination of the free Hamiltonian eigenstates. Fig. 12 shows the Larmor frequencies ω_e and ω_p of the electron-proton pair. By applying an RF field with a frequency equal to the sum ($\omega_e + \omega_p$) or difference ($\omega_e - \omega_p$) of the Larmor frequencies of the two interacting systems, transitions can occur where both proton and electron spins are flipped [63]. This allows the high electron

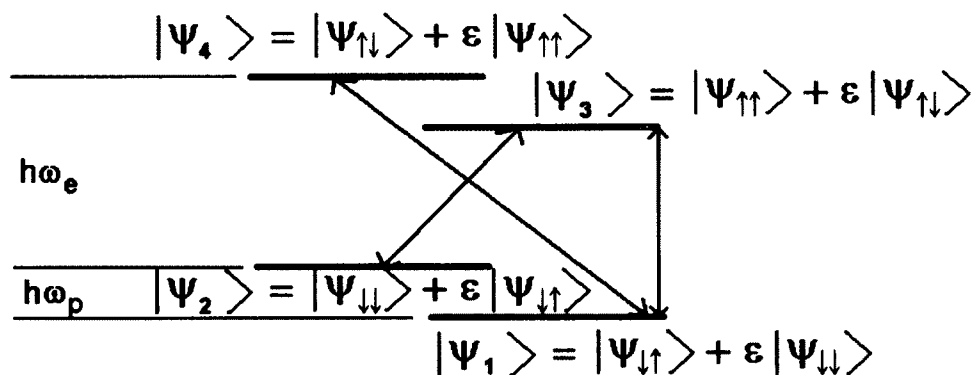


FIG. 12 The energy level diagram for an electron proton pair. The Larmor frequencies are $\omega_e = 140$ GHz and $\omega_p = 213$ MHz at 5 Tesla. The first arrow in the subscript represents electron spin, while the second arrow represents proton spin. The transitions from $|\Psi_1\rangle$ to $|\Psi_4\rangle$, and from $|\Psi_2\rangle$ to $|\Psi_3\rangle$ are induced by microwaves of frequencies $\omega_e + \omega_p$ and $\omega_e - \omega_p$ [64].

polarization to be transferred to the proton, and since the proton has a much longer relaxation time ($\sim 10 - 100$ s) than the electron (~ 1 ms), the electron can be re-used for additional transitions. The relaxation time is the time for the spin to flip back to its lower energy state. This technique also works for transferring polarization to other nuclear targets such as the deuteron. Using DNP, polarizations for the proton can reach 80-90% while the deuteron can reach 30-40%.

3.3.3 The CLAS Polarized Target

The CLAS target was designed to be placed in the limited space available in the center of CLAS. The target has two sets of superconducting magnetic coils that produce a 5 Tesla magnetic field in a direction either parallel or anti-parallel to the beam line. This magnetic configuration was chosen because the axis of the produced magnetic field is entirely longitudinal and therefore the incident electrons are not affected by the magnetic field. This configuration also protects the region 1 drift chambers from Møller scattering which produces low energy electrons, by steering them through a forward hole where there are no detector elements. Finally this configuration produces the uniform field needed for the DNP process. Table 4 lists the target magnet characteristics.

Table 4 Target magnet characteristics.

Maximum central magnetic field	5.1 Tesla
Current for full field	123.646 A
Field/Current	0.04125 Tesla/A
Central bore diameter	200 mm

Liquid helium is used to cool superconducting the magnet coils to 4.2 K, as shown in Fig. 13.

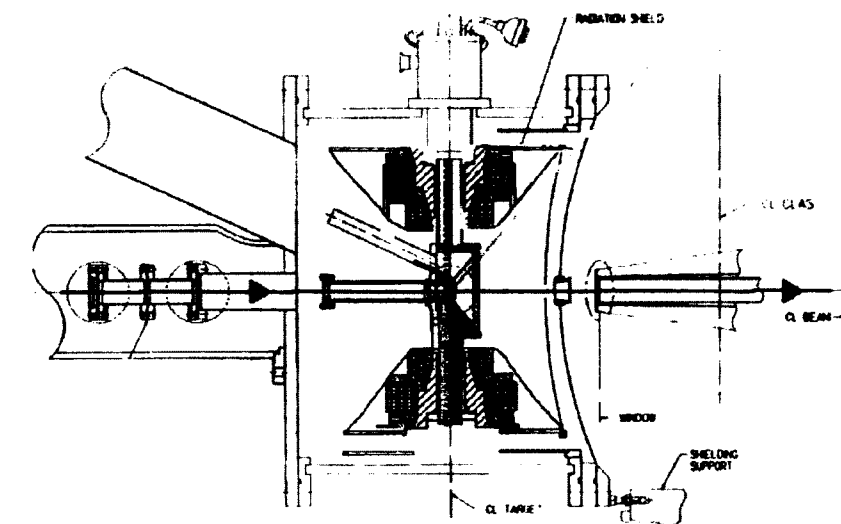


FIG. 13 Cross section of the target chamber in CLAS.

In the center of the magnet is a cylindrical hole 200 mm in diameter which houses the target stick which is inserted into a banjo shaped bore through a stainless steel tube. The banjo is filled with liquid helium and cooled down to $\sim 1\text{K}$ by a ^4He refrigerator. Liquid from the magnet buffer dewar is transferred to a separator pot where the liquid and vapor phases are separated using a sintered copper plate. The pressure in the separator is 600 mbar, so the helium is pre-cooled to $\sim 3.5\text{K}$. The cold vapor is pumped out and used to cool the radiation shields. The liquid phase is then collected at the bottom of the pot where it flows to a heat exchanger and fills the target holder via two needle valves. The incoming liquid is cooled when the outgoing vapor exchanges heat therefore cooling the banjo to $\sim 1\text{K}$. A microwave field ($\omega_e + \omega_p$ or $\omega_e - \omega_p$) irradiates the target material to

enhance target polarization through the DNP process described above. The field is created by a system of rectangular and circular wave guides ending in a trumpet near the target cell.

3.3.4 The Target Stick

For the desired proton and deuteron targets, frozen ammonia beads ($^{15}\text{NH}_3$ and $^{15}\text{ND}_3$) were used as target material and placed inside two target cells on an aluminum insert, as shown in Fig. 14. The other two cells contain carbon and helium. These are used for background measurements. The cells are 1 cm thick and 1.5 cm in diameter, and are made up of 0.2 mm thick plastic material with good resistance to radiation damage they have no polarizable molecules that can affect the NMR measurement. The target stick is inserted into the magnet core and can be moved in a vertical direction to place the target material of interest into the beam line.

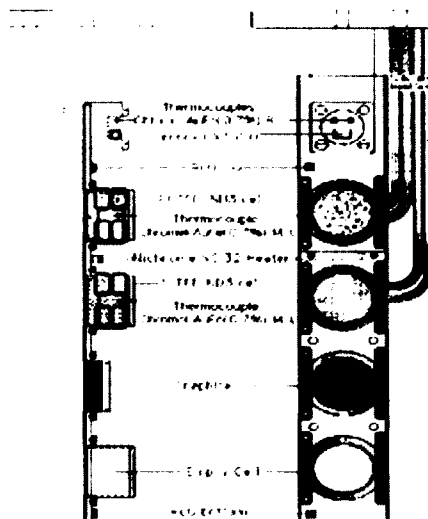


FIG. 14 Front and side view of the target stick that holds the target material. The top two places hold NH_3 and ND_3 , the third one holds carbon and the bottom is empty (except for the liquid Helium bath). The carbon and empty target chambers are used to study the background.

The CLAS target was located 60 cm upstream from the center of CLAS, which allowed the detection of electrons scattering at small angles, and therefore gave a better coverage at low Q^2 . All target components are controlled by an Epics interface.

3.3.5 NMR Measurement

Once the target is polarized, it is monitored using nuclear magnetic resonance (NMR) with a Q-meter technique. The polarization P is expressed

$$P \sim \int_0^{\infty} \chi''(\omega) d(\omega) \quad (86)$$

where ω is the angular frequency of the applied RF field and $\chi''(\omega)$ is the absorptive part of the nuclear susceptibility,

$$\chi(\omega) = \chi'(\omega) - i\chi''(\omega) \quad (87)$$

which is non-zero in a small range around the Lamor frequency of the proton or deuteron.

The polarized target material is contained in the NMR coil with an inductance L_c and resistance r_c . This coil is connected to a capacitor C and a damping resistor R using a commercially available Q-meter. This configuration forms a series LRC circuit where the target material modifies the inductance L_c , causing a change in the circuit impedance. If the circuit is driven by a frequency synthesizer that sweeps the RF frequency ω through the Lamor resonance, the target material either emits or absorbs energy causing an inductance change in the coil therefore causing an impedance change in the circuit. For a constant current, the impedance change is proportional to a complex voltage $V(\omega, \chi)$ whose real part is selected by a phase sensitive detector (PSD). The first step in the

measurement is to set the magnetic field such that the Larmor frequency of the spin species is not within the sweep range of the synthesizer. This makes a measurement of the frequency dependence of the output voltage to the NMR electronics, which is denoted as $\text{Re}\{V_o(\omega)\}$, and which is called the Q-curve. Next the field is set to the resonance value and the output voltage is measured and denoted as $\text{Re}\{V(\omega)\}$. This voltage is a superposition of the signal proportional to χ and the Q-curve,

$$V(Q) = V(\omega, \chi = 0). \quad (88)$$

These two signals are subtracted resulting in,

$$\chi''(\omega) \propto \text{Re}\{V(\omega)\} - \text{Re}\{V_o(\omega)\} \equiv S(\omega), \quad (89)$$

and the measured polarization is proportional to the integral of that signal,

$$P = k \int_{\omega_l}^{\omega_u} S(\omega) d(\omega) \quad (90)$$

where k is a constant determined by a thermal equilibrium calibration, and ω_l and ω_u are the lower and upper range of the frequency sweep [65].

Although analysis of the Q-curve was used for on-line polarization measurements and monitoring, an alternative method of extracting polarization using elastic scattering was ultimately used for data analysis. This method will be discussed in chapter 4.

3.4 THE CLAS DETECTOR

When the electrons scatter off the target, particles from this reaction are detected by the CLAS detector housed in Hall B. CLAS is the CEBAF Large Acceptance Spectrometer [31] which is a nearly 4π spectrometer that allows for the detection of multiple-particle final states. The individual detector elements, as well as the particle tracking systems will be discussed in the following sections.

3.4.1 The Torus Magnet

The CLAS detector is built around six superconducting coils which produce a toroidal magnetic field used to measure the momentum of charged particles from their trajectories. These six superconducting coils divide the detector into six identical sectors. They supply a magnetic field that points in the ϕ direction (azimuthal to the beam line) so the field is mostly perpendicular to the particle trajectory bending the particles either towards or away from the beam line. The standard configuration is for the negative charged particles to be bent in towards the beam line and is called “inbending”. The torus current was occasionally reversed in the experiment so that negative charged particles were bent away from the beam line, referred to as the “outbending” configuration. This was done in order to obtain greater kinematic coverage. The magnetic field varies from 0.5 Tesla m for large angle tracks to 2 Tesla m at forward angles for the high momentum tracks. The coils are designed with a specific shape ensuring that the magnetic field is close to zero at the beam axis where the target is placed (see Fig. 15). The torus configurations are listed in Table 5.

Table 5 Torus currents for EG1b.

Beam Energy (GeV)	Torus Current (A)
1.6	1500, -1500
1.7	-1500
2.5	-1500
4.2	2250, -2250
5.6	2250
5.73	2250, -2250
5.76	-2250

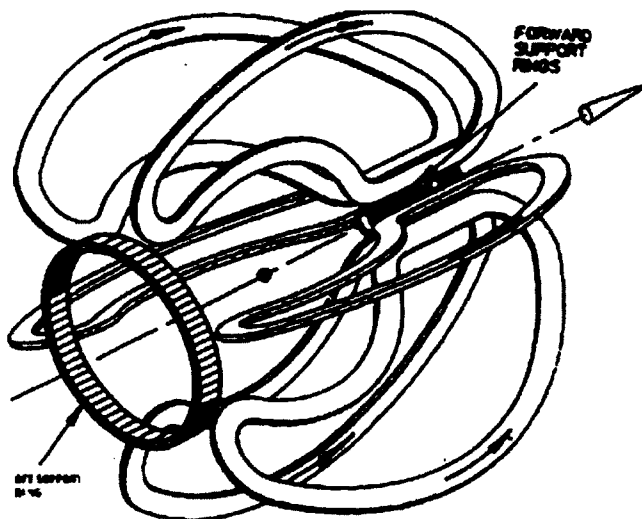


FIG. 15 The CLAS torus coils.

3.4.2 Drift Chambers

The first detector elements that scattered particles will usually traverse are the drift chambers. In CLAS, the momentum of charged particles is determined using a series of multi-wire drift chambers shown in Fig. 16 [66]. The drift chambers can detect charged particles over an angular range from 8° to 142° . Each of the six sectors contains its own set of three drift chambers, known as Regions 1, 2 and 3.

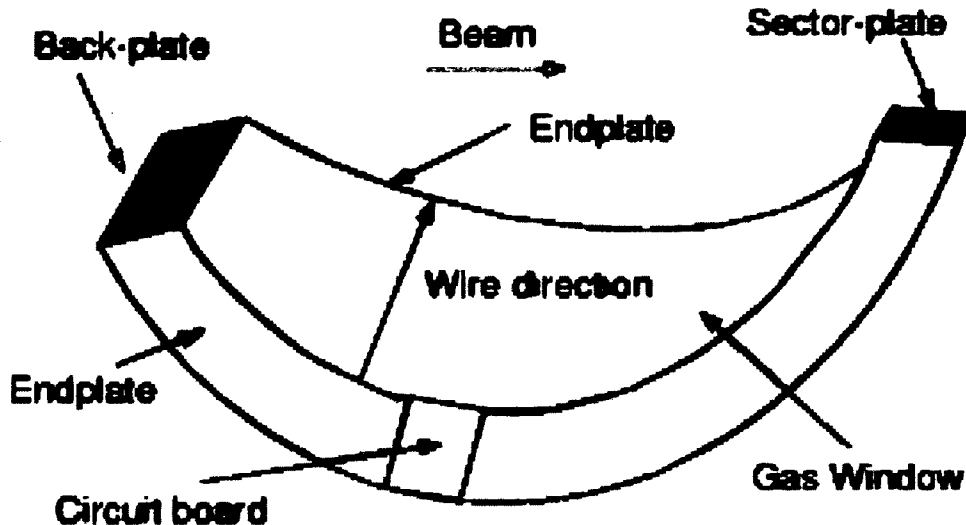


FIG. 16 One drift chamber "wedge". There are a total of 18 wedges arranged in six sectors in three regions.

Region 1 is the inner most region close to the beam line, where there is a low magnetic field. Region 2 is located between the torus coils where there is a high magnetic field. Region 3 is located outside the torus coils and is also in a low magnetic field.

Each region of drift chamber consists of two super-layers (one stereo and one axial) containing six layers of wires for each super-layer. The inner axial layer is oriented so that at the center of the sector, the wires are in the ϕ direction. The outer stereo layer of each region oriented at an angle of 6° relative to the axial wires. Because space is limited, the region 1 outer super-layer has four layers of wires instead of six. Fig. 17 shows the wire configuration in which is each sense wire is surrounded by six field wires making up a honeycombed pattern.

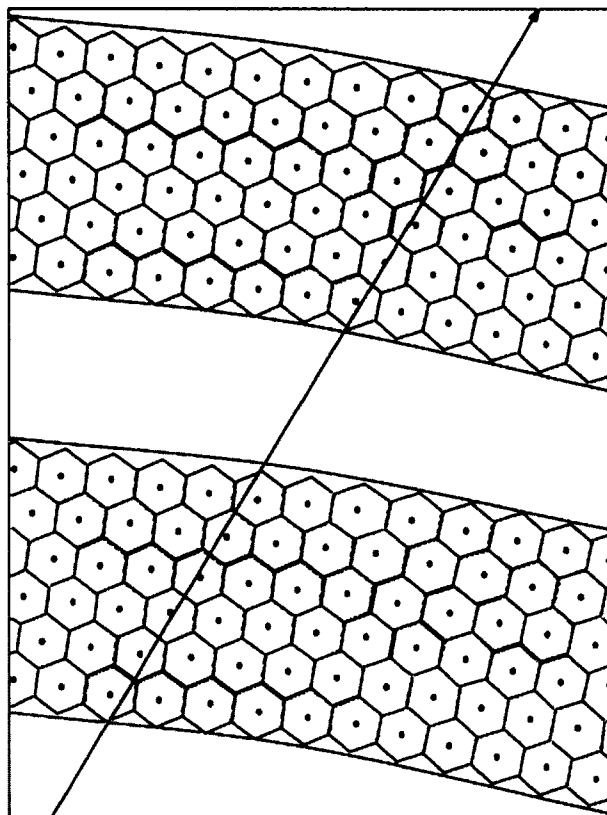


FIG. 17 Schematic showing two super-layers of drift chamber wires. The sense wires are at the center of the hexagons and the field wires are the hexagon vertices.

The sense wires are strung from 20 μm diameter gold-plated tungsten while the field wires are 140 μm diameter gold-plated aluminum. The chambers are filled with a constant pressure gas mixture of 88% argon and 12% CO_2 . This mixture was chosen since it has a high saturated drift velocity greater than 4 $\text{cm}/\mu\text{c}$ [66]. It has an operating voltage plateau of several hundred volts before breakdown. The electric field maintained in the gas is oriented such that when a charged particle passes through, the gas mixture is ionized which causes electrons to drift towards the sense wires (anodes) and the ions will drift towards the field wires (cathodes). When this happens, a signal is created at the

anode and stops a time to digital converter (TDC), which was initiated by a signal to the time of flight scintillators, to measure the drift time. The drift time determines the drift distance from a pre-determined calibration. The final particle trajectory is determined by fitting the track positions from each layer to a curve.

Since the sense wires are at positive potential and the field wires are held at negative potential with half the absolute value, this keeps the overall drift-chamber potential at zero, minimizing interference with other detector elements. During data taking, the rates in the drift chamber as well as the current and voltage in each group of 16 sense wires were monitored to ensure that the entire drift chamber was supplied with the necessary high voltage and that none of the wires had tripped.

3.4.3 Čerenkov Detector

The next detector element to be traversed by the scattered particles is the Čerenkov detector shown in Fig. 18. These detectors are used for particle identification, mainly used to distinguish electrons from other negatively charged particles, such as π^- [67]. When a charged particle travels through a medium faster than the speed of light in that medium, Čerenkov light is emitted. This process occurs at a threshold given by $\beta = 1/n$ where n is the index of refraction of the given medium.

The Čerenkov detectors are located in between the region 3 drift chambers and the time of flight counters, and they cover a range of θ from 8° to 45° . Each Čerenkov detector is filled with perfluorobutane (C_4F_{10}) gas at atmospheric pressure, which is constantly recirculated with the pressure kept at a constant value using a system of pumps and valves. Perfluorobutane was chosen such that only charged particles with a mass

close to the electron mass will be fast enough to produce Čerenkov light. It has an index of refraction ($n = 1.00153$) resulting in excellent light transmission properties [68]. This gas separates electrons from pions up to a pion momentum around 2.7 GeV. The index of refraction corresponds to a threshold for particle energy equal to

$$E = \frac{m}{\sqrt{1-\beta^2}} = \frac{n}{\sqrt{n^2-1}} m, \quad (91)$$

where n is the index of refraction and m is the particle rest mass in MeV. For perfluorobutane, $E = 18.1m$ which yields a threshold of 9 MeV for electrons and a much higher (~ 2.7 GeV) threshold for pions.

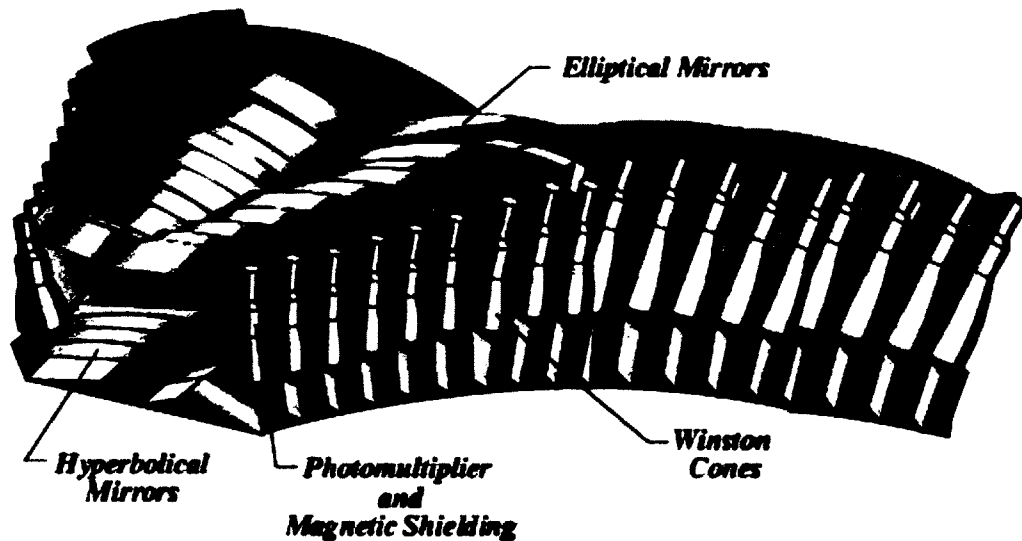


FIG. 18 The Čerenkov detector for one sector.

Each of the six sectors of CLAS has its own Čerenkov detector and each detector consists of a series of 18 pairs of photo-multiplier tubes (PMTs) and mirrors, see Fig. 18. The acceptance of the Čerenkov detector is maximized by placing the PMTs behind the

torus coils that block the scattered particles. Each pair of mirrors creates a segment that lies in a position of relatively constant θ , and the width of the segment increases as θ increases. This configuration allows the forward region of the sector to be covered. This θ segmenting of the detector allows Čerenkov information to be compared to the trajectory of particles to help determine which particle in that event caused the Čerenkov signal.

3.4.4 Time of Flight

After the Čerenkov detector, the scattered particles travel through the time of flight scintillators [84]. The time of flight detector is a series of scintillating paddles with a pair of PMTs attached to light guides at each end of the scintillating paddle, as shown in Fig. 19. Signals from the PMTs are readout by TDCs and analogue-to-digital converters (ADCs). This detector is used to determine a particle's time of flight by comparing the time at which the particle struck the scintillator with the event start time as determined by the accelerator RF signal mentioned in section 3.2.6. For electron beams, the RF beam bucket that contains the trigger electron is determined by requiring a signal in the electromagnetic calorimeter and in the Čerenkov detector in coincidence. Because the electron travels at a velocity that is indistinguishable from the speed of light ($\beta = 1$), the electron track can be used to calculate the time it left the target. This electron can now be used to provide the interaction time for all particles.

The time of flight system is located in between the Čerenkov detectors and the electromagnetic calorimeter and covers an area of 206 m^2 . There are 48 paddles that are 5.08 cm thick, 13 to 22 cm wide, and increase in length with their distance from the beam

line. This configuration covers a large range of θ from 8° to 142° . The length varies from 32 cm at the forward angle to 450 cm at large angles. Bicron BC-408 was selected as the scintillation material since it yields an attenuation length of 500 cm [69]. The time of flight system was designed to optimize time resolution, which varies from 80 ps for short paddles to 160 ps for longer paddles. Accurate timing is needed to separate pions from kaons up to 2 GeV. Each paddle has a silica optical fiber located at its center. This allows ultra-violet laser light to be sent to the paddles for time of flight calibrations.

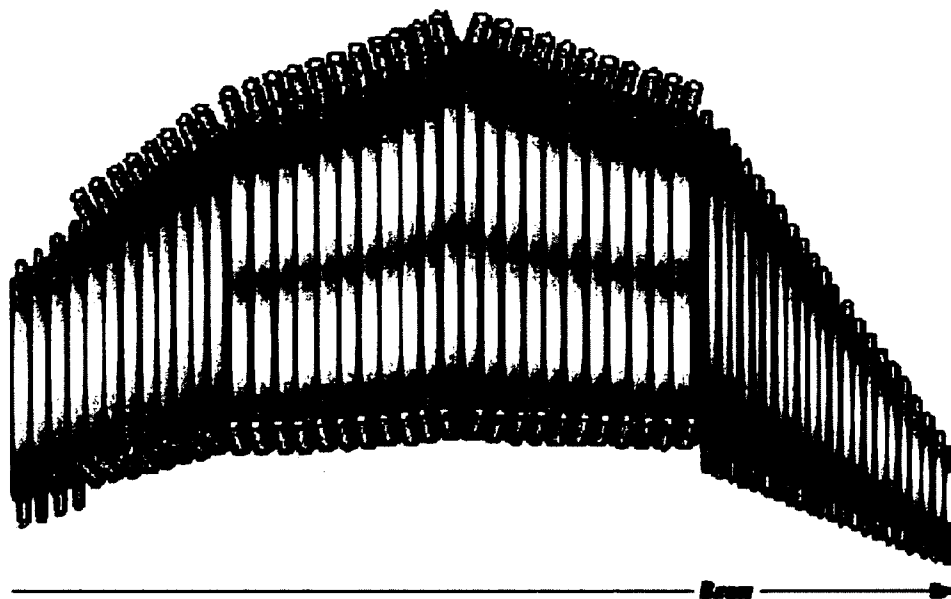


FIG. 19 Scintillators for the time of flight detector. The forward angle paddles are attached to 2 inch PMTs while the rest of the paddles are attached to 3 inch PMTs.

3.4.5 Electromagnetic Calorimeters

The final detector element the scattered particles encounter is the electromagnetic calorimeter. The forward calorimeter, which occupies a region in θ from 8° to 45° in the

polar angle, is a lead-scintillator electromagnetic sampling calorimeter consisting of six modules. It is used as part of the primary electron trigger for CLAS, and is helpful in discriminating electrons from pions. It can also be used to detect neutral particles [70]. As mentioned in the previous section, the Čerenkov detector is used for pion rejection but is only good for low momentum pions below the 2.7 GeV threshold. At high momentum, pions can be identified based on the energy deposition pattern in the electromagnetic calorimeter. This is possible due to the different mechanisms by which pions and electrons deposit their energy. When electrons come in contact with the lead layers of the calorimeter, they create an electromagnetic shower by emitting photons which in turn produce electron positron pairs which then emit photons, and so on. It is this shower effect that causes the electrons to deposit their energy in the calorimeter. In contrast, pions are minimum ionizing. They deposit a fixed amount of energy in the calorimeter regardless of the pion momentum.

The calorimeter is made up from a lead-scintillator sandwich with a lead:scintillator thickness ratio of 0.2 shown in Fig. 20. This requires 40 cm of scintillator for every 8 cm of lead in each module. Approximately 1/3 of the electromagnetic shower energy is deposited in the scintillator [70]. The shape of each module is an equilateral triangle, one for each sector of CLAS. The scintillator layers are made up of 36 strips of scintillator material which are oriented parallel to one side of the triangle. Then for each successive layer of scintillator, the scintillator strips are rotated 120° resulting in three orientations. Each orientation consists of 13 layers broken into an inner group of 5 layers and an outer group of 8 layers for a total of 39 lead-scintillator layers in each module. This orientation is used to determine particle position by comparing intersections of hits

in all three orientations. The light produced in the scintillators is sent to a PMT by a fiber optic light guide. The PMT signal is then sent to a TDCs for data acquisition. There are also a pair of large angle calorimeters, with a similar configuration, which are used for the measurement of particles at large polar angles.

3.5 DATA ACQUISITION AND TRIGGER

The event trigger condition for the EG1 experiment was the detection of a hit in the Čerenkov counter and the electromagnetic calorimeter in coincidence above a previously determined threshold. For EG1, the threshold levels were 150 mV for the electromagnetic calorimeter and 38 mV for the Čerenkov counter. High energy scattered electrons accounts for 60% of the triggers at the 2.7 GeV beam energy.

The remaining events are due to noise or fast hadrons that produce a signal in the Čerenkov counter. These events are rejected in the event reconstruction process. The data acquisition system (DAQ) records ADC and TDC information from the various detector elements if the event satisfies this trigger condition. The DAQ rate for the EG1 experiment was ~ 4 MHz.

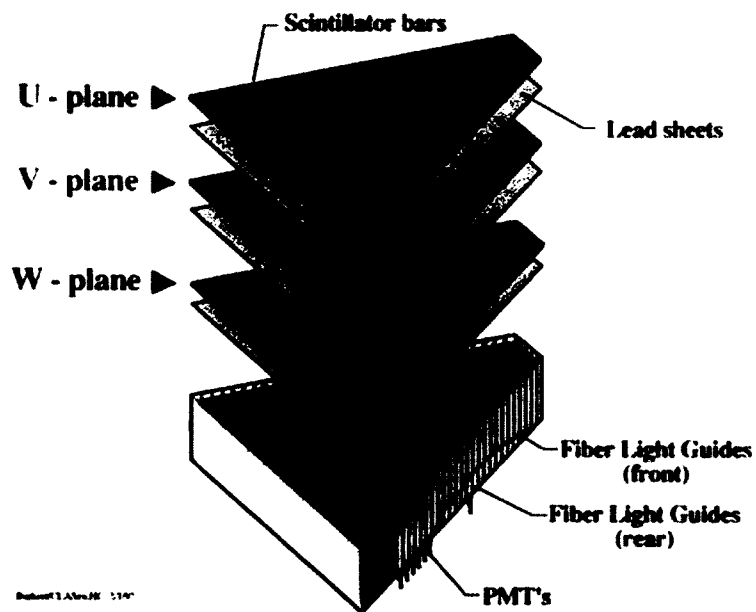
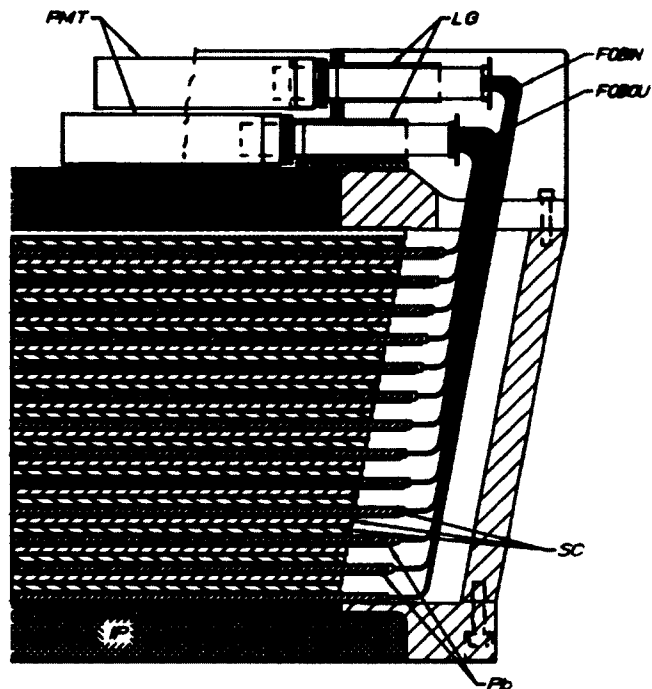


FIG. 20 Cross section of the forward calorimeter showing the lead scintillator sandwich (top) and exploded view of the lead scintillator sandwich (bottom) showing the orientation of the different layers.

3.6 TRACKING AND START TIME RECONSTRUCTION

Every detector in CLAS has a corresponding reconstruction package. These codes produce BOS files with the reconstructed data. This code is written in standard Fortran-77 [71]. The track (position and angle) of a charged particle at the target is reconstructed with the use of drift chamber and time of flight information. It is performed in two steps. In step one, individual tracks are fit to the hit-wire positions of the drift chambers. The track segments for all three regions are collected then linked to form a particle track candidate. This is known as hit-based tracking. The preliminary particle momentum and charge are determined along with the extrapolation of the track to the outer detector elements and target interaction vertex from the hit pattern. In step two, the particle flight time from the target to the time of flight scintillators is used to correct measured drift times [72]. Fig. 21 shows a typical event track.

Once the reconstructed data are stored in the BOS format, the data are calibrated and processed into a data storage tape (DST) format. A program that processes the information in the DST file is used to form ntuples, rootfiles or other datafiles. The calibration and analysis of these data are described in Chapter 4.

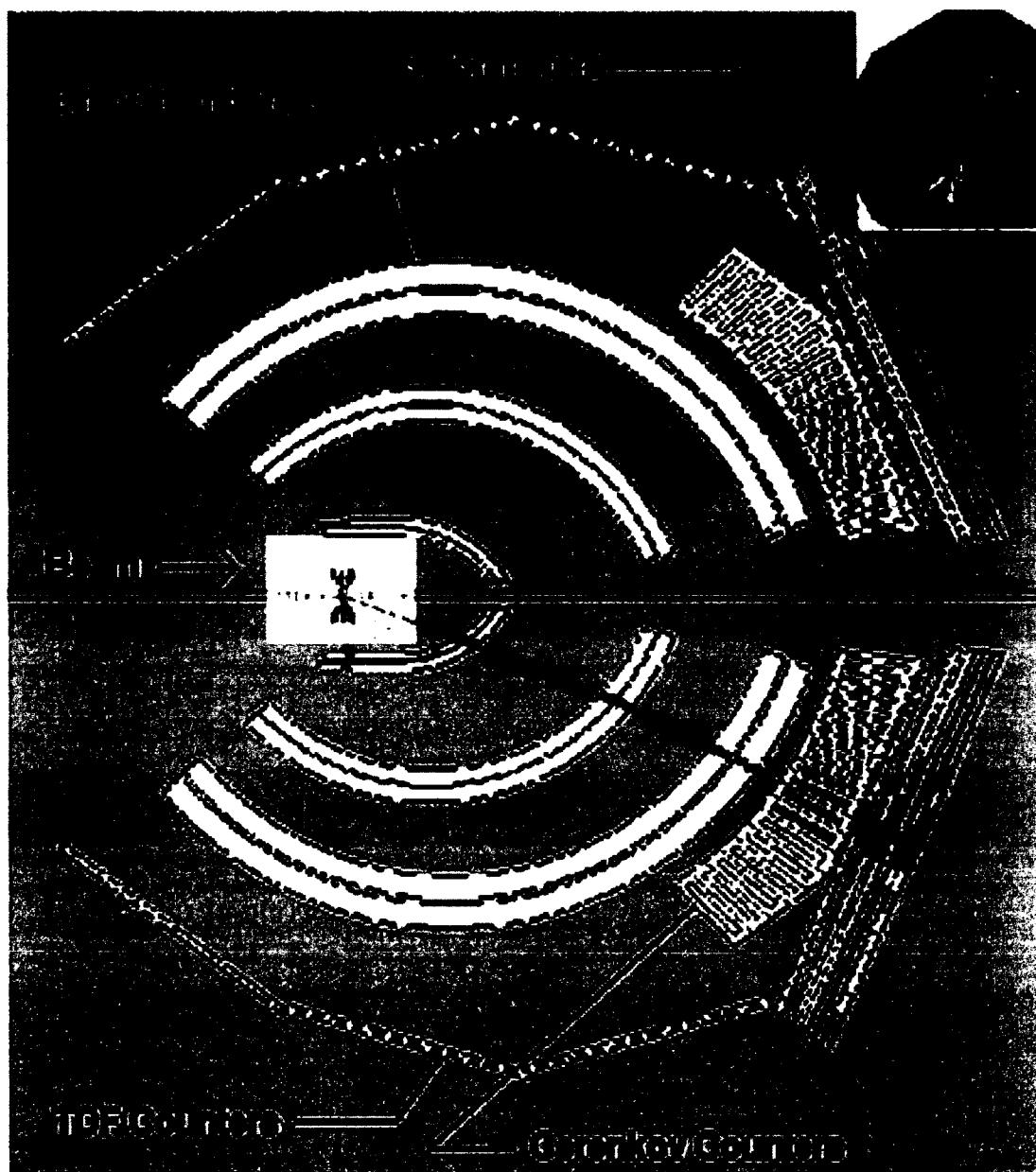


FIG. 21 Particle tracks showing the matching of tracks from the drift chambers to the other detector elements.

CHAPTER 4

DATA ANALYSIS

4.1 INTRODUCTION

The main goal of this analysis is to extract single and double spin asymmetries from the EG1 data for π^- production on deuterium. We analyze the data in two different channels;

$D(e,e'\pi^-)p$ and $D(e,e'\pi^-)n$, assuming that the neutron is at rest in the deuteron.

The data sets used in this analysis have beam energies 1.6, 1.7, 2.5 and 4.2 GeV. Because the region of interest for this analysis is the resonance region, the 5.6 and 5.7 GeV data sets has been omitted.

In this chapter the steps required to select good data and correct for known problems is explained. The physics analysis, including the calculation of asymmetries is presented in Chapter 5.

4.2 DETECTOR CALIBRATION

The raw CLAS data (ADC and TDC values for each detector that had a hit) must be processed in order to get useful physics quantities such as particle momentum or identification. This is done using the RECSIS (CLAS reconstruction) software package. All of the data are calibrated, but the relevant parameters are determined from only 10% of the data. Both energy and time calibrations are determined and checked, accounting for any modifications due to different run conditions or changes in detector response. These calibrations were done by different members of the EG1 collaboration. The calibration of the EC timing was done by the author and is explained in more detail. Only after obtaining satisfactory results for the calibration does the full data processing take

place.

4.2.1 Time of Flight Calibration

The time of flight (TOF) scintillators are critical in the identification of hadrons. For instance, the RF offset and paddle-to-paddle corrections have a large impact on the calculated event start time and particle velocity, so care must be given to make these calibrations as accurate as possible. For this reason the first calibration to be performed is for the TOF. The TOF calibration is crucial for accurate time-based tracking in the drift chambers, as well as to normalize timing for the Čerenkov detector and the electromagnetic calorimeter. Several steps are used in calibration [73].

The key thing is to determine accurate timing for each beam energy and torus configuration. The ADC and TDC channels from each PMT are calibrated and the constants are obtained by analyzing data with dedicated DAQ configurations for the experimental run. A signal is incident on the PMT at a start time and the signal is recorded as exact time. Calibrations feed LED signals to the scintillators for each PMT where a pedestal value is calculated. The pedestal (P) corresponds to the ADC channel when no data are present and is measured by taking data with a pulsar trigger. This pedestal value is subtracted from the measured value of the ADC channel, A , to determine the true signal amplitude A' using

$$A' = A - P. \quad (92)$$

An input from a pulse generator is used to calibrate the TDC signal to the true signal time,

$$t = c_0 + c_1 T + c_2 T^2, \quad (93)$$

where T is the raw time in units of TDC channels and t is the corrected time in ns. Then

laser light generated by photodiodes on PMTs calibrate against dependence of TDC signals on ADC amplitudes or cross walk,

$$t_w = t - f_w\left(\frac{A'}{Th}\right) + f_w\left(\frac{600}{Th}\right), \quad (94)$$

with Th being the TDC channel number corresponding to the leading pulse edge and,

$$\begin{aligned} f_w(x) &= \frac{w_1}{x^{w_2}} \quad \text{for } (x < w_0) \\ f_w(x) &= \frac{w_1}{w_0^{w_2}}(1 + w_2) - \frac{w_1 w_2}{w_0^{w_2+1}} \quad \text{for } (x > w_0), \end{aligned} \quad (95)$$

where w_0 , w_1 and w_2 are fit parameters that were determined for each PMT separately using the laser calibration system. When there is consistent time and amplitude response, then we can establish left-right PMT time alignment. This is done by taking left-right signal time offset determined by

$$\Delta t = (edge_L + edge_R)/v_{eff}, \quad (96)$$

where $edge_L$ and $edge_R$ are the edges of the distribution and v_{eff} is the effective velocity in the scintillator material. Next the energy loss and attenuation length are calibrated.

This is done by calibrating $\delta E/\delta x$ in the scintillator material. Finally, there are numerous paddle-to-paddle corrections where an offset c_{p2p} is determined for each paddle from a fit of scattered electron or pion data using

$$t_{L/R} = t_w \pm \frac{\delta_{LR}}{2} + c_{p2p}. \quad (97)$$

When offsets are corrected, the time of flight for any SC hit is

$$\bar{t} = \frac{t_L + t_R}{2}. \quad (98)$$

This is done in several iterations by checking the corrections on the data, then analyzing the run and checking the data quality [74].

4.2.2 Čerenkov Detector Calibration

The Čerenkov calibration is needed to determine detector efficiency and correct the time measurement. The subsystems that need calibration are the TDC (time calibrations), the pedestals (amplitude pedestal calibrations), and the photoE (single photoelectron position calibration). These calibrations are done without beam interactions using either cosmic particles or intrinsic photo-multiplier noise. The parameter T1 converts TDC channels to ns. The usual value of T1 is about 0.048 ns/channel. The calibration is done by sending a pulsar signal with different time delays to each TDC channel. The TDC response is fitted using a linear fit and T1 is the slope parameter for the channel-time dependence. Next the pedestals are subtracted for an accurate ADC measurement. The single photoelectron amplitude is calibrated which uses the self-triggering of the Čerenkov detector to see the noise function and to define the position of one photoelectron. Finally the time offset for the Čerenkov detector (T0) is calibrated during data analysis where you have the time measured both by the CC and TOF as well as the track length to the CC plane and SC plane. [75].

4.2.3 Drift Chamber Calibration

CLAS has six sectors of identical drift chambers, each separated into regions 1, 2, and 3. Each region has two superlayers. In regions 2 and 3 there are 12 layers of sense wires. In region 1 there are only 10 layers of sense wires. Each superlayer (consisting of 4 or 6 layers) of each sector is calibrated separately for a total of 36 sets of parameters. The drift time is scaled differently for each layer and is calculated automatically by the

calibration software. To describe the distance a charged particle track is from a sense wire, two variables are used. The distance of closest approach (DOCA) and the distance (DIST). The DOCA is the distance from the sense wire to the particle track determined by time-based-tracking. The DIST is the predicted distance from the sense wire to the track which is calculated from the drift time. Additionally a time residual is calculated from the two terms,

$$RESI = abs(DOCA) - (DIST). \quad (99)$$

This is the primary means of measuring the drift chamber resolution. The value of DIST is always positive while DOCA is either positive or negative depending on the particle track being either to the left or right of the closest sense wire. Drift chambers are calibrated by setting parameters for the drift velocity function in each superlayer of every sector. This function is the relation between the distance DIST and the measured drift time of the ions to the sense wires. These drift times are calculated from the wire's TDC value correcting for fixed cable and event delays. The time-to-distance function parameters are determined by fits to DOCA vs time plots. These parameters are stored in a file DC_DOCA.map. A timewalk correction is used to correct for the dependence of the time on the signal size, mostly from clustering effects in the drift chamber. The maximum drift time t_{max} which is the amount of time it takes an electron created at the edge of a drift chamber cell to travel to the center sense wire, is calculated for each sector. The drift velocity function depends on parameters (p_i) which must be determined from the data. The function for regions 1 and 2 is,

$$d = (p_1 \hat{t}) + (p_2 \hat{t}^2) + (p_3 \hat{t}^3) + (p_4 \hat{t}^4) + ((D_{max} - p_1 - p_2 - p_3) \hat{t}^5). \quad (100)$$

For region 3 the function is,

$$d = (p_1 \hat{t}) + \left(\frac{(D_{\max} - (p_1 t_{\max}))}{1 - p_2} \right) \hat{t}^{p_3} - p_2 \hat{t}^{p_4}, \quad (101)$$

where $p_1 - p_4$ are calibration parameters, D_{\max} is the (cell size)² and \hat{t} is the time normalized to t_{\max} . The calibration program determines the following parameters, the average local angle, the average magnetic field strength, the initial time T_0 and the maximum drift time T_{\max} . More details on drift chamber calibrations are available from Ref. 76.

4.2.4 Electromagnetic Calorimeter Calibration

The CLAS electron trigger is configured to accept only events that deposit more than minimum ionizing energy in the calorimeters, when in combination with the Čerenkov counters, which is not sufficient at high energies, reject pions. This requires that the EC response to a fixed energy deposition is independent of the hit position. Otherwise, the trigger response will not be uniform near threshold. This requires a uniform and accurate energy calibration at the beginning of the experiment so that the trigger does not have a position dependent bias. The matching of the PMT signals is done using cosmic runs detecting muons. Muons are chosen since they are minimum ionizing particles and their energy loss is well known. These cosmic runs were taken at the beginning of the experiment and the PMT gains were adjusted accordingly. The EC PMTs require internal calibrations for ADC pedestals as well as corrections to scintillator properties such as exponential attenuation. Gain matching is also required so the sum of the energy deposited in all EC scintillators totals

$$E = E_p \times f_s, \quad (102)$$

where E is the total energy, f_s is the sampling fraction and E_p is the total particle energy

[76]. Since the TOF timing, the EC timing is calibrated first the EC timing signal is calibrated to the TOF signal using a 5-parameter model to minimize the average difference between the TOF and EC signal time shown in Figs. 22 and 23.

The initial run of the calibration routine reads existing calibration constants and performs the fit to get new calibration constants. The initial plots show the TOF to EC signal time before calibration see Fig. 22 top. The calibration routine reads the input files and starts fitting the data and reads out new calibration constants to a file. These fits adjust that time so that the time difference between the TOF and EC is centered at zero see Fig. 23 top. This is done for each sector. This process is run over several iterations because there are several EC scintillators involved in each EC signal. Figs. 22 and 23 bottom shows time difference between the TOF and EC for the sector 2 electrons. Before calibration, the electron events are not centered at zero (on the y axis). After calibrations the events are centered at zero. When the time difference between the TOF and EC is centered at zero, the final calibration constants are saved in the data base.

This final calibration is important since it is the EC that is primarily used for identifying pions as well as distinguishing electron from photons based on time of arrival at the EC.

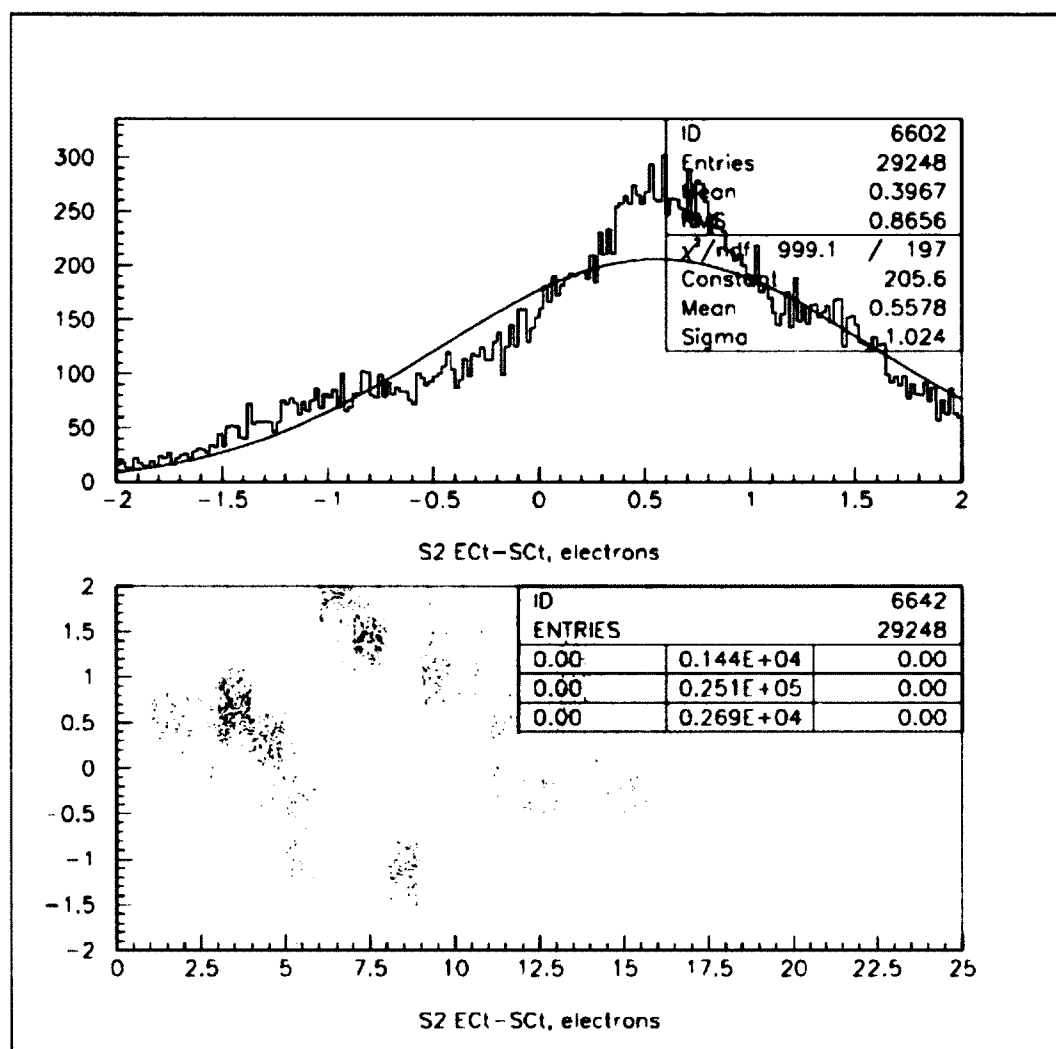


FIG. 22 Time difference between particle arrival at the time of flight and a scatter plot of events vs. Time difference between particle arrival at the time of flight and the EC before the EC timing calibration.

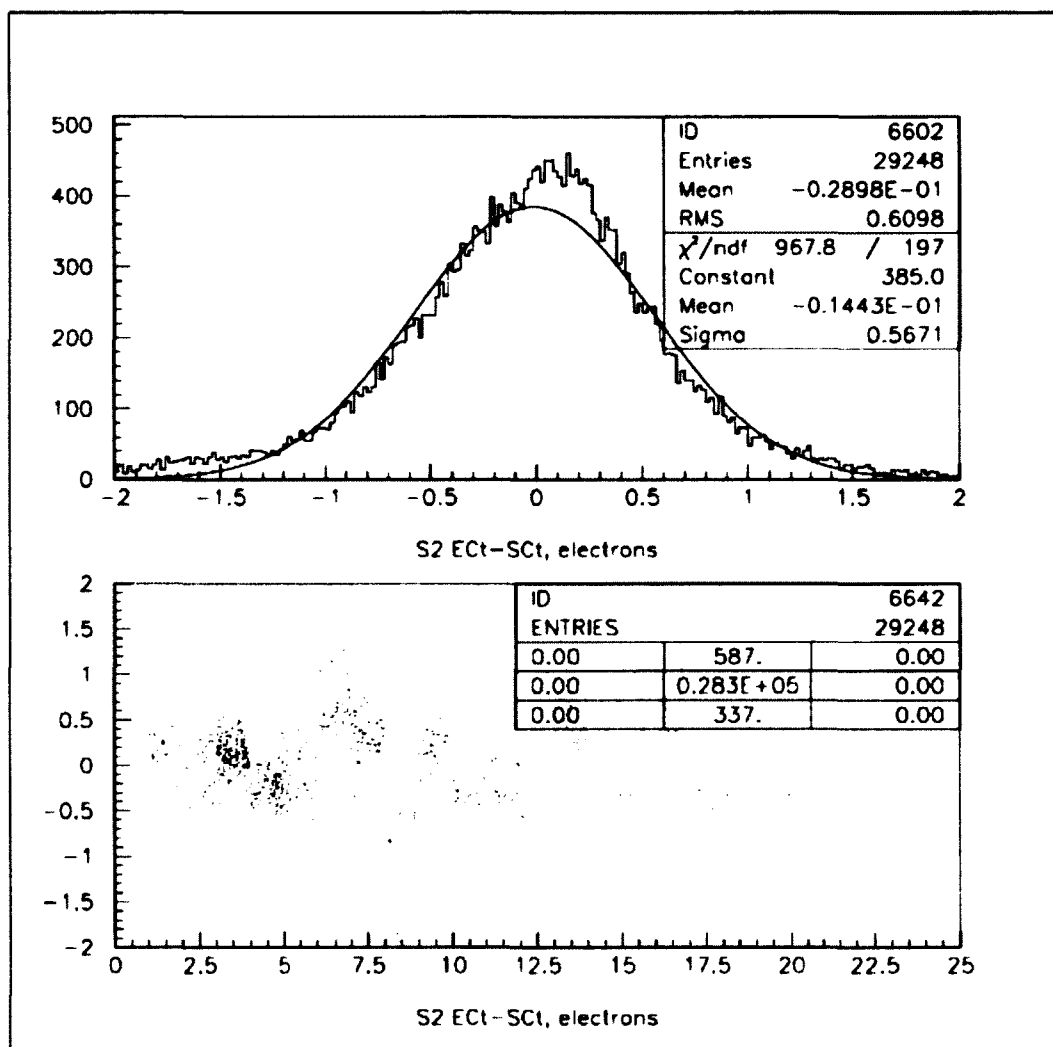


FIG. 23 Time difference between particle arrival at the time of flight and a scatter plot of events vs. Time difference between particle arrival at the time of flight and the EC after the EC timing calibration.

4.3 RUN SELECTION

In order to make an accurate asymmetry measurement, it is necessary to ensure that only the runs that contain good data are used. To select good runs, we eliminated the ones which had electron rates that were either much lower or much higher than other runs of the same type (same target, torus field, beam energy, etc). There were runs that were miscategorized with either the wrong target, the wrong half wave plate, or the wrong target polarization orientation. These were corrected by an analysis subroutine that was able to correct these values in the datafiles. In the end, we have a list of good data runs, (see Table 6), for every target type, target polarization, beam energy and torus polarization.

Table 6 Summary of the EG1b data set. Tthe asterisk shows the ND₃ data sets which are reported here. Table courtesy of Nevzat Guler [77].

Run Numbers	Beam Energy (GeV)	Torus Current (A)
*25488 - 25559; 25669 - 26221	1.606	+1500
26222 - 26359	1.606	-1500
28512 - 28526	1.723	+1500
*27644 - 27798; 28527 - 28532	1.723	-1500
27205 - 27351	2.286	+1500
*28001 - 28069	2.561	+1500
*27799 - 27924; 27924 - 27995	2.561	-1500
27936 - 27941	2.792	-1500
*28074-28277;28482-28494;28506-28510	4.238	+2250
*28280 - 28479; 28500 - 28505	4.238	-2250
27356 - 27364; 27386 - 27499	5.615	+2250
27366 - 27380	5.615	-2250
27069 - 27198	5.725	+2250
26874 - 27068	5.725	-2250
26468 - 26722; 26776 - 26851	5.743	-2250

For this analysis, good runs include ND₃ and carbon target runs. The data are checked by performing a number of tests on all runs that survived event reconstruction, and comparisons are made regarding the information about these runs entered into the logbook and the CLAS database.

4.3.1 Target Material

The first check is to see if the inclusive count rates are appropriate for the target type. Different targets have slightly different densities and cross-sections. The inclusive electron count rate can be used to determine the target material. The target material is cross referenced with the target data in the logbook.

4.3.2 Event Rates

To make sure that the data have suitable beam quality, detector function and efficiency, either the inclusive electron or exclusive $e^-\pi^-$ rates for each run were monitored. During the data processing all run files were monitored and histograms were checked for problems. However, some runs that passed event reconstruction may contain problems such as detector inefficiency or loss of polarization during the experiment. To check for this the rates, which are the number of events normalized to the accumulated charge, N/FC, measured by the Faraday cup, were plotted. If any run in a particular beam energy and torus setting has an N/FC rate either lower or higher than the rest of the rates, it could be an indication of a problematic and therefor would be excluded from further data analysis. Fig. 24 show both the inclusive and exclusive rates for 2.5 GeV ND₃ and carbon data.

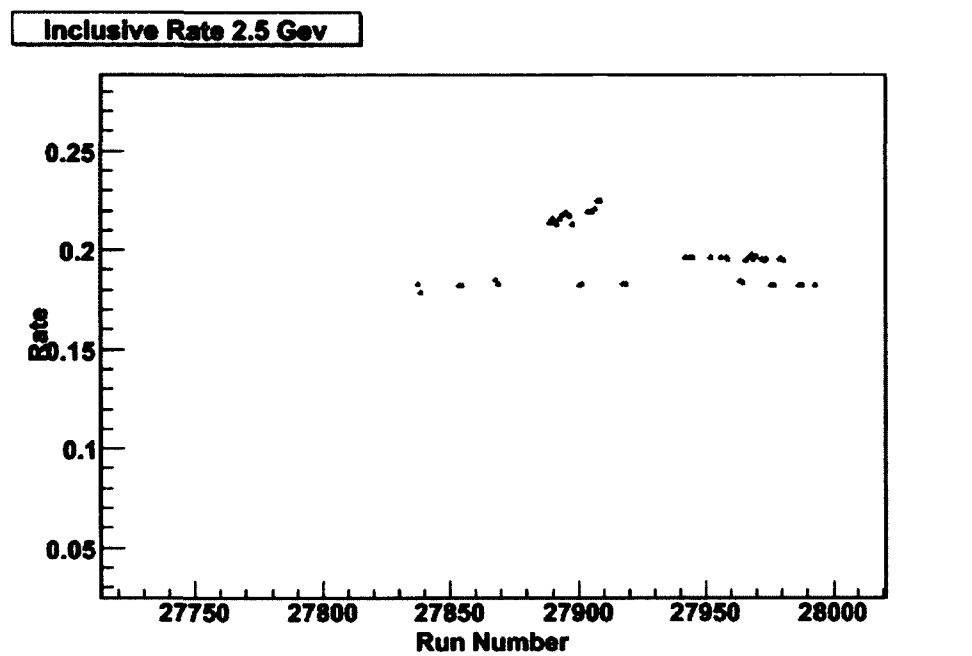


FIG. 24 Inclusive count rates for 2.5 GeV out bending data. The blue points are the ND₃ positive target polarization rates, the green points are the ND₃ negative target polarization rates and the red points are the carbon target rates.

4.4 CORRECTIONS

Once the problematic or bad runs have been identified and removed from the data set to be analyzed, further corrections are needed to ensure that each event has the correct beam helicity, half wave plate status, and target polarization orientation, and that the kinematic quantities for each particle in the final state are calculated correctly. The final correction package includes z vertex, raster and momentum corrections. The first correction is the raster and z vertex correction because all other corrections rely on an accurate z vertex position of the event.

4.4.1 Raster Correction

The frozen NH₃ and ND₃ target material can lose polarization due to beam heating and melting. To avoid this thermal effect, the beam is rastered over the surface of the

target. Rastering the beam is a process in which the beam is moved by small amounts perpendicular to the beam direction quickly over time. This pattern traces out the same area on the target per unit time regardless of where the beam spot is located. This distributes the beam heating over the entire face of the target. The tracking assumes that the x and y beam position are zero when it calculates the tracking of a particle in CLAS. However, the beam position x and y are not zero due to rastering, which means that the particle travels a different distance through the target magnetic field than what was assumed by the tracking software. This effect can be corrected by knowing the position of the beam for each event [78]. The z vertex position is corrected first according to

$$v'_z = v_z + \frac{x'}{\tan \theta}, \quad (103)$$

where v_z is the vertex position on the \hat{z} axis as determined by the tracking software, v'_z is the corrected position, θ is the particle trajectory angle relative to the beamline, and x' is the total distance the particle traveled, which is not accounted for by the tracking software,

$$x' = \frac{x \cos \phi_0 + y \sin \phi_0}{\cos(\phi - \phi_0)}, \quad (104)$$

where ϕ is the azimuthal angle of the particle given by,

$$\phi = \tan^{-1} \frac{P_y}{P_z}, \quad (105)$$

and ϕ_0 is the angle that corresponds to the center of the sector in which the particle was detected. Since the distance traveled by the particle is different than originally determined, the azimuthal angle ϕ is incorrectly calculated and must be corrected. Since

the field and correct path length are known, ϕ_c can be calculated

$$\phi_c = \phi + q \cdot 50 \cdot \frac{100}{\left(\frac{33.356}{P_t} \right)} \quad (106)$$

This leads to a correction to P_x and P_y that preserves the total transverse momentum $P_t = P_x P_y$, where q is the particle charge, 50 is the target field in Kilogauss, 100 converts cm to m and 33.356 is $1/c$ in appropriate units.

It is necessary to know the position of the beam spot to perform these corrections. Since there is no measurement for the beam spot position (x and y), these values must be determined by other means. This is done using an ADC measurement that records the output power supplied to the raster magnets. The ADC values are then converted to x and y positions. These coordinates are determined by fitting electron and proton coincidence events for the z vertex position, which should be identical for both particles. The x and y positions are related to the ADC values by,

$$x = (ADC_x - ADC_{x'}) \cdot C_x \quad (107)$$

$$y = (ADC_y - ADC_{y'}) \cdot C_y, \quad (108)$$

where ADC_x and ADC_y are the ADC values for x and y . $ADC_{x'}$ and $ADC_{y'}$ are values that correspond to the position at the center of the target. C_x and C_y are constants that convert ADC counts to centimeters. The final outputs are stored as variables ϕ , P_x , P_y and v_z for each event in the datafile.

4.4.2 Z Vertex Correction

After applying the raster correction to each particle in the event, the average

vertex position is calculated using the vertex position of charged particles that come from the interaction. This is done by assigning a vertex resolution σ_z to each particle,

$$\sigma_z = 0.1 / (\beta p_t), \quad (109)$$

where p_t is the transverse momentum of each particle, $\beta = p/E$, where p is the total momentum and E is the total energy of each particle. The vertex position of the event is determined by summing over the vertex position of all particles, weighted by the vertex resolution:

$$z_{acg} = \frac{\sum_i z_i / \sigma_{zi}^2}{\sum_i 1 / \sigma_{zi}^2}. \quad (110)$$

4.4.3 Beam Helicity Switching

The beam polarization is switched at a rate of 30 Hz in a pseudo-random order. Periods of constant electron helicity which occur ~ 0.03 s are referred to as buckets. One helicity bucket (either parallel or anti-parallel) is chosen at random and is followed by a bucket of the opposite helicity, as shown in Fig. 25. This ensures that there is roughly equal statistics for both positive and negative beam helicity. A sync pulse with a frequency of twice the helicity identifies the time of the helicity flip. On occasion, the sequence can be broken by accelerator trips or misread helicity sync signals, which can lead to un-paired helicity buckets. These un-paired helicity buckets are identified and rejected in software [77].

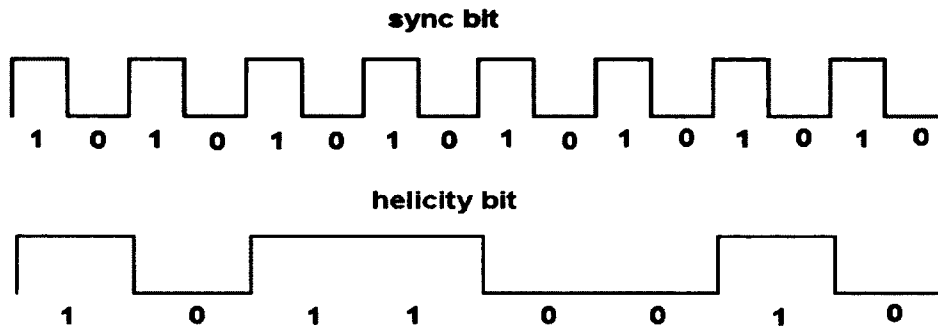


FIG. 25 Helicity sync bit and helicity bit. The helicity bit has half the frequency of the sync bit. A bucket of helicity is always followed by a bucket of opposite helicity. Note that the first “0” helicity bit is the start of a pair.

4.4.4 Target and Beam Helicity Sign

The sign of the inclusive elastic asymmetry is well known. By calculating the asymmetry in the elastic region for each run the sign of the product of beam helicity and target polarization is checked and corrected. This asymmetry test also verifies the status of the half wave plate, which changes the sign of the electron polarization.

4.4.5 Momentum Corrections

The reconstruction of particle trajectories and momenta from the tracking software requires accurate knowledge of the drift chambers and torus magnetic field. The reconstructed particle momentum can be incorrect due to a slightly different torus field than that used in the reconstruction software. Similarly, misalignments between drift chambers can result in a poor determination of particle momentum [79]. The quality of the momentum reconstruction can be checked by the position of the elastic peak in the invariant mass spectrum which should be at $W = 0.938$ GeV. Both momentum, dp , and

scattering angle, dq , corrections are parametrized, and the parameters are determined by fitting to the data using the 4-momentum conservation for fully exclusive values and W elastic peak position as a constraint. Fig. 26 shows the W elastic peak before and after corrections. The corrected W elastic peak is centered at 0.938 GeV [77].

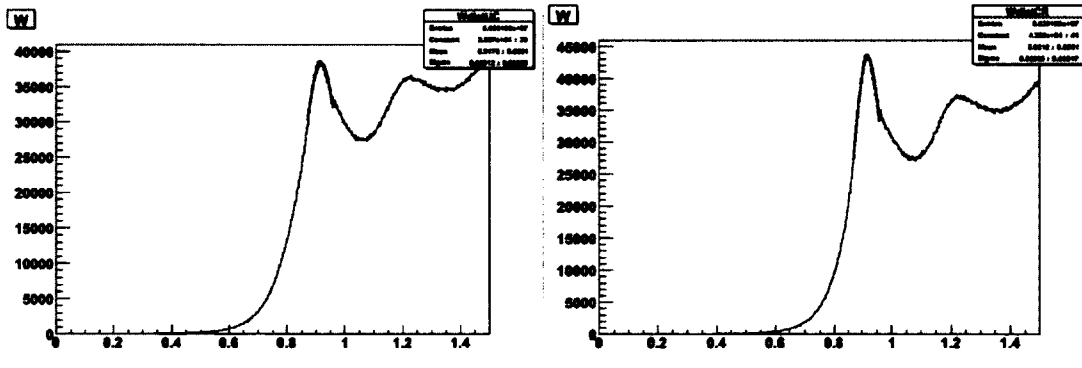


FIG. 26 The W spectrum before (left) and after (right) momentum corrections. Plot courtesy of Nevzat Guler [77].

4.4.6 Multiple Scattering Corrections

In addition to the momentum corrections due to differences in the torus field or drift chamber misalignment, there are corrections to a particle's momentum that arise from multiple scattering that can occur in the target. Multiple scattering can result in a shift of the z vertex position for each particle. The multiple scattering correction uses the weighted average of all the reconstructed vertex positions in each event to estimate the amount of multiple scattering for each scattered particle as it travels out of the target and corrects the momentum accordingly for each particle [80].

4.4.7 Energy Loss

There is an additional correction to account for the amount of energy that is lost in

the beam upstream of the scattering point and in the scattered particle on the way out of the target. This correction is performed by determining the average corrected reconstructed vertex for all particles in an event and assuming that this is the location where scattering occurred. The beam energy in each kinematic calculation as well as outgoing particle momenta are adjusted to account for this energy loss.

4.4.8 Target Magnetic Field

There is also an effect from the target field that exists outside the region 1 drift chambers. Because the target has a 5T field along the beam direction, the charged particle trajectory is identified. This is called the phi kick. The reconstruction software assumes this field to be zero outside the innermost layer of DC1 when calculating momentum and angles. The angle ϕ for each charged particle must be corrected to account for this extra magnetic field.

4.5 FIDUCIAL CUTS

Sometimes it is useful to place a geometrical cut on the efficient (fiducial) regions of the Čerenkov detector. This is due to limitations due to the reflective loss within the mirror geometry which can cause inefficiencies in the Čerenkov detector for some particle events. These cuts ensures that electrons are identified using a reliable region of the detector with reliably known and consistent efficiencies.

4.5.1 Determining Inefficient CC regions

To implement the fiducial cuts, a criterium for determining the expected average number of photoelectrons in each region of the Čerenkov detector was established. The fiducial region of the detector must be determined by looking at the expected number of photoelectrons that should be produced by an electron, determined using a function

developed by Alexander Vlassov [81, 82]. This is a function to determine the expected number of photoelectrons in the CC as a function of particle track coordinates. The elastic electron scattering events were used to determine the average number of photoelectrons. Event selection included cuts on the missing mass (W), vertex position and energy deposited in the electromagnetic calorimeter. Restrictions on the geometrical matching of the track's x and y coordinates from the electromagnetic calorimeter and Čerenkov counters are defined by placing a limit on the track's deviation. To calculate the actual efficiency as a function of θ and ϕ in each sector, it was assumed that the number of photoelectrons generated by a hit in the detector region obeys a Poisson distribution. The efficiency at any point in the CC can be determined by finding the percentage in the Poisson distribution (with a mean value determined by A. Vlassov's function) that remain after all events with less than 2.0 photoelectrons are removed. Therefore, the efficiency of a detector location can be expressed in terms of the expected photoelectrons (μ) and a minimum photoelectron cutoff (c) as

$$efficiency = \sum_{n>c} \frac{\mu^n e^{-\mu}}{n!} \quad (111)$$

4.5.2 Determining Fiducial Cut Boundaries

If the expected number is too small, then that region is deemed too inefficient, and a cut is applied to exclude that region, as shown in Fig. 27. An efficiency of 80% or greater was required and events were collected for each θ and ϕ bins that satisfied the efficiency requirements. The geometric values of the fiducial cuts were determined by Robert Fersch [74]. By defining a boundary in the plane θ vs ϕ , an efficient region was determined for different electron momenta in 0.15 GeV bins. The parameterized

boundary functions in θ , and ϕ were determined using 6 parameters for inbending data sets and 10 parameters for outbending data sets. Fiducial cuts are necessary to select the efficient region for calculating beam and target polarization, as well as background calculations in which data from different targets are being compared. Fiducial cuts will minimize fluctuations in acceptance or efficiency with different target types. These electron fiducial cuts are applied, however, due to the nature of exclusive analysis, pion fiducial cuts are not applied.

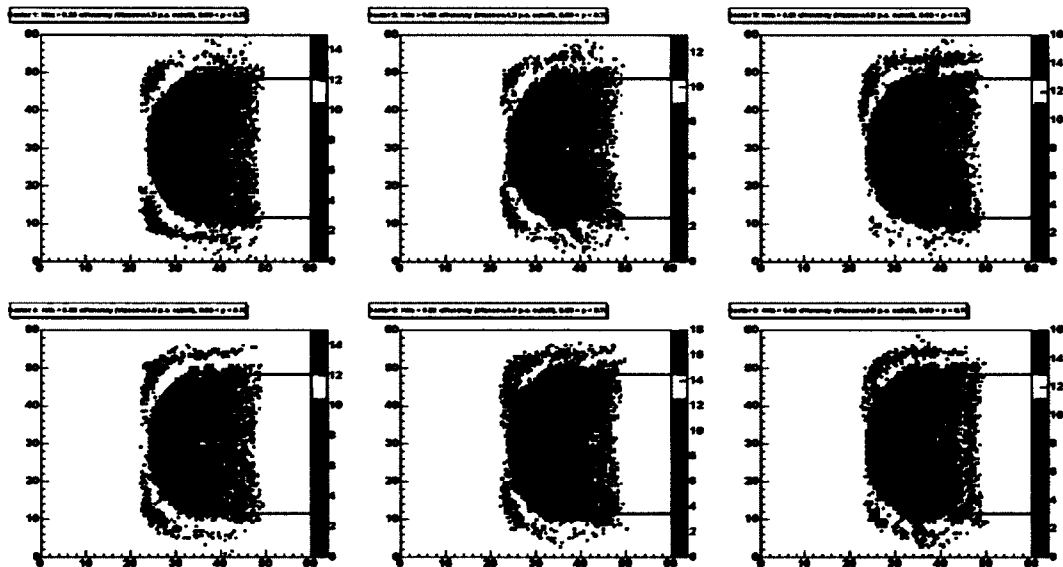


FIG. 27 Number of Cerenkov photoelectrons as a function of θ and ϕ as measured by the drift chambers for each sector for the 2.5 GeV inbending data. The electron fiducial cuts are shown as the black line. These plots are courtesy of R. Fersch [74].

4.6 PARTICLE IDENTIFICATION

Once the good data are selected and kinematic variables are corrected, the

particles in each event must be identified. The detection of charged or neutral particles is possible with the CLAS detector using one or more of the detector components. Even though particles are given preliminary identification during the event reconstruction process, a more precise determination can be made by the introduction of additional constraints in the form of kinematic cuts. These cuts are used to define electron, π^- and proton candidates for this analysis.

4.6.1 Electron Identification

The RECSIS software identifies an electron event trigger by requiring a hit in the Čerenkov counter and a shower in the electromagnetic calorimeter from a negatively charged particle [72]. The Čerenkov counter is used because all but the highest momentum pions are traveling too slow to produce Čerenkov radiation in the detector. It is common for a negatively charged pion to pass the RECSIS electron identification, so more strict cuts are applied on the Čerenkov counter and electromagnetic calorimeter signals to further select good electrons as the trigger particle.

The first cut to distinguish electrons from pions is applied to the Čerenkov counter. Fig. 28 shows a typical distribution of the number for photoelectrons ($\times 10$) produced by Čerenkov light. The peak at around 1 photoelectron is mainly due to pions. Electrons have a broad spectrum peaking greater than 2 photoelectrons. We require that the number of photoelectrons is greater than 2 to minimize the number of pions in our trigger. This requirement does remove good electrons as well.

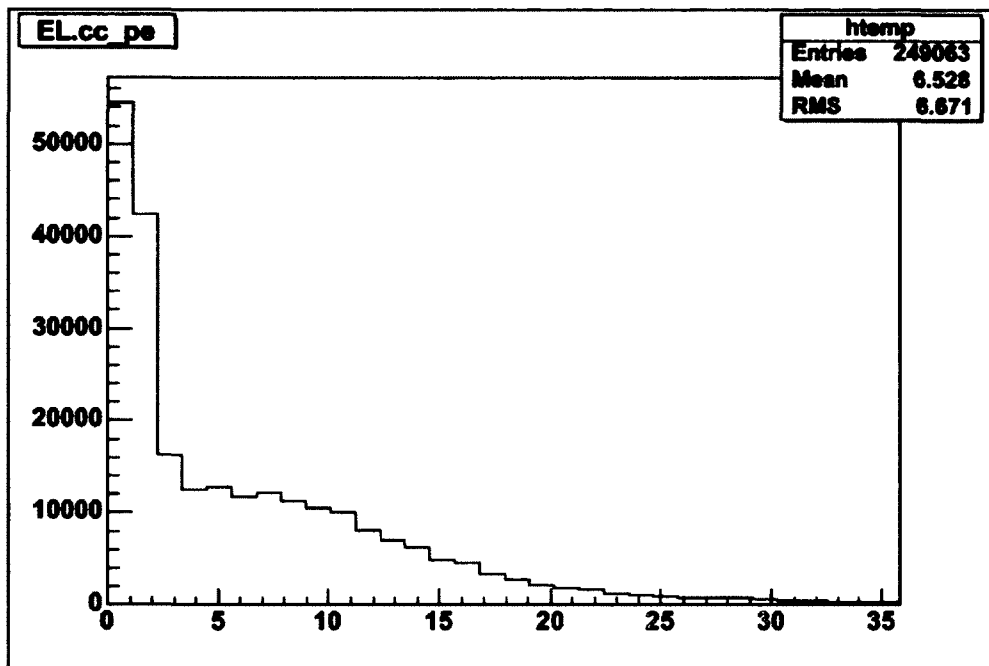


FIG. 28 Number of photoelectrons in the Čerenkov detector. The large peak around 1 is mainly from pions. A good electron is required to have more than 2 photoelectrons in the Čerenkov detector.

An additional cut is placed on the electromagnetic calorimeter. The fraction of energy that is detected in the scintillators is called the sampling fraction, which depends on the details of the Pb/scintillator sandwich mentioned in Chapter 3 and has a value of approximately 0.27. When electrons interact with the calorimeter material, they shower and deposit all of their energy in the calorimeter (see section 3.4.5). Therefore electrons deposit more energy in the inner calorimeter than the outer calorimeter. However pions are minimum ionizing particles and therefore deposit the same amount of energy in the calorimeter regardless of the pion momentum. Fig. 29 (top) shows a plot of the total energy deposited in the calorimeter versus the energy deposited in the inner calorimeter. A cut on the inner calorimeter is applied to eliminate events triggered by pions.

Additionally, Fig. 29 (bottom) shows the total energy as a fraction of momentum versus energy deposited in the inner calorimeter as a fraction of momentum. The electrons occupy a well defined region in the plot. An additional cut is applied to select electrons. There are different cuts for the lower and upper momentum range as seen in Fig. 30. Table 7 shows a detailed list of all cuts applied to identify an electron.

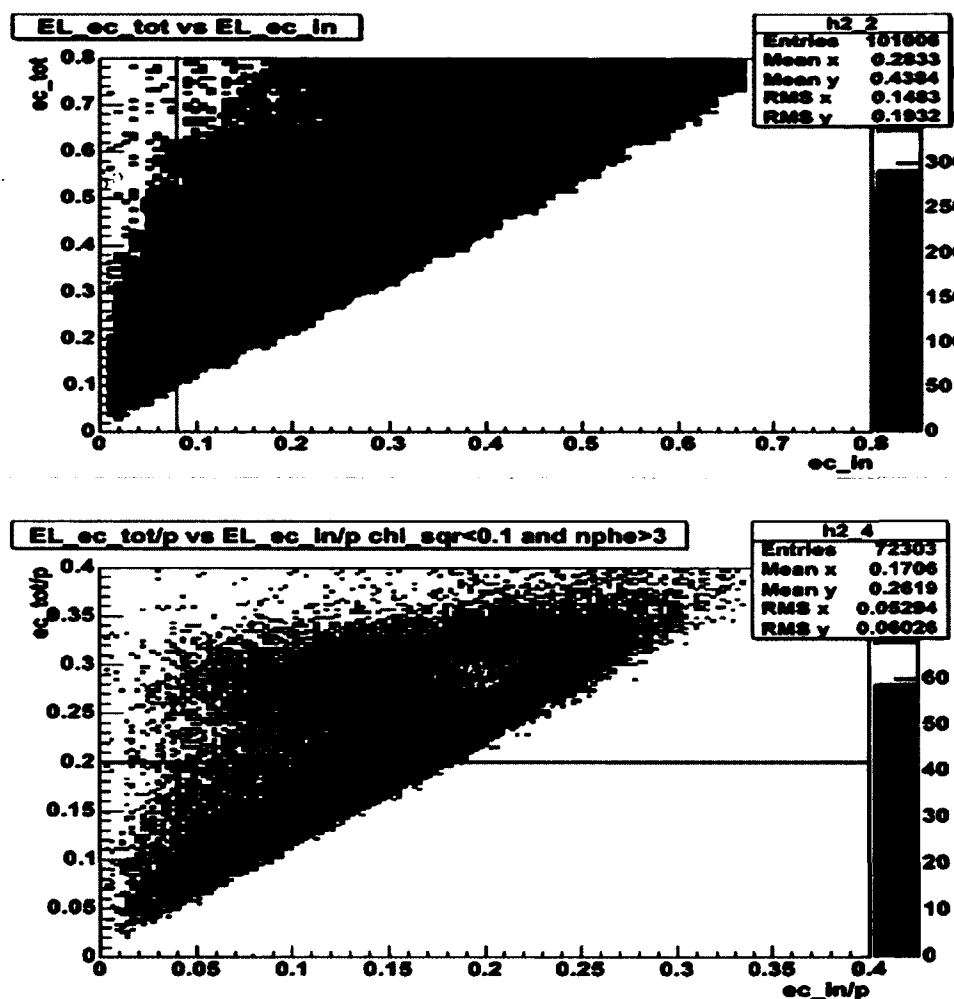


FIG. 29 Total energy deposited in the calorimeter vs. energy deposited in the inner calorimeter (top). The higher intensity region at EC_inner near 0.06 GeV are pions. A cut of $ec_inner > 0.08$ GeV is applied. The lower plot shows total calorimeter energy as a fraction of momentum vs. energy as a fraction of momentum for the inner calorimeter. A cut of $Ec_tot/p > 0.2$ is applied.

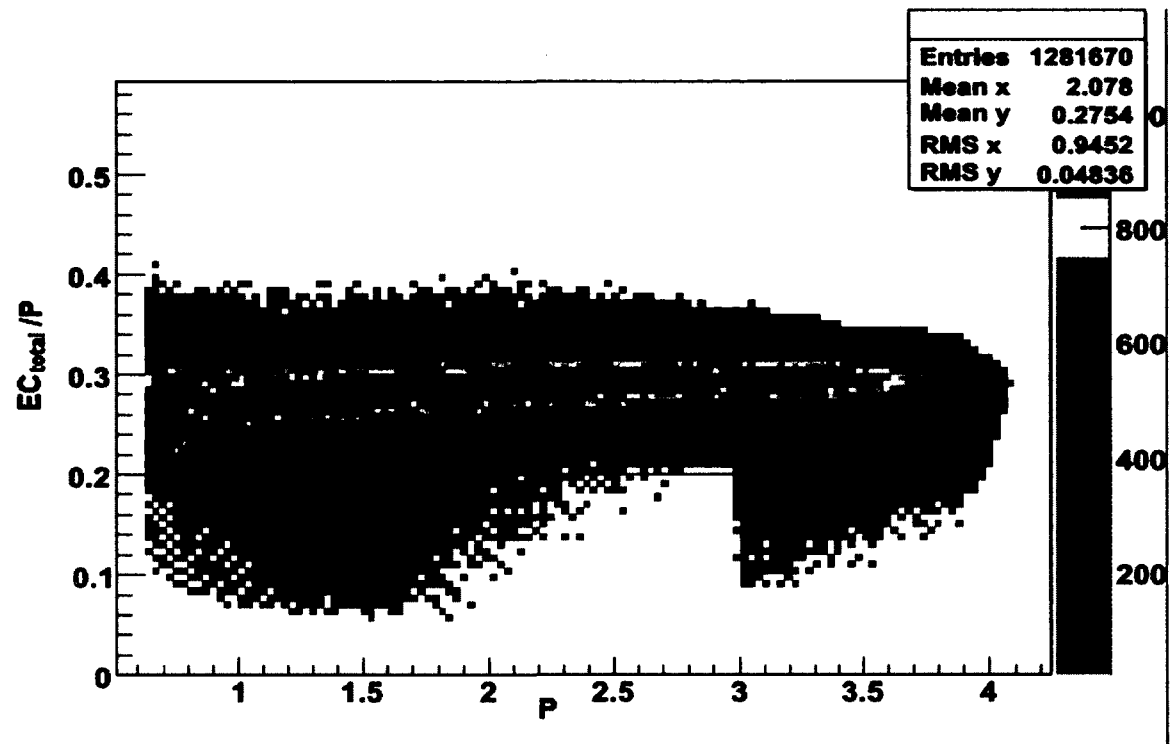


FIG. 30 Total energy deposited in the calorimeter as a fraction of momentum vs. momentum showing the cut applied for lower momentum and higher momentum.

Table 7 Standard electron cuts. The left and right columns represent the cuts depending on the electron momentum.

$P_e \leq 3 \text{ GeV}$	$P_e > 3 \text{ GeV}$
$\chi_{cc}^2 < 0.12$	$\chi_{cc}^2 < 0.12$
$N_{pe} > 2$	$N_{pe} > 0.5$
$EC_{in} > 0.06$	$EC_{in} > 0.06$
$EC_{tot}/P > 0.2$	$EC_{tot}/P > 0.24$
$P_e > 10\%$ of the beam energy and $<$ beam energy	
$8.5^\circ < \text{Drift Chamber } \theta < 49^\circ$	
Electron fiducial cuts applied	

4.6.2 π^- Identification

The π^- is identified primarily by comparing the time a particle arrives at the TOF with the time of flight calculated from the path length and momentum as measured by the

drift chambers. This time difference Δt is,

$$\Delta t = (TOF_{time} - START_{time}) - \frac{l}{c \sqrt{\frac{p^2}{p^2 + M_{\pi^-}^2}}}, \quad (112)$$

where TOF_{time} is the TDC readout from the time of flight scintillator for that particle, $START_{time}$ is the time the particle scattered from the target, (as determined by the trigger electron which has a speed is very close to the speed of light and independent of its momentum). The variable l is the path length of the particle trajectory determined by the drift chambers, p is the particle momentum which is also determined by the drift chambers, M_{π^-} is the mass of the pion and c is the speed of light in appropriate units (cm/ns). For pions, the assumption of using the pion mass in Equation 112 is accurate and Δt should be close to zero. Other particles with different mass will show up at different values of Δt . Additionally, a pion must have a negative charge and must fail the the electron identification cut as a whole (ie, if the particle passes all the electron ID cuts, it will not be considered as a pion candidate). A cut of $-0.8 < \Delta t < 0.8$ is applied for pion candidates, (see Fig. 31).

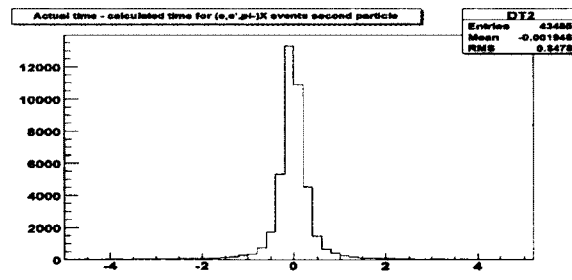


FIG. 31 Time difference (Equation 111) for negatively charged particles that do not pass the electron cut.

4.6.3 Proton Identification

The proton can also be identified in a similar manner as the pion. The proton identification is made using the time of flight and path length in the same manner as π^- identification but substituting the mass of the proton into the equation for Δt ,

$$\Delta t = (TDC_{time} - START_{time}) - \frac{l}{c \sqrt{\frac{p^2}{p^2 + M_p^2}}} . \quad (113)$$

A proton is required to have a positive charge. Again a cut of $-0.8 < \Delta t < 0.8$ is applied to the proton candidates.

4.7 EXCLUSIVE CHANNEL SELECTION

It is possible to analyze single and double spin asymmetries for two possible channels, $n(e,e'\pi^-)p$, which has more statistics but more background, and $d(e,e'\pi^-)p$, which is a sub-set of the $n(e,e'\pi^-)p$ channel, has a cleaner background but less statistics. In the first channel, we assume that the neutron is at rest in the deuteron and that the proton in the deuteron is a spectator (also at rest).

4.7.1 The $n(e,e'\pi^-)p$ Channel

The $n(e,e'\pi^-)p$ channel is selected with the identification of an electron and pion as mentioned in the previous sections. In addition, the undetected proton is identified by using the missing mass technique. The missing mass for $n(e,e'\pi^-)X$ events is defined using the conservation of energy and momentum,

$$M_x^2 = ((E + M_n) - (E' + E_{\pi^-}))^2 - (\vec{k} - (\vec{k}' + \vec{p}_{\pi^-}))^2 . \quad (114)$$

The M_x^2 distribution is peaked at the mass of the proton, as shown in Fig. 32 top. A cut of $0.88 \text{ GeV} < M_x < 1 \text{ GeV}$ is applied to select $n(e,e'\pi^-)p$ events.

4.7.2 The $d(e,e'\pi^-p)$ Channel

We can also study the $d(e,e'\pi^-p)$ channel because there are three charged particles in the final state. Once the detected electron, pion and proton are identified, the missing mass for $d(e,e'\pi^-p)X$ events can be calculated using conservation of energy and momentum

$$M_x^2 = \left((E + M_d) - (E' + E_{\pi^-} + E_p) \right)^2 - \left(\vec{k} - (\vec{k}' + \vec{p}_{\pi^-} + \vec{p}_p) \right)^2. \quad (115)$$

The M_x^2 distribution is peaked at the mass of the proton as expected. Again a cut of $0.88 \text{ GeV} < M_x < 1.0 \text{ GeV}$ is applied to identify the second proton. Fig. 32 bottom shows this missing mass spectrum.

4.8 BACKGROUND

In order to calculate the asymmetry, the relative number of counts for electron scattering from the polarized deuteron in $^{15}\text{ND}_3$ must be found. Scattering from unpolarized target materials, such as the Nitrogen and Helium, dilutes the value of the asymmetry. This effect can be corrected for exclusive channels by comparing the missing mass spectrum for the ND_3 target data to that for the ^{12}C target data. The ND_3 missing mass spectrum has a sharp proton peak. The broader background underneath the peak comes from the contribution of ^{15}N and other target materials (e.g. foils). A correction factor is applied to normalize the ^{12}C to the ^{15}N before subtraction [83]. In order to normalize the carbon spectrum to the nitrogen in the ND_3 spectrum, both the spectra were integrated in a range well below the proton peak, but in a region of good statistics. After the number of events were determined for ND_3 and carbon in this region, a scale factor f_b was calculated using

$$f_b = \frac{N_{ND_3}}{N_{^{12}C}}. \quad (116)$$

The entire missing mass carbon spectrum is then multiplied by this scale factor to simulate the nitrogen. To determine the missing mass spectrum for the deuteron alone, the scaled carbon spectrum is subtracted from the ND₃ spectrum shown in Fig. 32. The ND₃/C scale factor was calculated for each target polarization and torus setting for each beam energy. This is needed because particle luminosities are different for different data sets.

To further refine the background subtraction, the missing mass spectrum was plotted in each invariant mass (W) bin, as shown in Figs. 34 and 35, since the missing mass spectra change the most rapidly as a function of W , as well as to check for the clarity of the proton peak and look for oversubtraction in each bin. In this method the low missing mass region was chosen for each individual W bin to eliminate over subtraction. The $n(e,e'\pi^-)p$ channel was chosen for the ^{12}C to ^{15}N scale factor due to higher statistics. The $d(e,e'\pi^-)p$ channels used the same scale factor.

The error associated with background subtraction has two parts. The first is a statistical error from the ^{12}C data. This error has been propagated into the statistical error for each asymmetry. The second error is a systematic error arising from the ratio of ^{12}C to ^{15}N . This error will be discussed along with other systematic errors in Chapter 5.

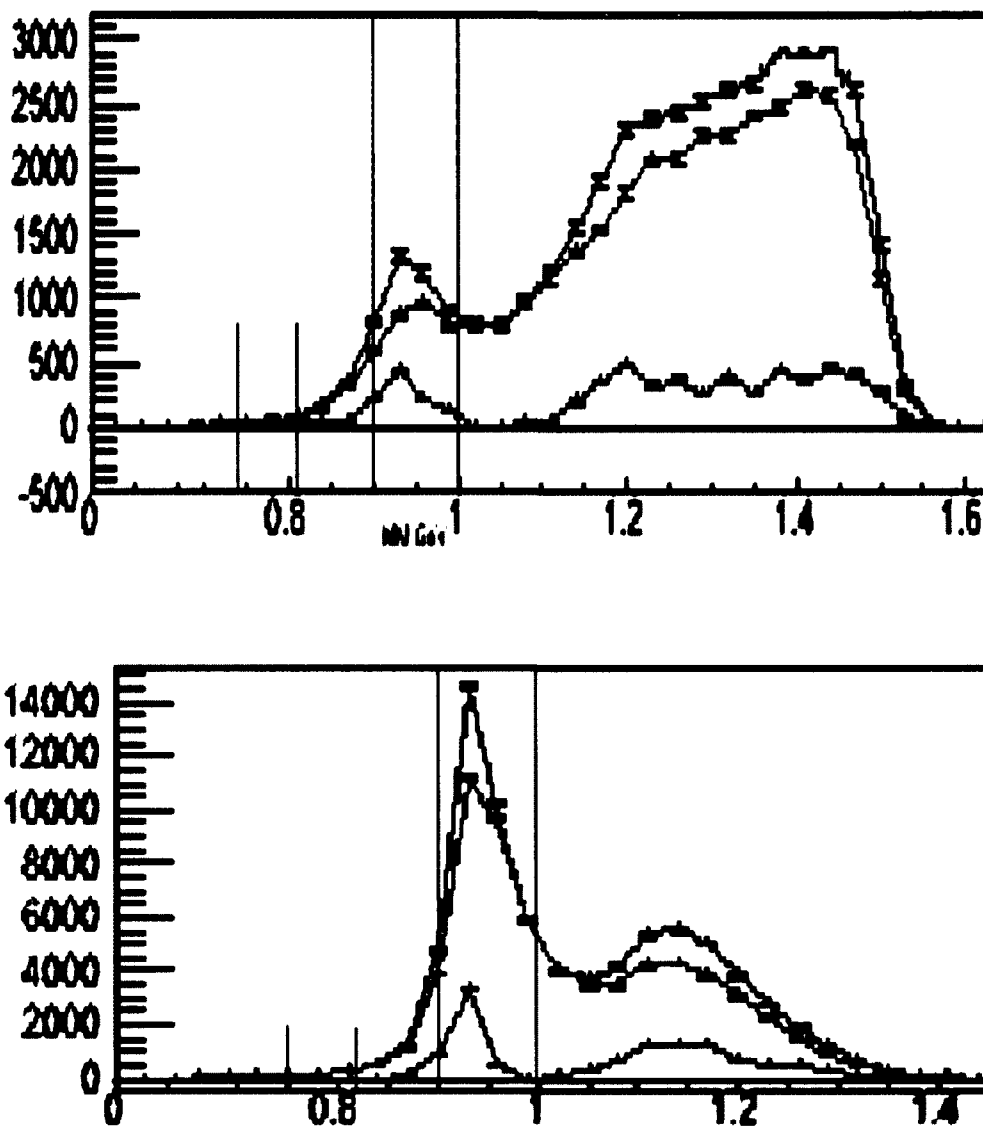


FIG. 32 The missing mass spectrum for ND_3 (top line) carbon (middle line) and the deuteron (bottom line) from the $n(e,e'\pi^-)p$ (top) and the $d(e,e'\pi^-)p$ (bottom) channels for 1.6 GeV beam energy. The short thick lines show the low missing mass region of $0.73 < \text{MM} < 0.83$ used to determine the ^{12}C to ^{15}N scale factor. The thin lines show the missing mass cut of $0.88 < \text{MM} < 1.0$ for event selection.

4.9 PION CONTAMINATION

One more correction would account for a small number of negatively charged pions being mistaken for electrons. The number of photoelectrons in the Čerenkov counter (see Fig. 28) shows a large peak at less than two photoelectrons which is most likely π^- misidentified as electrons. The selection of events for which the number of photoelectrons is greater than 2 greatly reduces the pion contamination, but does not eliminate the misidentified pions. For an inclusive analysis in which only the scattered electron is detected, further corrections are necessary to correct for those pions. However, due to the strict kinematic cuts required to identify the exclusive channel, pion contamination is even further reduced and would have a negligible contribution to our asymmetries. To verify this we adjusted our electron selection criteria to include primarily pions, rather than electrons, and performed the analysis as before. Fig. 33 shows the resulting missing mass distribution as the red curve compared to the original distribution in black. Clearly misidentified pions will not contribute to events selected with the missing mass cut.

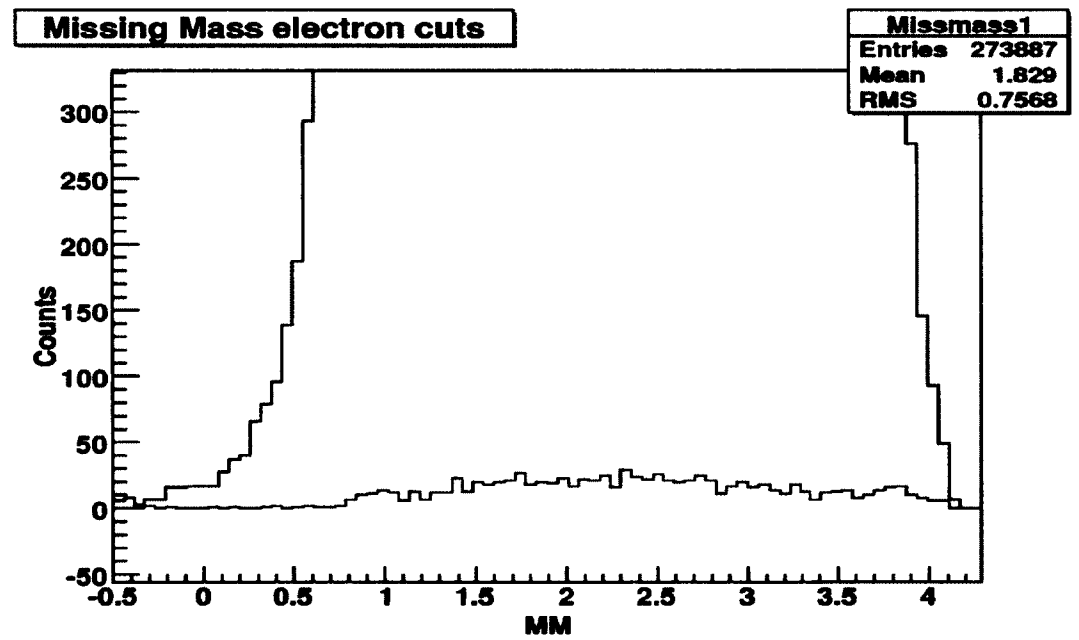
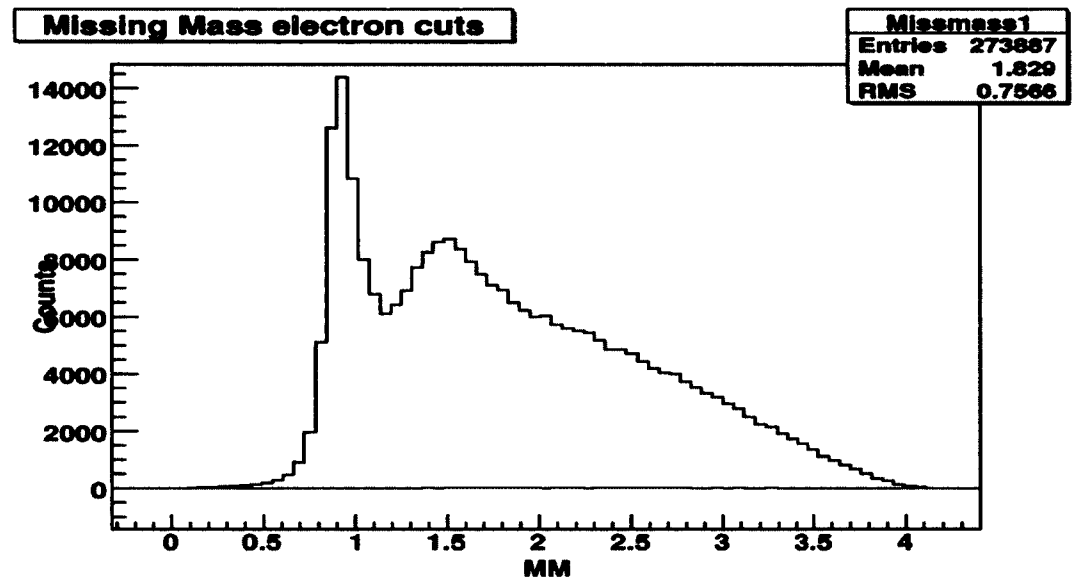


FIG. 33 Missing mass spectrum for $n(e,e'\pi^-)p$ using standard electron cuts (dark line) and using “pion” events (light line) top. The bottom plot is zoomed in to show the missing mass events using the pion selection.

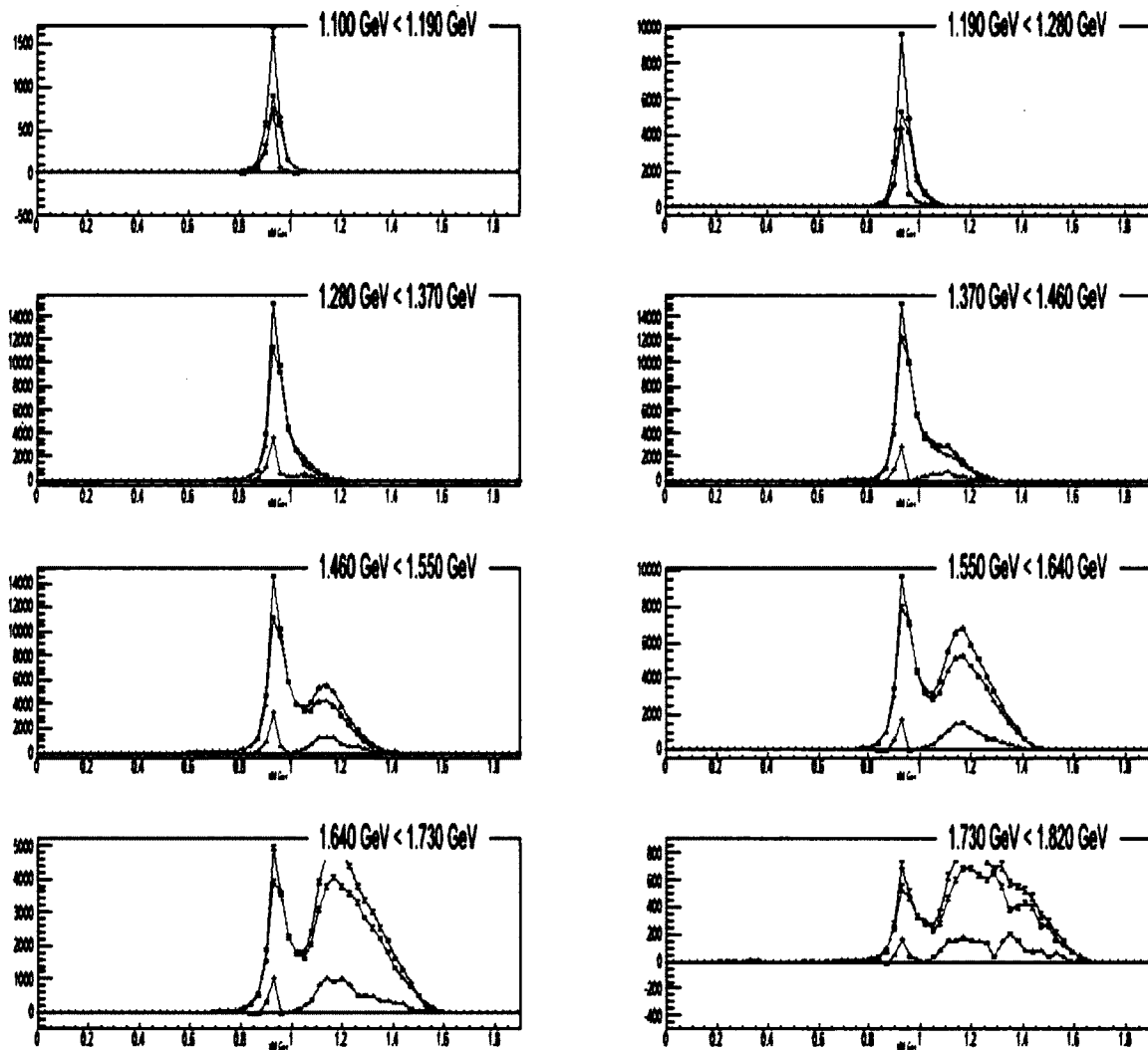


FIG. 34 The missing mass spectrum for ND₃ (top line) carbon (middle line) and the deuteron (bottom line) for 1.6 GeV beam energy in each invariant mass bin using the $d(e, e'\pi^-p)X$ channel.

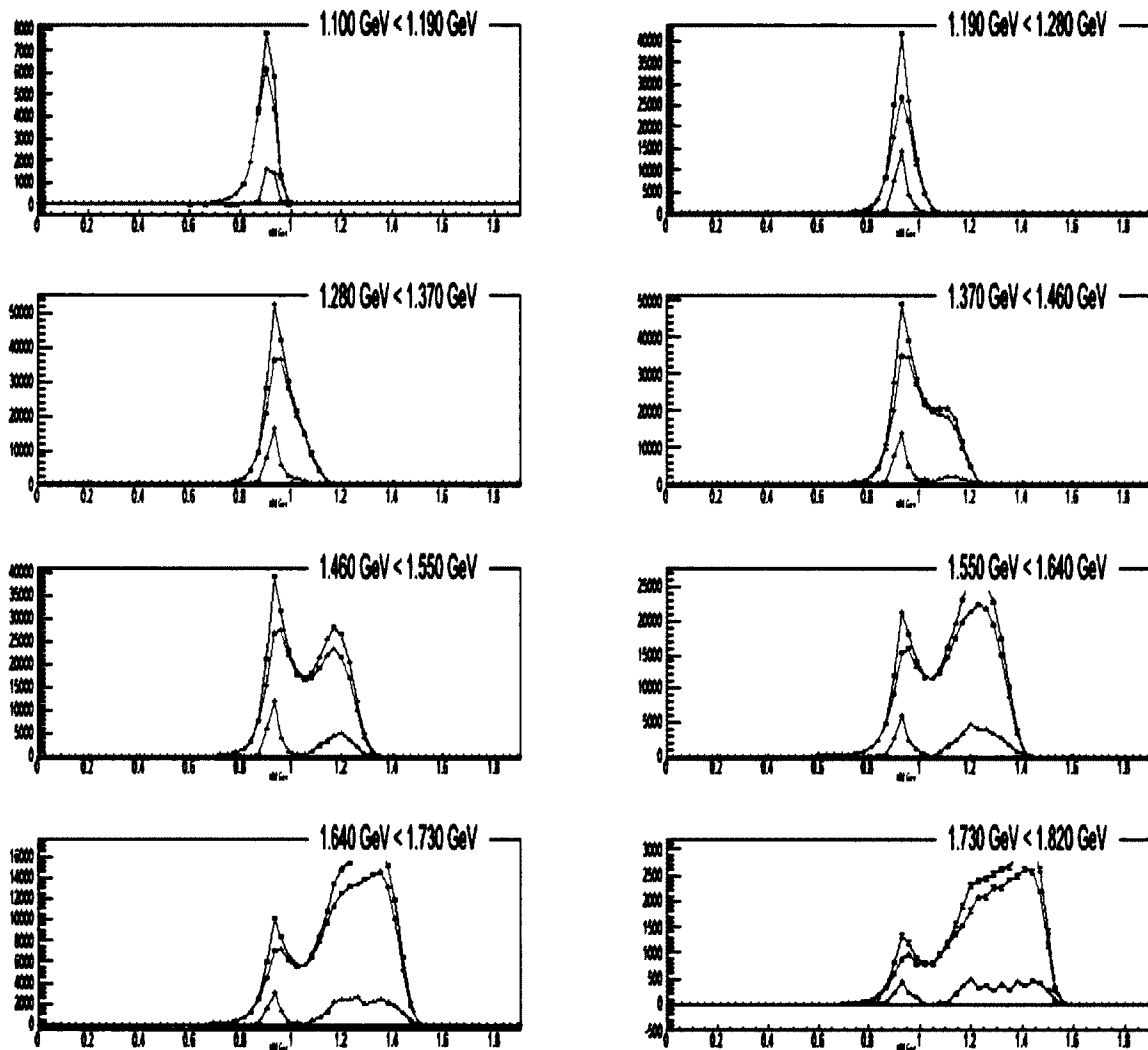


FIG. 35 The missing mass spectrum for ND₃ (top line) carbon (middle line) and the deuteron (bottom line) for 1.6 GeV beam energy in each invariant mass bin using the $n(e,e'\pi^-)X$ channel.

4.10 BEAM AND TARGET POLARIZATION ($P_B P_T$)

In an ideal case, single and double spin asymmetry measurements would be made with a 100% polarized electron beam and a 100% polarized ND₃ target, as discussed in section 2.6. In reality the electron beam is about 70% polarized, as measured by the Møller polarimeter, and the ND₃ target has polarizations ranging from 25% to 30%. The target polarization is measured using the NMR technique, although, due to the depolarization of the center of the target cell from the effects of the beam, the polarization measurement for the target is not as accurate as the beam measurement. Therefore, we use the data to extract the product of beam and target polarization, which is used to correct the measured double spin asymmetry

$$A = \frac{1}{P_B P_T} A_{measured}. \quad (117)$$

While the single target spin asymmetry is corrected using only the target polarization

$$A = \frac{1}{P_T} A_{measured}. \quad (118)$$

Since the beam and target polarization ($P_B P_T$) is one of the main sources of systematic error, a precise measurement is needed.

The product of beam and target polarization ($P_B P_T$) can be determined by analyzing the quasielastic asymmetry for inclusive D(e,e') events or for exclusive D(e,e'p) events and dividing by the theoretical elastic asymmetry on the nucleon, calculated using the Sachs form factors G_E and G_M . [84] The measured asymmetry is given by

$$A_1 = \frac{\sigma_{1/2} - \sigma_{3/2}}{\sigma_{1/2} + \sigma_{3/2}}, \quad (119)$$

and

$$A_2 = \frac{\sigma_{LT}}{\sigma_{1/2} + \sigma_{3/2}}, \quad (120)$$

where $\sigma_{1/2}$ and $\sigma_{3/2}$ are the cross sections for producing a spin-1/2 or spin-3/2 hadronic state following the absorption of the virtual photon by the nucleon, σ_{LT} is the interference cross section term. The theoretical elastic asymmetry for the nucleon is given by

$$A_{Theory} = \frac{\cos \theta^* \sqrt{1 - \epsilon^2} A_1 + \sin \theta^* \sqrt{2\epsilon(1 - \epsilon)} A_2}{1 + \epsilon \frac{Q^2}{\nu^2} \frac{G_E^2(Q^2)}{G_M^2(Q^2)}}, \quad (121)$$

where θ^* is the polar angle between the target spin direction and the virtual photon direction. A_1 and A_2 are the virtual photon asymmetries and G_E and G_M are the electric and magnetic form factors. For elastic scattering these values are given by:

$$A_1 = 1 \text{ and } A_2 = \sqrt{\frac{Q^2}{\nu^2} \left(\frac{G_E(Q^2)}{G_M(Q^2)} \right)}, \quad (122)$$

G_E and G_M are parameterized by [85].

$$G_E(Q^2) = \frac{1}{1 + p_2 Q^2 + p_4 Q^4 + p_6 Q^6 + \dots + p_{12} Q^{12}}, \quad (123)$$

$$GM(Q^2) = \frac{\mu_p}{1 + p_2 Q^2 + p_4 Q^4 + p_6 Q^6 + \dots + p_{12} Q^{12}},$$

Table 8 Fit parameters for the Rosenbluth Form Factors G_E and G_M [85].

Parameter	G_E	G_M
p_2	3.226	3.19
p_4	1.508	1.355
p_6	-0.3773	0.151
p_8	0.611	-0.0114
p_{10}	0.1853	5.33×10^{-4}
p_{12}	0.01596	-9.00×10^{-6}

Since the target material is a deuteron, not a nucleon, the theoretical quasi-elastic asymmetry for $d(e,e')$ was calculated by taking the average for the proton and neutron, weighted by their cross sections

$$A_{theory} = \frac{A_p \sigma_p + A_n \sigma_n}{\sigma_p + \sigma_n} \left(1 - \frac{3}{2} \omega_d \right), \quad (124)$$

while for $d(e,e'p)n$, A_p is used where $\omega_d \approx 0.05 \pm 0.02$ which is the probability of finding the deuteron in the D state [86]. The product of beam and target polarization can then be extracted using

$$P_b P_t = \frac{A_{measured}}{A_{theory}^d}, \quad (125)$$

after correcting for dilution.

In the following sections the criteria for determining good elastic events is described.

4.10.1 Exclusive $P_B P_T$

When considering quasi elastic ep scattering, one can also require the detection of the scattered proton to isolate events from the proton in the deuteron. This has the advantage of reducing the contributions of the unpolarized target material [87] and one can ignore (to first order) contributions from the polarized neutron in the deuteron.

Again, the scattered electron is identified using standard electron cuts. The proton is

identified by placing a cut of $-0.8 \text{ ps} < dt < 0.8 \text{ ps}$ on the time difference between the event start time and time calculated from the path length measured from the drift chambers (Equation 113). Further kinematic restrictions are needed to isolate quasi elastic ep events [88]. These kinematic variables exploit 4-momentum conservation and are placed on the proton depending on the kinematics of the electron to identify e-p events. The energy E'_e of the elastically scattered electrons is calculated by setting the invariant mass W equal to the mass of the proton M .

$$E'_e = \frac{E_{beam}}{1 + 2E_{beam} \sin^2(\theta_e/2)/M}, \quad (126)$$

where θ_e is the polar electron scattering angle.

Using conservation of energy,

$$E_{beam} + M = E'_e + E'_p, \quad (127)$$

and solving for the scattered proton energy,

$$E'_p = E_{beam} + M_p - \frac{M_p E_{beam}}{M_p + 2E_{beam} \sin^2 \frac{\theta_e}{2}}, \quad (128)$$

where E_{beam} is the beam energy. Setting $\sin^2\left(\frac{\theta_e}{2}\right) = \frac{1}{2}(1 - \cos(\theta_e))$, the energy of the proton becomes,

$$E'_p = E_{beam} + M - \frac{ME_{beam}}{M + E_{beam}(1 - \cos(\theta_e))}. \quad (129)$$

Using $E = \sqrt{P^2 + M^2}$, the

missing energy of the proton becomes

$$\Delta E = E_{beam} + M - \frac{ME_{beam}}{M + E_{beam} \left(1 - \frac{P_z}{P_e}\right)} - \sqrt{P_p^2 + M^2}. \quad (130)$$

With a constraint on the polar angle of θ_p less than 49° and using the conservation of momentum on the z axis,

$$E_{beam} = E'_e \cos \theta_e + P_p \cos \theta_p \quad (131)$$

gives

$$\cos(\theta_p) = \frac{E_{beam} - E'_e \cos(\theta_e)}{\sqrt{E_p^2 + M_p^2}}. \quad (132)$$

The missing polar angle becomes

$$\Delta \theta = \cos^{-1} \left(\frac{E_{beam} - (E_{beam} + M_p - E'_e) \cos \theta_e}{\sqrt{E_p^2 - M_p^2}} \right) - \cos^{-1} \left(\frac{P_{zp}}{P_p} \right). \quad (133)$$

For an e-p event to be elastic, ΔE and $\Delta \theta$ should be close to zero. Momentum in the ϕ plane is also conserved. Since the initial momentum is entirely in the z direction, the particles should scatter back to back with opposite azimuthal angle ϕ . The difference in this angle is defined by

$$\Delta \phi = |\phi_p - \phi_e| = \tan^{-1} \left(\frac{P_{yp}}{P_{zp}} \right) - \tan^{-1} \left(\frac{P_{ye}}{P_{xe}} \right). \quad (134)$$

Fig. 36 shows the difference in the out of plane angle ϕ for the electron and proton, which should peak around 180° . Figs. 37 and 38 show the missing energy and missing transverse momentum without any cuts and with cut of $177^\circ < \Delta \phi < 183^\circ$ and $0.88 \text{ GeV} < W < 1.02 \text{ GeV}$ applied.

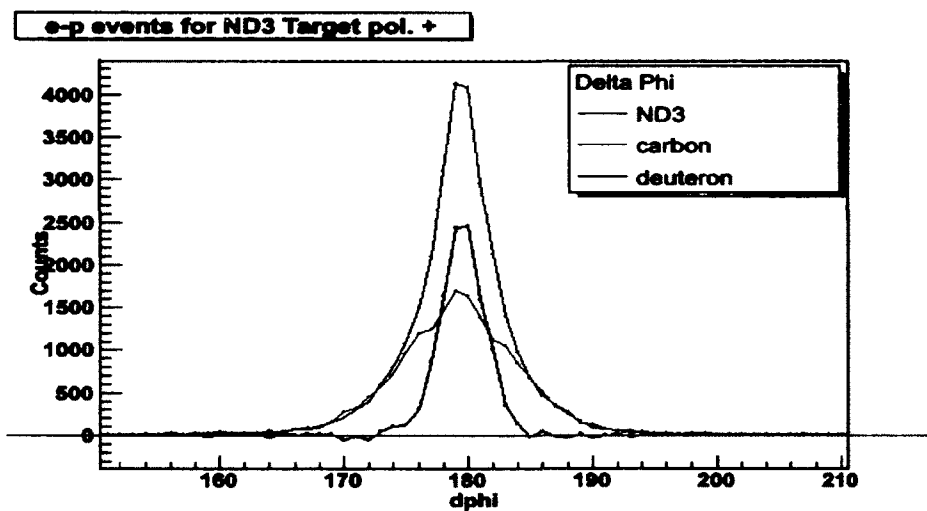


FIG. 36 $\Delta\phi$ for ND_3 (top line), carbon (wide center line) and the deuteron (narrow peak). A cut is applied from $177^\circ < \Delta\phi < 183^\circ$. The wings of the $\Delta\phi$ plot are used for the ^{12}C to ^{15}N scale factor for background subtraction.

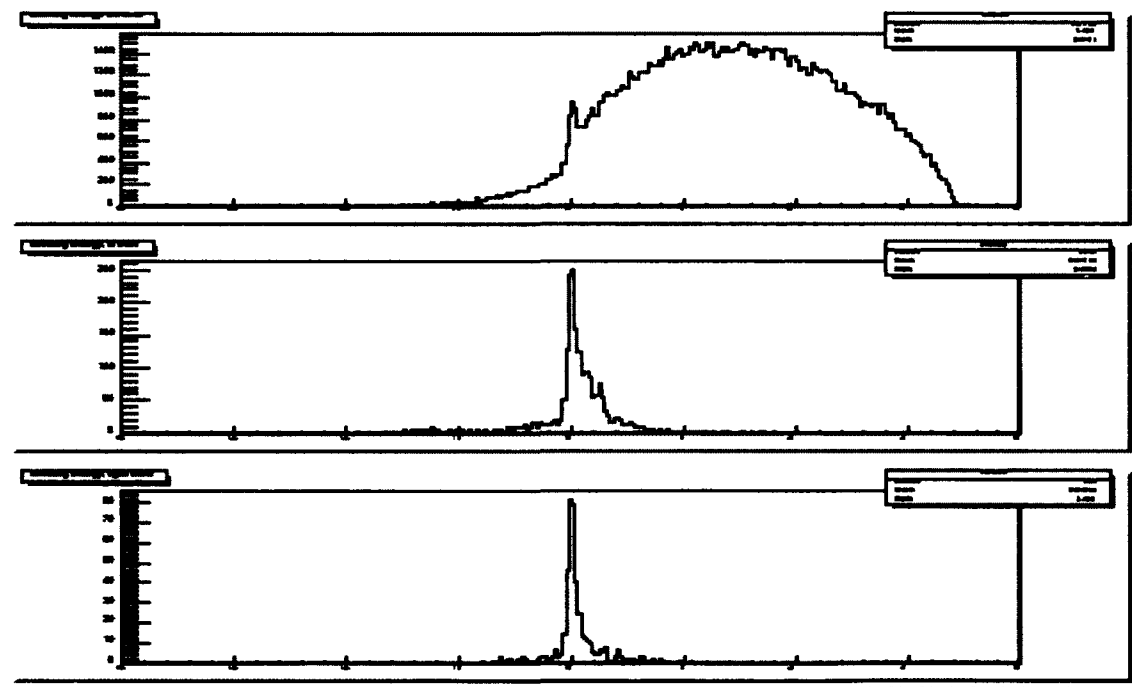


FIG. 37 Missing energy plots ΔE without cuts (top), with a cut on $\Delta\phi$ applied (middle) and cuts on $\Delta\phi$ and W in the elastic region applied (bottom).

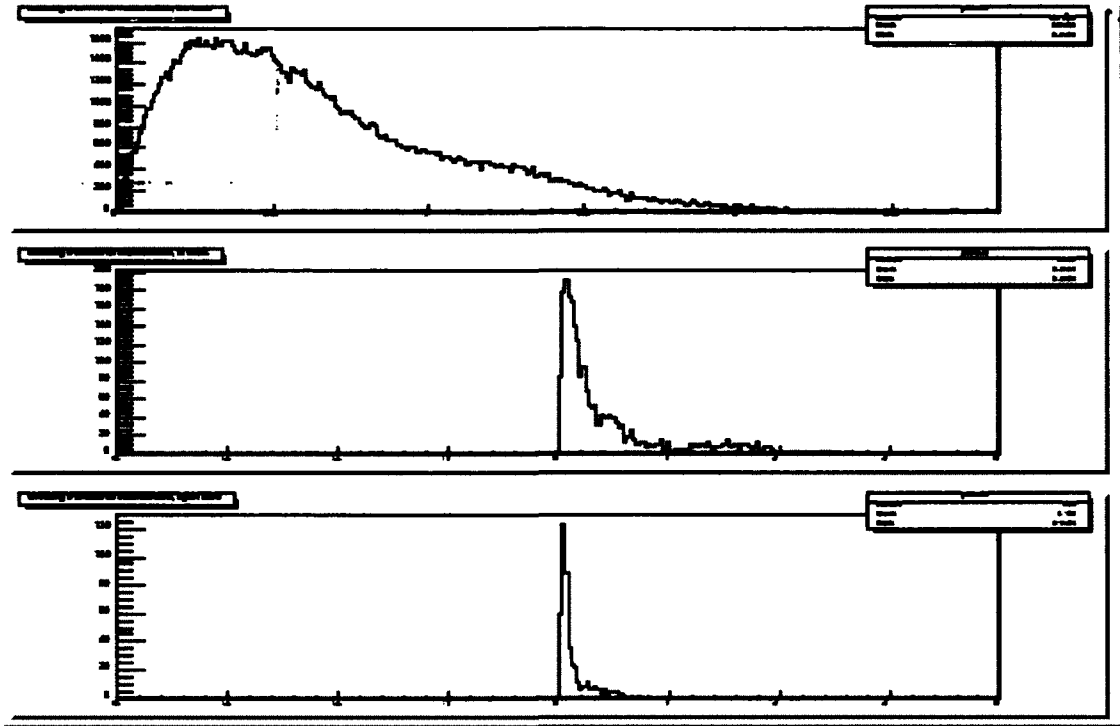


FIG. 38 Missing transverse momentum P_{zp} without cuts (top), with a cut on $\Delta\phi$ applied (middle) and cuts on $\Delta\phi$ and W in the elastic region applied (bottom).

Table 9 Proton identification.

$P \leq 3 \text{ GeV}$	$P > 3 \text{ GeV}$
$EC_{tot}/p > 0.15$	$EC_{tot}/p > 0.2$
$-2.0 < \Delta t < 2.0$	$-2.0 < \Delta t < 2.0$

Since the e-p events of interest are elastic, there should be an azimuthal angle of 180 degrees in the lab frame. This angle $\Delta\phi$ is plotted for ND₃ and carbon and the low and high ϕ regions are used to scale the carbon to the nitrogen background used for background subtraction, refer to Fig. 36. Table 9 shows the cuts applied for proton identification and Table 10 shows elastic event cuts. Events are collected for each helicity state to calculate the measured elastic asymmetry. Again, $P_B P_T$ is extracted by comparing the measured elastic asymmetry to the theoretical elastic asymmetry for the proton in

each Q^2 bin, as shown in Fig. 39.

Table 10 Cuts to ensure elastic events.

$\theta_p < 49^\circ$
$-2.0^\circ < \Delta\theta < 2^\circ$
$-0.08 \text{ GeV} < \Delta E < 0.08 \text{ GeV}$
$177^\circ < \Delta\phi < 183^\circ$
$0.9 \text{ GeV} < W < 1.0 \text{ GeV}$

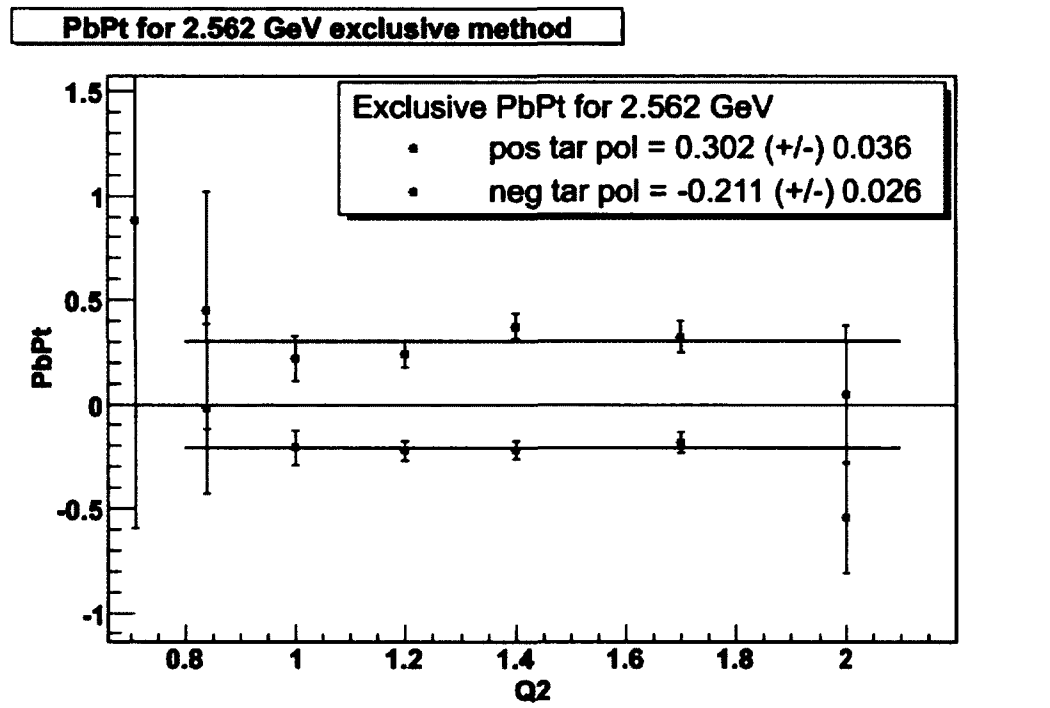


FIG. 39 Exclusive $P_B P_T$ for the 2.5 GeV outbending data set.

For this analysis, the exclusive method for extracting beam and target polarization was chosen. The values of $P_B P_T$ along with their uncertainties are shown in Table 11.

Table 11 Extracted values of $P_B P_T$ for deuteron runs in the EG1b data. The beam energy is labeled according to inbending torus configuration (+) or outbending torus configuration (-). These values are determined using exclusive events.

Beam Energy (GeV)	+ Target Polarization	-Target Polarization
1.6+	0.240±0.012	-0.180±0.013
1.7-	0.175±0.037	-0.251±0.038
2.5+	0.232±0.020	-0.193±0.019
2.5-	0.282±0.034	-0.216±0.032
4.2+	0.222±0.034	-0.147±0.035
4.2-	0.166±0.026	-0.211±0.047

Once the value of beam and target polarization is determined, the value of target polarization can be extracted. This can be done by dividing the $P_B P_T$ by P_B which is measured using the Møller polarimeter. The target polarization P_T is used to determine the target spin asymmetry.

Having determined the correction for beam and target polarization and background, asymmetries can now be analyzed. There are a few small corrections to asymmetries such as radiative corrections and acceptance effects which will be discussed in Chapter 5.

CHAPTER 5

RESULTS

5.1 INTRODUCTION

In the previous chapter the final state particle identification, the method for selecting good events for both the $n(e,e'\pi^-)p$ and $d(e,e'\pi^-)p$ channels, and determination of the product of beam and target polarization were described. Here we discuss the method for determining asymmetries from our data as well as the systematic uncertainties on these results. All of the energy settings from EG1b runs have been analyzed separately.

5.2 ASYMMETRIES

The polarized-dependent cross section for π^- electro-production has the form

$$\sigma = \sigma_0 + P_B \sigma_e + P_T \sigma_t - P_B P_T \sigma_{et}, \quad (135)$$

where σ_0 is the un-polarized cross section, σ_e is the polarized beam dependent cross section, σ_t is the polarized target dependent cross section and σ_{et} is the double polarization (beam and target dependent) cross section. P_B and P_T are the beam and target polarizations, respectively. The minus sign on the last term is chosen so that the double spin asymmetry is consistent with that used in inclusive analysis.

The events collected for each helicity state are N_{bt} where b indicates the beam and t indicates the target. A “+” or “-” is used to indicate positive or negative polarization for the beam or target. For example N_{-+} is the number of counts for negative beam and positive target polarizations.

The eg1b data were taken with four different helicity configurations, with the

electron and target spins alternating between positive and negative helicities. The electron helicity was reversed every 0.03 seconds. The electron polarization value is independent of the helicity state, which means that the absolute value of the polarization can be treated as being the same, with $P_B^+ \sim P_B^-$. The target polarization was reversed only once or twice for each data set and can have a large helicity dependence. The absolute values of target polarization are P_T^+ and P_T^- . It is convenient to express both beam helicities and target polarizations in terms of a ratio,

$$R_B = \frac{P_B^+}{P_B^-}, \quad (136)$$

and

$$R_T = \frac{P_T^+}{P_T^-}. \quad (137)$$

The number of events that were detected for each beam and target helicity state is proportional to the cross section for that state. For example

$$\sigma \propto \frac{N_{bt}}{FC_{bt}L_t}, \quad (138)$$

where L_t takes the target thickness into account. Usually the target thickness cancels in the ratio when calculating the asymmetry. However, while taking the 2.5 GeV outbending data, the target started leaking target material, which led to a different target thickness for positive and negative polarizations. The target spin asymmetry is particularly sensitive to this ratio.

For each helicity state, the number of events can be written explicitly in terms of the individual cross section terms:

$$N_{++} \propto L_+ FC_{++} (\sigma_0 + P_B^+ \sigma_e + P_T^+ \sigma_t - P_B^+ P_T^+ \sigma_{et}), \quad (139)$$

$$N_{+-} \propto L_- FC_{+-} (\sigma_0 + P_B^+ \sigma_e - P_T^- \sigma_t + P_B^+ P_T^- \sigma_{et}), \quad (140)$$

$$N_{-+} \propto L_+ FC_{-+} (\sigma_0 - P_B^- \sigma_e + P_T^+ \sigma_t + P_B^- P_T^+ \sigma_{et}), \quad (141)$$

$$N_{--} \propto L_- FC_{--} (\sigma_0 - P_B^- \sigma_e - P_T^- \sigma_t - P_B^- P_T^- \sigma_{et}). \quad (142)$$

Using these four equations, the four cross sections in brackets can be determined as a

function of the number of events for each helicity state [89]. First we define $P_B^+ = a$,

$P_B^- = b$, $P_T^+ = c$, and $P_T^- = d$. Equations 139 through 142 become

$$\frac{N'_{++}}{L_+} \propto [\sigma_0 + a\sigma_e + c\sigma_t - ac\sigma_{et}], \quad (143)$$

$$\frac{N'_{+-}}{L_-} \propto [\sigma_0 + a\sigma_e - d\sigma_t + ad\sigma_{et}], \quad (144)$$

$$\frac{N'_{-+}}{L_+} \propto [\sigma_0 - b\sigma_e + c\sigma_t + bc\sigma_{et}], \quad (145)$$

$$\frac{N'_{--}}{L_-} \propto [\sigma_0 - b\sigma_e - d\sigma_t - bd\sigma_{et}]. \quad (146)$$

Then we define a coefficient matrix M , such that

$$M = \begin{pmatrix} 1 & a & c & -ac \\ 1 & a & -d & ad \\ 1 & -b & c & bc \\ 1 & -b & -d & -bd \end{pmatrix}, \quad (147)$$

We note that the determinant of M , $|M|$, is a constant, and σ_i can be determined via

$$\sigma_i = \frac{|M_i|}{|M|}, \quad (148)$$

where

$$M_0 = \begin{pmatrix} \frac{N'_{++}}{L_+} & a & c & -ac \\ \frac{N'_{+-}}{L_-} & a & -d & ad \\ \frac{N'_{-+}}{L_+} & -b & c & bc \\ \frac{N'_{--}}{L_-} & -b & -d & -bd \end{pmatrix}, \quad (149)$$

$$M_T = \begin{pmatrix} 1 & a & \frac{N'_{++}}{L_+} & -ac \\ 1 & a & \frac{N'_{+-}}{L_-} & ad \\ 1 & -b & \frac{N'_{-+}}{L_+} & bc \\ 1 & -b & \frac{N'_{--}}{L_-} & -bd \end{pmatrix} \quad (150)$$

$$M_E = \begin{pmatrix} 1 & \frac{N'_{++}}{L_+} & c & -ac \\ 1 & \frac{N'_{+-}}{L_-} & -d & ad \\ 1 & \frac{N'_{-+}}{L_+} & c & bc \\ 1 & \frac{N'_{--}}{L_-} & -d & -bd \end{pmatrix} \quad (151)$$

$$M_T = \begin{pmatrix} 1 & a & c & \frac{N'_{++}}{L_+} \\ 1 & a & -d & \frac{N'_{+-}}{L_-} \\ 1 & -b & c & \frac{N'_{-+}}{L_+} \\ 1 & -b & -d & \frac{N'_{--}}{L_-} \end{pmatrix} \quad (152)$$

To get the unpolarized cross section σ_0 , we find $|M_0|$,

$$\begin{aligned}
|M_0| &= \frac{N'_{++}}{L_+} [a(-bcd + bcd) + d(b^2d + b^2c) + ad(bd + bc)] \\
&= \frac{N'_{++}}{L_+} [db(b+a)(d+c)]
\end{aligned} \tag{153}$$

For each helicity state, the counts have to be normalized to the luminosity for that state.

Since the absolute luminosity will be canceled in the asymmetry, only the relative luminosities for the different helicity states are required. These are determined by measuring the accumulated beam charge for each helicity state by means of a scalar readout from the Faraday Cup (FC). The ratios of luminosities are defined as:

$$f_0 = \frac{FC_{++}}{FC_{++}} = 1 \tag{154}$$

$$f_1 = \frac{FC_{++}}{FC_{-+}}, \tag{155}$$

$$f_2 = \frac{FC_{++}}{FC_{+-}}, \tag{156}$$

$$f_3 = \frac{FC_{++}}{FC_{--}}. \tag{157}$$

$$|M_0| = \frac{(a+b)(c+d)}{FC_{++}} \left[\frac{bdN_{++}}{L_+} + \frac{cbf_2N_{+-}}{L_-} + \frac{adf_1N_{-+}}{L_+} + \frac{acf_3N_{--}}{L_-} \right] \tag{158}$$

Taking the ratio $a/b \ll 1$

$$\sigma_0 = \frac{a(b+a)(c+d)}{FC_{++}|M|} \left[\frac{c}{L_-} (f_2N_{+-} + f_3N_{--}) + \frac{d}{L_+} (N_{++} + f_1N_{-+}) \right]. \tag{159}$$

Using the same method, the target spin asymmetry σ_T is

$$\sigma_T = \frac{a(b+a)(c+d)}{FC_{++}|M|} \left[\frac{1}{L_+} (N_{++} + f_1N_{-+}) - \frac{1}{L_-} (f_2N_{+-} + f_3N_{--}) \right]. \tag{160}$$

Since the asymmetry is the ratio of the polarized cross section, in this case, the polarized target cross section, to the unpolarized cross section, we can write the asymmetry

$$A_T = \frac{\sigma_T}{\sigma_0} = \frac{\left[\frac{1}{L_+} (N_{++} + f_1 N_{-+}) - \frac{1}{L_-} (f_2 N_{+-} + f_3 N_{--}) \right]}{\left[\frac{d}{L_+} (N_{++} + f_1 N_{-+}) + \frac{c}{L_-} (f_2 N_{+-} + f_3 N_{--}) \right]}. \quad (161)$$

Multiplying the numerator and denominator by L_+/d

$$A_T = \frac{\sigma_T}{\sigma_0} = \frac{\left[\frac{1}{d} (N_{++} + f_1 N_{-+}) - \frac{L_+}{dL_-} (f_2 N_{+-} + f_3 N_{--}) \right]}{\left[(N_{++} + f_1 N_{-+}) + \frac{L_+ c}{L_- d} (f_2 N_{+-} + f_3 N_{--}) \right]}. \quad (162)$$

Substituting back the definition of c and d and defining target thickness $R_r = \frac{L_+}{L_-}$, the

target spin asymmetry can be written

$$A_T = \frac{\sigma_T}{\sigma_0} = \frac{1}{P_T^-} \frac{(N_{++} + f_1 N_{-+}) - R_r (f_2 N_{+-} + f_3 N_{--})}{(N_{++} + f_1 N_{-+}) + R_r R_r (f_2 N_{+-} + f_3 N_{--})}. \quad (163)$$

Likewise, the beam spin and double spin asymmetries are

$$A_E = \frac{\sigma_E}{\sigma_0} = \frac{1}{P_B^+} \frac{(N_{++} - f_1 N_{-+}) + R_B R_T R_r (f_2 N_{+-} - f_3 N_{--})}{(N_{++} + f_1 N_{-+}) + R_T R_r (f_2 N_{+-} + f_3 N_{--})}, \quad (164)$$

$$A_{ET} = \frac{\sigma_{ET}}{\sigma_0} = \frac{1}{P_B^+ P_T^-} \frac{(f_1 N_{-+} - N_{++}) + R_B R_r (f_2 N_{+-} - f_3 N_{--})}{(N_{++} + f_1 N_{-+}) + R_T R_r (f_2 N_{+-} + f_3 N_{--})}. \quad (165)$$

Since the target is made up of frozen deuterated ammonia beads (ND_3), the nitrogen background has to be taken into account as mentioned in section 4.8. This is done by subtracting the Carbon from the counts in the denominator using a scalefactor

$$S_C^+ = \frac{ND_3^+}{C}, \text{ and } S_C^- = \frac{ND_3^-}{C}, \quad (166)$$

where ND_3^+ , ND_3^- and C are the number of events in the low missing mass region. We introduce new scale factors to account for the FC normalization

$$f_1' = \frac{FC_{++}}{FC_{++} + FC_{-+}}, \text{ and } f_{23}' = \frac{FC_{++}}{FC_{+-} + FC_{--}}, \quad (167)$$

and the asymmetries become,

$$A_{ET} = \frac{1}{P_B^+ P_T^-} \frac{(f_1 N_{-+} - N_{++}) + R_B R_R (f_2 N_{+-} - f_3 N_{--})}{(N_{++} + f_1 N_{-+} - S_C^+ f_1' N_C) + R_T R_R (f_2 N_{+-} + f_3 N_{--} - S_C^- f_{23}' N_C)}, \quad (168)$$

$$A_T = \frac{1}{P_T^-} \frac{(N_{++} + f_1 N_{-+}) - (f_2 N_{+-} + f_3 N_{--})}{(N_{++} + f_1 N_{-+} - S_C^+ f_1' N_C) + R_T (N_{+-} + N_{--} - S_C^- f_{23}' N_C)}, \quad (169)$$

$$A_E = \frac{1}{P_B^+} \frac{(N_{++} - f_1 N_{-+}) + R_B R_T R_R (f_2 N_{+-} - f_3 N_{--})}{(N_{++} + f_1 N_{-+} - S_C^+ f_1' N_C) + R_T R_R (f_2 N_{+-} + f_3 N_{--} - S_C^- f_{23}' N_C)}. \quad (170)$$

where N_C is the number of counts in carbon with the same kinematic cuts.

The statistical uncertainty for the three asymmetries given above are calculated using

$$\delta A = \sqrt{\left(\frac{\partial A}{\partial N_{++}}\right)^2 \delta N_{++}^2 + \left(\frac{\partial A}{\partial N_{-+}}\right)^2 \delta N_{-+}^2 + \left(\frac{\partial A}{\partial N_{+-}}\right)^2 \delta N_{+-}^2 + \left(\frac{\partial A}{\partial N_{--}}\right)^2 \delta N_{--}^2 + \left(\frac{\partial A}{\partial N_C}\right)^2 \delta N_C^2} \quad (171)$$

where $\delta N = \sqrt{N}$. Since the asymmetry is a ratio, it is useful to work with the numerator

U and denominator V separately. For example, for A_{ET}

$$U = (f_1 N_{-+} - N_{++}) + R_B R_R (f_2 N_{+-} - f_3 N_{--}) \quad (172)$$

$$V = \frac{1}{P_B^+ P_T^-} \left(f_1 N_{-+} + N_{++} - S_C^+ f_1' N_C \right) + R_T R_R \left(f_2 N_{+-} + f_3 N_{--} - S_C^- f_{23}' N_C \right), \quad (173)$$

and the partial derivative of the asymmetry is then calculated

$$\partial A = \frac{V \partial U - U \partial V}{V^2}. \quad (174)$$

The partial derivatives with respect to U and V are,

$$\frac{\partial U}{\partial N_{++}} = -1, \quad \frac{\partial U}{\partial N_{-+}} = f_1, \quad \frac{\partial U}{\partial N_{+-}} = R_B R_r f_2, \quad \frac{\partial U}{\partial N_{--}} = -R_B R_r f_3, \quad \frac{\partial U}{\partial N_C} = 0 \quad (175)$$

and

$$\begin{aligned} \frac{\partial N_{++}}{\partial V} &= P_B P_T, & \frac{\partial N_{-+}}{\partial V} &= P_B P_T f_1, & \frac{\partial N_{+-}}{\partial V} &= P_B P_T R_T R_r f_2, \\ \frac{\partial N_{--}}{\partial V} &= P_B P_T R_T R_r f_3, & \frac{\partial N_C}{\partial V} &= -P_B P_T \left[S_C^+ f_1' - S_C^- f_{23}' R_T R_r \right]. \end{aligned} \quad (176)$$

With $N' = fN$ the partial derivative with respect to the asymmetry is given by

$$\frac{\partial A_{ET}}{\partial N_{++}} = \frac{-(N'_{++} + N'_{-+} - S_C^+ N'_C) - R_T R_r (N'_{-+} + N'_{+-} - S_C^- N'_C) - (N'_{-+} - N'_{++}) - R_B R_r (N'_{-+} - N'_{--})}{P_B^2 P_T^2 \left[(N'_{++} + N'_{-+} - S_C^+ N'_C) + R_T R_r (N'_{-+} + N'_{+-} - S_C^- N'_C) \right]^2} \quad (177)$$

$$\frac{\partial A_{ET}}{\partial N_{-+}} = \frac{f_1 \left[(N'_{++} + N'_{-+} - S_C^+ N'_C) + R_T R_r (N'_{-+} + N'_{+-} - S_C^- N'_C) - (N'_{-+} - N'_{++}) - R_B R_r (N'_{-+} - N'_{--}) \right]}{P_B^2 P_T^2 \left[(N'_{++} + N'_{-+} - S_C^+ N'_C) + R_T R_r (N'_{-+} + N'_{+-} - S_C^- N'_C) \right]^2} \quad (178)$$

$$\frac{\partial A_{ET}}{\partial N_{+-}} = \frac{R_B R_r f_2 \left[(N'_{++} + N'_{-+} - S_C^+ N'_C) + R_T R_r (N'_{-+} + N'_{+-} - S_C^- N'_C) \right] - R_T R_r f_2 \left[(N'_{-+} - N'_{++}) + R_B R_r (N'_{-+} - N'_{--}) \right]}{P_B^2 P_T^2 \left[(N'_{++} + N'_{-+} - S_C^+ N'_C) + R_T R_r (N'_{-+} + N'_{+-} - S_C^- N'_C) \right]^2} \quad (179)$$

$$\frac{\partial A_{ET}}{\partial N_{--}} = \frac{-R_B R_r f_3 \left[(N'_{++} + N'_{-+} - S_C^+ N'_C) + R_T R_r (N'_{-+} + N'_{+-} - S_C^- N'_C) \right] - R_T R_r f_3 \left[(N'_{-+} - N'_{++}) + R_B R_r (N'_{-+} - N'_{--}) \right]}{P_B^2 P_T^2 \left[(N'_{++} + N'_{-+} - S_C^+ N'_C) + R_T R_r (N'_{-+} + N'_{+-} - S_C^- N'_C) \right]^2} \quad (180)$$

$$\frac{\partial A_{ET}}{\partial N_C} = \frac{(S_C^+ f_1' + R_T R_r S_C^- f_{23}') \left[(N'_{-+} - N'_{++}) + R_B R_r (N'_{-+} - N'_{--}) \right]}{\left[(N'_{++} + N'_{-+} - S_C^+ N'_C) + R_T R_r (N'_{-+} + N'_{+-} - S_C^- N'_C) \right]^2}. \quad (181)$$

Plugging these terms back into Equation 171, gives the total statistical error on the asymmetry measurement.

5.2.1 Binning

The asymmetries and the statistical uncertainties are extracted in four dimensional kinematic bins of W , $Q^2 \cos \theta^*$ and ϕ^* . Figs. 40 and 41 show the kinematic acceptance.

The binning was made up of 23 bins in W (90 MeV each), 10 $\cos\theta^*$ bins, 15 (24°) ϕ^* bins and 8 Q^2 bins. Tables 12 through 15 list the kinematic bins for this analysis. These bins are combined standard bins for the EG1b data set. The range is set to cover the kinematic regions for each of the beam energies ranging from 1.6 GeV to 4.2 GeV. The asymmetry in any given bin is independent of the acceptance in that bin, as long as the acceptance does not change drastically over the width of that bin. Because of this, the asymmetry can be determined without the need for any model of detector acceptance. For this reason small bins were used.

5.2.2 Combining Asymmetries

A_E , A_T , and A_{ET} were measured for $n(e,e'\pi^-)p$, where we assume the neutron is at rest, and $d(e,e'\pi^-)p$, in which we detect both a π^- and proton in the final state. The $n(e,e'\pi^-)p$ channel includes only events that are not included in the $d(e,e'\pi^-)p$ event sample. Missing mass cuts are applied in both cases as described in Chapter 4. The $d(e,e'\pi^-)p$ channel is fully exclusive and should have less background while the $n(e,e'\pi^-)p$ channel has greater statistics. However, this channel has a larger background contribution and may include some higher resonance tail within the missing mass

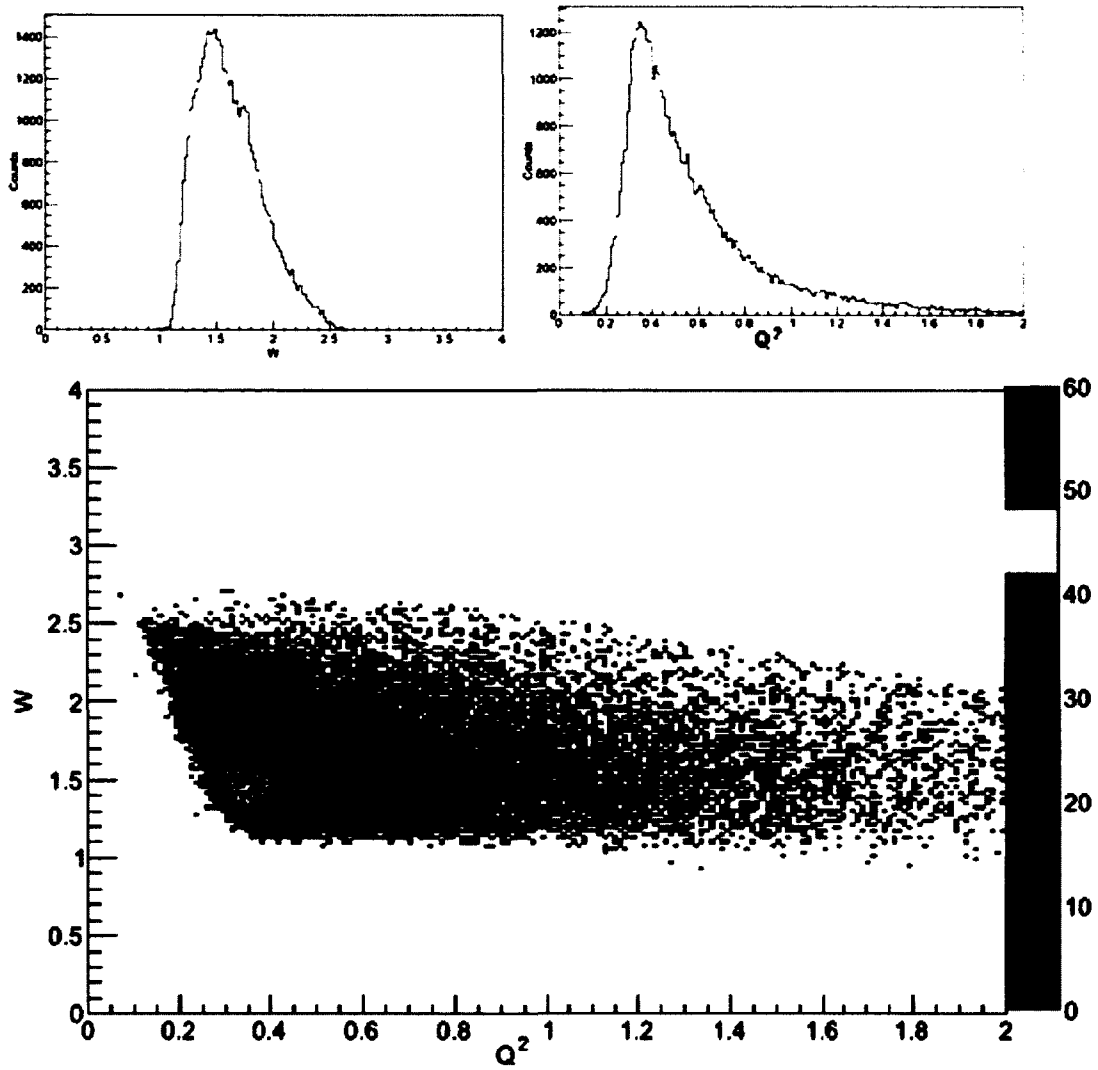


FIG. 40 Region of acceptance for W (top left), Q^2 (top right) and a 2-D distribution of Q^2 vs W (bottom) for 4.2 GeV data.

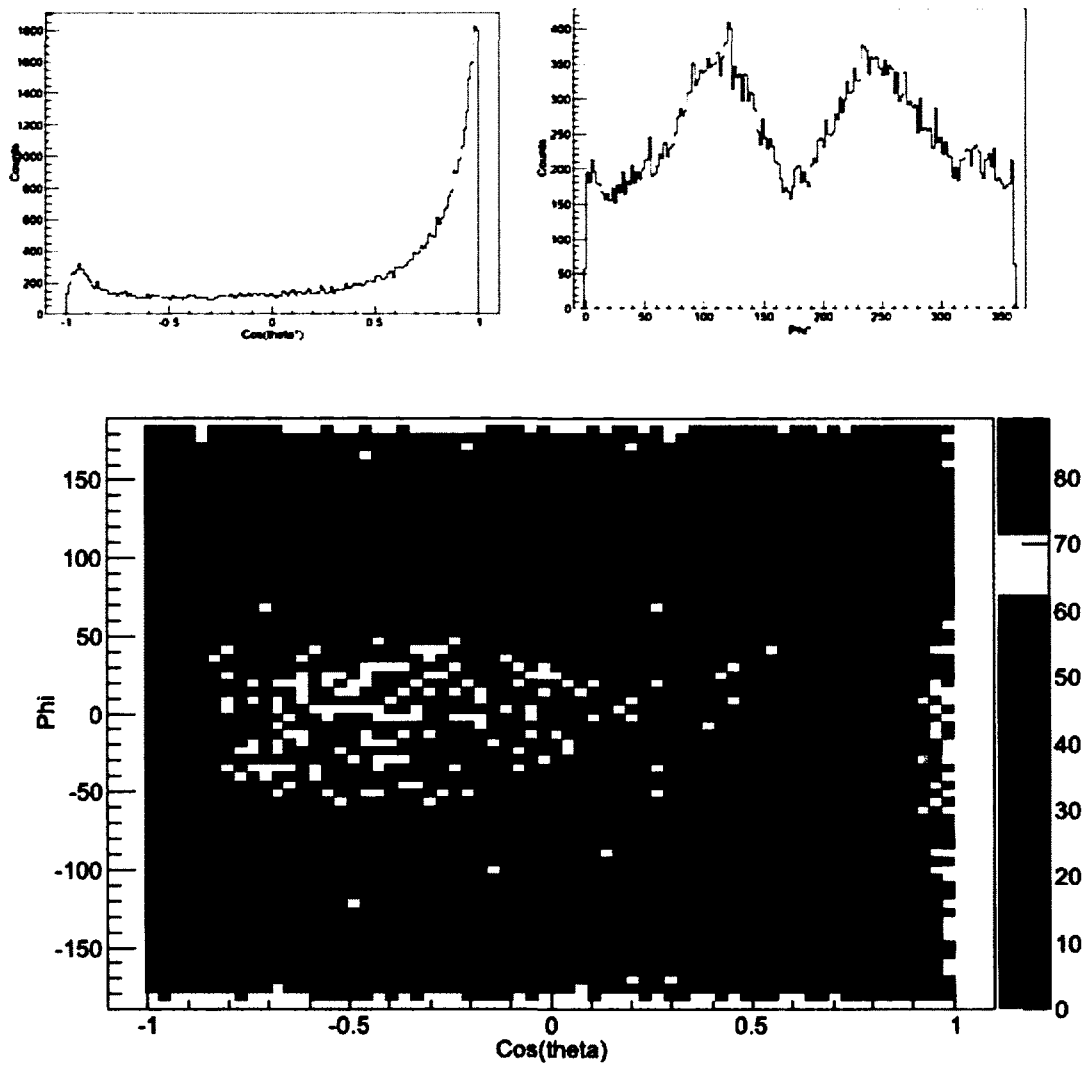


FIG. 41 Region of acceptance for $\cos\theta^*$ (top left), ϕ^* (top right) and a 2-D distribution of $\cos\theta^*$ vs ϕ^* (bottom) for 4.2 GeV data.

Table 12 Kinematic binning for the invariant mass W

W minimum (GeV)	W maximum (GeV)	Nominal Bin Center (GeV)
0.92	1.01	0.965
1.01	1.10	1.055
1.10	1.19	1.145
1.19	1.28	1.235
1.28	1.37	1.325
1.37	1.46	1.415
1.46	1.55	1.505
1.55	1.64	1.595
1.64	1.73	1.685
1.73	1.82	1.775
1.82	1.91	1.865
1.91	2.00	1.955
2.00	2.09	2.045
2.09	2.18	2.135
2.18	2.27	2.225
2.27	2.36	2.315
2.36	2.45	2.405
2.45	2.54	2.495
2.54	2.63	2.585
2.63	2.72	2.675
2.72	2.81	2.765
2.81	2.90	2.855

Table 13 Kinematic binning for the square of the momentum transfer Q^2

Q^2 minimum (GeV)²	Q^2 maximum (GeV)²	Nominal Bin Center (GeV)²
0.0	0.0452	0.023
0.0452	0.0919	0.07
0.0919	0.187	0.14
0.187	0.379	0.28
0.379	0.770	0.57
0.770	1.56	1.17
1.56	3.17	2.37
3.17	10.97	7.1

Table 14 Kinematic binning for ϕ^*

ϕ^* minimum (deg)	ϕ^* maximum (deg)	Nominal Bin Center (deg)
0	24	12
24	48	36
48	72	60
72	96	84
96	120	108
120	144	132
144	168	156
168	192	180
192	216	204
216	240	228
240	264	252
264	288	276
288	312	300
312	336	324
336	360	348

Table 15 Kinematic binning for $\cos(\theta^*)$

$\cos(\theta^*)$ minimum	$\cos(\theta^*)$ maximum	Nominal Bin Center
-1.0	-0.8	-0.9
-0.8	-0.6	-0.7
-0.6	-0.4	-0.5
-0.4	-0.2	-0.3
-0.2	0.0	-0.1
0.0	0.2	0.1
0.2	0.4	0.3
0.4	0.6	0.5
0.6	0.8	0.7
0.8	1.0	0.9

selection (refer to Figs. 34 and 35). A T- test was performed for asymmetries from both channels to see if the two channels are consistent

$$T_{test} = \frac{A_{\pi^-} - A_{\pi^-p}}{\delta A_{\pi^-}^2 - \delta A_{\pi^-p}^2}. \quad (182)$$

The T-test is performed only for bins in which we have a result for both cases. Fig. 42 shows the T-test on A_{et} and A_t for the 1.6 GeV data. There is a small 3-5% difference, which is well within the statistical uncertainty on the asymmetries, showing that the two channels are consistent. Figs. 43 through 47 show the T-test for all other energy data sets. The largest difference between the two channels is found in the 2.5 GeV data (negative target polarization), which showed an 8% effect. Because the asymmetries from the two channels are consistent, they were combined together, weighted by their uncertainties. This was done by using an error weighted sum, which takes into account quality of each individual asymmetry,

$$A_{Summed} = \frac{\sum_i A_i \delta A_i}{\sum_i \left(\frac{1}{\delta A_i}\right)^2}, \quad (183)$$

$$\delta A_{Summed} = \frac{1}{\sum_i \left(\frac{1}{\delta A_i}\right)^2}, \quad (184)$$

where A_i are the asymmetries to be summed, and δA_i are the statistical uncertainties for that bin. The asymmetries were then checked for consistency across torus polarization, again using the T-test in Equation 182. These T-tests show small differences as shown in

Figs. 48 through 50. The asymmetries for the inbending and outbending torus polarization were then combined using Equation 183. The final measured asymmetries were determined for the 1.6, 2.5, and 4.2 GeV data as a function of the four kinematic variables.

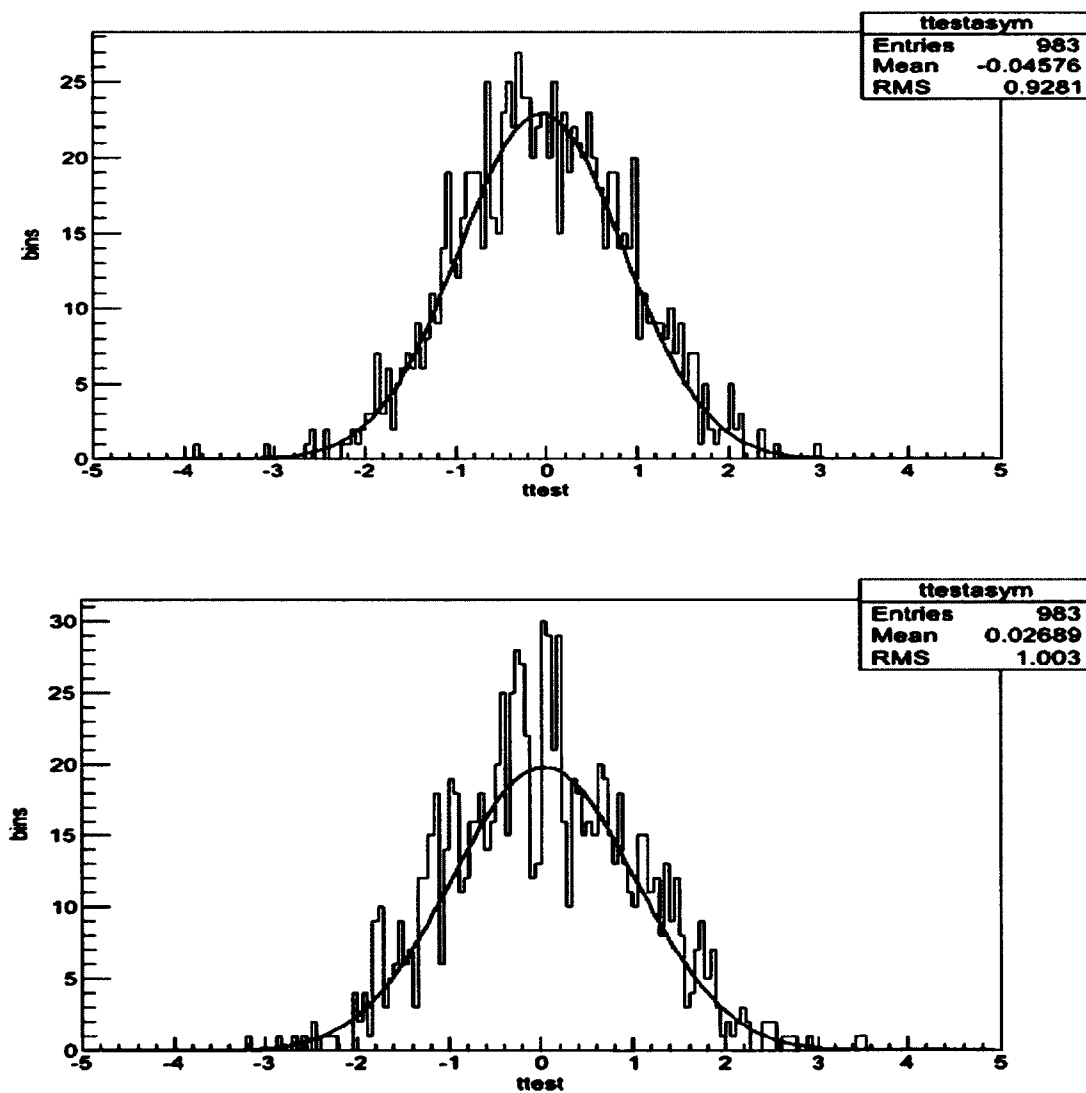


FIG. 42 T-test comparison for $n(e,e'\pi^-)p$ and $d(e,e'\pi^-)p$ for A_{et} (top) and A_t (bottom) for 1.6 GeV data.

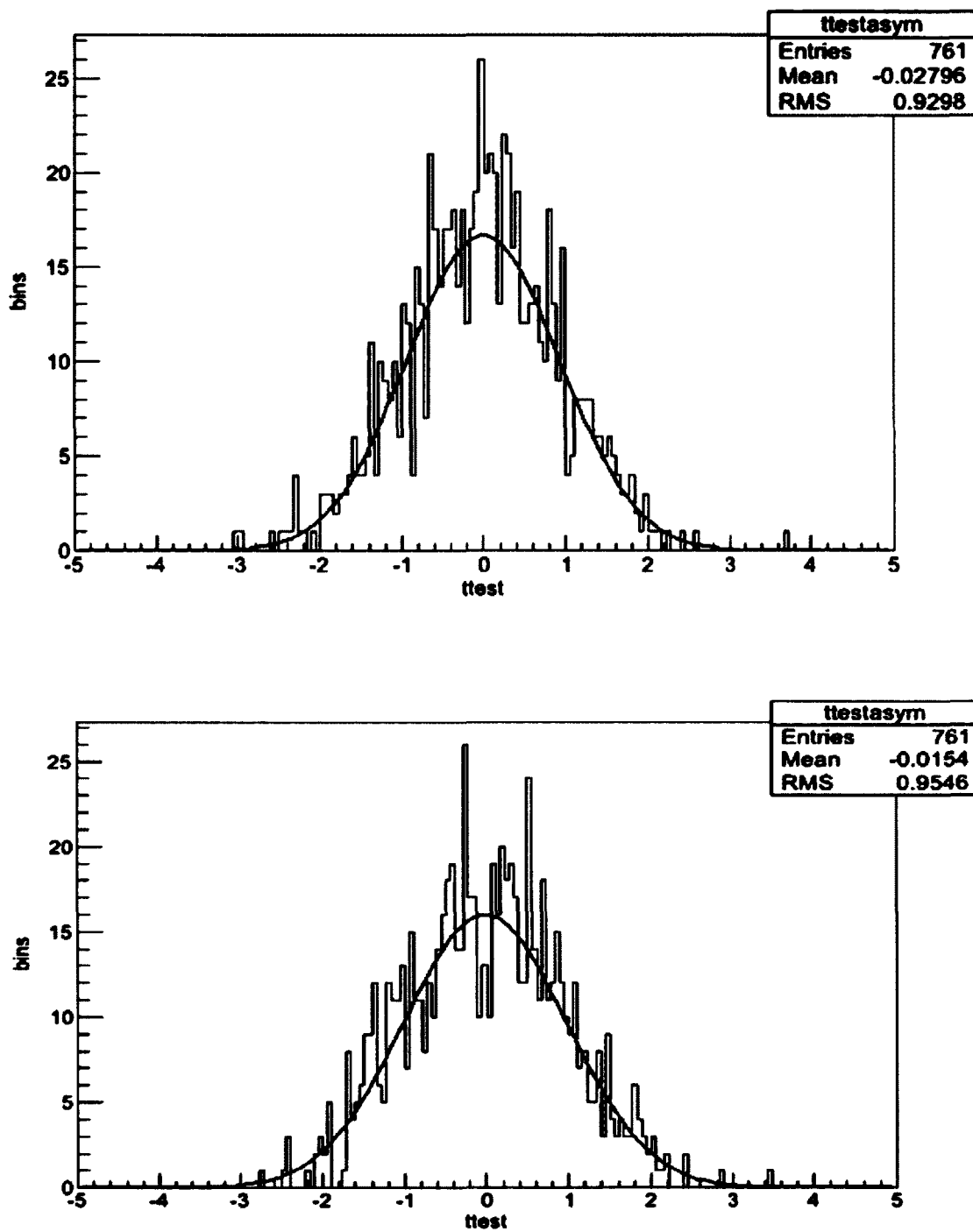


FIG. 43 T-test comparison for $n(e,e'\pi^-)p$ and $d(e,e'\pi^-)p$ for A_{et} (top) and A_t (bottom) for 1.7 GeV data.

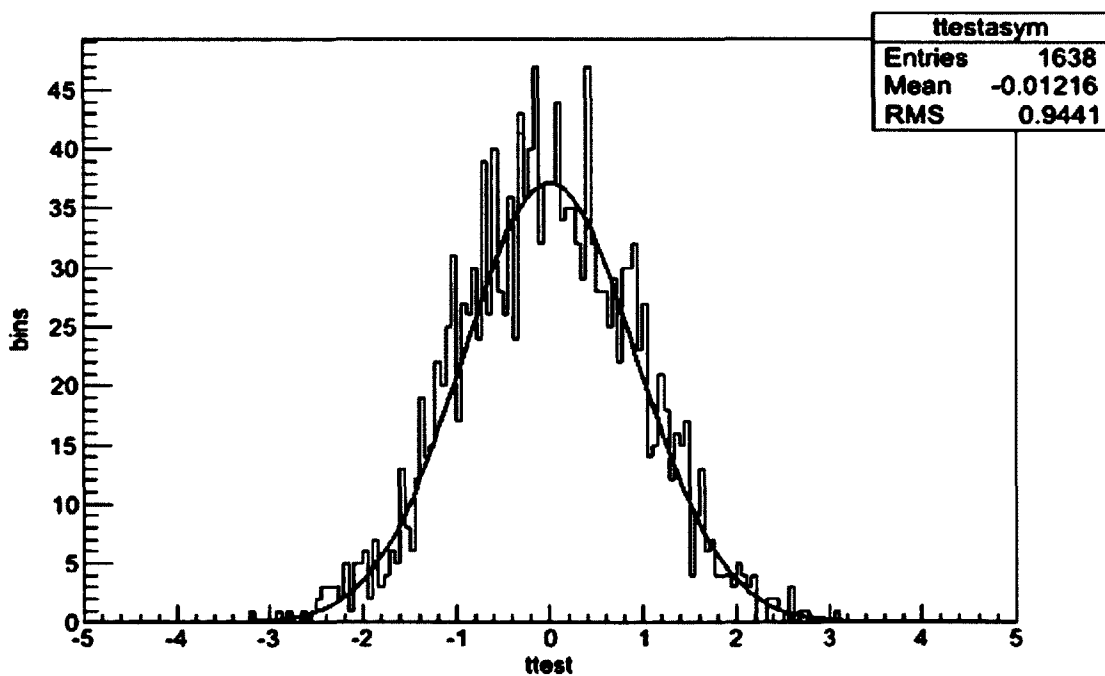
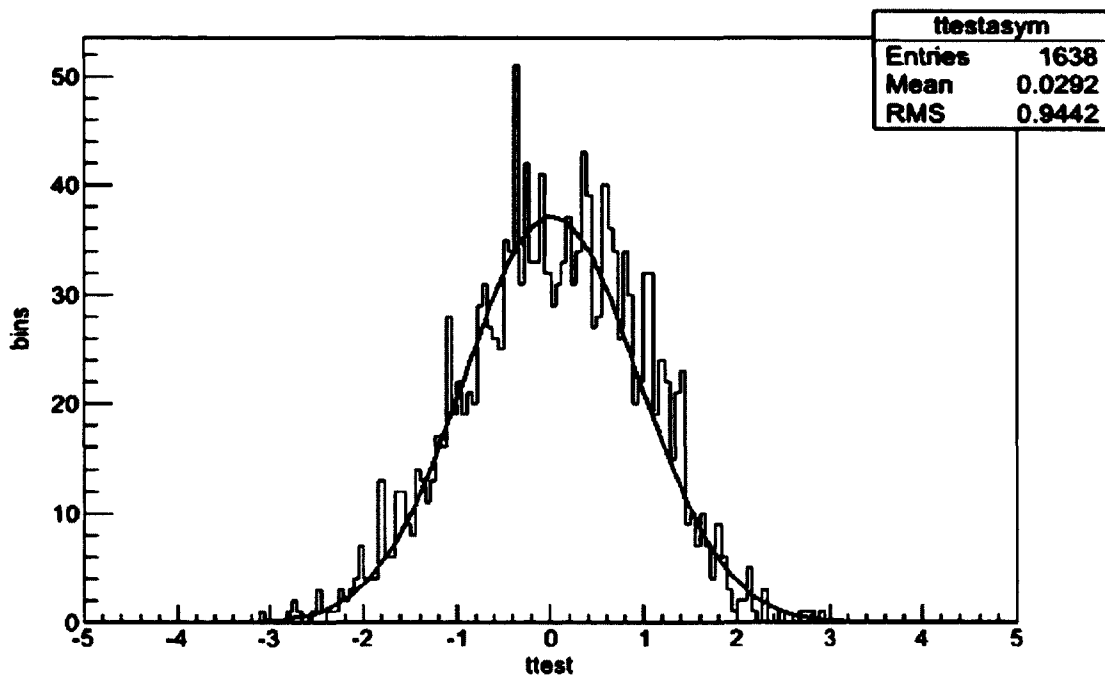


FIG. 44 T-test comparison for $n(e,e'\pi^-)p$ and $d(e,e'\pi^-)p$ for A_{ei} (top) and A_t (bottom) for 2.5 GeV positive torus polarization data.

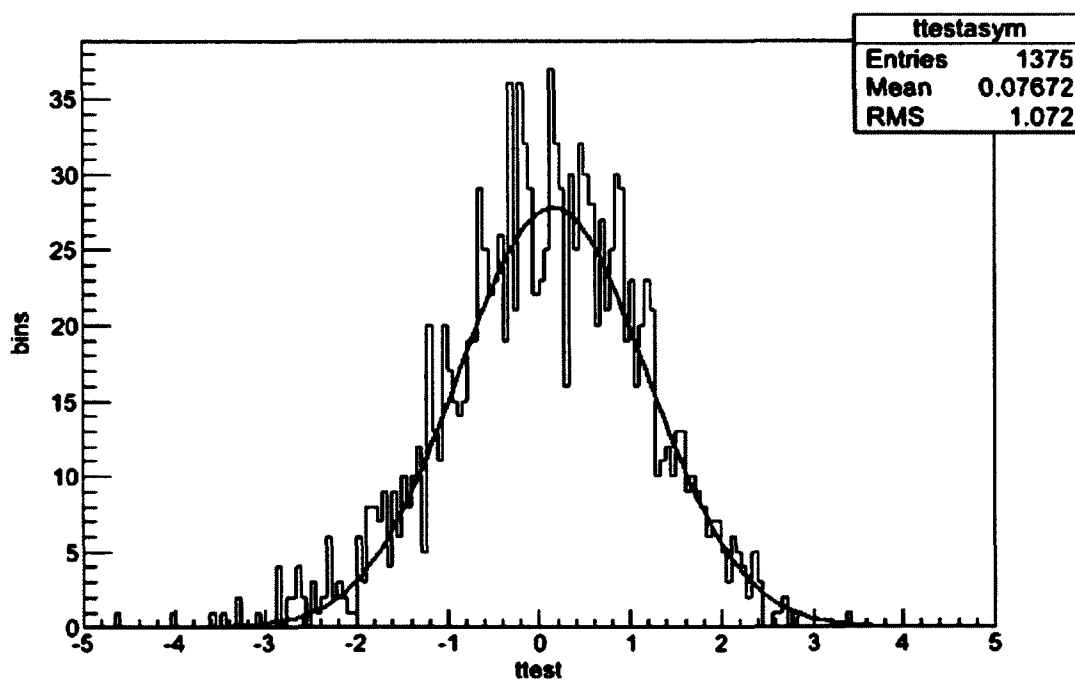
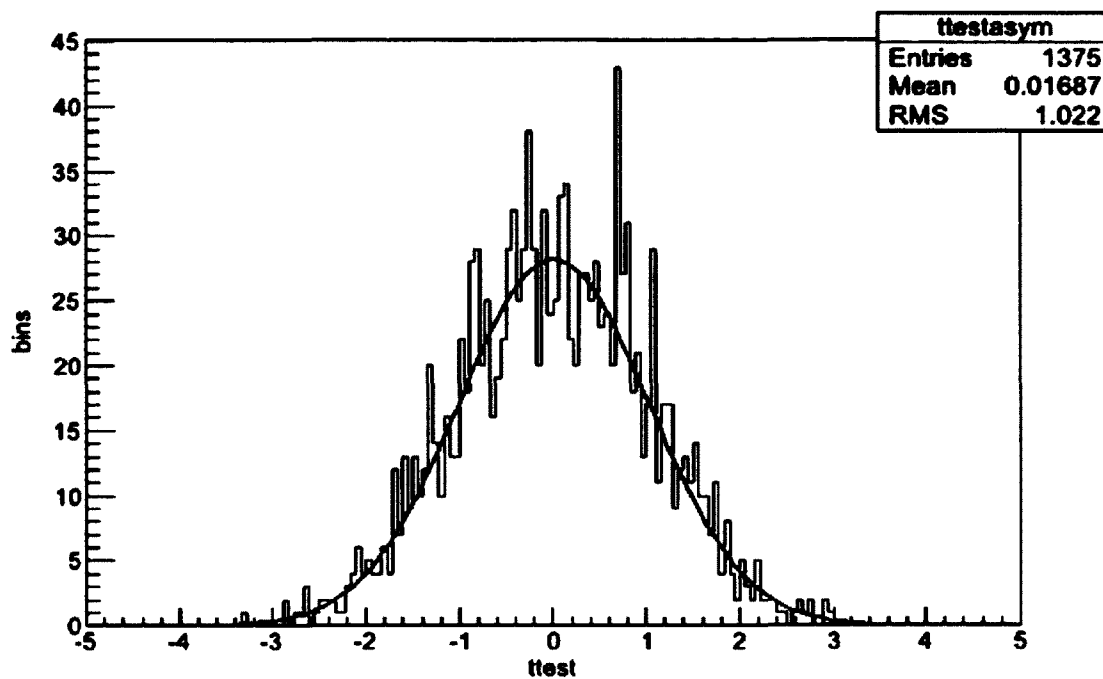


FIG. 45 T-test comparison for $n(e,e'\pi^-)p$ and $d(e,e'\pi^-)p$ for $A_{e\ell}$ (top) and A_ℓ (bottom) for 2.5 GeV negative torus polarization data.

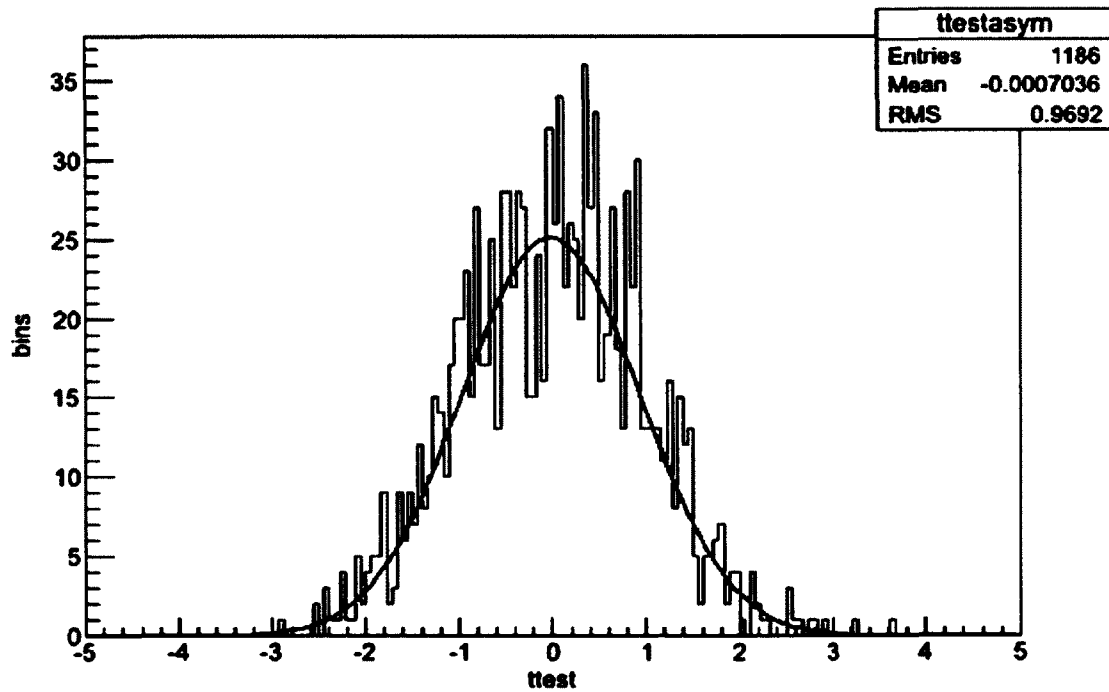
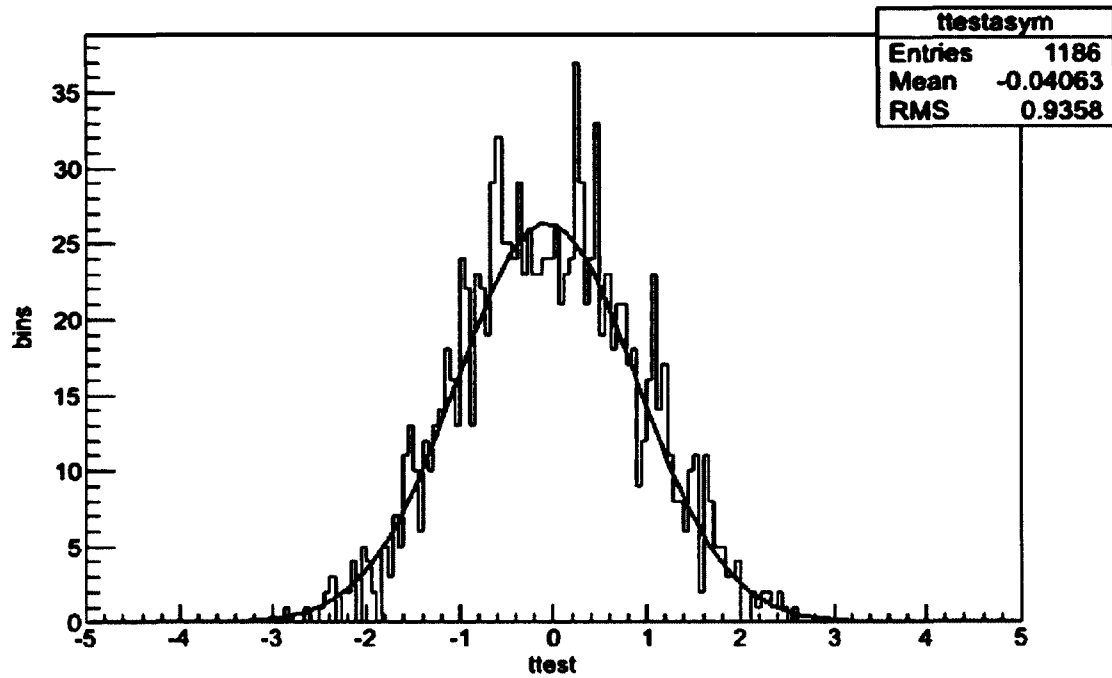


FIG. 46 T-test comparison for $n(e,e'\pi^-)p$ and $d(e,e'\pi^-)p$ for A_{et} (top) and A_t (bottom) for 4.2 GeV positive torus polarization data.

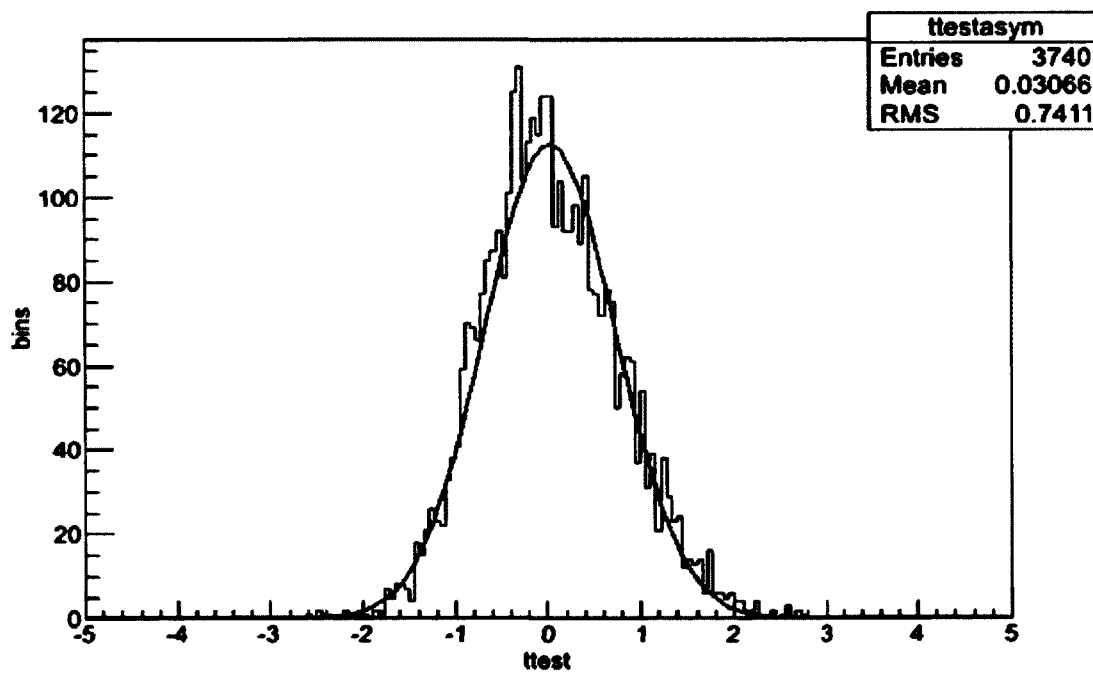
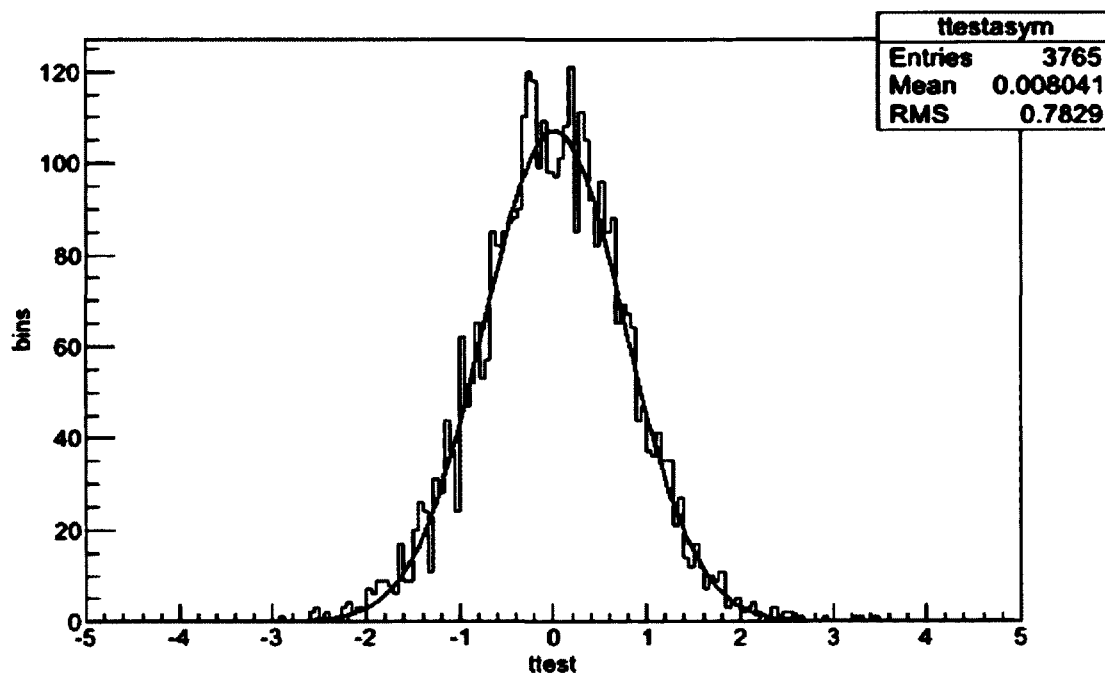


FIG. 47 T-test comparison for $n(e,e'\pi^-)p$ and $d(e,e'\pi^-)p$ for A_{et} (top) and A_t (bottom) for 4.2 GeV negative torus polarization data.

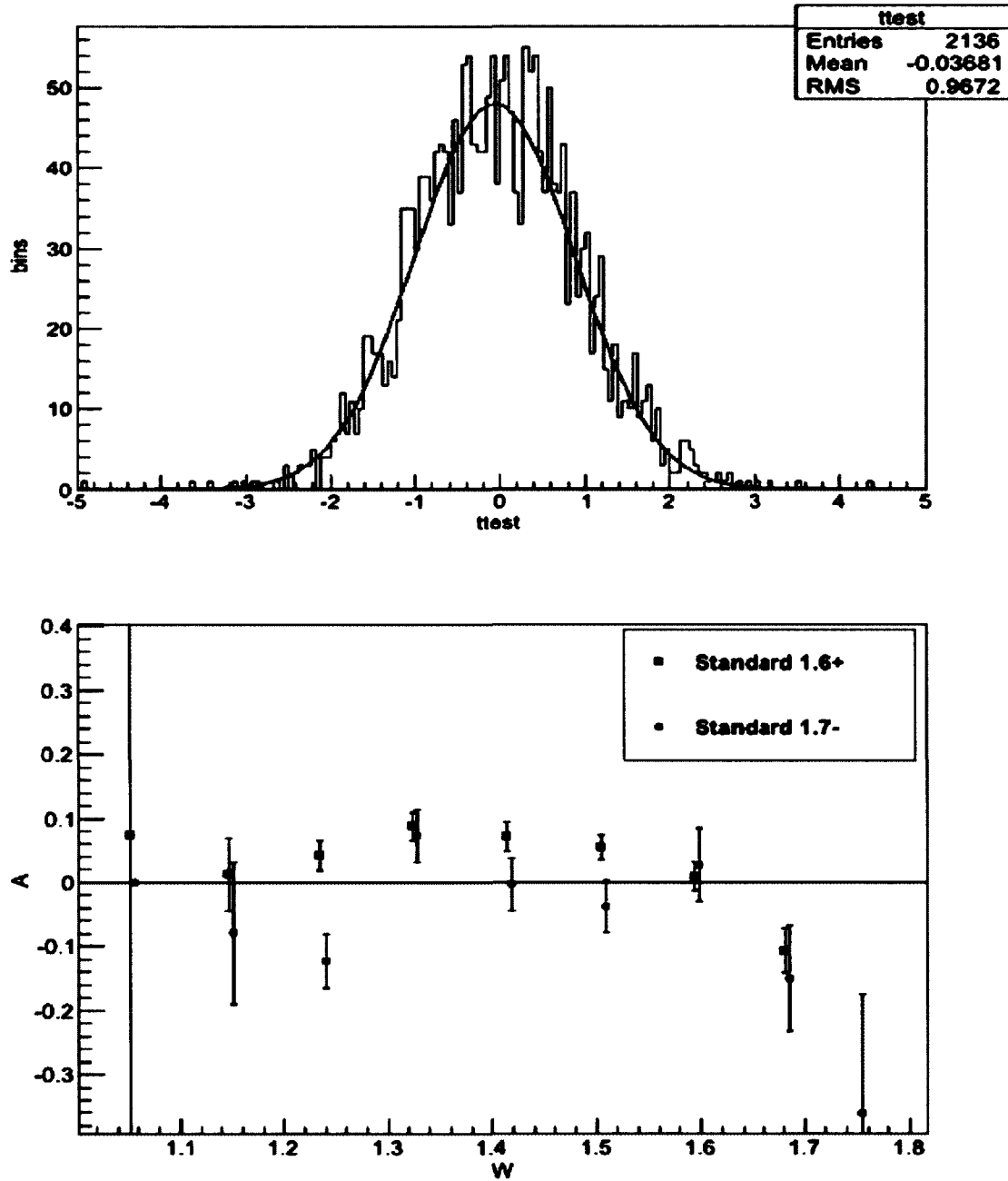


FIG. 48 T-test comparison of inbending 1.6 GeV data to outbending 1.7 GeV data (top) and a comparison of A_{et} as a function of W integrated over Q^2 , $\cos(\theta^*)$, and ϕ^* for each case (bottom). The red circles are inbending data and the blue squares are outbending data. Only bins that are in both contribute to both plots.

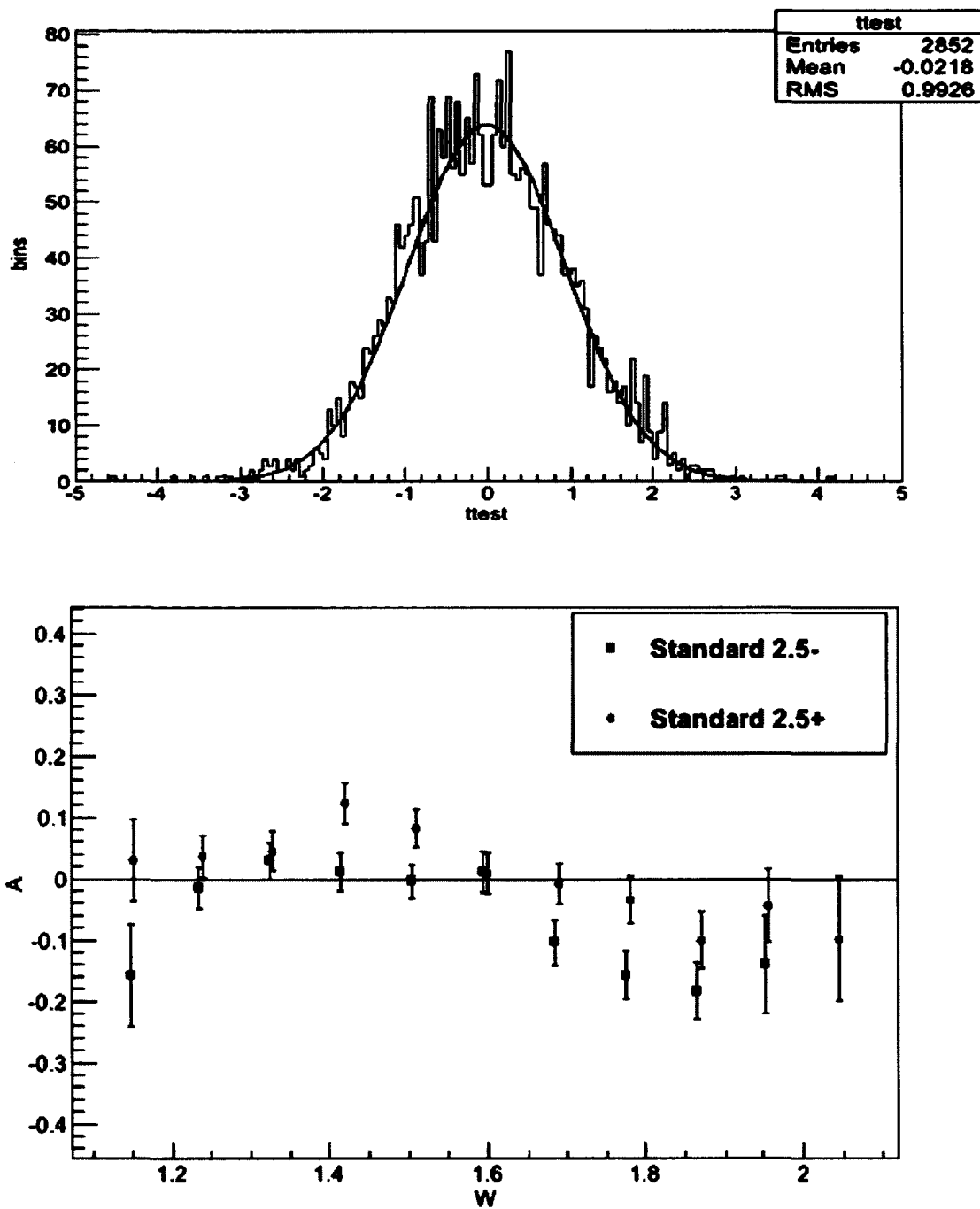


FIG. 49 T-test comparison of inbending 2.5 GeV data to outbending 2.5 GeV data (top) and a comparison of A_{et} as a function of W integrated over Q^2 , $\cos(\theta^*)$, and ϕ^* for each case (bottom). The red circles are inbending data and the blue squares are outbending data. Only bins that are in both contribute to both plots.

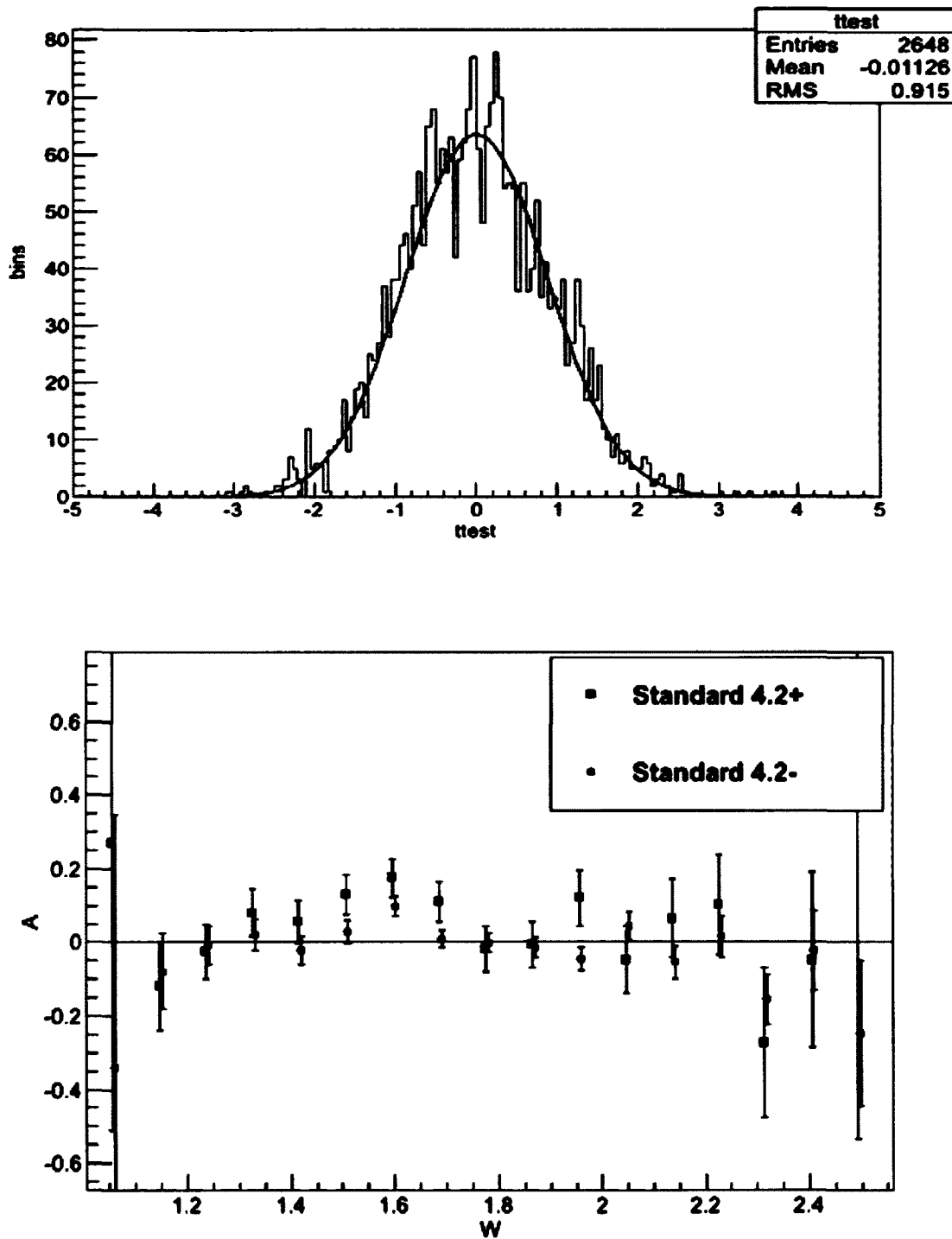


FIG. 50 T-test comparison of inbending 4.2 GeV data to outbending 4.2 GeV data (top) and a comparison of A_{et} as a function of W integrated over Q^2 , $\cos(\theta^*)$, and ϕ^* for each case (bottom). The red circles are inbending data and the blue squares are outbending data. Only bins that are in both contribute to both plots.

5.2.3 Determining the Ratio of Target Thickness R_r

To extract the single and double spin asymmetries, the ratio of target thicknesses for positive and negative target polarization is required (see Equations 168 – 170). The target spin asymmetry is particularly sensitive to this ratio. The target thickness ratio was determined from the Faraday Cup normalized inclusive electron events for positive and negative polarization data:

$$R_r = \frac{ND_3^+}{ND_3^-}, \quad (185)$$

with the charged normalized counts for each target type.

5.3 THE BEAM SPIN ASYMMETRY

Although the main focus of this analysis is to determine the target spin and double spin asymmetries, the beam spin asymmetry was extracted as well. Because there is no requirement for any target polarization, even the unpolarized nuclear targets (^{15}N , ^{14}He , foils) will contribute to the beam spin asymmetry. Therefore our extracted result is not attributable solely to the deuteron. Therefore a detailed analysis of A_e has not been done, but the beam spin asymmetry was extracted as an analysis check. As shown in Equation 27 the differential cross-section σ_e is dependent on a single response function R_{LT} which has a $\sin(\phi^*)$ dependence, so the measured beam spin asymmetry should have this simple $\sin(\phi^*)$ dependence. Fig. 51 shows a plot of A_e as a function of ϕ^* which shows this $\sin(\phi^*)$ dependence; the shape of the distribution agrees well with MAID, although MAID underpredicts the size of the asymmetry. When integrated over ϕ^* , A_e as a function W averages to zero as expected (see Fig. 52).

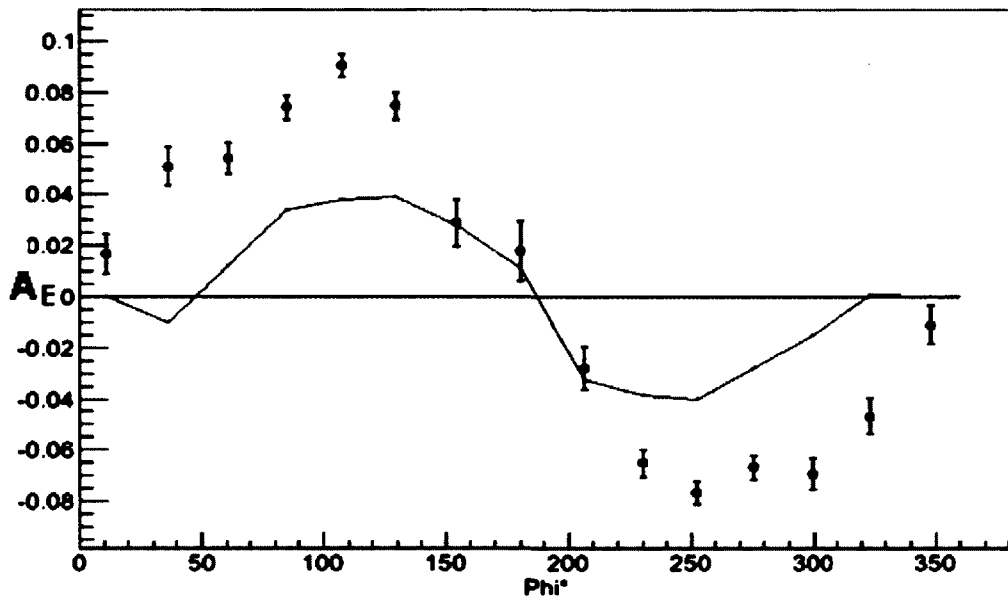


FIG. 51 A_E as a function of ϕ^* showing the expected $\sin(\phi^*)$ dependence for the 1.6 GeV data. The solid line is MAID.

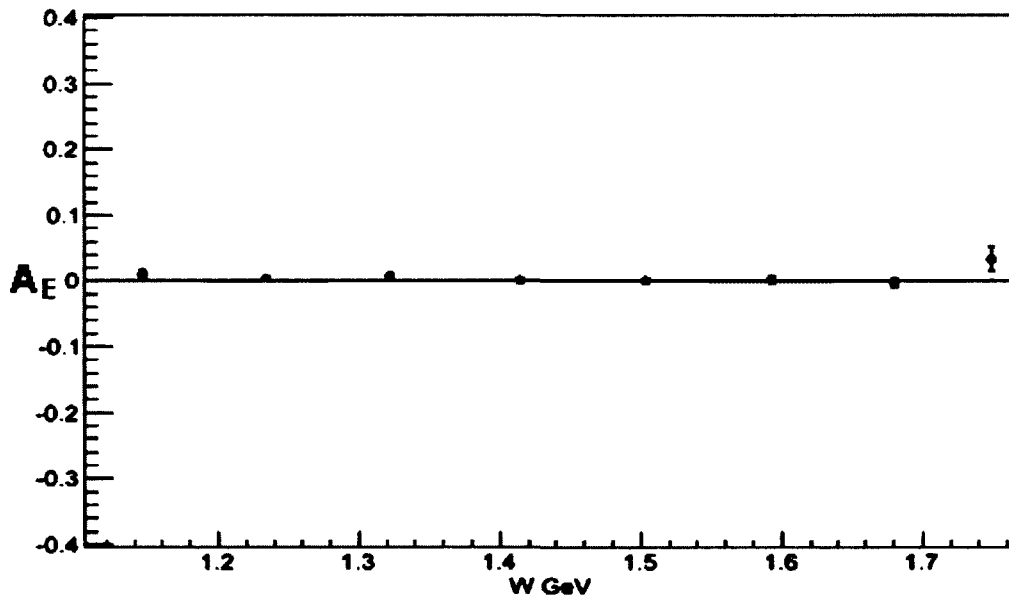


FIG. 52 A_E as a function of W integrated over Q^2 , $\cos(\theta^*)$ and ϕ^* for the 1.6 GeV data.

5.4 THE TARGET SPIN ASYMMETRY

The target spin asymmetry was extracted using Equation 169 in the four dimensional kinematic bins of W , Q^2 , $\cos\theta^*$, and ϕ^* . The target spin asymmetry has a more complex combination of response functions with different angular distributions. Like A_E , A_T has an anti-symmetric distribution in ϕ^* , and when integrated over ϕ^* , A_T as a function of the other three kinematic variables should average to zero. Fig. 53 shows A_T as a function of ϕ^* integrated over Q^2 and $\cos\theta^*$ for three regions of W . The asymmetries show an odd function of $\sin(\phi^*)$ and reasonable agreement with MAID. When integrated over ϕ^* , A_T as a function of W averages to zero. Finally, A_T as a function of ϕ^* for five $\cos(\theta^*)$ bins in three regions of W are shown in Figs. 54 – 56. Each plot represents an average over two $\cos(\theta^*)$ bins using Equation 183. The asymmetries are roughly consistent with the MAID model in the second and third resonance region. However, in the delta resonance region we note significant discrepancies at forward and backwards θ^* .

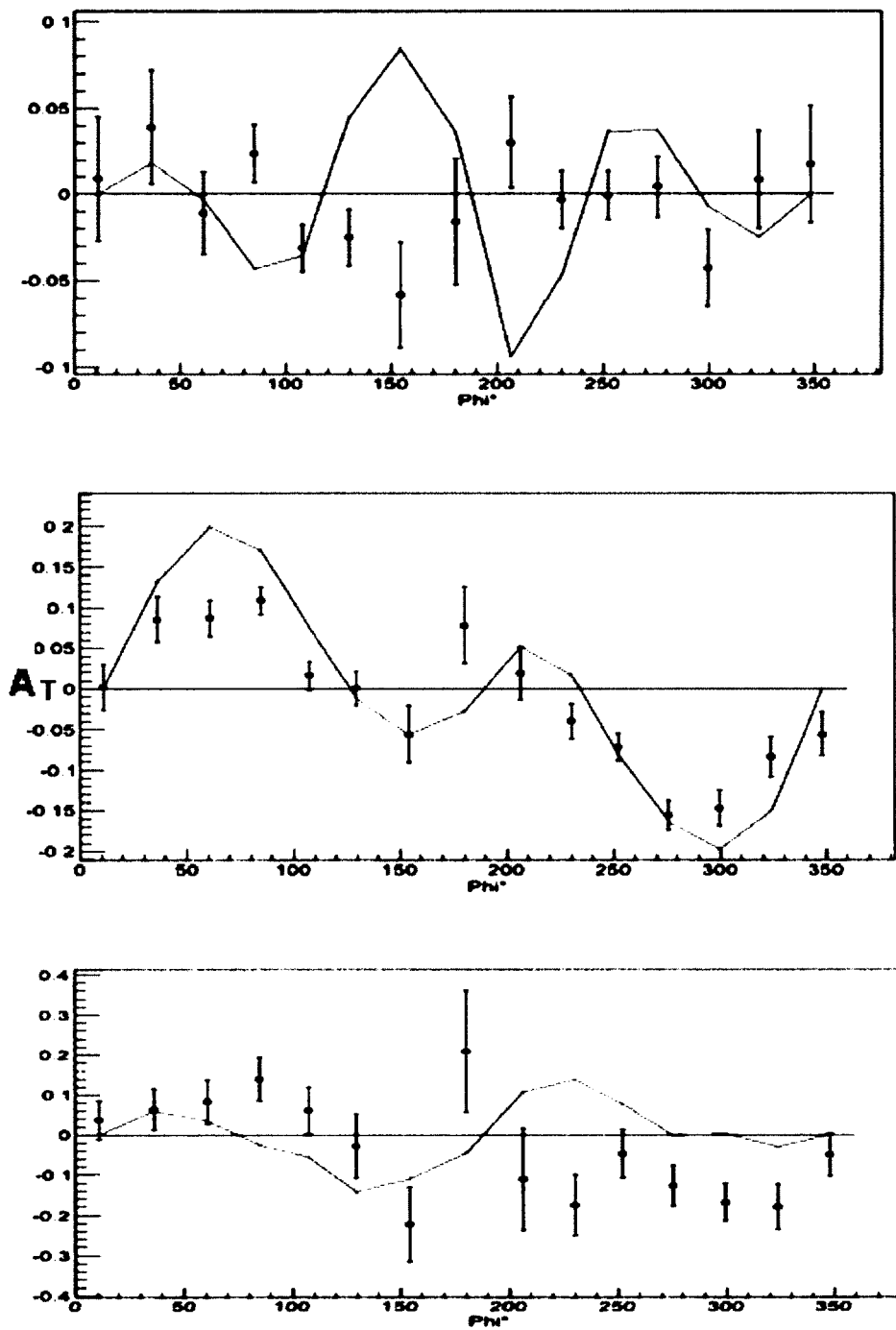


FIG. 53 A_T as a function of ϕ^* integrated over Q^2 , $\cos\theta^*$, and for W in the delta region (top), the S_{11} region (middle), and high W (bottom) for the 1.6 GeV data.

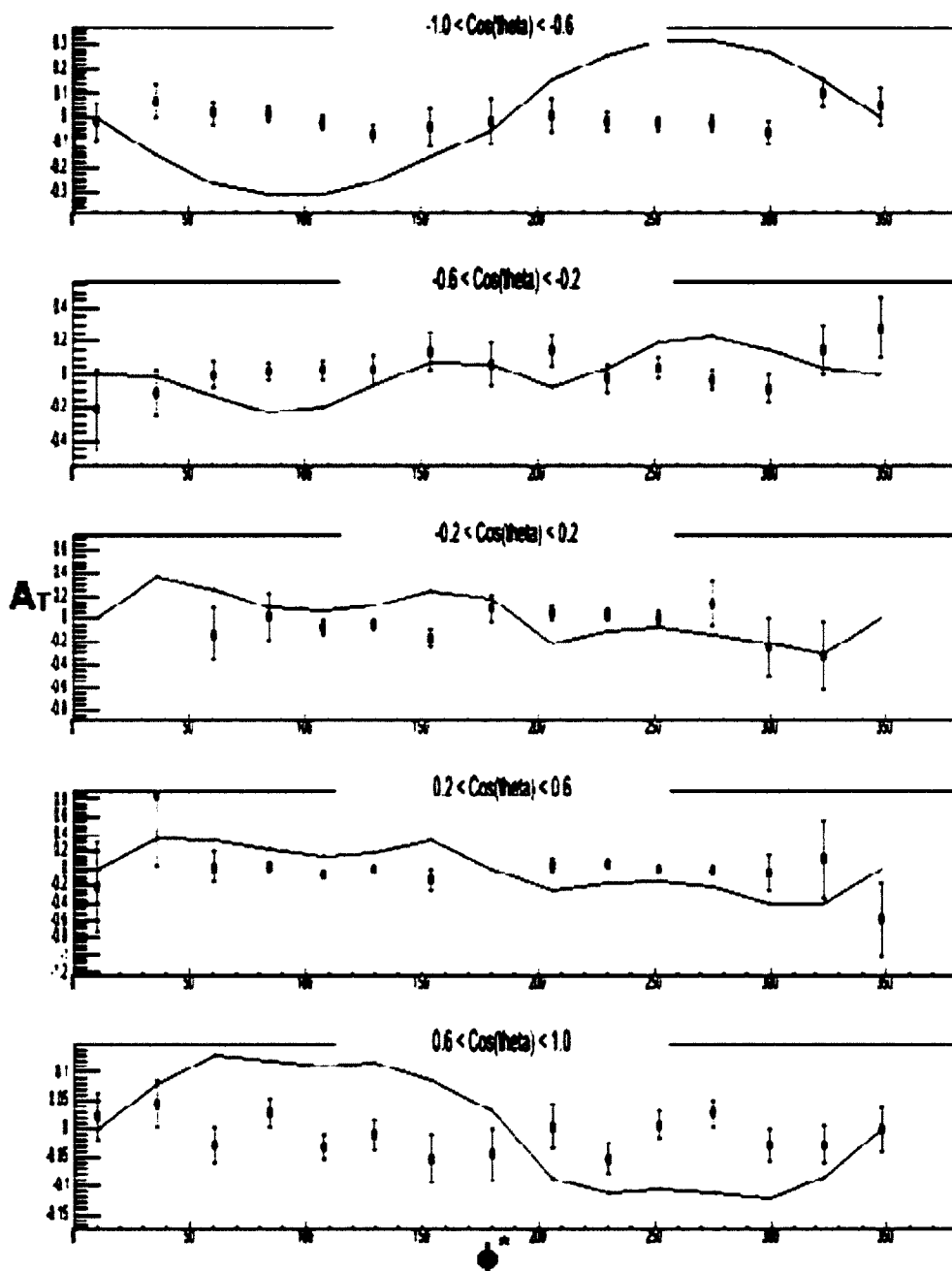


FIG. 54 A_T as a function of ϕ^* for five $\cos\theta^*$ bins in the delta region, $1.01 \text{ GeV} < W < 1.37 \text{ GeV}$ for 1.6 GeV data.

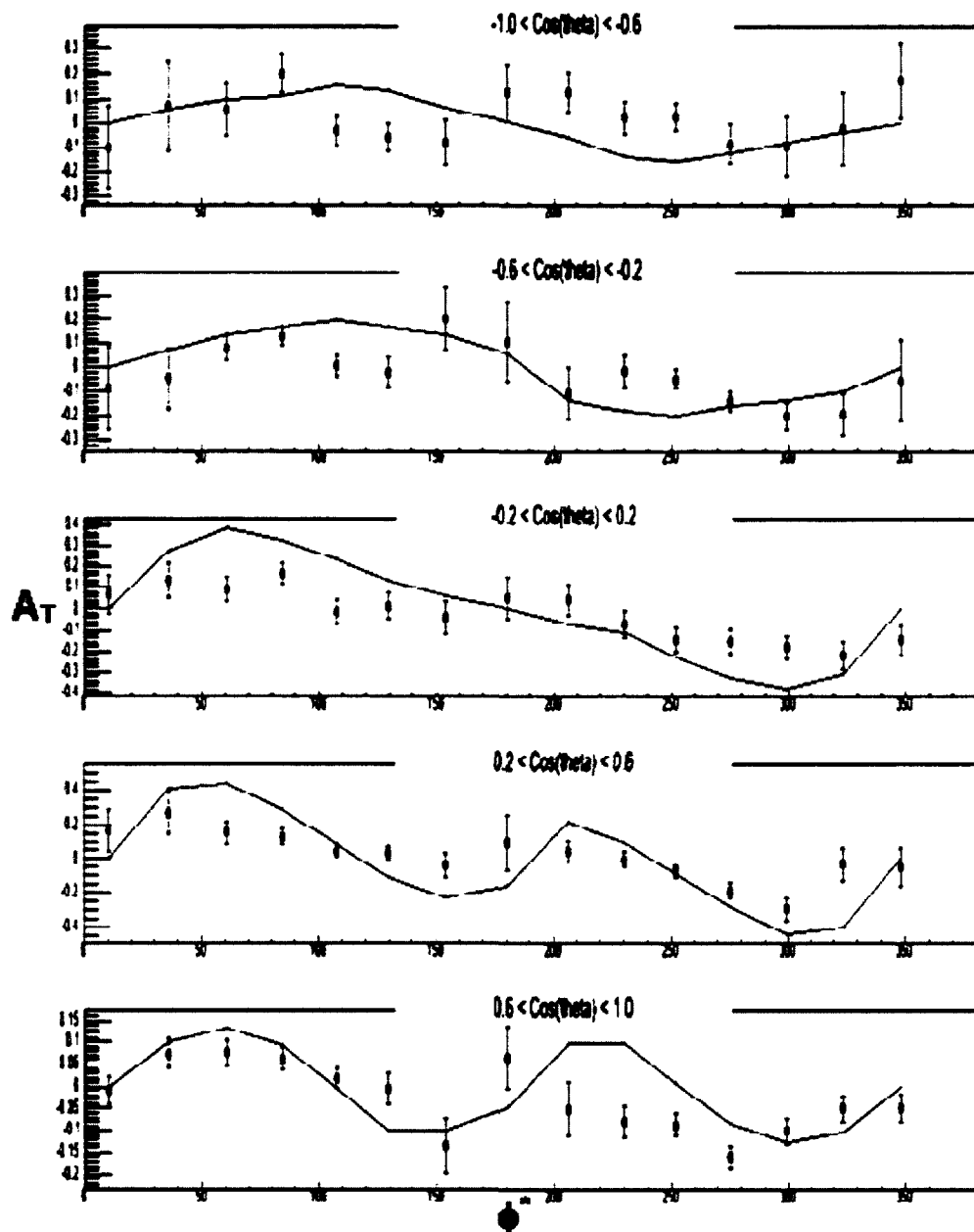


FIG. 55 A_T as a function of ϕ^* for five $\cos\theta^*$ bins in the S_{II} region, $1.37 \text{ GeV} < W < 1.55 \text{ GeV}$ for 1.6 GeV data.

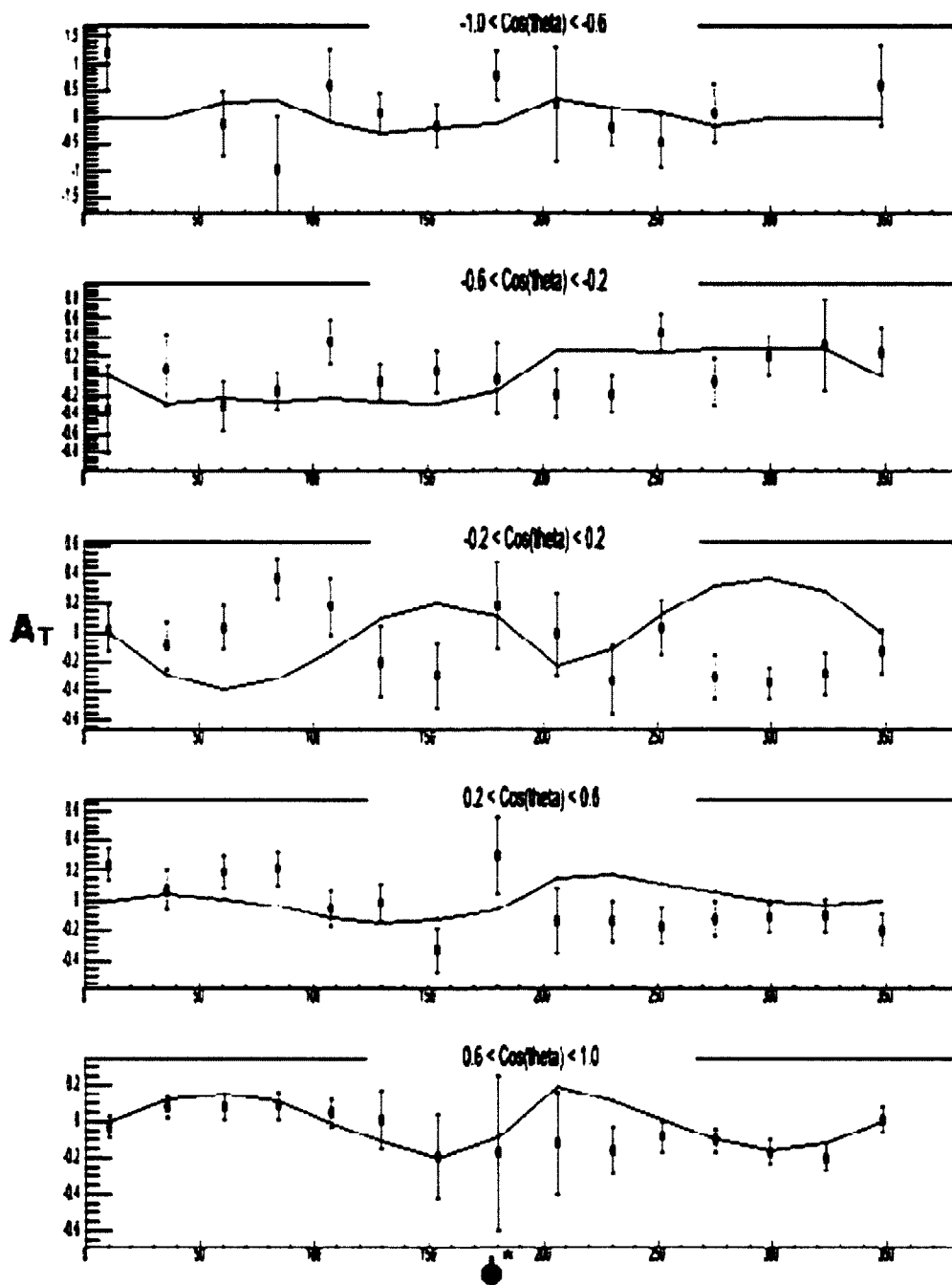


FIG. 56 A_T as a function of ϕ^* for five $\cos\theta^*$ bins at high W , $1.64 \text{ GeV} < W < 1.73 \text{ GeV}$ for 1.6 GeV data.

5.5 THE DOUBLE SPIN ASYMMETRY

The double spin asymmetry was extracted in each of the four dimensional kinematic bins of W , $Q^2 \cos\theta^*$ and ϕ^* using Equation 168. The double spin asymmetry has an even more complex combination of response functions with different angular distributions than the target spin asymmetry. Unlike A_E , and A_T , which have an anti-symmetric distribution in ϕ^* , A_{ET} has a symmetric distribution in ϕ^* ; when integrated over ϕ^* , A_{ET} as a function of the other three kinematic variables is non-zero. Fig. 57 shows the structure of A_{et} as a function of W for all three beam energies when integrated over the other three kinematic variables. Figs. 58 through 60 show A_{ET} as a function of W for increasing Q^2 for each energy. Clearly the MAID model agrees best with the data at low W , which is not surprising because multi-pion channels open up at high W that MAID does not include in its prediction. Figs. 61 – 69 show A_{ET} as a function of ϕ^* for five $\cos(\theta^*)$ bins (each one averaged over two bins) and two Q^2 bins for each of the three resonance regions. There is good agreement with MAID in the delta region, even at forward angles, but in the S_{11} region there are significant discrepancies in the bins which have sufficient statistical precision to do a comparison. In most kinematic regions, there is good agreement between the data and MAID.

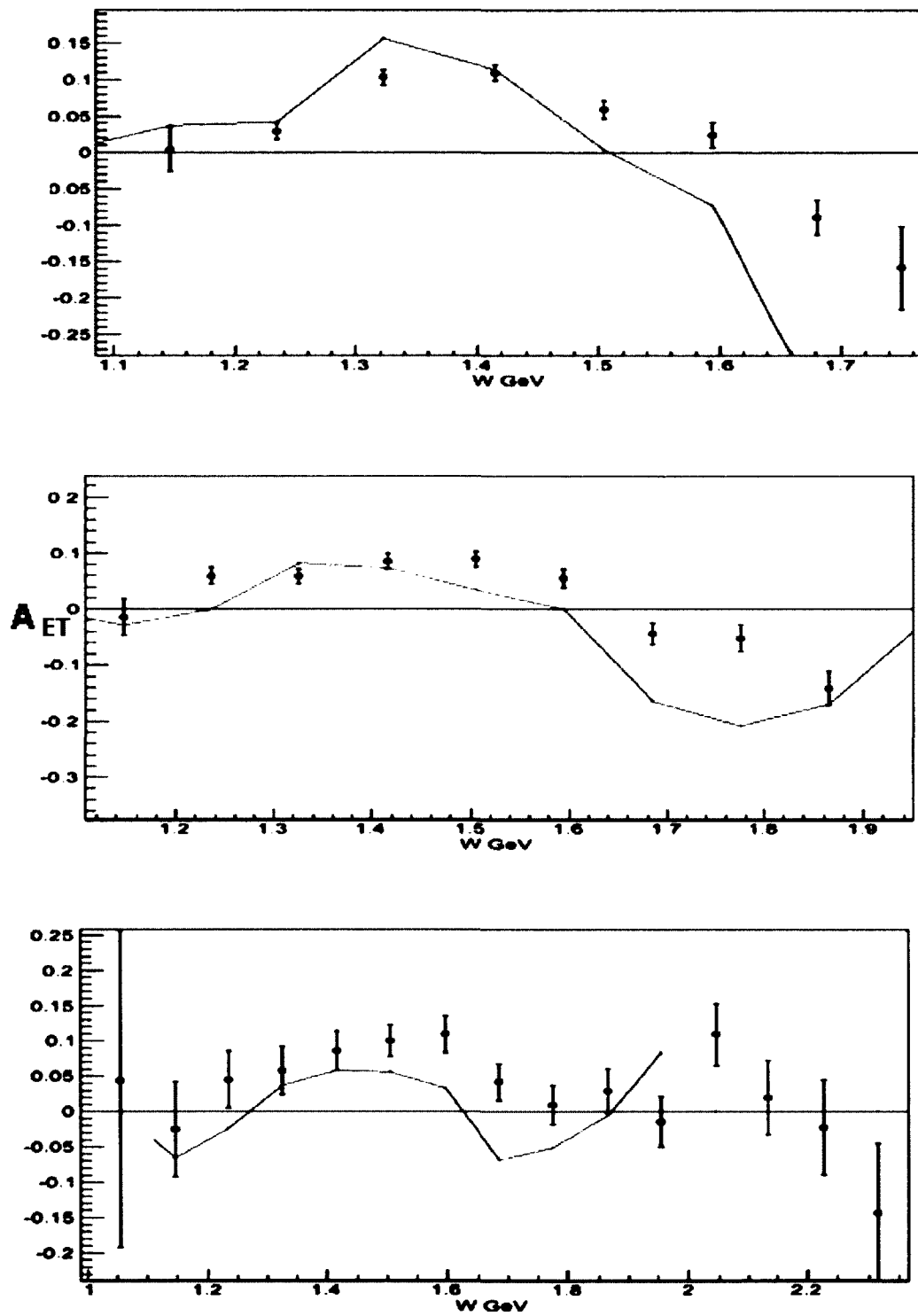


FIG. 57 A_{E1} as a function of W integrated over ϕ^* , $\cos\theta^*$, and Q^2 for 1.6 GeV (top), 2.5 GeV (middle) and 4.2 GeV (bottom). The MAID model, shown in the solid line, is valid up to 2 GeV.

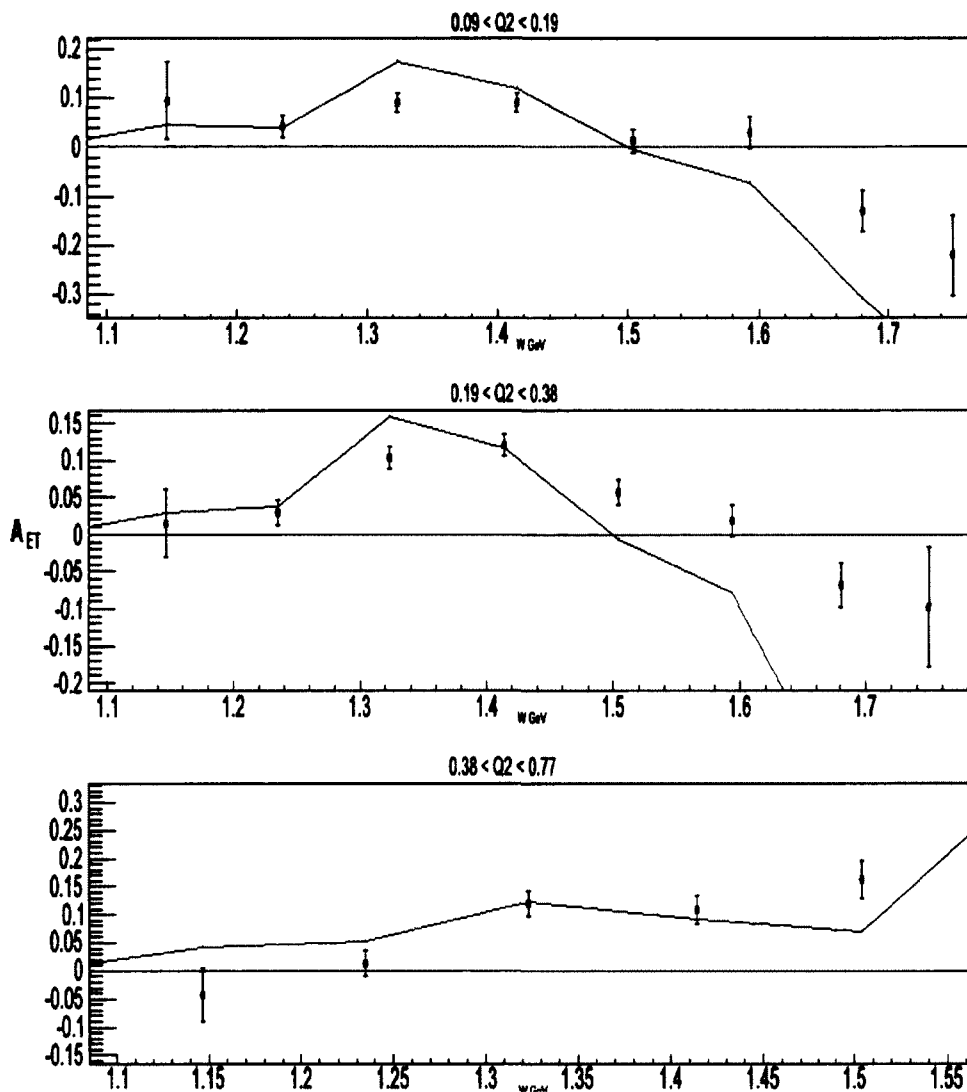


FIG. 58 A_{ET} as a function of W for three Q^2 bins integrated over $\cos\theta^*$ and ϕ^* for the 1.6 GeV data.

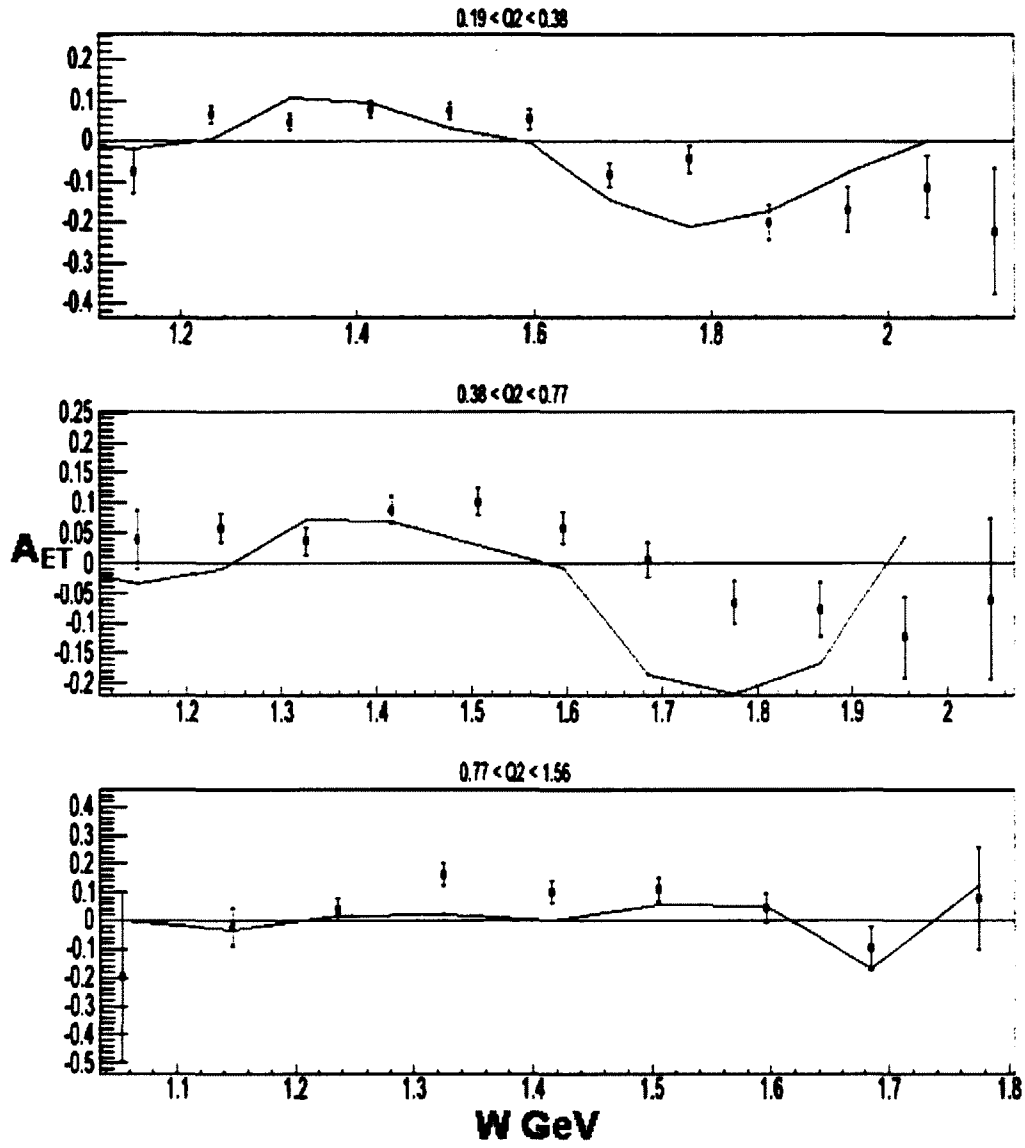


FIG. 59 A_{ET} as a function of W for three Q^2 bins integrated over $\cos\theta^*$ and ϕ^* for the 2.5 GeV data.

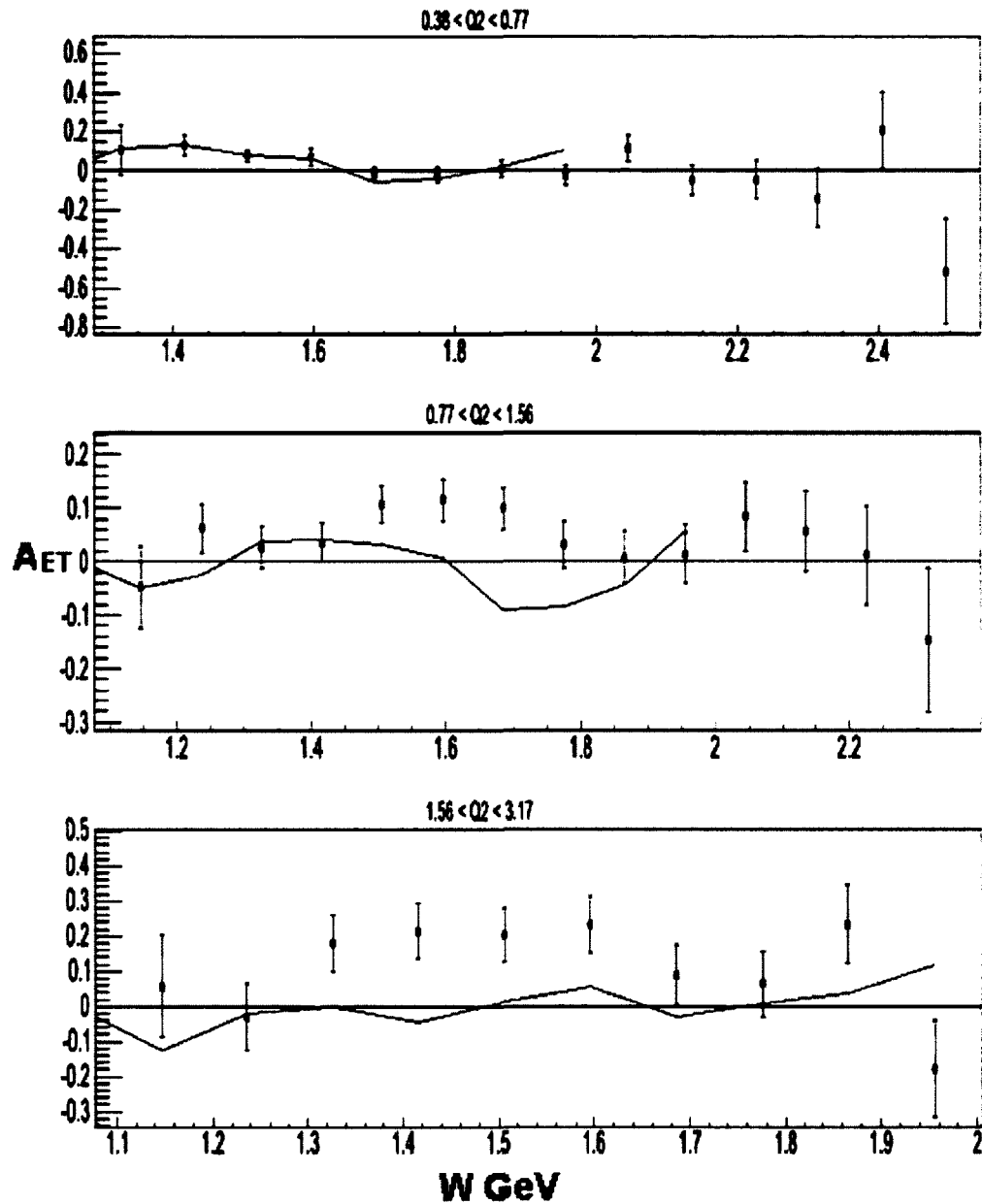


FIG. 60 A_{ET} as a function of W for three Q^2 bins integrated over $\cos\theta^*$ and ϕ^* for the 4.2 GeV data.

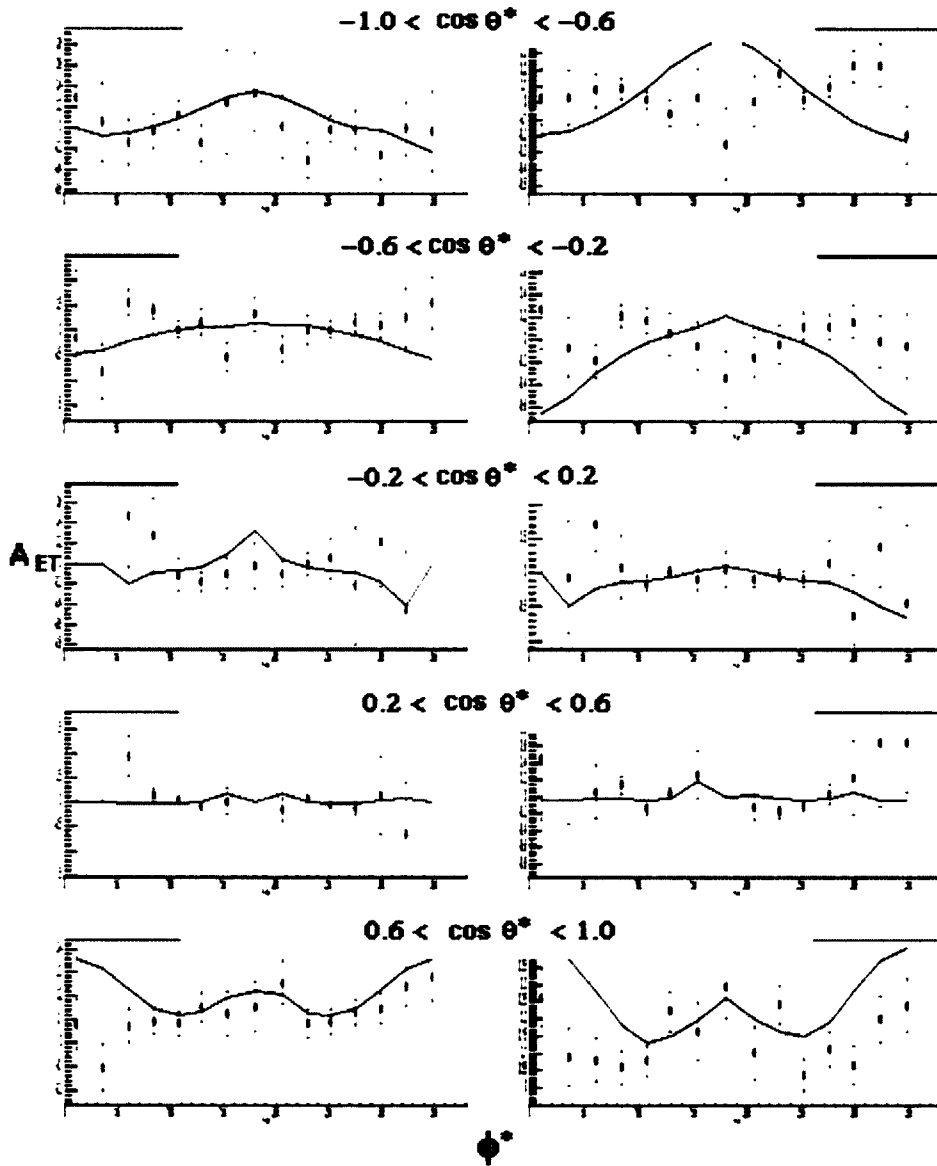


FIG. 61 A_{ET} as a function of ϕ^* for five $\cos \theta^*$ bins in two Q^2 bins, $0.09 < Q^2 < 0.19$ (left) and $0.19 < Q^2 < 0.38$ (right), in the delta region $1.01 < W < 1.37$ GeV for 1.6 GeV data.

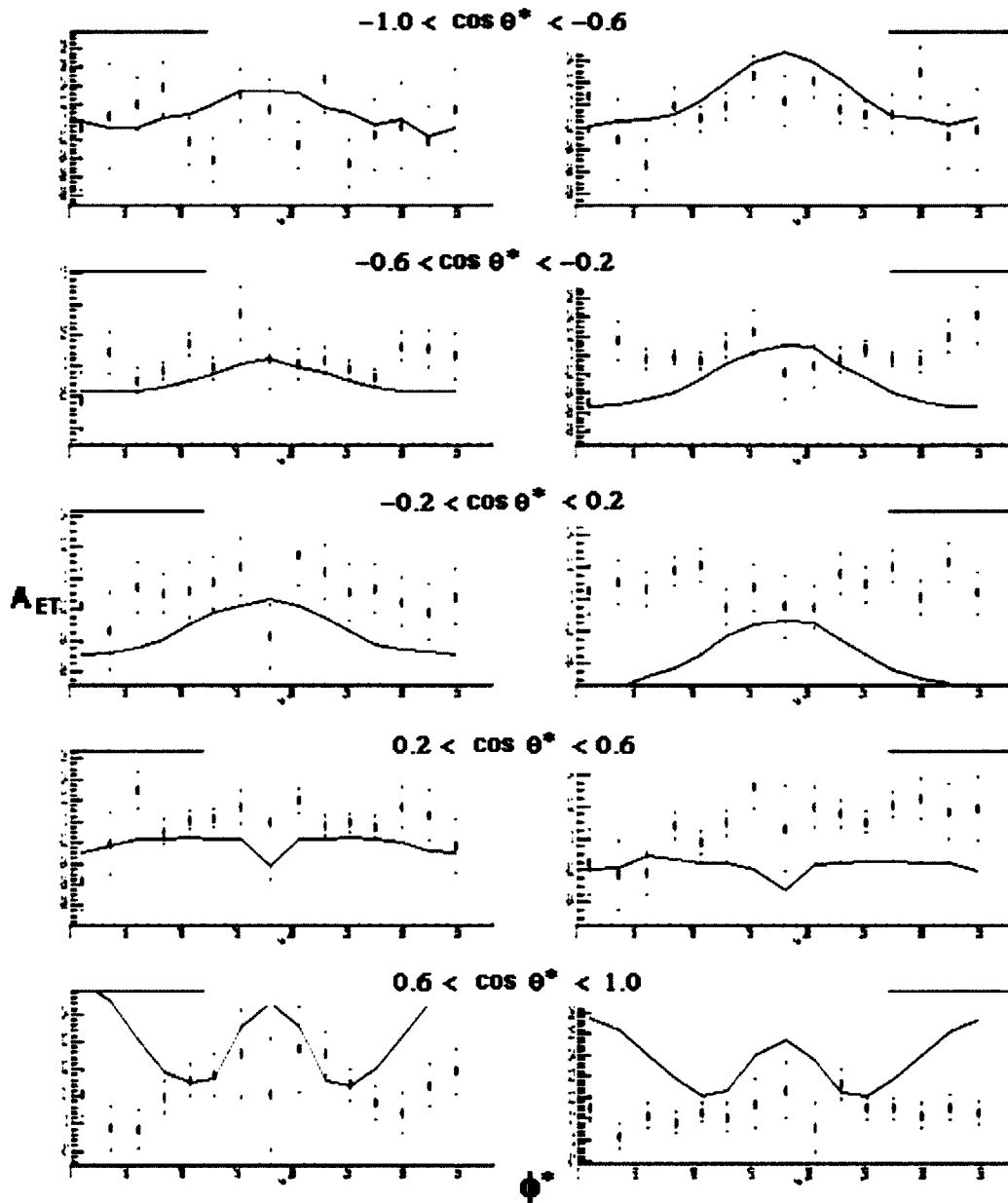


FIG. 62 A_{ET} as a function of ϕ^* for five $\cos\theta^*$ bins in two Q^2 bins, $0.09 < Q^2 < 0.19$ (left) and $0.19 < Q^2 < 0.38$ (right), in the S_{II} region $1.37 < W < 1.55$ GeV for 1.6 GeV data.

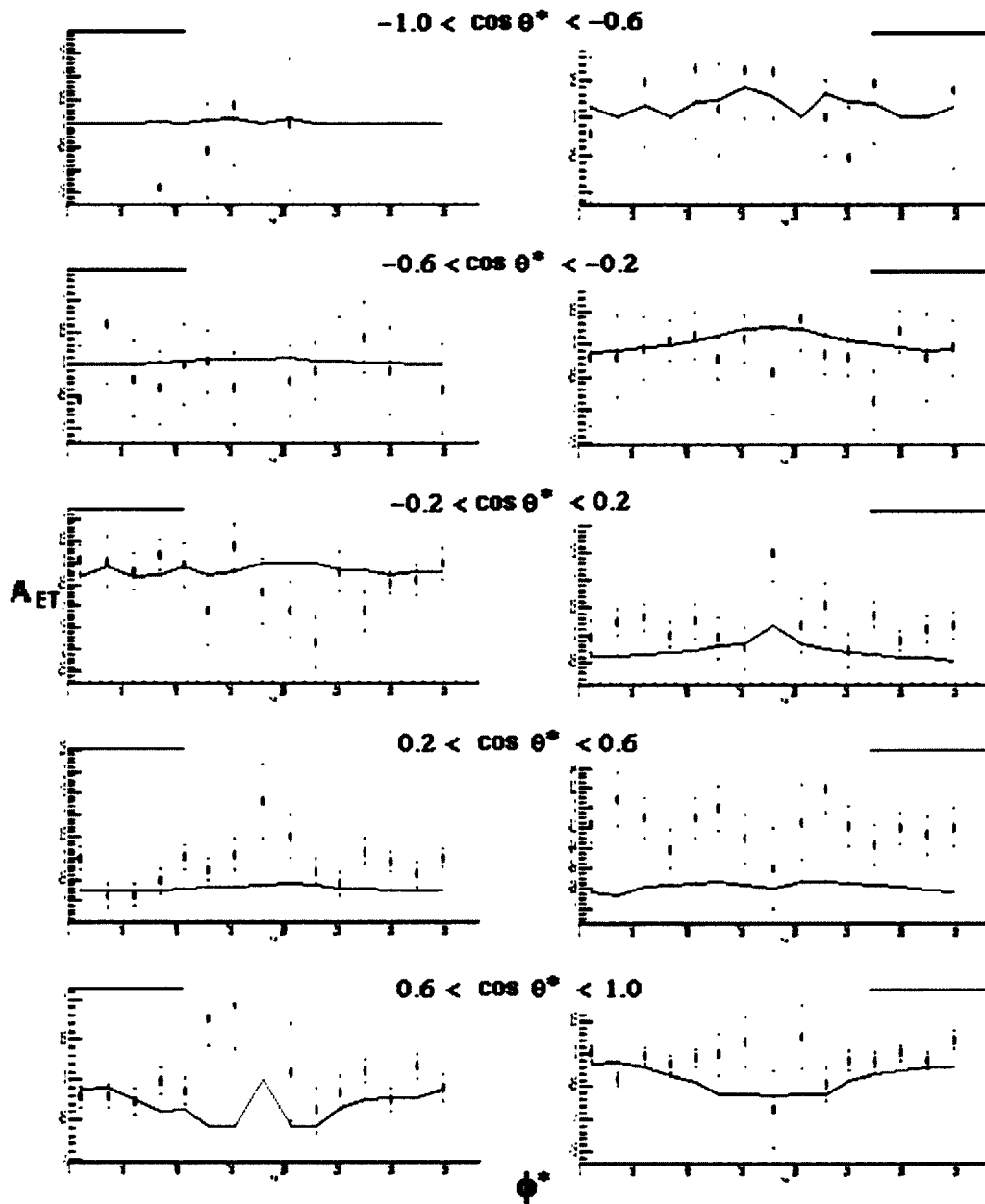


FIG. 63 A_{ET} as a function of ϕ^* for five $\cos \theta^*$ bins in two Q^2 bins, $0.09 < Q^2 < 0.19$ (left) and $0.19 < Q^2 < 0.38$ (right), in the high W region $1.64 < W < 1.82$ GeV for 1.6 GeV data.

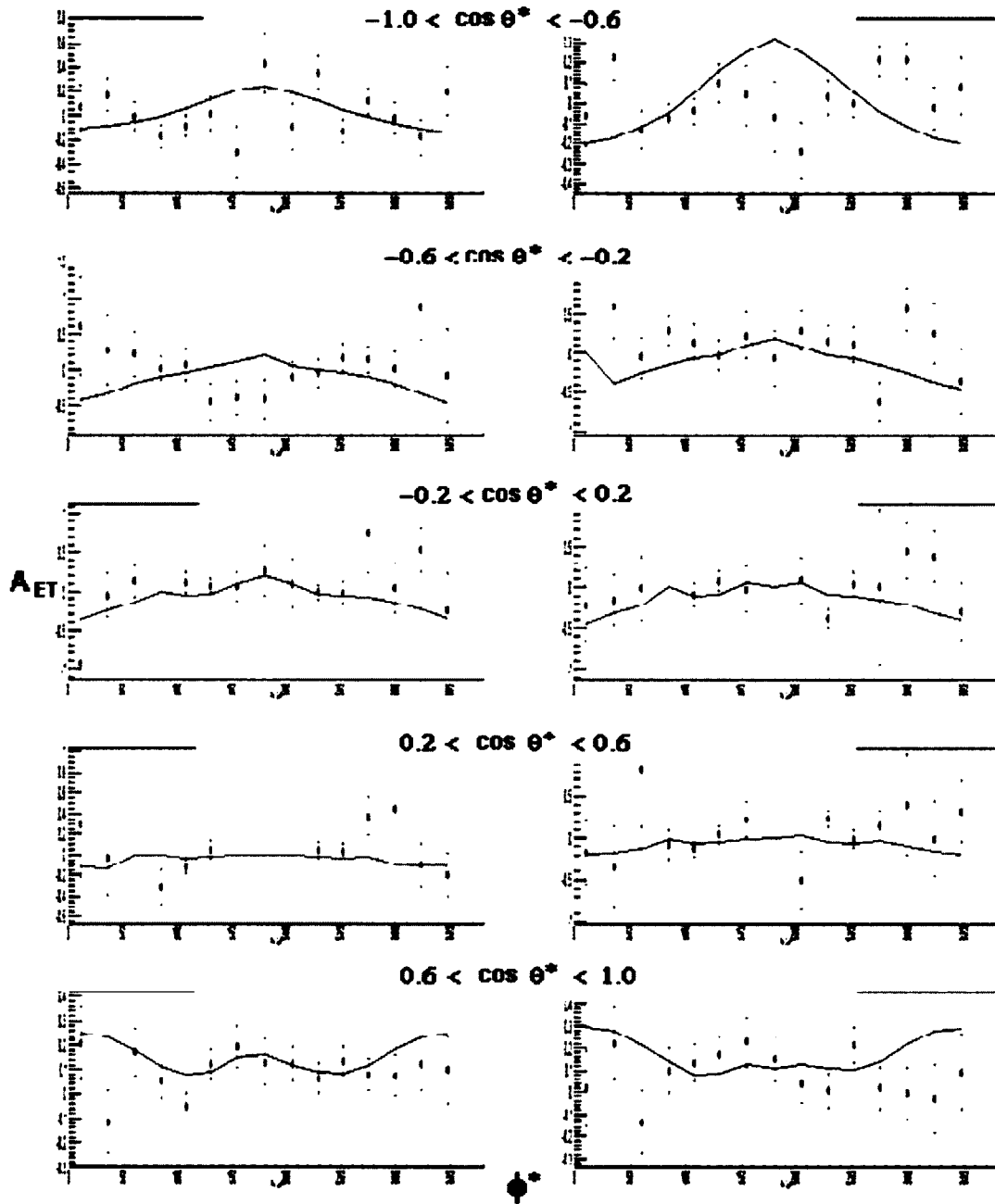


FIG. 64 A_{ET} as a function of ϕ^* for five $\cos \theta^*$ bins in two Q^2 bins, $0.19 < Q^2 < 0.38$ (left) and $0.38 < Q^2 < 0.77$ (right), in the delta region $1.01 < W < 1.37$ GeV for 2.5 GeV data.

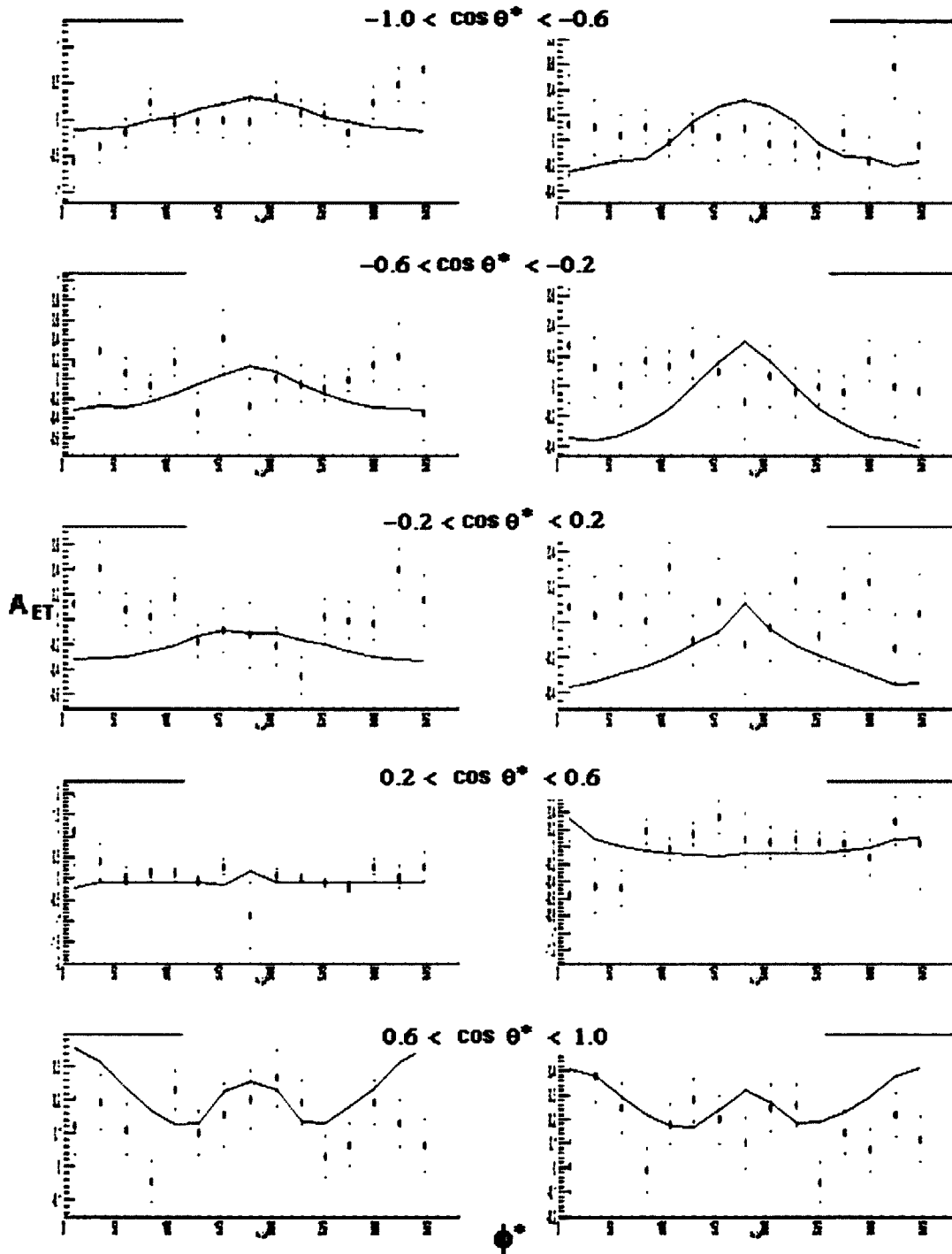


FIG. 65 A_{ET} as a function of ϕ^* for five $\cos \theta^*$ bins in two Q^2 bins, $0.19 < Q^2 < 0.38$ (left) and $0.38 < Q^2 < 0.77$ (right), in the S_{II} region $1.37 < W < 1.55$ GeV for 2.5 GeV data.

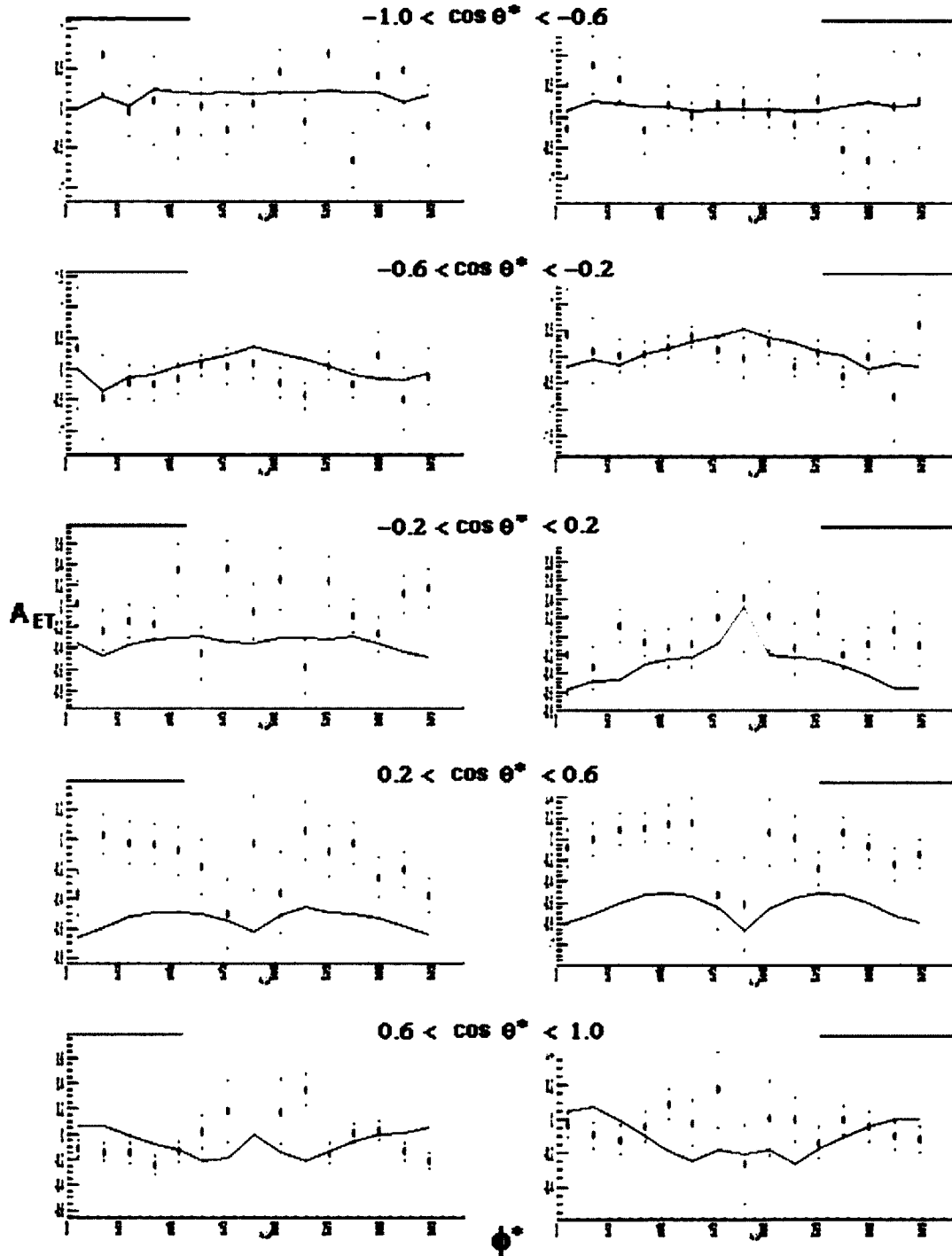


FIG. 66 A_{ET} as a function of ϕ^* for five $\cos\theta^*$ bins in two Q^2 bins, $0.19 < Q^2 < 0.38$ (left) and $0.38 < Q^2 < 0.77$ (right), in the high W region $1.64 < W < 2.0$ GeV for 2.5 GeV data.

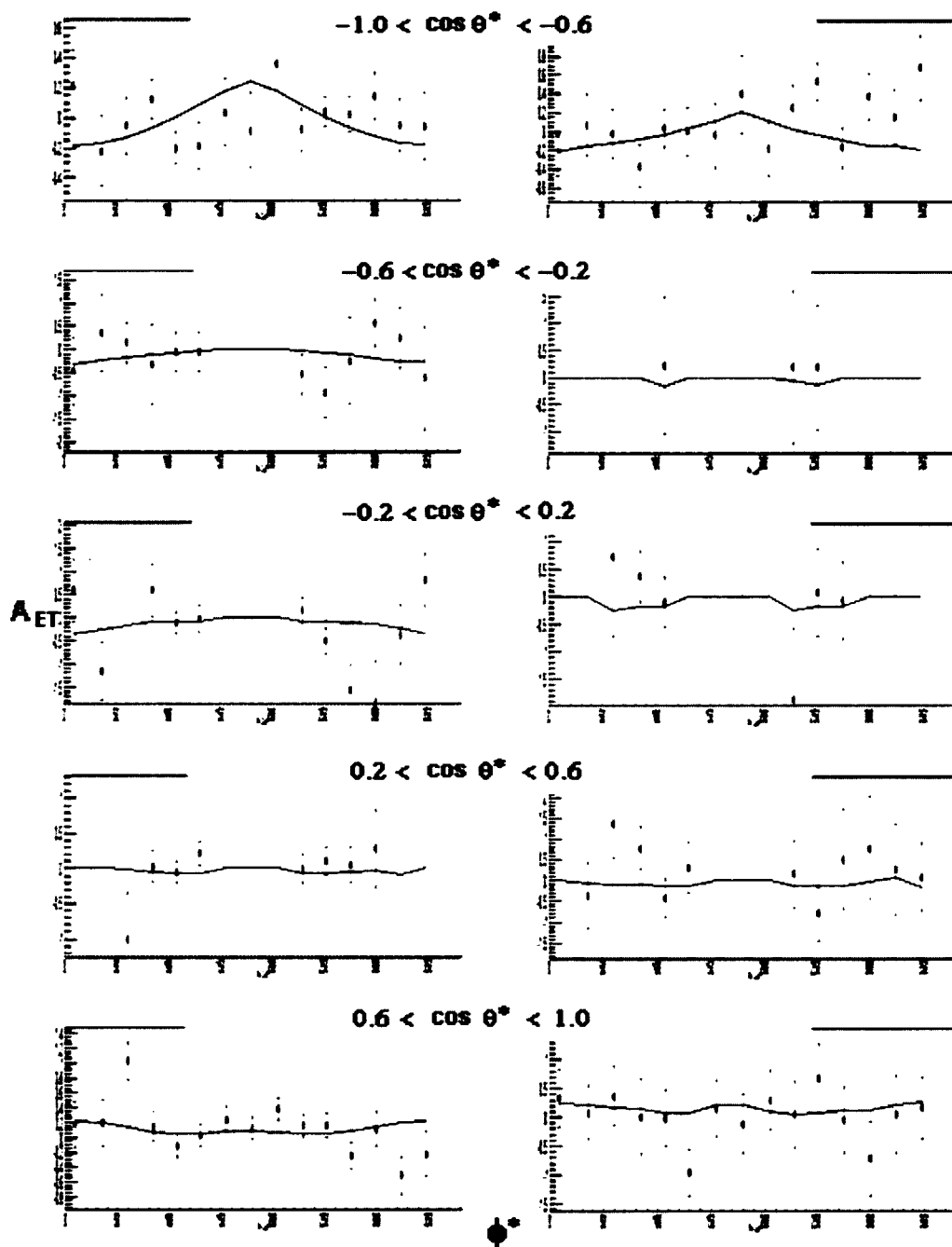


FIG. 67 A_{ET} as a function of ϕ^* for five $\cos\theta^*$ bins in two Q^2 bins, $0.77 < Q^2 < 1.56$ (left) and $1.56 < Q^2 < 3.17$ (right), in the delta region $1.01 < W < 1.37$ GeV for 4.2 GeV data.

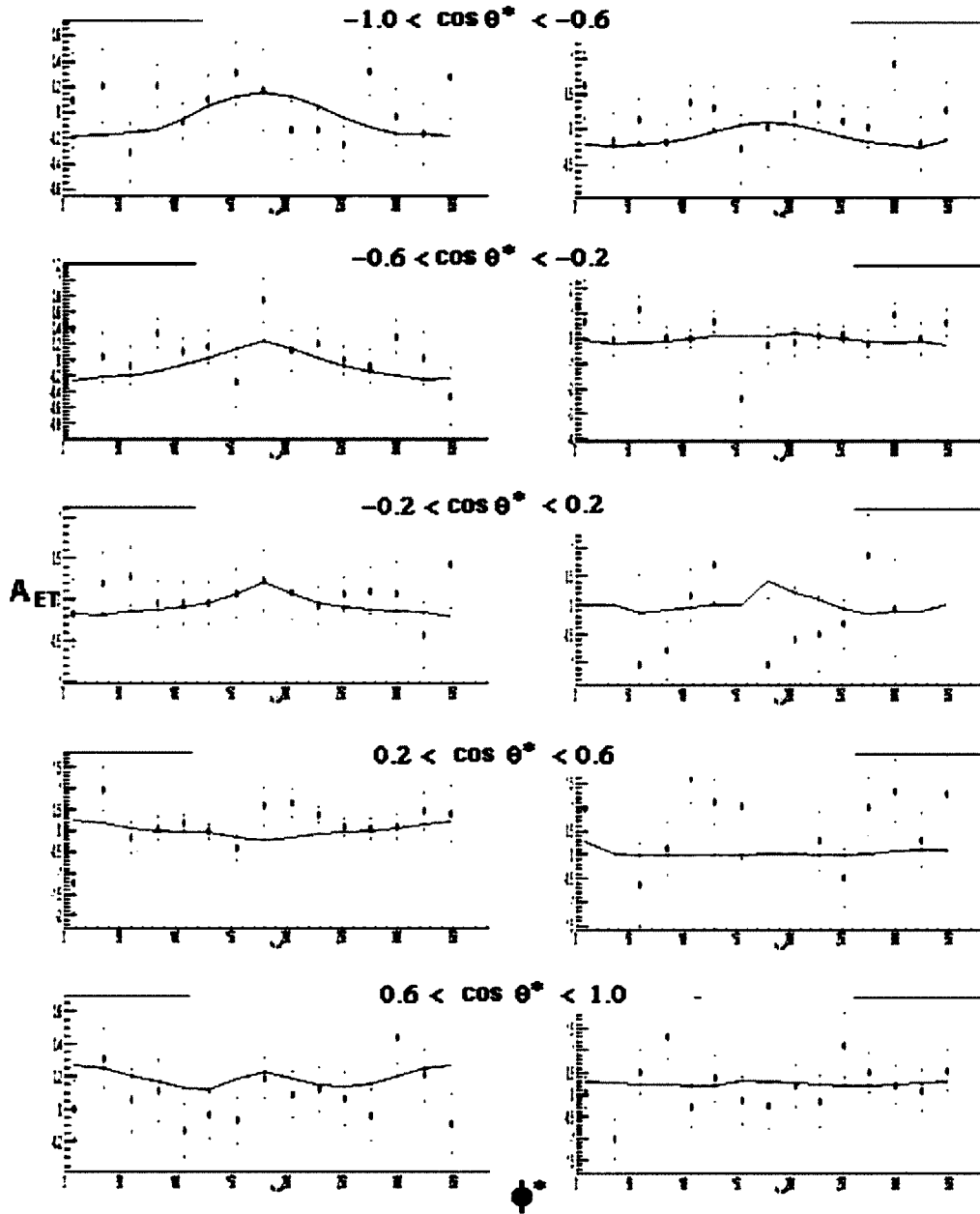


FIG. 68 A_{ET} as a function of ϕ^* for 2 five $\cos \theta^*$ bins in two Q^2 bins, $0.77 < Q^2 < 1.56$ (left) and $1.56 < Q^2 < 3.17$ (right), in the S_{II} region $1.37 < W < 1.55$ GeV for 4.2 GeV data.

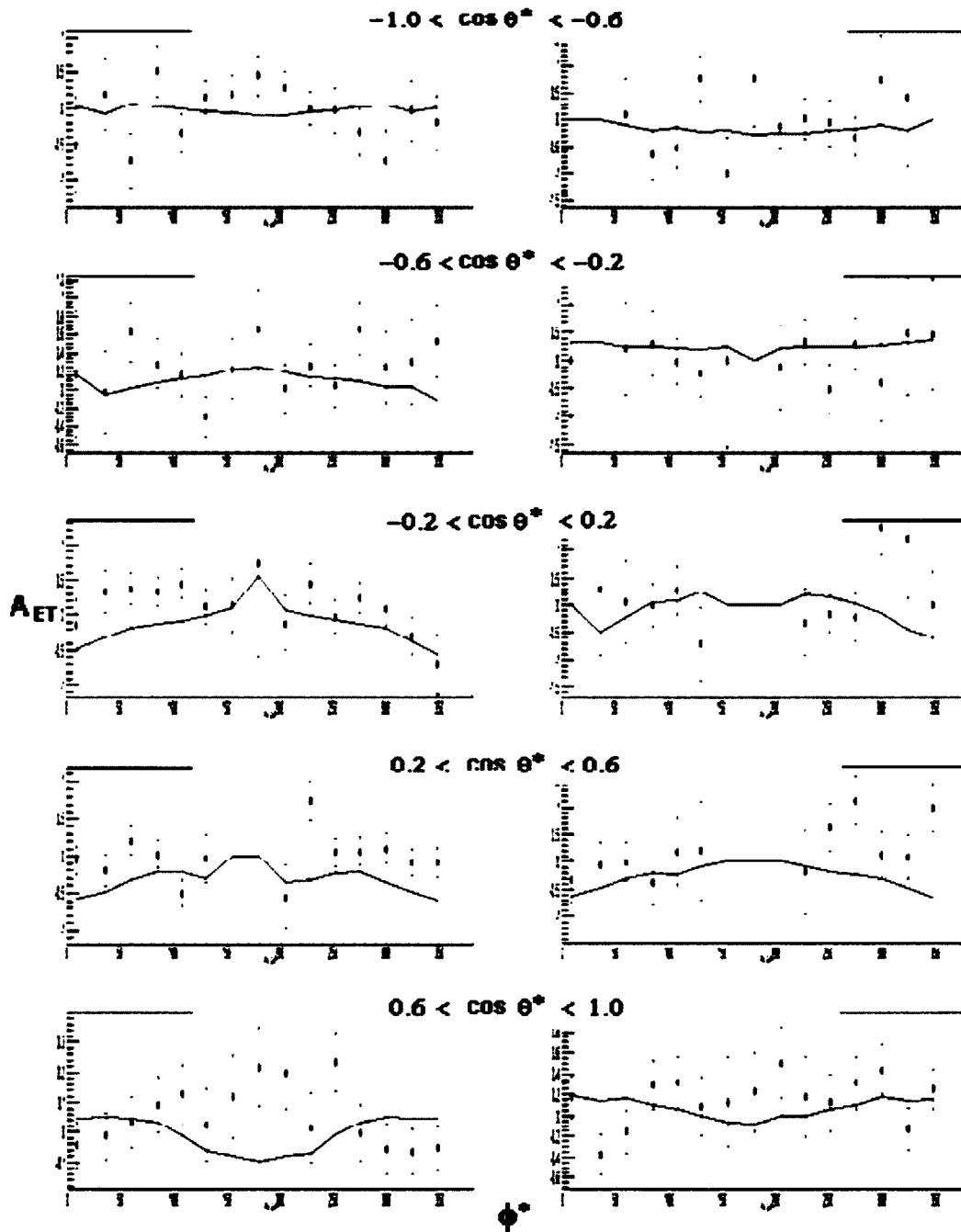


FIG. 69 A_{ET} as a function of ϕ^* for five $\cos \theta^*$ bins in two Q^2 bins, $0.77 < Q^2 < 1.56$ (left) and $1.56 < Q^2 < 3.17$ (right), in the high W region $1.64 < W < 2.9$ GeV for 4.2 GeV data.

5.6 CORRECTIONS TO ASYMMETRIES

In Chapter 4 the procedure for subtracting the nitrogen background was described in detail as well as the determination of pion contamination and beam and target polarization. Here we describe two additional issues that might affect our asymmetries.

5.6.1 Acceptance Correction

In calculating cross sections it is important to know the acceptance of CLAS. Because the asymmetry is a ratio of cross sections, the acceptance ideally cancels out in the ratio. However, because the ϕ^* dependence of the numerator and denominator in the asymmetry are different, gaps in the ϕ^* coverage can affect the asymmetry. In principle this effect is negligible for small bins as long as the acceptance does not change dramatically over that bin. The asymmetries presented here are extracted in small kinematic bins to minimize this acceptance effect.

5.6.2 Radiative Corrections

In electron scattering, it is possible for the electron to radiate a real photon before or immediately after it exchanges a virtual photon with the nucleon. This will result in a beam or scattered electron energy that is different from its measured value for that scattering event. This is important for cross section measurements, but is reduced in asymmetry measurements due to a partial cancellation in the ratio. Radiative effects are predicted to be extremely small due to the tight constraints on the missing mass cuts in this analysis. These missing mass cuts restrict the allowed phase space for emitted photons. In a previous π^+ electro-production analysis, asymmetries were calculated using

the MAID prediction with and without radiative effects [27]. These calculations showed negligible changes to the asymmetry measurement.

5.7 SYSTEMATIC UNCERTAINTY

We have identified several aspects of the analysis that might be a source of systematic uncertainty. An investigation of these issues is presented in the following sections.

5.7.1 Subtraction of the Nitrogen Background

The subtraction of the non-deuteron background events was described in section 4.8. We use carbon to model the nitrogen and use the invariant mass below the quasi elastic peak to normalize the carbon to the ND_3 . The statistical uncertainty on this ratio is σ_B . The systematic uncertainty on the background subtraction is determined by increasing the ND_3/C ratio by $0.5\sigma_B$ and redoing the asymmetry calculation. The standard asymmetry was calculated for the first half of the data set and the systematic asymmetry with the increased ND_3/C ratio, was calculated for the 2nd half of the data set. The results were compared using a T-test. The mean shift is listed in Tables 16 – 18 for each data set.

5.7.2 Detector Acceptance

A comparison of inbending and outbending data for a given beam energy was made using kinematic bins that had results from both data sets. This test was done since the acceptance for the positive torus current is slightly different than the acceptance for negative torus current, which has acceptance at lower Q^2 . The T-test distribution are shown for A_{ET} in Figs. 46 – 48. The only data set that shows a significant shift between inbending and outbending results is 2.5 GeV for the target spin asymmetry. The mean shifts are listed in Tables 16 – 18.

Another method of checking the systematic uncertainty due to detector efficiency or acceptance is to do an analysis on different regions of the detector. For this analysis we compare the asymmetry extracted using sectors 1, 2, and 3 to the asymmetry extracted using sectors 4, 5, and 6. The T-tests show negligible shifts for all but 2.5 GeV A_T . A final check on the acceptance effect was done by comparing the asymmetry measured using a fiducial cut (see Chapter 4), to select the efficient region of the detector compared to the asymmetry using no fiducial cut. Since these differences were significant for several data sets, we applied fiducial cuts to all data as part of the standard analysis.

5.7.3 Event Selection

The most crucial cut for our event selection is the requirement that the missing mass in the reaction be that of a proton (see section 4.7). We studied this cut by comparing asymmetry results from the upper and lower half of the missing mass cut region, as shown in Fig. 70. The reason for varying the missing mass cut is to exclude other multi-particle final states which can have different asymmetries. If this cut is bad or in the wrong place it would change the asymmetry. Asymmetries were calculated using the lower missing mass cut and compared to the asymmetry calculated with the higher missing mass cuts using a T-test. Another check on event selection is to apply a narrow missing mass cut of $0.92 \text{ GeV} < W < 0.96 \text{ GeV}$ and compare it to the wings of the missing mass cut $0.88 \text{ GeV} < W < 0.92 \text{ GeV}$ and $0.96 \text{ GeV} < W < 1.0 \text{ GeV}$ (see Fig. 71). The results of the worst data set, again, for the systematic error on event selection is the 2.5 GeV A_T . T-tests are compared to the statistical uncertainty and shown in Tables 16 through 18.

5.7.4 $P_B P_T$

An Asymmetry measurement for a particular beam energy involves the determination of $P_B P_T$ from four data sets, positive and negative target polarizations as well as inbending and outbending. To evaluate the systematic uncertainty on the final asymmetry, we change the value of $P_B P_T$ by one sigma for one of the four data sets and re-calculate the final asymmetry. The difference between the systematic and standard asymmetry for each of the four data sets is added in quadrature to the other relevant systematic uncertainties to produce a final systematic error for each 4-D bin.

5.7.5 Summary of Systematic Uncertainties

In general, if the mean shift in the T-test is less than ~ 2 sigma, we conclude that the systematic error from the source is negligible (see Tables 16 – 18). $P_B P_T$ is the main source of systematic uncertainty for each data set. In addition the background subtraction is significant for A_T for the 1.6 GeV data. We did not extract final target spin asymmetries for the 2.5 and 4.2 GeV data because of other systematic effects. For the 2.5 GeV data we know that we lost target material at one point, which causes the ratio R_r to deviate from 1.

To get the final systematic error, the asymmetry was calculated for each systematic effect and the difference from the standard asymmetry was calculated. Each difference was added in quadrature for a total systematic uncertainty. These values are calculated on a bin by bin basis. The mean uncertainty for the 1.6 GeV data was 0.2 and for the 2.5 and 4.2 GeV data the mean systematic uncertainty was of 0.04 and 0.07, respectively.

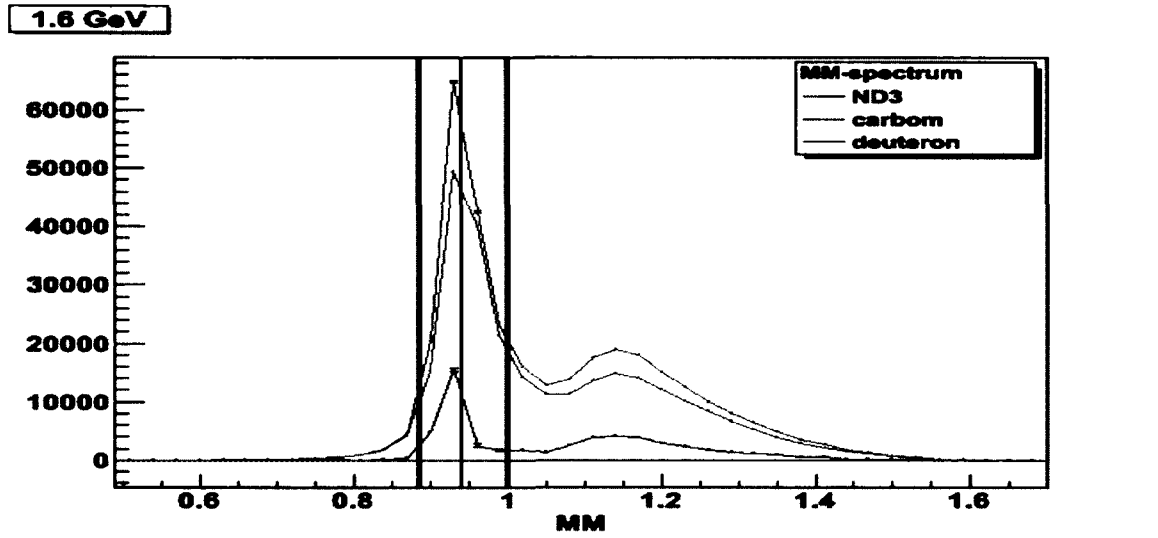


FIG. 70 Missing mass for the $d(e,e'\pi^-p)X$ reaction. The black lines indicate the standard missing mass cut ($0.88 \text{ GeV} < MM < 1.0$). The red line divides the missing mass cut region into the lower missing mass cut ($0.88 \text{ GeV} < MM < 0.94 \text{ GeV}$) and the upper half of the missing mass cut ($0.94 \text{ GeV} < W < 1.0 \text{ GeV}$).

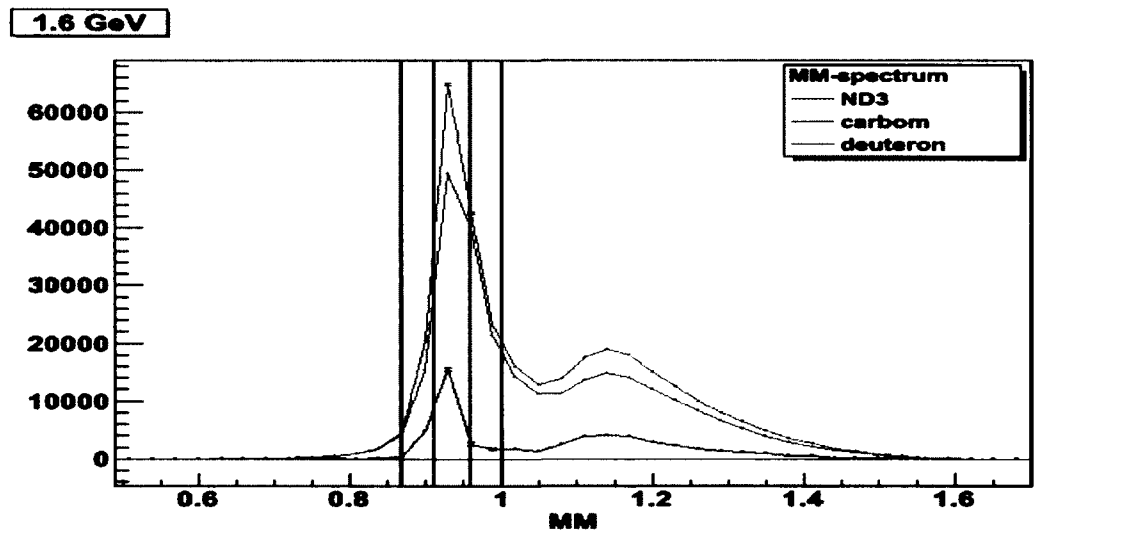


FIG. 71 Missing mass for the $d(e,e'\pi^-p)X$ reaction. The blue lines indicate the standard missing mass cut ($0.88 \text{ GeV} < MM < 1.0$). The red lines show the narrow missing mass cut region ($0.92 \text{ GeV} < MM < 0.96 \text{ GeV}$). The systematic uncertainty is calculated by comparing the asymmetry calculated from the narrow missing mass region with the lower and upper missing mass wings ($0.88 \text{ GeV} < MM < 0.92 \text{ GeV}$ and $0.96 \text{ GeV} < MM < 1.0 \text{ GeV}$).

Table 16 Mean of the T-test distribution and the expected statistical uncertainty for each systematic effect for 1.6 and 1.7 GeV data.

A_{et} for 1.6 GeV inbending data

Systematic Change	T-test Mean	$1/\sqrt{N_{entries}}$
Background change ND_3/C by 0.5σ	0.025	0.023
1.6 inbending vs. 1.7 outbending	0.037	0.022
Sectors 1, 2, and 3 vs. Sectors 4, 5, and 6	0.038	0.021
Fiducial cuts vs. no fiducial cuts	0.026	0.023
Lower MM cut vs. upper MM cut	0.037	0.033
Narrow MM cut vs. MM wings	0.048	0.022

A_{et} for 1.7 GeV outbending data

Systematic Change	T-test Mean	$1/\sqrt{N_{entries}}$
Background change ND_3/C by 0.5σ	0.019	0.019
1.6 inbending vs. 1.7 outbending (see above)	-	-
Sectors 1, 2, and 3 vs. Sectors 4, 5, and 6	0.005	0.019
Fiducial cuts vs. no fiducial cuts	0.013	0.018
Lower MM cut vs. upper MM cut	0.034	0.020
Narrow MM cut vs. MM wings	0.002	0.019

A_t for 1.6 GeV inbending data

Systematic Change	T-test Mean	$1/\sqrt{N_{entries}}$
Background change ND_3/C by 0.5σ	0.137	0.023
1.6 inbending vs. 1.7 outbending	0.019	0.022
Sectors 1, 2, and 3 vs. Sectors 4, 5, and 6	0.030	0.021
Fiducial cuts vs. no fiducial cuts	0.134	0.023
Lower MM cut vs. upper MM cut	0.044	0.033
Narrow MM cut vs. MM wings	0.006	0.022

A_t for 1.7 GeV outbending data

Systematic Change	T-test Mean	$1/\sqrt{N_{entries}}$
Background change ND_3/C by 0.5σ	0.117	0.019
1.6 inbending vs. 1.7 outbending (see above)	-	-
Sectors 1, 2, and 3 vs. Sectors 4, 5, and 6	0.001	0.019
Fiducial cuts vs. no fiducial cuts	0.111	0.018
Lower MM cut vs. upper MM cut	0.001	0.020
Narrow MM cut vs. MM wings	0.017	0.019

Table 17 Mean of the T-test distribution and the expected statistical uncertainty for each systematic effect for 2.5 GeV data.

A_{et} for 2.5 GeV inbending data

Systematic Change	T-test Mean	$1/\sqrt{N_{entries}}$
Background change ND_3/C by 0.5σ	0.021	0.020
1.6 inbending vs. 1.7 outbending	0.022	0.020
Sectors 1, 2, and 3 vs. Sectors 4, 5, and 6	0.013	0.019
Fiducial cuts vs. no fiducial cuts	0.016	0.018
Lower MM cut vs. upper MM cut	0.004	0.018
Narrow MM cut vs. MM wings	0.031	0.019

A_{et} for 2.5 GeV outbending data

Systematic Change	T-test Mean	$1/\sqrt{N_{entries}}$
Background change ND_3/C by 0.5σ	0.027	0.020
1.6 inbending vs. 1.7 outbending (see above)	-	-
Sectors 1, 2, and 3 vs. Sectors 4, 5, and 6	0.020	0.017
Fiducial cuts vs. no fiducial cuts	0.021	0.018
Lower MM cut vs. upper MM cut	0.004	0.018
Narrow MM cut vs. MM wings	0.0003	0.017

A_t for 2.5 GeV inbending data

Systematic Change	T-test Mean	$1/\sqrt{N_{entries}}$
Background change ND_3/C by 0.5σ	0.103	0.019
1.6 inbending vs. 1.7 outbending	0.176	0.019
Sectors 1, 2, and 3 vs. Sectors 4, 5, and 6	0.005	0.019
Fiducial cuts vs. no fiducial cuts	0.063	0.018
Lower MM cut vs. upper MM cut	0.069	0.019
Narrow MM cut vs. MM wings	0.012	0.019

A_t for 2.5 GeV outbending data

Systematic Change	T-test Mean	$1/\sqrt{N_{entries}}$
Background change ND_3/C by 0.5σ	0.656	0.019
1.6 inbending vs. 1.7 outbending (see above)	-	-
Sectors 1, 2, and 3 vs. Sectors 4, 5, and 6	0.099	0.017
Fiducial cuts vs. no fiducial cuts	0.653	0.018
Lower MM cut vs. upper MM cut	0.216	0.018
Narrow MM cut vs. MM wings	0.050	0.017

Table 18 Mean of the T-test distribution and the expected statistical uncertainty for each systematic effect for 4.2 GeV data.

A_{et} for 4.2 GeV inbending data

Systematic Change	T-test Mean	$1/\sqrt{N_{entries}}$
Background change ND_3/C by 0.5σ	0.007	0.026
1.6 inbending vs. 1.7 outbending	0.011	0.019
Sectors 1, 2, and 3 vs. Sectors 4, 5, and 6	0.020	0.025
Fiducial cuts vs. no fiducial cuts	0.001	0.025
Lower MM cut vs. upper MM cut	0.023	0.025
Narrow MM cut vs. MM wings	0.038	0.023

A_{et} for 4.2 GeV outbending data

Systematic Change	T-test Mean	$1/\sqrt{N_{entries}}$
Background change ND_3/C by 0.5σ	0.005	0.015
1.6 inbending vs. 1.7 outbending (see above)	-	-
Sectors 1, 2, and 3 vs. Sectors 4, 5, and 6	0.018	0.014
Fiducial cuts vs. no fiducial cuts	0.032	0.014
Lower MM cut vs. upper MM cut	0.007	0.013
Narrow MM cut vs. MM wings	0.023	0.014

A_t for 4.2 GeV inbending data

Systematic Change	T-test Mean	$1/\sqrt{N_{entries}}$
Background change ND_3/C by 0.5σ	0.075	0.026
1.6 inbending vs. 1.7 outbending	0.010	0.019
Sectors 1, 2, and 3 vs. Sectors 4, 5, and 6	0.022	0.025
Fiducial cuts vs. no fiducial cuts	0.062	0.025
Lower MM cut vs. upper MM cut	0.037	0.025
Narrow MM cut vs. MM wings	0.072	0.025

A_t for 4.2 GeV outbending data

Systematic Change	T-test Mean	$1/\sqrt{N_{entries}}$
Background change ND_3/C by 0.5σ	0.505	0.015
1.6 inbending vs. 1.7 outbending (see above)	-	-
Sectors 1, 2, and 3 vs. Sectors 4, 5, and 6	0.012	0.014
Fiducial cuts vs. no fiducial cuts	0.486	0.014
Lower MM cut vs. upper MM cut	0.018	0.014
Narrow MM cut vs. MM wings	0.062	0.014

CHAPTER 6

OUTLOOK AND CONCLUSION

The purpose of this analysis was to gain an understanding of the double spin and single spin asymmetries A_{et} and A_t for exclusive π^- electro-production. The data were collected in Hall B at Jefferson Lab during the EG1 run period using a polarized electron beam and a polarized ND₃ target. The beam was polarized using a strained GaAs-cathode and the target was polarized at approximately 1K in a 5 Tesla magnetic field using microwaves to increase polarization by Dynamic Nuclear Polarization. The final state particles were detected with the nearly 4π CEBAF Large Acceptance Spectrometer or CLAS.

The EG1 run period actually consisted of two different run periods, EG1a and EG1b, also called EG2000. The results presented in chapter 5 were obtained using the later EG1b data at beam energies of 1.6, 1.7, 2.5 and 4.2 GeV with torus settings of 1500, -1500, 2250 and -2250. The negative or outbending torus settings have an acceptance of lower Q^2 than the positive torus settings. In addition to the ND₃ target, a carbon target was inserted to subtract the background from the ND₃ data. The asymmetries were analyzed for two reaction channels, $n(e,e'\pi^-)P$ and $d(e,e'\pi^-)P$. For the $n(e,e'\pi^-)P$ channel, only the scattered electron and pion were detected, and we assumed that the target neutron was at rest. One advantage of π^- electro-production channel from the deuteron is that there are three charged particles in the final state, so that it was possible to identify $d(e,e'\pi^-)P$ events. In the $n(e,e'\pi^-)P$ channel we only included events that did not pass the cuts for the $d(e,e'\pi^-)P$ channel, in order to have two completely separate data sets. Asymmetries for the two channels were compared using a T-test and were

shown to be compatible. The two channel asymmetries were combined using an error weighted sum and presented as final results. The asymmetries were compared to the MAID2007 model.

The asymmetries are non-zero and show a reasonable agreement with MAID despite the fact that there was low deuteron polarization and low statistics. Since MAID is the result of a fit to existing data, the level of agreement implies that the results of this analysis are consistent with earlier experimental results. However, we do find kinematic regions in which the agreement is not good, particularly at high W and in some angular distributions. MAID agrees with the data at in the delta resonance region but underpredicts the data starting in the 2nd resonance region. Interestingly, both the A_{et} asymmetries and MAID are positive in the delta region where it was assumed to be negative as expected of a spin 3/2 resonance. Given our acceptance and the fact that we are investigating the $n \rightarrow \pi^- p$ channel, we suspect that the nonresonant terms dominate over the delta resonance production for our data. Ultimately these data present new polarization observables in approximately 4500 bins, which should be included in future fits and result in a better phenomenological model.

In 2005, a new experiment was conducted in Hall B using much of the same equipment but with a modified Čerenkov detector in one sector of CLAS allowing for an improved detection of electrons at small polar angles [90]. This will increase the statistics and kinematic coverage, especially at the low Q^2 region. After a scheduled upgrade of the CEBAF accelerator, another experiment is approved to run with a polarized target and polarized electron beam [91, 92]. Data from that experiment will greatly increase the kinematic range for single and double spin asymmetries.

These results for the $\pi^- p$ channel and their comparison with model predictions will allow us to build a better understanding of the spin structure of the neutron in the resonance region.

LITERATURE CITED

- [1] O. W. Greenberg, *Am. J. Phys.* **50**, 1074 (1982).
- [2] M. Gell-Mann, *Phys. Rev.* **125**, 1067 (1962).
- [3] M. Gell-Mann, *Phys. Lett.* **8**, 214 (1964).
- [4] D. Griffiths, *Introduction to Elementary Particles*, J. Wiley & Sons, Inc. (1987).
- [5] H. Yukawa, *Proc. Phys. Math. Soc. Japan* **17**, 48 (1935).
- [6] B. Povh *et al.*, *Particles and Nuclei" 3rd Edition*, Springer (1999).
- [7] O. W. Greenberg, *Phys. Rev. Lett.* **13**, 598 (1964).
- [8] Particle Data Group, *Phys. Rev. D* (2006).
- [9] F. W. Brasse *et al.*, *Nucl. Phys.* **B110**, 413 (1976).
- [10] I. Niculescu *et al.*, *Phys. Rev. D* **58**, 032003 (1998).
- [11] A. Biselli *et al.*, *Phys. Rev. C* **68**, 202 (2003).
- [12] R. DeVita *et al.*, *Phys. Rev. Lett.* **88**, 820 (2002).
- [13] V. Burkert *et al.*, *Measurement of the Polarized Structure Functions in Inelastic Electron Proton Scattering Using the CEBAF Large Acceptance Spectrometer*, CEBAF Proposal, PR-91-023 (1991).
- [14] S. E. Kuhn *et al.*, *The Polarized Structure Function G_{1n} and the Q^2 Dependence of the Gerasimov-Drell-Hern Sum Rule for the Neutron*, CEBAF Proposal, PR-93-009(1993).
- [15] R. Minehart *et al.*, *Measurement of Single Pion Electroproduction from the Proton with Polarized Beam and Polarized Target using CLAS*, CEBAF Proposal, PR-93-036 (1993).
- [16] J. Bjorken and S. Drell, *Relativistic Quantum Mechanics*, McGraw-Hill, (1964).
- [17] A. S. Raskin and T. W. Donnelly, *Ann. Phys.* **191**, 78 (1989).
- [18] D. Drechsel and L. Tiator, *J. Phys. G: Nucl. Part. Phys.* **18**, 449 (1992).

- [19] C. W. Akerlof *et al.*, Phys. Rev. Lett. **16**, 147 (1966); **163**, 1482 (1967).
- [20] E. Amaldi, S. Fubini, and G. Furlan, *Pion-electroproduction, Electroproduction at Low Energy and Hadron Form Factors*, Springer-Verlay, Berlin, Heidelberg, New York, (1979).
- [21] A. Bartl and W. Majerotto, Nucl. Phys. **B62**, 267 (1973).
- [22] G. Knochlein, D. Drechsel, and L. Tiator, Z. Phys. **A352**, 327 (1995).
- [23] G. F. Chew, M. L. Goldberger, and L. Tiator, Phys. Rev. **106**, 1345 (1957).
- [24] D. Drechsel, O. Hanstein, S. S. Kamalov, and L. Tiator, Nucl. Phys. **A645**, 145 (1999).
- [25] S. E. Kuhn, *Nucleon Structure Functions Experiments and Models*, HUGS Proceedings, Newport News Virginia (1998).
- [26] Y. Prok, PhD. Thesis, University of Virginia (1997).
- [27] Mehmet Bektasoglu, PhD Thesis, Old Dominion University (2002).
- [28] I. G. Aznauryan and V.D. Burkert, Prog. Part. Nucl.Phys. **67** 1 (2012).
- [29] W. Albrecht *et al.*, Nucl. Phys. **B25**, 1 (1970); **B27**, 615 (1971).
- [30] R. Siddle *et al.*, Nucl. Phys. **B35**, 93 (1971).
- [31] R. W. Lourie, *Workshop on Electron-Nucleon Scattering*, EPIC, Italy (1993).
- [32] C. Becchi, and G. Morpurgo, Phys. Lett. **17**, 352 (1969).
- [33] I. G. Aznauryan et al., Phys. Rev. C **78**, 045209 (2008).
- [34] F. E. Close and F. J. Gilman, Phys. Lett. B **38**, 541 (1972).
- [35] V. Burkert, *International Conference on the Structure of Baryons and Related Mesons*, Yale University, (1992).
- [36] R. Thompson *et al.*, Phys. Rev. Lett. **86**, 1702 (2001).
- [37] S. Capstick, *Measurement of the Double Spin Asymmetry*, CEBAF-TH-92-09 (1992).
- [38] R. L. Crawford and W. T. Morton, Nucl. Phys. **B211**, 1 (1983).

- [39] N. Isgur and G. Karl, Phys. Rev. **D19**, 2653 (1979).
- [40] N. Isgur and G. Karl, Phys. Lett. **B72**, 109 (1977).
- [41] S. Capstick and N. Isgur, Phys. Rev. **D34**, 2809 (1982).
- [42] J. F. Donoghue, E. Golowich, and B. R. Holstein, *Dynamics of the Standard Model*, Cambridge University Press, (1992).
- [43] J. Gasser and H. Leatwyler, Phys. Reports, **87**, 77 (1982).
- [44] S. Weinberg, Phys. Lett. **B251**, 288 (1990); Nucl. Phys. **B363**, 3 (1991).
- [45] C. Ordóñez and U. van Kolck, Phys. Lett. **B291**, 459 (1992).
- [46] H. J. Rothe, World Scientific Lecture Notes in Physics, Vol. 59 World Scientific, Singapore (1997).
- [47] F. A. Berends, A. Donnachie, and D. L. Weaver, Nucl. Phys. **B4**, 1, 54, 103
- [48] R. L. Walker, Phys. Rev. **182**, 1729 (1969).
- [49] R. A. Arndt, I. I. Strakovsky, R. L. Workman, and M. M. Pavan, Phys. Rev. **C52**, 2120 (1995).
- [50] D. Drechsel, O. Hanstein, S. S. Kamalov, and L. Tiator, Nucl. Phys. **A645**, 145 (1999).
- [51] M. Goldberger, and Watson, *Collision Theory*, Robert E. Krieger Publishing Company (1975).
- [52] V. D. Burkert and T. S. H. Lee, *Electromagnetic Meson Production in the Nucleon Resonance Region*, International Journal of Modern Physics E, (2004).
- [53] I. G. Aznauryan, Phys. Rev. **C68**, 065209 (2003).
- [54] <http://wwwkph.kph.uni-mainz.de/MAID/maid2007/maid2007.html>
- [55] <http://gwdac.phys.gwu.edu>
- [56] R. A. Arndt, I. I. Strakovsky, R. L. Workman, Phys. Rev. **53**, 439 (1996).
- [57] H. A. Grunder *et al.*, Nucl. Phys. **A478**, 831c (1988).
- [58] C. Leemann, *et al.*, Annu. Rev. Nucl. Part. Sci. **413** (2001)

- [59] T. Maruyama, E. L. Garwin, R. Prepost and G. Zapalac, Phys. Rev. **B46**, 4261 (1992).
- [60] E. Leader, *Spin in Particle Physics*, Cambridge University Press, (2005).
- [61] D. G. Crabb and W. Meyer, Annu. Rev. Nucl. Part. Sci., **47**, 67 (1997).
- [62] M. Borghini *et al*, CERN Yellow Report **68-32** (1968).
- [63] D. G. Crabb, *Solid Polarized Targets*, Workshop Held at the American Physical Society, DNP, Virginia (1994).
- [64] C. D. Keith *et al.*, Nucl. Instr. and Meth. **A501**, 327 (2003).
- [65] C. M. Dulya *et al.*, Nucl. Instr. and Meth. **A356**, 88 (1995).
- [66] M. D. Mestayer *et al.*, Nucl. Instr. and Meth. **A449**, 81 (2000).
- [67] G. Adams *et al.*, Nucl. Instr. and Meth. **A465**, 414 (2001).
- [68] B. A. Mecking *et al.*, Nucl. Instr. and Meth. **A465**, 414 (2001).
- [69] E. S. Smith *et al.*, Nucl. Instr. and Meth. **A432**, 265 (1999).
- [70] M. Amarian *et al.*, Nucl. Instr. and Meth. **A460**, 460 (2001).
- [71] V. Blobel *et al.*, *The BOS System for the CLAS Detector: Dynamic Memory Management*, (November 1995).
- [72] S. Stepanyan, *Simple Event Builder (SEB) in the framework of RECIS*, (1997).
- [73] E. S. Smith *et al.*, *Calibration of the CLAS TOF System*, CLAS-NOTE 1999-011 (2003).
- [74] R. Fersch, Ph.D. thesis, College of William and Mary (2008).
- [75] A. Vlassov *et al.*, *CLAS Cerenkov Detector Calibrations*, CLAS-NOTE 1999-005 (1999).
- [76] D. Lawrence, M. Mestayer *CLAS Drift Chamber Calibrations: Software and Procedures*, CLAS-NOTE 1999-018 (1999)
- [77] N. Guler Ph.D. Thesis Old Dominion University (2009).
- [78] P. Bosted, S. Kuhn, and Y. Prok, CLAS-NOTE 2003-008 (2003).

- [79] A. Klimenko, and S. Kuhn, CLAS-NOTE 2003-005 (2003).
- [80] P. Bosted, and H. Avakian, CLAS-NOTE 2006-006 (2006).
- [81] A. Vlassov, CLAS Cerenkov Counter Study
- [82] <http://userweb.jlab.org/~vlassov/cc/index.html>
- [83] P. Bosted, and R. Fersch *et al.* Phys. Rev. **C78** 015202 (2008).
- [84] P. Bosted, Phys. Rev. **C51**, 409 (1995).
- [85] J. Arrington, Phys. Rev. C **69**, 022201 (2004).
- [86] S. Kuhn “*Data Analysis for EG1*” (analysis document)
<http://www.jlab.org/Hall-B/secure/eg1/AnalysisDoc/EG2000ata/Analysis.Pdf>.
- [87] P. Bosted, EG1b-Note-PB1
<http://www.jlab.org/Hall-B/secure/eg1/EG2000/Bosted/background>.
- [88] P. Bosted (private communication).
- [89] G. Dodge (private communication).
- [90] M. Ripani, *et al.* *The GDH Sum Rule with Nearly Real Photons and the Proton g1 Structure at Low Momentum Transfer* E03-006 (2003).
- [91] S. Kuhn, (private communication).
- [92] S. Kuhn, *et al.*, *The Longitudinal Spin Structure of the Nucleon*, PR12-06-109 (2006).

APPENDIX A
CROSS SECTIONS IN TERMS OF HELICITY AMPLITUDES

The unpolarized term depends on four of the eleven terms and is expressed [26]

$$\frac{d\sigma_0}{d\Omega_\pi} = \sigma_T + \varepsilon\sigma_L + \varepsilon\sigma_{TT} \cos 2\phi^* + \sqrt{\frac{1}{2}\varepsilon(1+\varepsilon)}\sigma_{LT} \cos \phi^*, \quad (186)$$

where σ_T is the unpolarized cross section for unpolarized transverse virtual photons, $\varepsilon\sigma_L$ is the cross section for longitudinal virtual photons. The σ_{TT} term is for the cross section due to transverse linear polarization of the virtual photons and the last term describes the interference between the longitudinal and transverse components of the cross section. These four unpolarized cross section terms can be written in terms of the helicity amplitudes described in Equations ((26) – (29)):

$$\sigma_T = \frac{|\bar{p}_\pi|W}{k_\gamma m_N} \frac{1}{2} \left(|h_+^N|^2 + |h_+^F|^2 + |h_-^N|^2 + |h_-^F|^2 \right), \quad (187)$$

$$\sigma_L = \frac{|\bar{p}_\pi|W}{k_\gamma m_N} \left(|h_0^N|^2 + |h_0^F|^2 \right), \quad (188)$$

$$\sigma_{TT} = \frac{|\bar{p}_\pi|W}{k_\gamma m_N} \frac{1}{2} \left(|h_-^N|^2 + |h_-^F|^2 - |h_+^N|^2 - |h_+^F|^2 \right), \quad (189)$$

$$\sigma_{LT} = \frac{|\bar{p}_\pi|W}{k_\gamma m_N} 2 \operatorname{Re} \left(h_0^N h_-^{N*} + h_0^F h_-^{F*} \right), \quad (190)$$

where \bar{p}_π is the pion momentum in the center of mass frame [26].

For a longitudinally polarized electron beam and unpolarized nucleon target, the cross section gains a new term,

$$\sigma_e = -h_e \frac{|\bar{p}_x|W}{k_\gamma m_N} \sqrt{2\varepsilon(1-\varepsilon)} \sin \phi^* \operatorname{Im}(h_0^N h_-^{N^*} + h_0^F h_-^{F^*}), \quad (191)$$

where h_e is the electron beam helicity.

Following the notation of reference [26] we have

$$\begin{aligned} \sigma_i = & \frac{|\bar{p}_x|W}{k_\gamma m_N} \{P_x[-\sqrt{2\varepsilon(1+\varepsilon)} \sin \phi^* \operatorname{Im} X_1 - \varepsilon \sin 2\phi^* \operatorname{Im} X_2] \\ & - P_y[\operatorname{Im} Y_1 + \varepsilon \cos 2\phi^* \operatorname{Im} Y_2 + 2\varepsilon \operatorname{Im} Y_3 + \sqrt{2\varepsilon(1+\varepsilon)} \cos \phi^* \operatorname{Im} Y_4] \\ & - P_z[\varepsilon \sin 2\phi^* \operatorname{Im} Z_2 + \sqrt{2\varepsilon(1+\varepsilon)} \sin \phi^* \operatorname{Im} Z_1]\}, \end{aligned} \quad (192)$$

where the X , Y and Z terms are written as a function of the helicity amplitudes:

$$\begin{aligned} X_1 &= h_0^F h_+^{N^*} + h_0^N h_+^{F^*} \\ X_2 &= h_-^F h_+^{N^*} + h_-^N h_+^{F^*} \end{aligned} \quad (193)$$

$$\begin{aligned} Y_1 &= h_+^N h_+^{F^*} + h_-^N h_-^{F^*} \\ Y_2 &= h_-^N h_-^{F^*} - h_+^N h_+^{F^*} \\ Y_3 &= h_0^N h_0^{F^*} \\ Y_4 &= h_0^N h_-^{F^*} - h_0^F h_-^{N^*} \end{aligned} \quad (194)$$

$$\begin{aligned} Z_1 &= h_0^N h_+^{N^*} - h_0^F h_+^{F^*} \\ Z_2 &= h_-^N h_+^{N^*} - h_-^F h_+^{F^*} \end{aligned} \quad (195)$$

Finally the double polarization term that is written

$$\begin{aligned} \sigma_{ei} = & -h_e \frac{|\bar{p}_x|W}{k_\gamma m_N} \{-P_x[\sqrt{2\varepsilon(1-\varepsilon)} \cos \phi^* \operatorname{Re} X_1 + \sqrt{1-\varepsilon^2} \operatorname{Re} X_2] \\ & + P_y[\sqrt{2\varepsilon(1-\varepsilon)} \sin \phi^* \operatorname{Re} Y_4] \\ & + P_z[\sqrt{1-\varepsilon^2} \operatorname{Re} Z_2 + \sqrt{2\varepsilon(1-\varepsilon)} \cos \phi^* \operatorname{Re} Z_1]\}. \end{aligned} \quad (196)$$

APPENDIX B

RESPONSE FUNCTIONS IN TERMS OF HELICITY AMPLITUDES

$$R_T^0 = \frac{1}{2} (|H_1|^2 + |H_2|^2 + |H_3|^2 + |H_4|^2) \quad (197)$$

$$R_T^0 = -\text{Im}\{H_1^* H_2 + H_3^* H_4\} \quad (198)$$

$$R_L^0 = |H_5|^2 + |H_6|^2 \quad (199)$$

$$R_L^y = -2\text{Im}\{H_5^* H_6\} \quad (200)$$

$$R_{LT}^0 = \frac{1}{\sqrt{2}} \text{Re}\{H_5^* H_1 - H_5^* H_4 + H_6^* H_2 + H_6^* H_3\} \quad (210)$$

$$R_{LT}^x = \frac{1}{\sqrt{2}} \text{Im}\{-H_5^* H_2 + H_5^* H_3 - H_6^* H_1 - H_6^* H_4\} \quad (202)$$

$$R_{LT}^y = \frac{1}{\sqrt{2}} \text{Im}\{-H_5^* H_2 - H_5^* H_3 + H_6^* H_1 - H_6^* H_4\} \quad (203)$$

$$R_{LT}^z = \frac{1}{\sqrt{2}} \text{Im}\{-H_5^* H_1 - H_5^* H_4 + H_6^* H_2 - H_6^* H_3\} \quad (204)$$

$$R_{TT}^0 = \text{Re}\{-H_1^* H_4 + H_2^* H_3\} \quad (205)$$

$$R_{TT}^x = \text{Im}\{H_1^* H_3 - H_2^* H_4\} \quad (206)$$

$$R_{TT}^y = \text{Im}\{H_1^* H_3 + H_2^* H_4\} \quad (207)$$

$$R_{TT}^z = -\text{Im}\{H_1^* H_4 + H_2^* H_3\} \quad (208)$$

$$R_{LT}^0 = \frac{1}{\sqrt{2}} \text{Im}\{-H_5^* H_1 + H_5^* H_4 - H_6^* H_2 - H_6^* H_3\} \quad (209)$$

$$R_{LT}^x = \frac{1}{\sqrt{2}} \text{Re}\{H_5^* H_2 - H_5^* H_3 + H_6^* H_1 + H_6^* H_4\} \quad (210)$$

$$R_{LT}^y = \frac{1}{\sqrt{2}} \operatorname{Re}\{-H_5^* H_2 - H_5^* H_3 + H_6^* H_1 - H_6^* H_4\} \quad (211)$$

$$R_{LT}^z = \frac{1}{\sqrt{2}} \operatorname{Re}\{H_5^* H_1 + H_5^* H_4 - H_6^* H_2 + H_6^* H_3\} \quad (212)$$

$$R_{TT}^x = \operatorname{Re}\{H_1^* H_2 + H_3^* H_4\} \quad (213)$$

$$R_{TT}^z = \frac{1}{2} (|H_1|^2 - |H_2|^2 + |H_3|^2 - |H_4|^2) \quad (214)$$

APPENDIX C

HELICITY AMPLITUDES IN TERMS OF CGLN AMPLITUDES

$$H_1 = -\frac{1}{\sqrt{2}} \sin \theta^* (F_3 + F_4 \cos \theta^*) \quad (215)$$

$$H_2 = -\frac{1}{\sqrt{2}} (2F_1 - 2F_2 \cos \theta^* + F_4 \sin^2 \theta^*) \quad (216)$$

$$H_3 = -\frac{1}{\sqrt{2}} F_4 \sin^2 \theta^* \quad (217)$$

$$H_4 = \frac{1}{\sqrt{2}} \sin \theta^* (2F_2 + F_3 + F_4 \cos \theta^*) \quad (218)$$

$$H_5 = F_5 + F_6 \cos \theta^* \quad (219)$$

$$H_6 = F_6 \sin \theta^* \quad (220)$$

APPENDIX D

CGLN AMPLITUDES IN TERMS OF DERIVATIVES OF LEGENDRE

POLYNOMIALS

$$F_1 = \sum_{l \geq 0} \{ (M_{l+} + E_{l+}) P'_{l+1} + [(l+1)M_{l+} + lM_{l-} - P'_{l-1}] \} \quad (221)$$

$$F_2 = \sum_{l \geq 1} [(l+1)M_{l+} + lM_{l-} P'_l] \quad (222)$$

$$F_3 = \sum_{l \geq 1} [(E_{l+} - M_{l+}) P''_{l+1} + E_{l-} + M_{l-} P''_{l-1}] \quad (223)$$

$$F_4 = \sum_{l \geq 2} (M_{l+} - E_{l+} - M_{l-} + E_{l-} P'_l) \quad (224)$$

$$F_5 = \sum_{l \geq 0} [(l+1)L_{l+} P'_{l+1} - lL_{l-} P'_{l-1}] \quad (225)$$

$$F_6 = \sum_{l \geq 1} [lL_{l-} - (l+1)L_{l+}] P'_l \quad (226)$$

APPENDIX E

PROPERTIES OF THE RESONANCES IN THE FIRST THREE RESONANCE REGIONS

Table 19 Masses, half-widths, isospin, values for $\Gamma_{\pi N}/\Gamma$ along with associated pole positions from SM95 solutions. Corresponding residues are given as a modulus in MeV and phase in degrees.

Resonance	W_R (MeV)	$\Gamma/2$ (MeV)	Isospin	$\Gamma_{\pi N}/\Gamma$	Pole (MeV)	Residue
P ₃₃ (1232)	1233	57	3/2	~1.0	1211- <i>i</i> 50	(38,-22)
P ₁₁ (1440)	1467	220	1/2	0.68	1346- <i>i</i> 88	(42,-101)
D ₁₃ (1520)	1515	53	1/2	0.61	1515- <i>i</i> 55	(34,7)
S ₁₁ (1535)	1535	33	1/2	0.31	1501- <i>i</i> 62	(31,-12)
F ₁₅ (1680)	1678	63	1/2	0.68	1670- <i>i</i> 76	(29,-6)
S ₁₁ (1650)	1667	45	1/2	~1.0	1673- <i>i</i> 41	(22,29)
D ₁₅ (1675)	1673	77	1/2	0.38	1663- <i>i</i> 76	(29,-6)
S ₃₁ (1620)	1617	54	3/2	0.29	1585- <i>i</i> 52	(14,-121)

APPENDIX F

MISSING MASS SPECTRA FOR OTHER ENERGY DATA

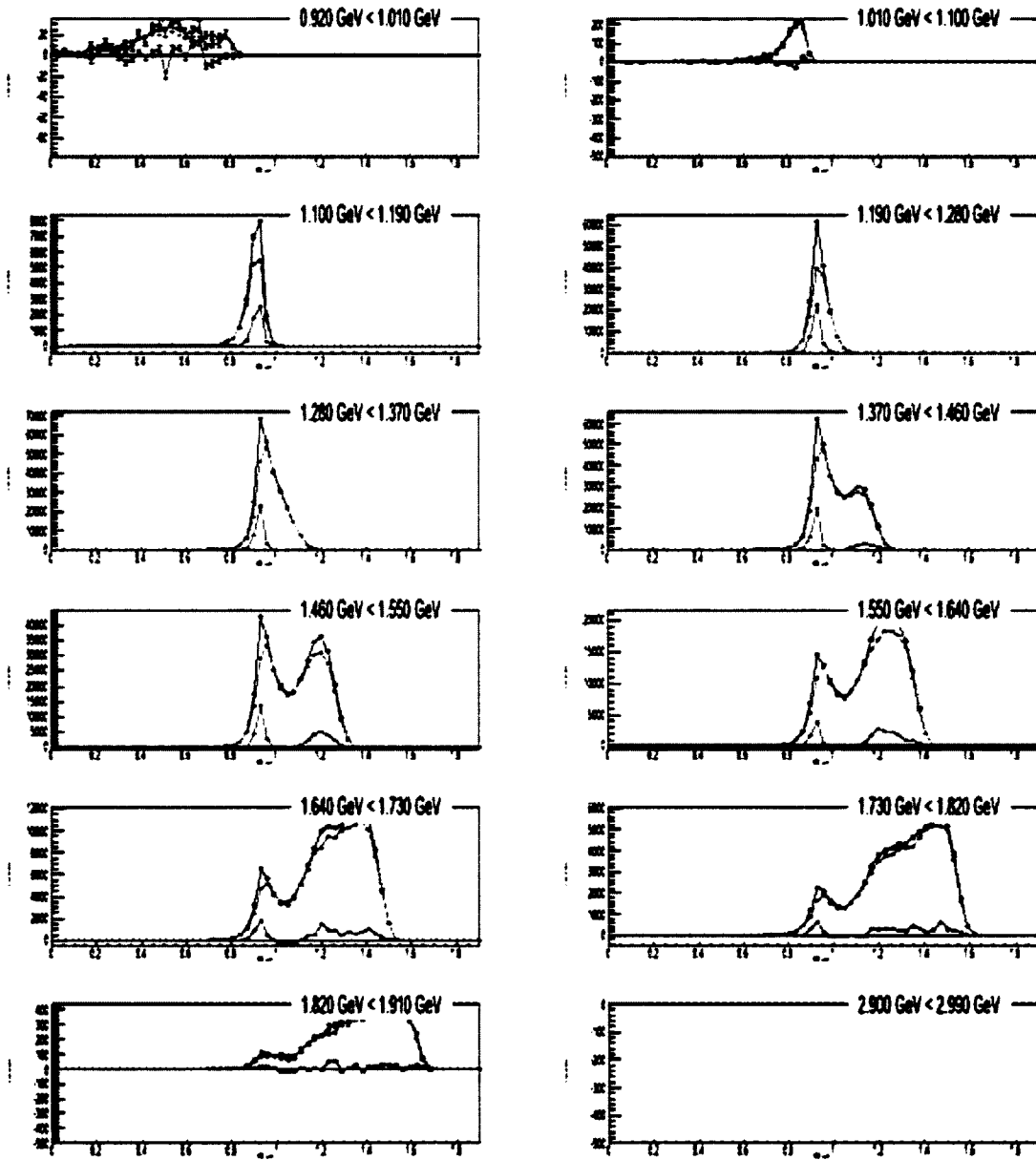


FIG. 72 Missing mass spectrum for $n(e, e'\pi^-)X$ for 1.7 GeV negative torus.

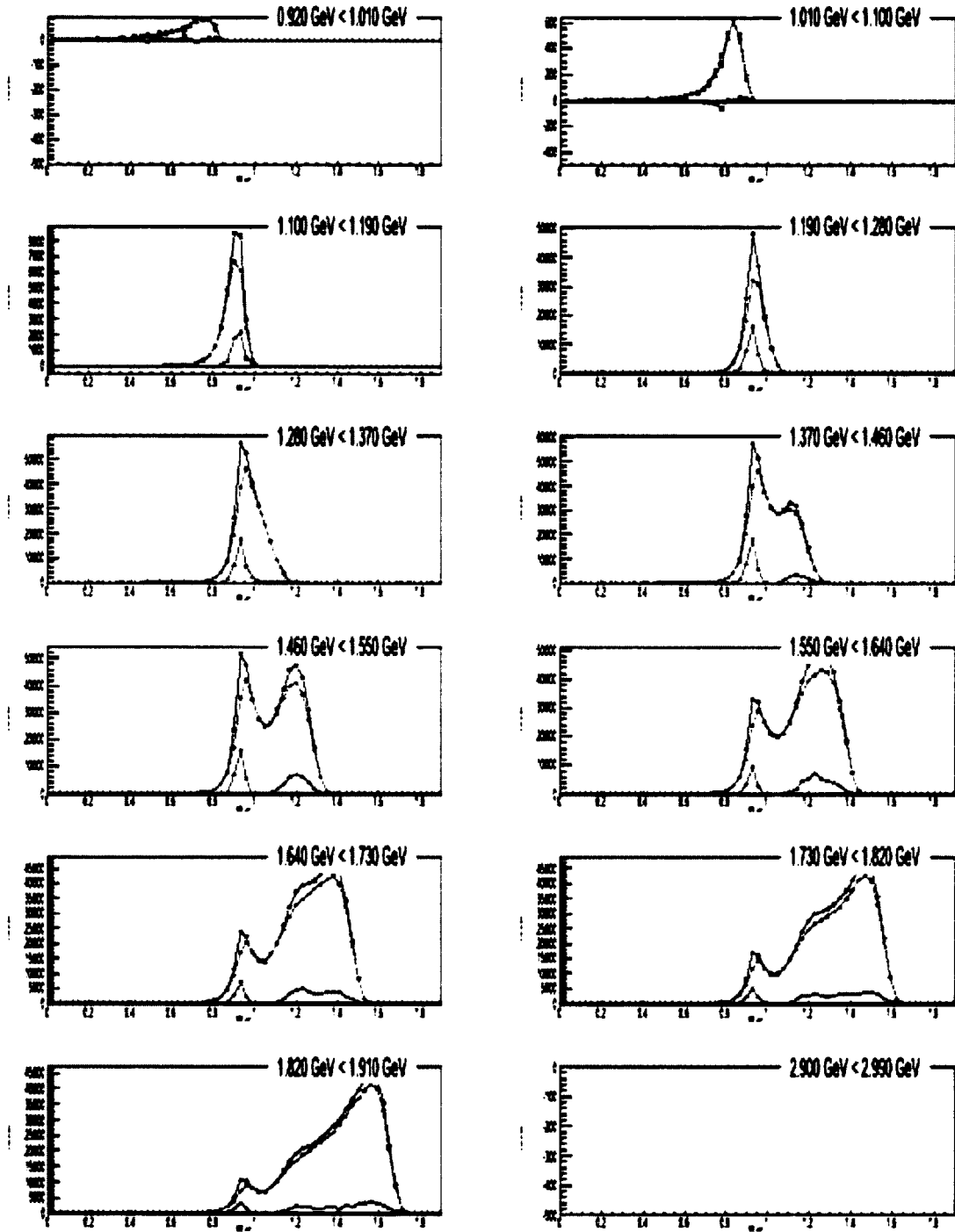


FIG. 73 Missing mass spectrum for $n(e, e'\pi^-)X$ for 2.5 GeV negative torus.

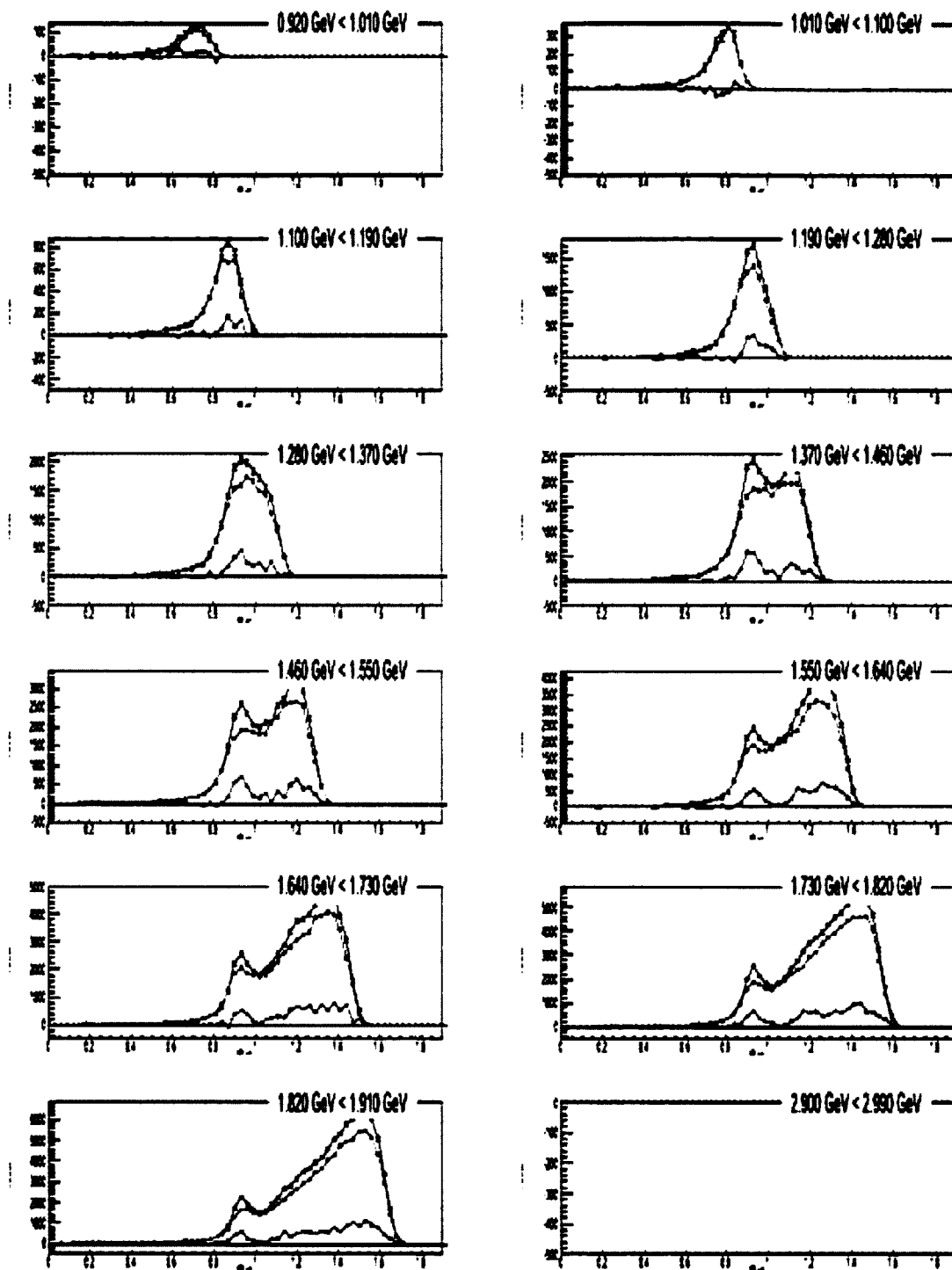


FIG. 74 Missing mass spectrum for $n(e, e' \pi^-) X$ for 4.2 GeV positive torus.

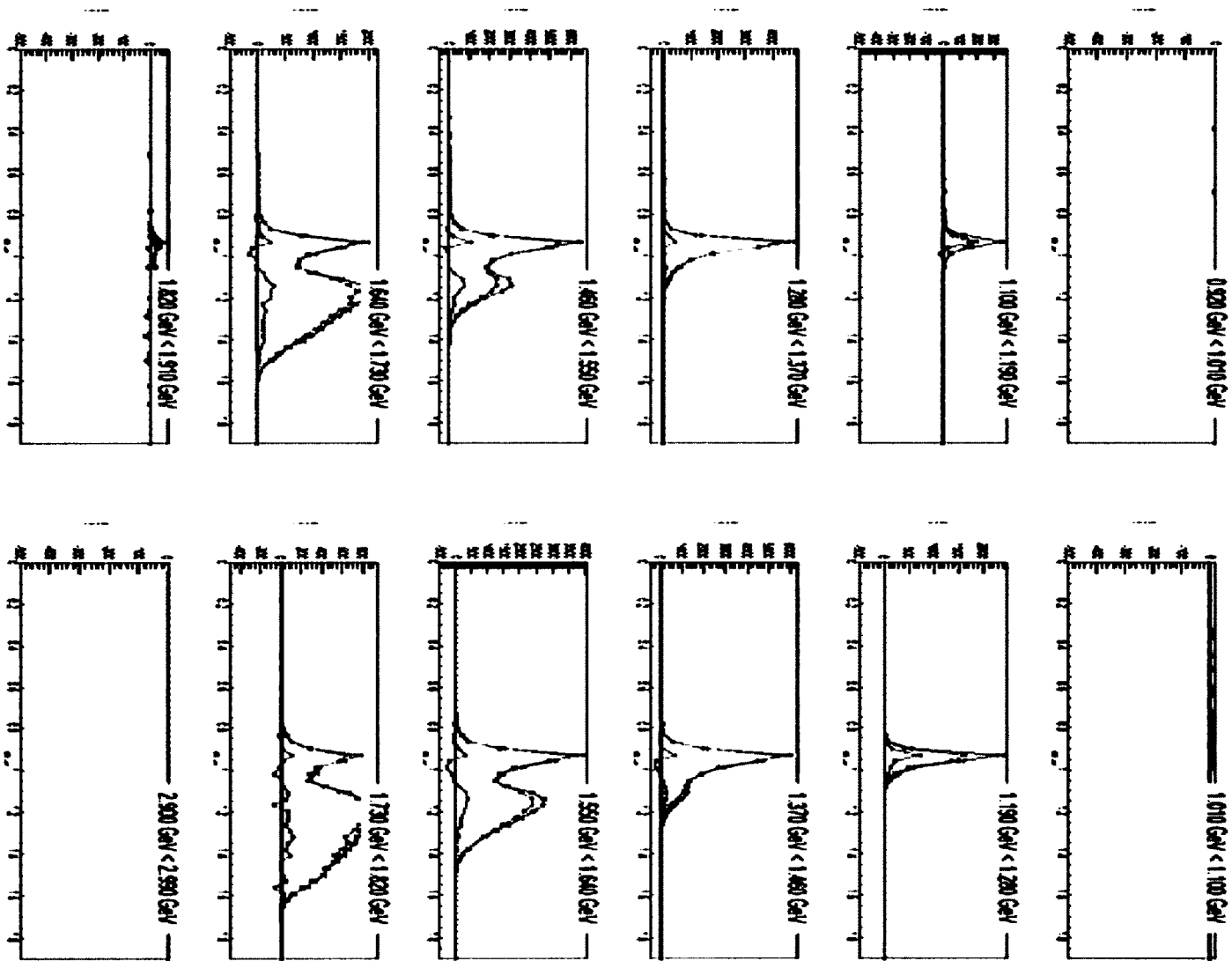


FIG. 75 Missing mass spectrum for $d(e,e'\pi^-)X$ for 1.7 GeV negative torus.

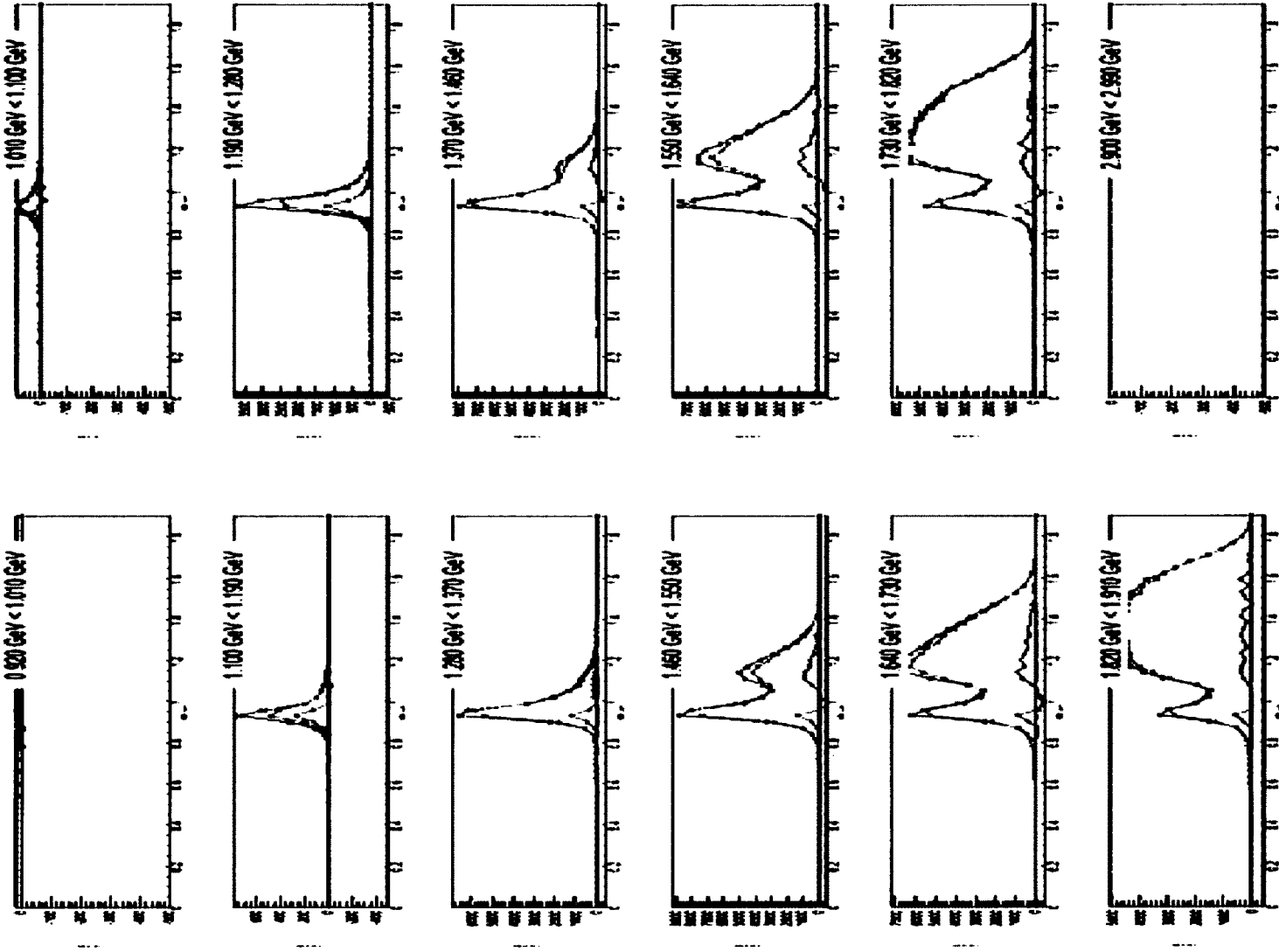


FIG. 76 Missing mass spectrum for $d(e, e' \pi^+ P)X$ for 2.5 GeV negative torus.

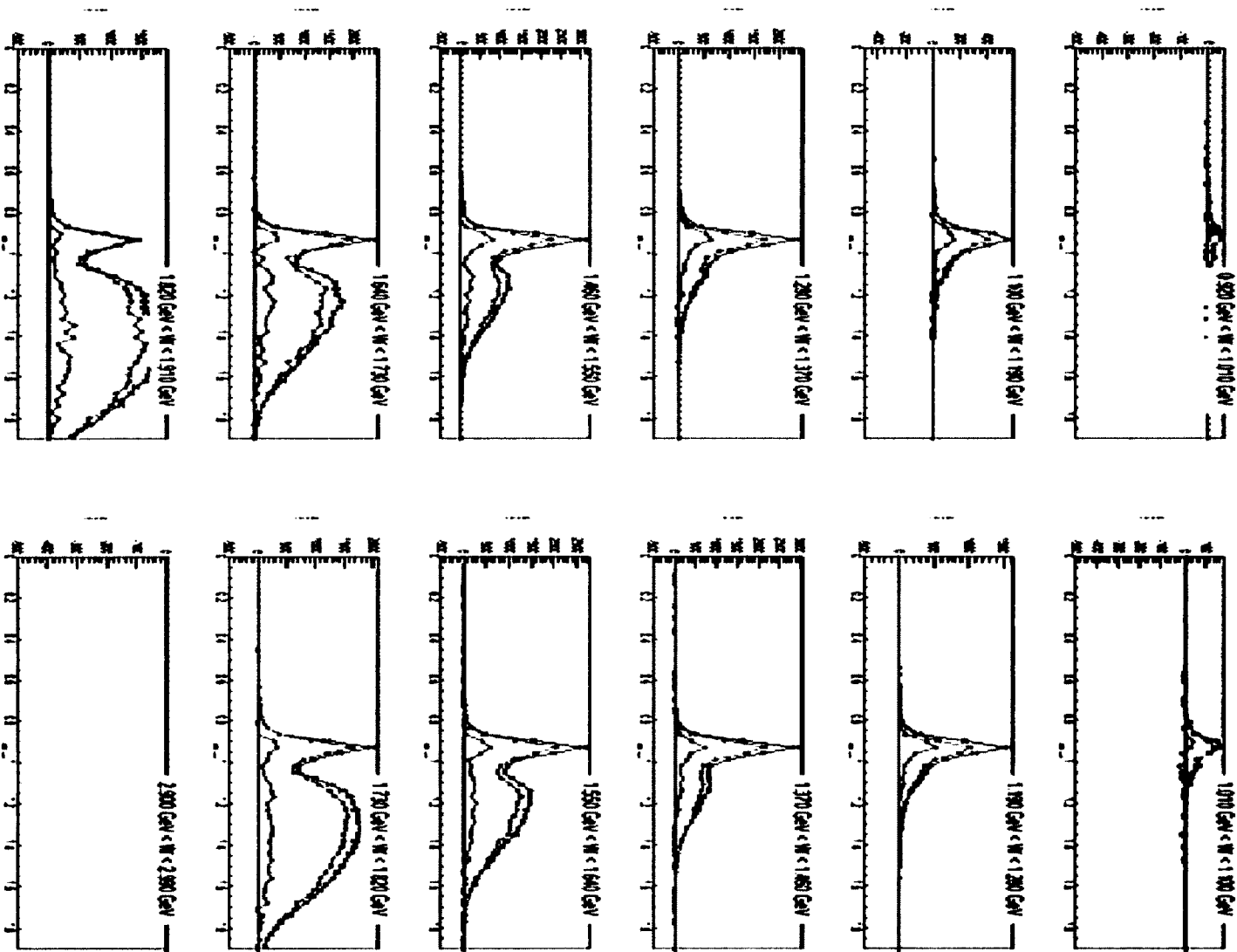


FIG. 77 Missing mass spectrum for $d(e,e'\pi^-)X$ for 4.2 GeV positive torus.

VITA

Sharon Lee Careccia
Physics Department
Old Dominion University
Norfolk, VA 23529

Education

Ph.D. Physics

Old Dominion University, Norfolk, Va. 2003 – 2011

M. S. Physics

Old Dominion University, Norfolk, Va. 2003

Bachelor of Science Physics

Old Dominion University, Norfolk, Va. 2001

Bachelor of Science Engineering Technology

Old Dominion University, Norfolk, Va. 1992

Teaching Experience

Teaching Assistant

Old Dominion University, Norfolk, Va. 2002 – 2012

Engineering Technology Instructor

ITT Technical Institute, Norfolk, Va. 1994 – 2000

AutoCAD Lab TA

Old Dominion University 1989 – 1992

Professional Affiliations

APS – American Physical Society

Jefferson Lab Users Group

Hall-B Collaboration